MODIFICATION OF NANO-SIZED ZINC ZEOLITIC 2-METHYLIMIDAZOLATE FRAMEWORKS (ZIF-8) BY SOLVENT ASSISTED LIGAND EXCHANGE AND POST-SYNTHETIC MODIFICATION TO ENHANCE FUNCTIONALITY TOWARDS CATALYSIS, GAS STORAGE AND DRUG DELIVERY

A thesis submitted in accordance with the requirements for the degree

Philosophiae Doctor

in the

Department of Chemistry

Faculty of Natural and Agricultural Sciences

at the

University of the Free State

by

Chih-Wei Tsai

Supervisor

Dr. E.H.G. Langner

2017

Acknowledgements

I would hereby like to thank all my friends, family and colleagues for their friendship, guidance, motivation amd support throughout my studies. Without them this study would not been possible. Special appreciation must be made to the following people:

My utmost repsect, acknowledgement and thank you to my promoter (Dr. Ernie Langner) for all your excellent guidance, patience, leadership, diligence and preseverance throughout the duration of my studies and the time devoted to my studies. You pull me throught the toughest time of my project.

I would like to acknowledge the head of the Physical chemistry group Prof. J.C. Swarts for his leadership, guidance and advice during my studies.

I would like to thank Dr. Elizabeth Erasmus for XPS analysis, Dr. Melanie Rademeyer for PXRD measurements and Dr. Linette Twigge for NMR analysis.

I would like to thank Dr. Valeska Ting and Dr. Mi Tian for high pressure Hydrogen adsorption studies and their hospitality during our stay at the University of Bath, United Kingdon.

My heartfelt gratitude to my parents, Kuo-Tsung and Feng-Chi Tsai, thank you for your continuous support, guidance, patience, inspiration and motivation throughout especially during tough times during my studies.

The Physical Chemistry group, thank you all for support, guidance and the good times we spend together not only as fellow work colleagues but as good friends throughout this study.

The Chemistry department and the University of the Free State, thank you for available resources and facilities.

To my friends, Shaun Murrel and Nadine Meyer, thank you for reading and assistance with language and grammar to make my thesis easier to understand.

The National Research Foundation and the University of the Free State, thank you for the financial support, without it I would not have achieve anything.

Table of contents

Table of Contents

Abstract

Zeolitic Imidazolate Framework-8 nanoparticles (nZIF-8) were successfully synthesized during isothermal benchtop reactions, with different reagent concentrations in methanol. At an optimal concentration, an average particle size of 22 nm was achieved for nZIF-8_{1500} with an external surface area of 320 m^2 g^{-1}. Addition of triethylamine (TEA) in different molar ratios during synthesis, increased the yield of nZIF-8 from 40 to 85 %. Particle sizes decreased to 16 nm at high TEA concentrations.

Time resolved Solvent Assisted Ligand Exchange (SALE) of nZIF-8 with 2-mercaptobenzimidazole, 2-aminobenzimidazole, 2-phenylimidazole and presynthetic modified benzimidazole-thioesters, resulted in a ~13% exchange of the 2-methylimidazolate linkers of nZIF-8. Following an identical SALE procedure, the exchange with imidazole and 2-nitroimidazole, both without any attached benzene rings, reached a maximum exchange of 86 and 66 %, resulting in new zni and frl topologies respectively. All the SALE processes gave particle sizes below 100 nm, except when 2-mercaptobenzimidazole and 2-nitroimidazole were used. All nZIF-8 materials with SOD topologies remained microporous throughout the SALE process. Four different post synthetic modification (PSM) techniques were developed for amino- and ester functionalised nZIF-8 particles. PSM of lithiated SALEM-2 with $(PPh_3)_2PdCl_2$, gave a 1.2 wt % Pd content, with an improved BET surface area (100 m^2 g^{-1} larger). An iron content of 8.3 wt % was achieved *via* amidation of amino functionalised nZIF-8 with ferrocenecarboxylic acid. Sebacoyl chloride and polyacrylic acid were successfully anchored to the surface of amino functionalised nZIF-8.

The SALE products of nZIF-8 were screened for catalysis of the Knoevenagel condensation between ferrocenecarboxaldehyde and malononitrile. Amine-containing nZIF-8 gave a lower TOF than nZIF-8_{1500}, suggesting a different catalytic pathway *via* an imine route. CO_2 adsorption of nZIF-8 was doubled to 77 cm^3 g^{-1}, after SALE with imidazole derivatives containing NO_2 and SH electron withdrawing groups. H_2 uptake of all nZIF-8 derivatives was on par with the Chahine rule, with SALEM-2_{16h}-Pd adsorbing 3.07 wt % of H_2 at 77 K.

Keywords: ZIF-8, nanoparticles, particle size, surface area, solvent assisted ligand exchange, post synthetic modification, ferrocene, gas storage, heterogeneous catalysis, Knoevenagel condensation.

Opsomming

Zeolitiese Imidasolaat Netwerk-8 nanodeeltjies (nZIF-8) is suksesvol gesintetiseer tydens isotermiese mengreaksies, met verskillende reagenskonsentrasies in metanol. By ‘n optimale konsentrasie is ‘n gemiddelde deeltjiegrootte van 22 nm vir nZIF-8_{1500} verkry, met ‘n eksterne oppervlakarea van 320 m^2 g^{-1}. Byvoeging van trietielamien (TEA) in verskillende molverhoudings tydens sintese, het die opbrengs van nZIF-8 van 40 na 85% verhoog. Die deeltjiegrootte het afgeneem tot 16 nm by hoë TEA konsentrasies.

Tydsveranderlike, oplosmiddelgesteunde liganduitruiling (SALE) van nZIF-8 met 2-merkaptobensimidasool, 2-aminobensimidasool, 2-fenielimidasool en pre-sinteties gemodifiseerde bensimidasool-tioësters, het ‘n ~13 % uitruiling van die 2-metielimidasool skakels van nZIF-8 tot gevolg gehad. Tydens ‘n identiese SALE proses, het die liganduitruiling met imidasool en 2-nitroimidasool, beide sonder enige aangehegde benseenringe, ‘n maksimum uitruiling van 86 en 66 % bereik, met nuwe zni en frl topologieë onderskeidelik. Al die SALE prosesse het deeltjiegroottes onder 100 nm tot gevolg gehad, buiten wanneer 2-merkaptobensimidasool en 2-nitroimidasool gebruik is. Alle nZIF-8 materiale met SOD topologieë het regdeur die SALE proses mikroporeus gebly. Vier verskillende na-sintese modifikasietegnieke (PSM) is ontwikkel vir amino- en estergefunksionaliseerde nZIF-8 deeltjies. PSM van gelitieerde SALEM-2 met $(PPh_3)_2PDCl_2$, het `n 1.2 wt % Pd inhoud, met `n verbeterde BET oppervlak area (100 m^2 g^{-1} groter) tot gevolg gehad. `n Ysterinhoud van 8.3 wt % is bereik *via* amidasie van die amino-gefunksionaliseerde nZIF-8 met ferroseenkarboksielsuur. Sebakoïelchloried en poli-akrielsuur is suksesvol geanker aan die oppervlakte van amino-gefunksionaliseerde nZIF-8.

Die SALE produkte van nZIF-8 is ondersoek as kataliste vir die Knoevenagel kondensasie tussen ferroseenkarboksaldehied en malonnitriel. Amienbevattende nZIF-8 het `n laer TOF as nZIF-$8_{1500}$ getoon, wat op `n ander katalitiese roete, *via* `n imien, gedui het. CO_2 adsorpsie van nZIF-8 het verdubbel tot 77 cm^3 g^{-1}, na SALE met imidasool derivate wat NO_2 en SH elektronontrekkende groepe bevat. H_2 opname van alle nZIF-8 derivate het die Chahine reël gevolg, met SALEM-2_{16h}-Pd wat 3.07 wt % H_2 by 77 K geabsorbeer het.

Sleutelwoorde: ZIF-8, nanodeeltjies, deeltjiegrootte, oppervlakarea, oplosmiddelgesteunde liganduitruiling, na-sintese aanpassing, ferroseen, gasberging, heterogene katalis, Knoevenagel kondensasie.

List of Abbreviations

5-FU	5-fluorouracil
acac	Acetylacetonate
AFM	Atomic Force Miscroscopy
NH_2BzIm	2-aminobenzimidazole
bdc	1,4-benzenedi-carboxylate
bdc-Br	2-bromo-1,4-benzenedicarboxylate
BET	Brunauer-Emett-Teller
BODIPY	dipyrro-methene
bpdc-NH_2	2-amino-4,4'-biphenyldicarboxylate
BzIm	Benzimidazole
cbIm	Chlorobenzimidazole
CCDC	Cambridge Crystallographic Data Centre
C-dots	Carbon nanodots
Cp	cycopentadienyl
CTAB	Cetyltrimethylammonium bromide
CTAB	Cetyltrimethylammonium bromide
dabco	1,4-diazabicyclo[2.2.2]octane
DEF	N,N-diethylformamide
dhbc	2,5-dihydroxybenzoate
DMF	N,N-Dimethylformamide
DOX	Doxorubicin
dped	meso-1,2-di(4-pyridyl)-1,2-ethanediol
EDS	Energy-dispersive X-ray Spectroscopy
EISA	Evaporated Induced Self Assembly
eV	Electron Volts
fbIm	5-(trifluoromethyl)benzimidazol
FcCHO	Ferrocenecarboxaldehyde
FTIR	Fourier Transform Infrared
FWHM	Full Width at Half Maximum
ICP-OES	Inductively Coupled Plasma – Optical emission spectrometry

List of Abbreviations

IM	Imidazolate
Ir(COD)(MeCp)	(methylcyclopentadienyl)(1,5-cyclooctadiene)iridium(I))
MeIM	2-methylimidazolate
MeOH	Methanol
MIL	Matériaux de l'Institut Lavoisier
MOF	Metal Organic Framework
MWCO	Molecular-weight cutoffs
nbIm	5-nitrobenzimidazolate
nbp	4,4'-(2,6-naphthalenediyl)bipyridine
nBuLi	n-Butyllithium
ndc	1,4-naphthalenedicarboxylate
nIm	nitroimidazolate
NMR	Nuclear Magnetic Resonance
NTB	Nitrilotrisbenzoic acid
nZIF-8	nanoparticles Zeolitic Imidazolate Framework 8
PSM	Post Synthetic Modification
pur	purine
PXRD	Powder X-ray Diffraction
SALE	Solvent Assisted Ligand Exchange
SEM	Scanning Electron Microscopy
SSNMR	Solid State Nuclear Magnetic Resonance
STP	Standard Temperature Pressure
TEA	triethylamine
TEM	Transmission Electron Microscopy
TGA	Thermogravimetric Analysis
THF	Tetrahydrofuran
tmbbp	2,3,5,6-Tetramethyl-1,4-bis(4-pyridyl)benzene
tmbebp	2,3,5,6-Tetramethyl-1,4-bis-ethynyl-(4-pyridyl)-benzene)
TOF	Turnover Frequency
UV/vis	Ultratviolet/visible spectroscopy
XPS	X-ray photoelectron spectroscopy

1 Introduction

1.1 Introduction

The search for new materials with real life applications has always been challenging. One such family of crystalline and microporous materials, known as zeolites, were first discovered as natural compounds in 1765 by Cronstedt.[1] Although artificial synthesis of zeolites began in 1862, it was only during the 1950s, with the discovery of artificial synthesis routes allowing the formation of different and exotic structures, that zeolites found substantial application in, industry.[2,3] Since then, extensive research on zeolites led to a wide range of applications from catalysis to gas separation and ion-exchange. Recently, investigations started on zeolites as drug carriers.[3,4] This ongoing search for versatility and the improvement of zeolites also gave rise to Metal Organic Frameworks or MOFs, organic-inorganic hybrid coordination polymers with unique porous structures and crystalline properties, some similar to zeolites.

After the term MOFs was introduced in 1995, the variety of these compounds increased dramatically after the early 2000s, with over 6000 MOF structures identified since 2010.[5] MOFs can form one, two or three dimensional rigid structures during crystallization, with metal centres interlinked through coordination with organic bridging ligands.[6] Although various synthetic techniques have been developed for MOFs, solvothermal conditions are the most commonly used, and even led to the discovery of MOF nanoparticles in 2003.[7] One unique characteristic of MOFs is their extreme surface areas reaching over 7000 $m^2 g^{-1}$, even larger than those of zeolites and activated carbon.[8] MOFs, with their high chemical and thermal stability, ranging from 250 till 500 ℃, and variety of different pore aperture sizes,[5] have opened doors to a number of applications like heterogeneous catalysis, gas separations, membranes, microelectronics and drug delivery, to name a few.[5,9,10] MOFs are also feasible candidates for reaching the U.S. Department of Energy's targets to adsorb 5.5 wt % of hydrogen in various adsorption systems by 2015.[11,12,13] In terms of carbon dioxide capture or separation, MOFs have shown great improvement over existing materials such as industrially available BPL carbon.[14,15] One drawback of zeolites is their lack of versatility for functionalization, which is limited to only a few moieties. MOFs, on the other hand, have organic linkers which can be chemically tailored for post synthetic modifications (PSM) to enhance functionality.[5,16] PSM remains challenging due to low reactivity

when treating the insoluble solid MOFs as molecules. By synthesising the MOFs as nanoparticles, better reactivity may be achieved.

A subclass of MOFs with zeolitic characteristics, known as Zeolitic imidazolate frameworks (ZIFs), first reported in 2006 will be the main focus of this study.[17] ZIFs have imidazolate derivatives as organic linkers, tetrahedrally coordinated to bivalent metal (M^{2+}) cations, with a unique bonding angle of 145° that mimics the Si-O-Si angle found in zeolites (**Figure 1.1, p 2**). The classification of ZIF structures is based on the zeolite system, with the sodalite (SOD) topology being the most commonly found for ZIFs.

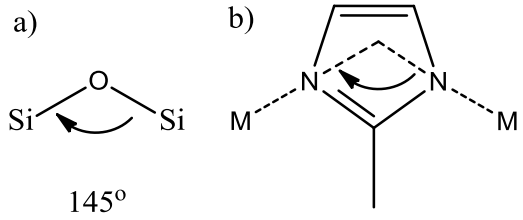

Figure 1.1 Bridging angles of 145° between a) silicon and oxygen in zeolites and b) metal center and imidazolate linkers in ZIFs.

The nano-sized variant of ZIF-8 (nZIF-8), constructed from zinc metal centres and 2-methylimidazolate ligands, will serve as the base material in this study. The micro-sized variant is commercially available as Basolite® Z1200. Nanoparticles, with their larger external surface area when compared to their micro-sized counterparts, have great potential in industrial applications. ZIF-8, with its SOD topology and truncated octahedral shape, has a BET surface area of 1600 $m^2\ g^{-1}$ and a pore aperture of 3.4 Å . ZIF-8 is thermally stable up to 400 ℃, and has attracted attention due to its potential in gas storage, gas separation, sensors, catalysis and drug delivery.[18] The catalytic activity of nZIF-8, in terms of this study, is the result of active groups on the external surface of the particles. To enhance the properties of nZIF-8 in this regard various techniques can be employed: particle size control using a combination of appropriate reaction conditions (concentration and temperature) and trimethylamine to give smaller particles with a larger external surface area and expose the active Lewis acid and basic sites for heterogeneous catalysis, such as Knoevenagel condensation. Modification of the organic linkers can be achieved *via* solvent assisted ligand exchange (SALE), where the 2-methylimidazolate linkers can be replaced by different, functionalized imidazolates, while maintaining the SOD structure. The additional functional groups may be further post synthetically modified towards new applications. Ferrocene, an organometallic compound with an Fe^{2+} centre, has shown promising results in antitumor trials as well as catalysis. Targeted and safe administering of anti-cancer drugs in the body remains a challenge. Nano-ZIF-8 has potential as such a drug carrier. In

general, this study is focused on the chemical enhancements of nZIF-8 through new synthetic avenues, to produce nanoparticles that are diversely functionalized and aimed at a variety of applications.

1.2 Aims of this study

With this background, this study with focus on the following:

1) The synthesis of ZIF-8 nanoparticles smaller than 30 nm by applying particle size control through the effect of solvent (methanol) to reagents ratio to maximise the external surface area, as well as the effect of trimethylamine as additive, to maximise the yield. These measures will be weighed against the ease of isolating the particles from suspension.
2) Pre-synthetic modification and characterisation (^{1}H NMR and FT-IR) of imidazole ligands by the attachment of long alkyl chains (where n = 1, 2, 3 and 4) with ester functional groups. These modified imidazoles will be introduced into nZIF-8 *via* SALE to provide active sites for the attachments of drugs and catalysts.
3) Synthesis of suitable ferrocene derivatives with aldehyde and amine functional groups (characterised by ^{1}H NMR and FT-IR) for catalytic testing as well as post synthetic grafting *via* biodegradable bonds to the external surface area of modified ZIF-8 nanoparticles.
4) Optimised, as well as time resolved Solvent Assisted Ligand Exchange (SALE) of nZIF-8 with a series of imidazolate linkers functionalised with thiol, ester, amine, nitro or phenyl functional groups, some suitable for anchoring specific molecules. The effect of these new functional groups on the structure and chemical composition of nZIF-8 will be thoroughly investigated. The extent of ligand exchange on the external surface will be quantified.
5) Post synthetic modification *via* grafting of various moieties (ferrocenyl derivatives (drugs), $(PPh_3)_2PdCl_2$ (catalyst), sebacoyl chloride (short alkyl chain) and polyacrylic acid (polymer)) onto the surface of SALE ZIF compounds.
6) All synthesised nanoparticles *via* SALE and PSM will be characterised by infrared spectroscopy (FR-IR), ^{1}H nuclear magnetic resonance (NMR), ^{13}C solid-state nuclear magnetic resonance (SSNMR), transmission electron spectroscopy (TEM), and powder X-ray diffraction (PXRD). Metal elements in the compounds will be identified by energy dispersive X-ray spectroscopy, X-ray photoelectron spectroscopy (XPS) and inductively coupled plasma optical emission spectrometry (ICP-OES).

7) Porosity analyses (BET surface area, t-plot external surface area and micropore volume) will be performed on all ZIF derivatives with the Accelerated Surface Area and Porosity Analyser (ASAP).

8) Thermal analyses of all ZIF derivatives to establish their thermal stability and decomposition behaviour.

9) Catalytic testing using a Knoevenagel condensation, with modified nZIF-8 nanoparticles as catalysts, will be followed by UV/vis. The effect of various functional groups and structures on catalytic activity will be investigated. The effect of surface bound NH_2 functionalities on the catalytic activity of SALE nZIF-8 particles will be quantified.

10) The effect of various functional groups attached to SALE nZIF nanoparticles on their CO_2 and H_2 adsorption capabilities will be investigated by low pressure surface area and porosity analysis (CO_2) and high pressure sorption measurements (H_2).

1.3 References

1 M. E. Davis, *Nature*, 2002, **417**, 813–821.

2 N. E. R. Zimmermann and M. Haranczyk, *Cryst. Growth Des.*, 2016, **16**, 3043–3048.

3 E. M. Flanigen, R. W. Broach and S. T. Wilson, *Zeolites in Industrial Separation and Catalysis*, John Wiley & Sons, 2010, 2010.

4 J. M. Rosenholm and M. Lindén, *J. Control. Release*, 2008, **128**, 157–164.

5 H. Furukawa, K. E. Cordova, M. O'Keeffe and O. M. Yaghi, *Science*, 2010, **9**, 1230444.

6 S. L. James, *Chem. Soc. Rev.*, 2003, **32**, 276–288.

7 N. Stock and S. Biswas, *Chem. Rev.*, 2012, **112**, 933–969.

8 O. Farha, I. Eryazici, N. C. Jeong, B. Hauser, C. Wilmer, A. Sarjeant, R. Snurr and S. Nguyen, *J. Am. Chem. Soc.*, 2012, **134**, 15016–15021.

9 S. Eslava, L. Zhang, S. Esconjauregui, J. Yang, K. Vanstreels, M. R. Baklanov and E. Saiz, *Chem. Mater.*, 2013, **25**, 27–33.

10 Y. Cui, B. Li, H. He, W. Zhou, B. Chen and G. Qian, *Acc. Chem. Res.*, 2016, **49**, 483–493.

11 Y. Basdogan and S. Keskin, *CrystEngComm*, 2014, **17**, 261–275.

12 H. W. Langmi, J. Ren, B. North, M. Mathe and D. Bessarabov, *Electrochim. Acta*, 2013, **128**, 368–392.

13 A. G. Wong-Foy, A. J. Matzger and O. M. Yaghi, *J. Am. Chem. Soc.*, 2006, **128**, 3494–3495.

14 A. Phan, C. J. Doonan, F. J. Uribe-Romo, C. B. Knobler, M. Okeeffe and O. M. Yaghi,

Acc. Chem. Res., 2010, **43**, 58–67.

15 K. Sumida, D. L. Rogow, J. A. Mason, T. M. McDonald, E. D. Bloch, Z. R. Herm, T. H. Bae and J. R. Long, *Chem. Rev.*, 2012, **112**, 724–781.

16 T. Yokoi, Y. Kubota and T. Tatsumi, *Appl. Catal. A Gen.*, 2012, **421-422**, 14–37.

17 K. S. Park, Z. Ni, A. P. Côté, J. Y. Choi, R. Huang, F. J. Uribe-Romo, H. K. Chae, M. O'Keeffe and O. M. Yaghi, *Proc. Natl. Acad. Sci. U. S. A.*, 2006, **103**, 10186–10191.

18 B. Chen, Z. Yang, Y. Zhu and Y. Xia, *J. Mater. Chem. A Mater. energy Sustain.*, 2014, **2**, 16811–16831.

INTRODUCTION

2 Literature Survey

2.1 Introduction

Since the discovery of natural crystalline microporous materials - known as zeolites - in the late 1750s, over 170 structures had been identified. The material consisting, of AlO_4 and SiO_4 linked together by oxygen ions in a tetrahedral framework may have acidic, basic and neutral properties. Zeolites were used as the first molecular sieves to adsorb water and it was only later from 1959, when the first zeolites were used as catalysts. The past 6 decades, from the 1950s, have seen a wide expansion in the use of zeolites in industry, mainly for gas separation, petroleum cracking, ion exchange, water purification, drug delivery and catalysis.[1,2] The use of zeolitic catalysts greatly increased the conversion and yield during fuel synthesis and refinery by over 30 %.[3] A decrease in coke formation was observed but also a low octane count. Y-zeolites are the most frequently used with some of the aluminium removed from the framework.[4] Zeolites were synthesised artificially by hydrothermal crystallization since the early 1940s this led to the continuous discovery of new structures in the search for catalysts with high selectivity and is still a wide area of research today.[2,3] The drive to develop new porous materials lead to the recent discovery of porous coordination polymers, also known as metal organic frameworks (MOFs). Easily accessible metal ions and functionalizable organic linkers are used to make up the integral part of the framework that can mimic the topologies of zeolites to further improve or match properties (chemical resistance, pore size , thermal stability).[4,5] MOFs as a new area of study continue to attract large interest amongst scientists and industry.

MOFs have great capability to be used in catalysis and can be used as Lewis acid catalysts, Brønsted acid catalysts, base catalysts, enantioselective catalysts, C-C bond formation polymerization catalysts and can also be used as supports for nano-metallic particles and organometallic moieties supported on the MOFs to act as catalysts.[6]

This work will focus mainly on ZIF-8 (ZIF = Zeolitic Imidazolate Framework), a sub class of MOFs, with special emphasis on methods for improved synthesis, characterisation, ligand exchange, post synthetic modification and applications in catalysis, gas storage and drug carriers.

2.2 Metal Organic Framework

The Hofmann complex ($Ni(CN)_2(NH_3).C_6H_6$) was discovered in 1897, as a coordination network which can encapsulate benzene rings. Researchers have expanded the Hofmann complex to synthesise new materials having larger cavities. Robson reported the first example of an organic coordination network in 1989. It was only in 1995 where two independent groups, Zaworotko and Yaghi, synthesised the first MOFs with pore sizes larger than zeolites and in the late 1990s the first gas adsorption properties of MOFs were reported by Kitagawa *et al.*[7] Since this work there have been a few well-known MOFs synthesised with unique structures and having a wide range of diverse properties. For example: MIL-100(Fe) for hydrophilic properties[8], IRMOF-3 as a base catalyst[6], HKUST is highly hydrophilic and a Lewis acid[6], MOF-177 for high CO_2 adsorption[9], BioMIL-1 for being biodegradable[10], NU-110E with extremely high surface areas[11] and ZIFs for hydrophobic properties[8], nanoparticles and zeolite properties[12].

2.2.1 Pore Size of MOFs

Natural zeolites consist of small pores which limits catalysis of large molecules and when pores are too large it imposes confinement effects. However, MOFs have a diverse range of pore sizes and structures which can be synthesised with pores ranging from ultra-microporous to mesoporous (**Figure 2.1, p 9**) which provides a wide range of pore sizes for various applications.[6] Some MOFs contains multi "cage" pore (structure) systems such as the HKUST-1, having channels that intersect at cavities with diameters of 11 Å and 13 Å which is interconnected with "windows" (apertures) of 6.9 Å and secondary pores of 6.9 Å in diameter with a 4.1 Å window.[13]

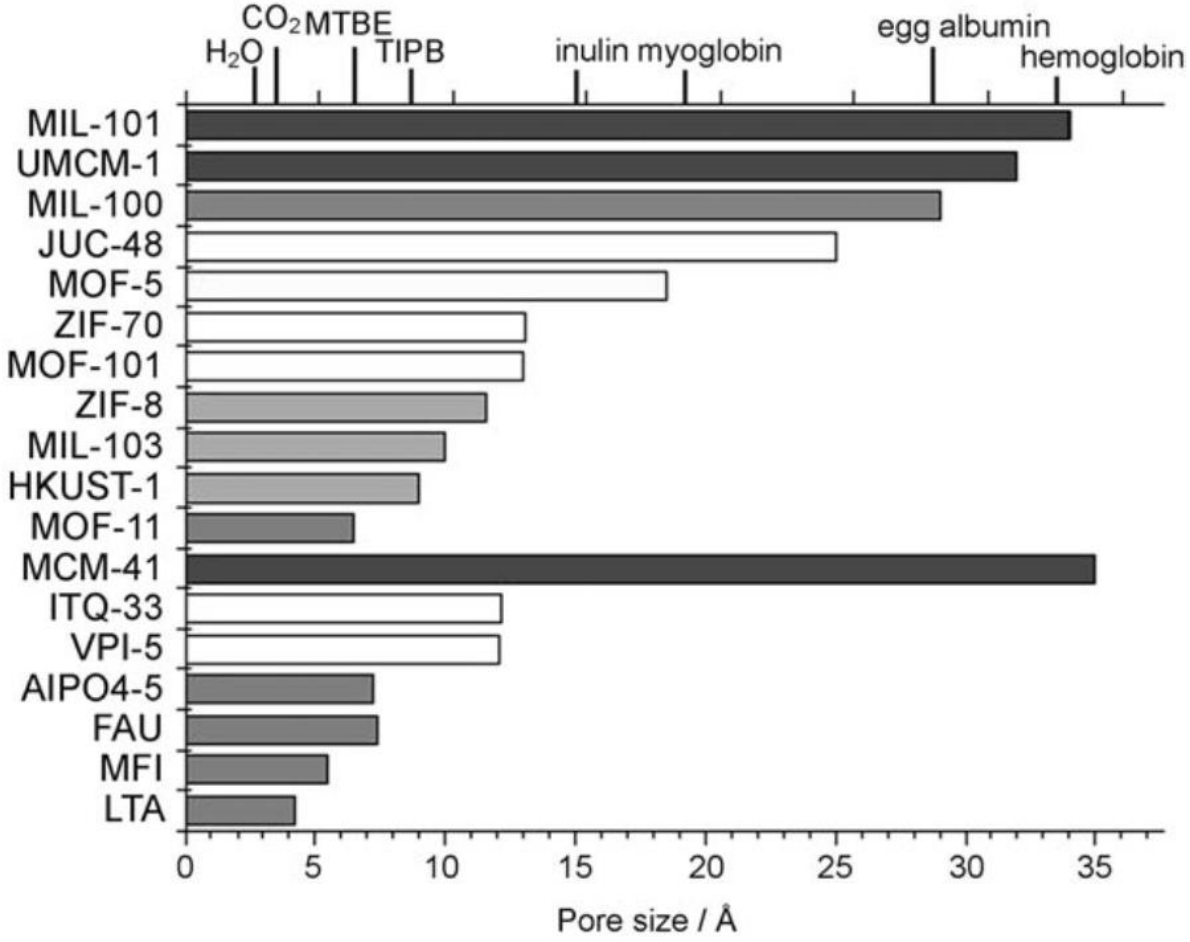

Figure 2.1 Graph comparison of MOFs (from MIL-101 down to MOF-11) pore size to aluminosilicates (aluminosilicates: MCM- 41, ITQ-33, VPI-5, FAU, MFI, LTA) and aluminophosphates (aluminophosphates: AlPO4-5). Size of guest molecules are also listed.[6] (Reprinted (adapted) with permission from D. Farrusseng, S. Aguado and C. Pinel, *Angew. Chemie - Int. Ed.*, 2009, **48**, 7502–7513. Copyright (2009) Wiley)

2.2.2 Pore Flexibility of MOFs

Unlike zeolites, which have a rigid structure, MOFs have dynamic features, caused by rotation in the organic parts due to external stimulation such as heat or guest molecules, *e.g.* the aromatic ligands in IRMOF and $Zn_4O(NTB)_2$ (NTB = nitrilotrisbenzoic acid).[14,15] Another example is MIL-53, which can shrink or expand the pores thus having a breathing effect cause by the polarity of guest molecules like CO_2. A fairly nonporous coordination polymer, Cu(4,4′-bipy)$(dhbc)_2 \cdot H_2O$ (4,4′-bipy = 4,4′-bipyridine; dhbc = 2,5-dihydroxybenzoate), transforms to a porous material during gas adsorption where at a certain pressures the "gate" opens.[16]

2.2.3 Post Synthetic Modification (PSM) of MOFs

In 1990 Robson *et al*. suggested that the building blocks of the frameworks can be chemically modified after construction of the lattice.[17] This has been achieved with microporous silicates (MCM-41) where an organic silane was attached to the surface providing functional groups such as thiols and amines to enhance catalytic ability or to complex various metals.[18,19,20] MOFs, like zeolites, are insoluble, which can be challenging in terms of solubility, diffusivity, reactivity and characterisation. The huge advantage of MOFs is that it is composed of organic building blocks, and is thus not limited to the use of silanes. The organic building blocks could be premade with functional groups before the crystallization of MOFs. Despite having functional groups only a few attempts have been made to graft or post synthetically modify MOFs.[21] PSM is a great method to introduce additional functionality to MOFs, especially to linkers where modification is not compatible or stable during MOF synthesis. IRMOF-3 is one of the few MOFs with amino functional groups ,which was initially post synthetically modified with acid anhydride[22] (**Figure 2.2.a, p 10**) or isocyanates to produce urea functionalized MOFs[23] (**Figure 2.2.b, p 10**). During another form of PSM, coordinate covalent modification an organic linker on the framework is modified with different chelators (-OH or -COOH groups) to complex metal ions as described by the reaction with aldehydes to form imines and subsequently binding with $V(O)acac_2$ (acac = acetylacetonate) (**Figure 2.2.c, p 10**) by Rosseinsky *et al*.[24]

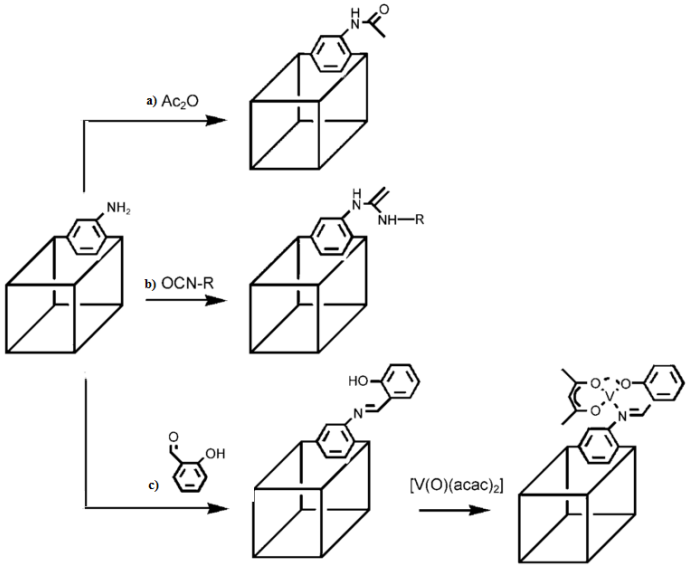

Figure 2.2 Post synthetic modification on amino groups examples a) acid anhydride b) isocyanates and c) aldehydes to vanadium complex.[6] (Reprinted (adapted) with permission from D. Farrusseng, S. Aguado and C. Pinel, *Angew. Chemie - Int. Ed.*, 2009, **48**, 7502–7513. Copyright (2009) Wiley)

A number of MOFs with amino groups have been tested and were successful for post synthetic modification: NH_2MILs[25,26], DMOF-NH_2[27], ring opening of 1,3-propane-sulfone and 2-methylaziridine in IRMOF-3[28] and formation of sulphide and sulfone on 4,40-biphenyldicarboxylate containing MOFs[29] etc[30]. MOFs with protected groups can be used to form unique MOFs which can be deprotected to allow further functionisation on the interior and exterior of the MOF.[31,32]

A simple method for MOFs to contain ferrocene (**Chapter 2.5, p 37**), for its biomedical applications, is by incorporating ferrocene into the pores especially in MIL-53, MIL-47 and MOF-5 which have pores large enough for ferrocene to enter.[33,34] Post synthetic modification with ferrocene compounds has recently been investigated. In 2009 Meilikhov *et al*. targeted the exposed OH groups on the terminal Al metal centres of MIL-53(Al). The OH group was then covalently bonded with 1,1′-ferrocenediyl-dimethylsilane having a 0.25 mol equivalent per unit of MIL-53.[35] Recent studies of MOFs containing amine group namely; IRMOF-3, UMCM-1NH_2, Zn_4O(bpdc-NH_2)$_3$ (bpdc-NH_2 = 2-amino-4,4'-biphenyldicarboxylate) and MIL-53-NH_2 showed that they can form amide bonds (**Scheme 2.1**, **p 11**) with ferrocene derivatives (ferrocenecarboxylic anhydride). Depending on pore size, the conversion obtained was 5 % (IRMOF-3) to 100 % (Zn_4O(bpdc-NH_2)$_3$) after 3 days.[36] The MOF Zn_4O(bdc-Br)$_3$ (bdc-Br = 2-bromo-1,4-benzenedicarboxylate) with a functional Br group on the benzene rings was subjected to palladium catalysed Suzuki coupling, to achieve binding of ferroceneboronic acid on the benzene ring with a 6 % conversion.[37]

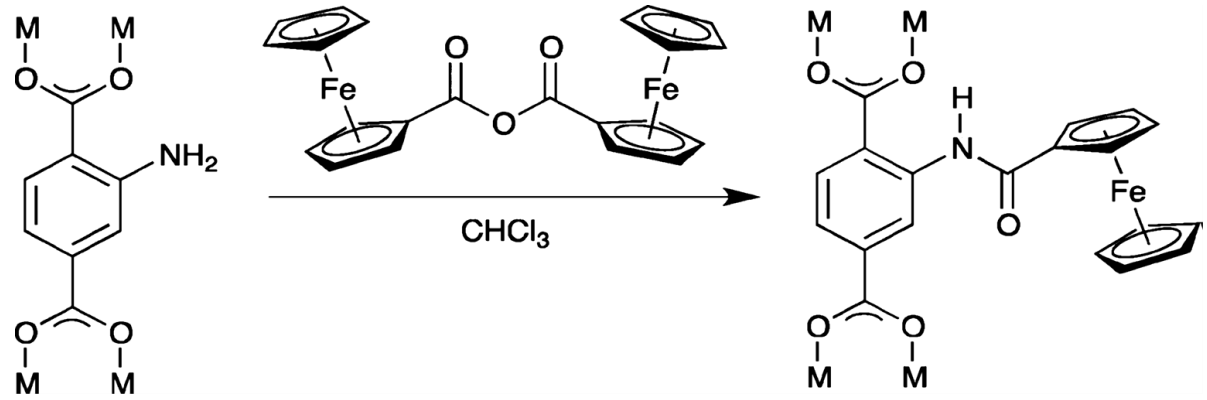

Scheme 2.1 Post Synthetic modification of Zn_4O(bpdc-NH_2)$_3$ MOF with ferrocenecarboxylic anhydride forming amide bonds.[36] (Reprinted (adapted) with permission from J. E. Halls, A. Hernán-Gómez, A. D. Burrows and F. Marken, *Dalton Trans.*, 2012, **41**, 1475–80.)

A well-known method to post-synthetically modify MOFs is by replacing the organic linkers by using solvent assisted ligand exchange (SALE). The advantage of SALE is to modify MOFs while retaining the parent MOF topology. The role of the solvent is still unclear but recent studies suggest that SALE is dependent on the solubility of the linkers in solution.[38] Recent studies show SALE can be targeted specifically on the external surface area. Kondo *et al.* work on a series of MOFs namely: $Zn_2(bdc)_2(dabco)$ and $Zn_2(ndc)_2(dabco)$ (bdc = 1,4-benzenedi-carboxylate, ndc = 1,4-naphthalenedicarboxylate, dabco = 1,4-diazabicyclo[2.2.2]octane), where the linkers was exchanged with boron dipyrro-methene (BODIPY) fluorescent dye and only the external surface was modified.[39]

Recent studies have proved the capabilities of SALE to increase the pore width of MOFs by replacing the existing organic linker with longer organic linkers in a pillared paddlewheel system (**Figure 2.3, p 12**). The length of the linker (dped) of SALEM-5 is 9 Å , which can be exchanged with the longer linker (tmbebp) (17 Å) to form SALEM-8.[40]

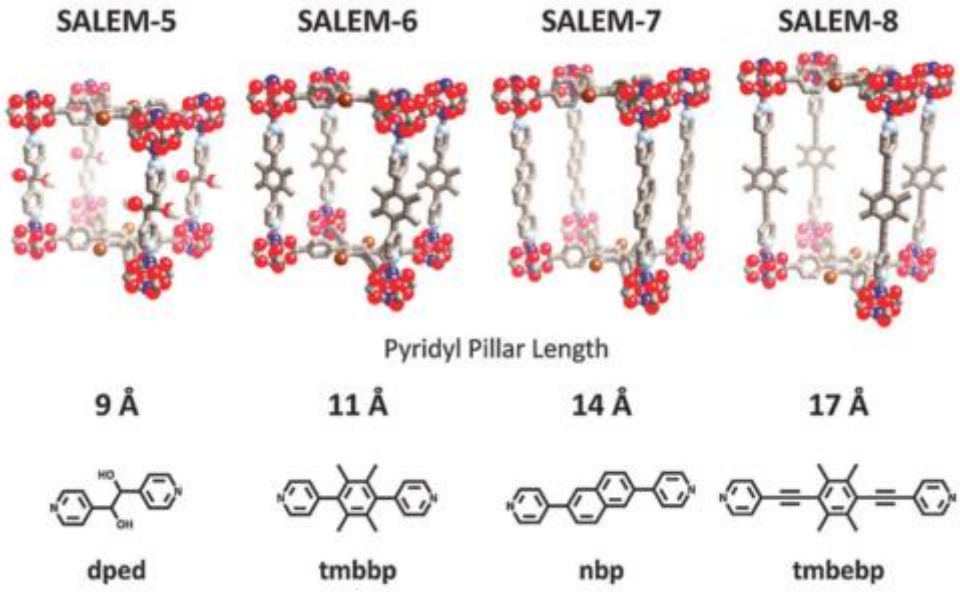

Figure 2.3 Increasing pore size: SALEM-5 with a series of pillared-paddlewheel MOFs by SALE. Length of the linkers in Å (dped = meso-1,2-di(4-pyridyl)-1,2-ethanediol , tmbbp = 2,3,5,6-Tetramethyl-1,4-bis(4-pyridyl)benzene, nbp = 4,4'-(2,6-naphthalenediyl)bipyridine, tmbebp = 2,3,5,6-Tetramethyl-1,4-bis-ethynyl-(4-pyridyl)- benzene).[38] (Reprinted (adapted) with permission from P. Deria, J. E. Mondloch, O. Karagiaridi, W. Bury, J. T. Hupp and O. K. Farha, *Chem Soc Rev*, 2014, **43**, 5896–5912.)

Recent PSM by SALE has been performed on ZIFs which will be discussed later (**Chapter 2.4, p 31**). In this study, ZIFs will form the main topic with ZIF-8 as the substrate for all the materials made.

2.2.4 Multivariate MOFs

A different approach to incorporate MOFs with various functional groups is by having multiple linkers in the synthesis process.[41] This process is still limited as linkers with different derivatives or length can produce a large variety of structures or amorphous materials. Deng *et al*. managed to synthesise eighteen multivariate MOF-5 structures containing up to eight different linkers in one phase. MOF-5 is originally made up of 1,4-benzenedicarboxylate where 8 different derivatives containing $-NH_2$, -Br, $-(Cl)_2$, $-NO_2$, $-(CH_3)_2$, $-C_4H_4$, $-(OC_3H_5)_2$, and $-(OC_7H_7)_2$ functional groups (**Figure 2.4, p 13**) was used. MOFs containing up to eight different derivatives were synthesise with different ratios. Interestingly they have reported that multivariate MOF-5 has shown improved H_2 uptake and better CO_2/CO selectivity than the original MOF-5.[42]

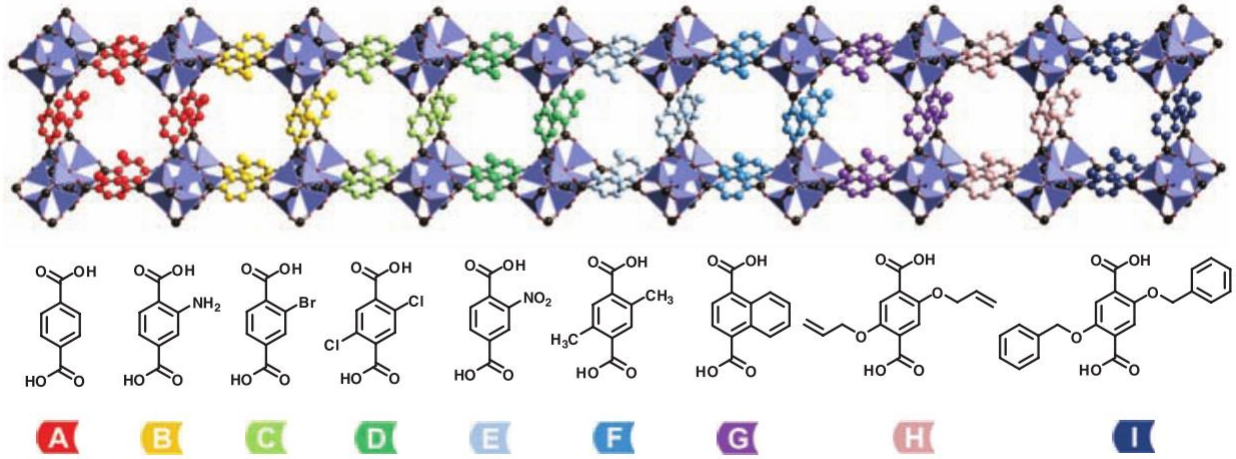

Figure 2.4 Multivariate A.) MOF-5 with 8 different derivatives B.) $-NH_2$, C.) -Br, D.) $-(Cl)_2$, E.) $-NO_2$, F.) $-(CH_3)_2$, G.) $-C_4H_4$, H.) $-(OC_3H_5)_2$, and I.) $-(OC_7H_7)_2$.[42] (Reprinted (adapted) with permission from H. Deng, C. J. Doonan, H. Furukawa, R. B. Ferreira, J. Towne, C. B. Knobler, B. Wang and O. M. Yaghi, *Science (80).*, 2010, **327**, 846–850. Copyright (2010) Science.)

2.3 Characteristics and Properties of Zeolitic Imdidazolate Framework (ZIF)

The focus of this study is on Zeolitic Imidazolate Frameworks (ZIF), a subclass of MOFs having unique properties from both MOFs and zeolites combined. ZIFs are composed of bivalent metal (M^{2+}) cations of mainly zinc or cobalt linked together by anionic imidazolate organic ligands in a tetrahedral coordination around the metal centre. Synthesising porous ZIFs is still challenging, as a number of Fe(II), Co(II), Cu(II) and Zn(II) compounds with different imidazolate (azolates) ligands gave rings, chains or zeolite-like tetrahedral nets that are nonporous or highly dense with low-symmetry.[12,43] The main feature for ZIFs is the ability to form structures or topologies similar to those of zeolites. The 145° angle between the nitrogen on the 1,3-positions of the imidazolate anion ring and the metal centre, mimics the Si-O-Si angle found in zeolites (**Scheme 2.2, p 14**). The organic linkers of the ZIF give cages or channels rather than the silicate oxide surfaces found in conventional zeolites.[12] ZIFs are mainly joined together by the small pore windows of the large cavities. Within the 5 years since 2010 more than 90 ZIF compounds have been synthesised compared to the more than 190 zeolites.[5,44]

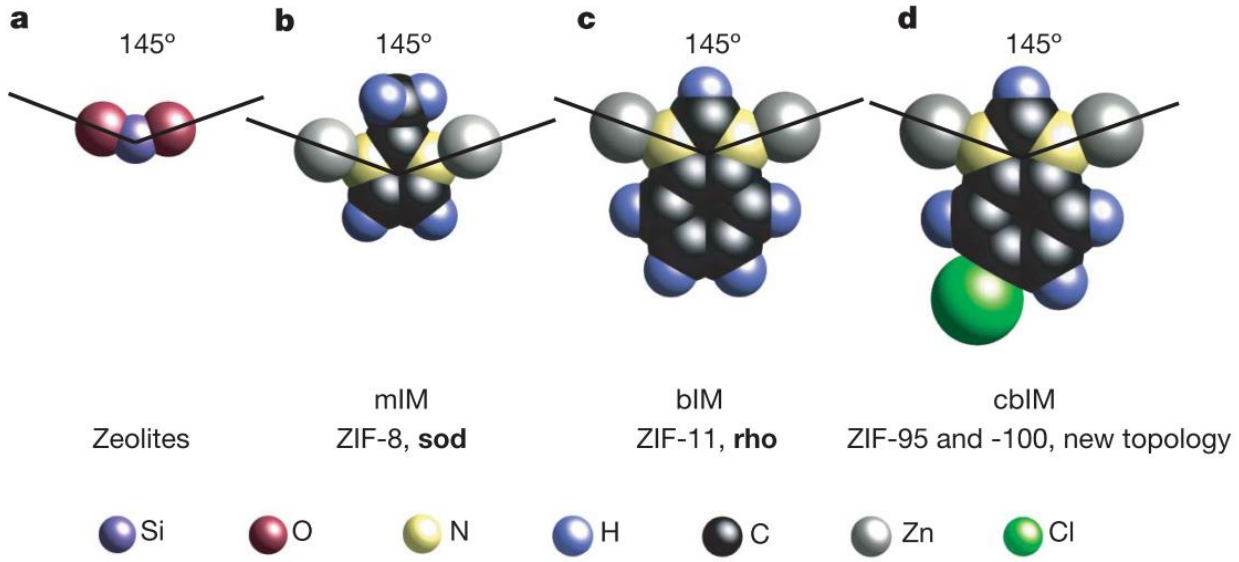

Scheme 2.2 The 145° bridging angles a) zeolites b) ZIF-8 c) ZIF-11 and d) ZIF-95 and ZIF-100. Elements represent by coloured balls.[12] (Reprinted (adapted) with permission from B. Wang, A. P. Côté, H. Furukawa, M. O'Keeffe and O. M. Yaghi, *Nature*, 2008, **453**, 207–211.Copyright (2008) Nature PublishingGroup.)

2.3.1 Introduction to ZIFs

The first twelve ZIFs from 1 to 12 (**Table 2.1, p 16**) was synthesised in 2006 by Park *et al.* using three imidazolate ligands *i.e*. imidazole (Im), 2-methylimidazole (MeIm) and benzimidazole (BzIm). Different metal centres were also used *e.g*. cobalt, zinc and indium. Indium and zinc were used in ZIF-5 to synthesise the first multi metal ZIF.[12] $Zn(Im)_2$ was synthesised in the 1980s, but the porosity was unknown, while $Zn(bzIm)_2$ coordination polymer was synthesised and crystal data was obtained in 2003.[45,46] The synthesis technique mostly relied on solvothermal methods - reacting a suitable hydrated metal salt or complex and a suitable organic imidazole linker. The synthesis was performed in a high boiling amide solvent such as N,N-diethylformamide (DEF) or N,N-Dimethylformamide (DMF) at 150 °C. The ZIF product was easily isolated by centrifugation or filtration after 48-96 hours.[12] Solvothermal conditions allow deprotonation of the imidazole linker by the amines from the thermal degradation of the amide solvent and the crystals usually form during the cooling process in moderate to high yields. The molar ratio and concentration between the metal ions and organic linkers as well as external factors such as temperature plays an important role in the synthesising of mono-crystalline materials. The bridging organic linker is expected to play a secondary role in directing the topology of the ZIF.[44] Even at these controlled conditions, in some cases the synthesis is only possible in small-scale reactions with yields only sufficient for single crystal analysis. Industrial large scale synthesis still remains challenging and only possible for a few ZIFs (e.g. ZIF-8 (Basolite Z1200)).[12,44,47]

Table 2.1 Well known ZIF compounds: composition, Net and structural parameters.[12,44,48,49]

ZIF-n	Composition	Net	Zeolite	d,[§] Å	N[¶]	Cage[*]
ZIF-1	$Zn(Im)_2$	crb	BCT	6.94	12	$[6^2.8^2]$
ZIF-2	$Zn(Im)_2$	crb	BCT	6.00	12	$[6^2.8^2]$
ZIF-3	$Zn(Im)_2$	dft	DFT	8.02	16	$[6^2.8^4]$
ZIF-4	$Zn(Im)_2$	cag	-	2.04	20	$[4^2.6^8]$
ZIF-5	$In_2Zn_3(Im)_{12}$	gar	-	3.03	20	$[4^2.6^8]$
ZIF-6	$Zn(Im)_2$	gis	GIS	8.80	20	$[4^6.8^4]$
ZIF-7	$Zn(BzIm)_2$	sad	SOD	4.31	24	$[4^6.6^8]$
ZIF-8	$Zn(MeIm)_2$	sad	SOD	11.60	24	$[4^6.6^8]$
ZIF-9	$Co(BzIm)_2$	sad	SOD	4.31	24	$[4^6.6^8]$
ZIF-10	$Zn(Im)_2$	mer	MER	12.12	24	$[4^{12}.8^6]$
ZIF-11	$Zn(BzIm)_2$	rho	RHO	14.64	48	$[4^{12}.6^8.8^6]$
ZIF-12	$Co(BzIm)_2$	rho	RHO	14.64	48	$[4^{12}.6^8.8^6]$
ZIF-14	$Zn(eIm)_2$	ana	ANA	2.2	24	$[6^2.8^3]$
ZIF-20	$Zn(Pur)_2$	lta	LTA	15.4	48	$[4^{12}.6^8.8^6]$
ZIF-23	$Zn(abIm)_2$	dia	-	4.2	10	$[6^4]$
ZIF-60	$Zn(Im)_{1.5}(mIm)_{0.5}$	mer	MER	9.4	24	$[4^{12}.8^6]$
ZIF-62	$Zn(Im)_{1.75}(bIm)_{0.25}$	cag	-	1.3	20	$[4^2.6^8]$
ZIF-68	Zn(bIM)(nIM)	gme	GME	10.3	24	$[4^6.8^3.12^2]$
ZIF-69	Zn(cbIM)(nIM)	gme	GME	7.8	24	$[4^6.8^3.12^2]$
ZIF-70	$Zn(Im)_{1.13}(nIM)_{0.87}$	gme	GME	15.9	24	$[4^6.8^3.12^2]$
ZIF-71	$Zn(dcIm)_2$	rho	RHO	16.5	48	$[4^{12}.6^8.8^6]$
ZIF-73	$Zn(nIM)_{1.74}(mbIM)_{0.26}$	frl	-	1	16	$[4^4.6^2.8^2]$
ZIF-74	Zn(nIm)(mbIm)	gis	GIS	2.6	20	$[4^6.8^4]$
ZIF-76	Zn(Im)(cbIm)	lta	LTA	12.2	48	$[4^{12}.6^8.8^6]$
ZIF-77	Zn(nIm)	frl	-	3.6	16	$[4^4.6^2.8^2]$
ZIF-95	$Zn(cbIm)_2$	poz	-	33.6 x 23.9	48	$[3^{16}.4^{28}.8^2.12^4]$
ZIF-95	$Zn(cbIm)_2$	poz	-	41.1 x 33.9	80	$[3^{32}.4^{36}.8^2.10^8.12^4]$
ZIF-100	$Zn(cbIm)_2$	moz	-	67.2	264	$[3^{48}.4^{108}.12^{26}]$

[§]Diameter of largest sphere that will fit in the framework. [¶] Number of vertices of the largest cage.

[*] Number of membered rings and size.

The twelve initial ZIFs have unique topologies, with a large variety of structures similar to those of zeolites (shown in **Figure 2.5, p 17**), as expected from the unique binding 145° bond angle. ZIFs related to zeolites have nets of ANA, MER, BCT, DFT, GIS, GME, LTA, RHO and SOD with two novel topologies, poz and moz.[50] The SOD topology is of main interest as it produces ZIFs with porous structures. The SOD topology is also amongst one of the more difficult topologies to obtain as it is found to be the least stable amongst high end geometries especially in $Zn(Im)_2$ polymorphs. Therefore, it is unlikely to synthesise $Zn(Im)_2$ ZIFs with SOD topology with conventional solvothermal methods. ZIF-8 with SOD topology was found to have a lower density compared to more scalable and non-scalable ZIFs or polymorphs.[47]

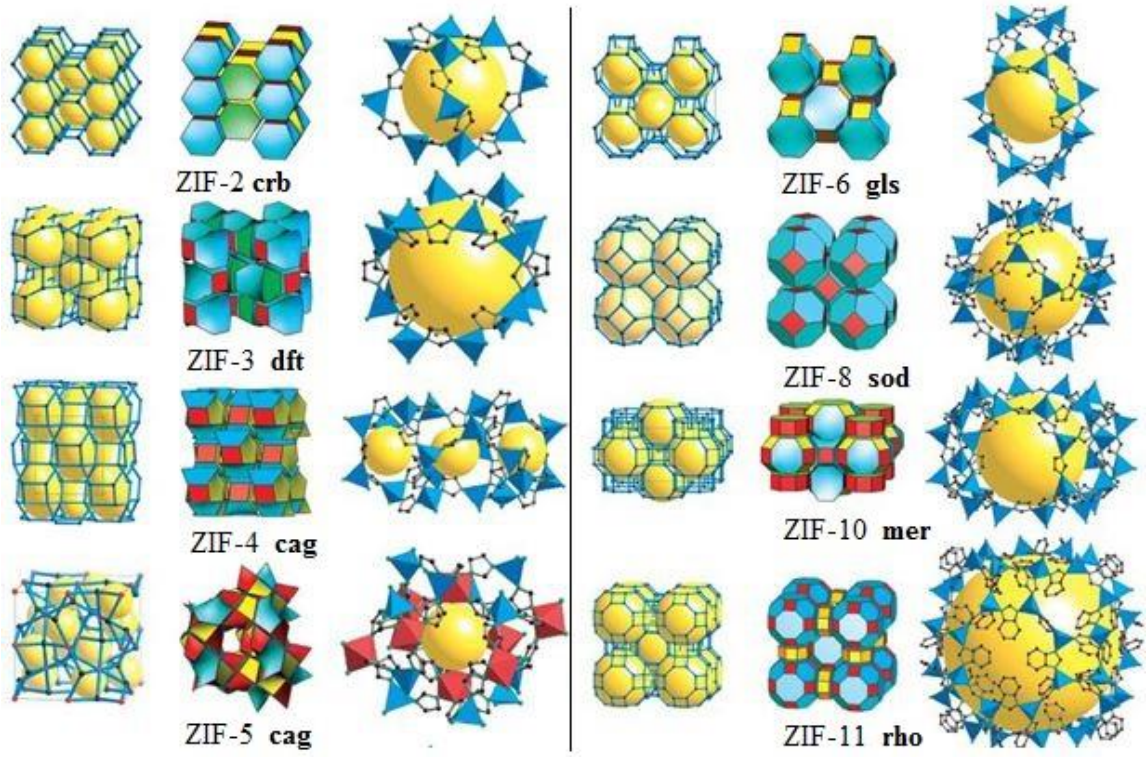

Figure 2.5 Single crystal x-ray structures of selected ZIFs: The network topology is shown as a stick diagram (left) and with tiling (center). The largest cage is represented by a yellow ball (right), with ZnN_4 tetrahedra shown in blue and, octahedra for ZIF-5, InN_6 shown in red. H atoms are omitted for clarity.[12] (Reprinted (adapted) with permission from K. S. Park, Z. Ni, A. P. Cote, J. Yong, R. Huang, F. J. Uribe-Romo, H. K. Chae, M. O'Keeffe, O. M. Yaghi, *PNAS*, 2006, **103**, 10186-10191. Copyright (2006) PNAS.)

Of the initial twelve ZIFs, only three have zeolite SOD topology, namely ZIF-7, ZIF-8 and ZIF-9. Only two, ZIF-4 and ZIF-5, did not obtain zeolite structures and have the smallest cavities. The largest pore aperture of the 6 membered ring of ZIF-8 is 3.4 Å (**Figure 2.6, p 18**) which is much smaller than Y Zeolites with an aperture of 8 Å.[4] However, ZIF-8 with its SOD topology has a cavity of 11.6 Å represented by the yellow sphere in (**Figure 2.6, p 18**) and shown in (**Table 2.1, p 16**) which is larger than the cavity of the zeolite counterpart because of the imidazole linker. ZIF-8 has a cubic space group of $I\bar{4}3m$ with a unit cell dimension of 16.32 Å as shown in (**Figure 2.6, p 18**).

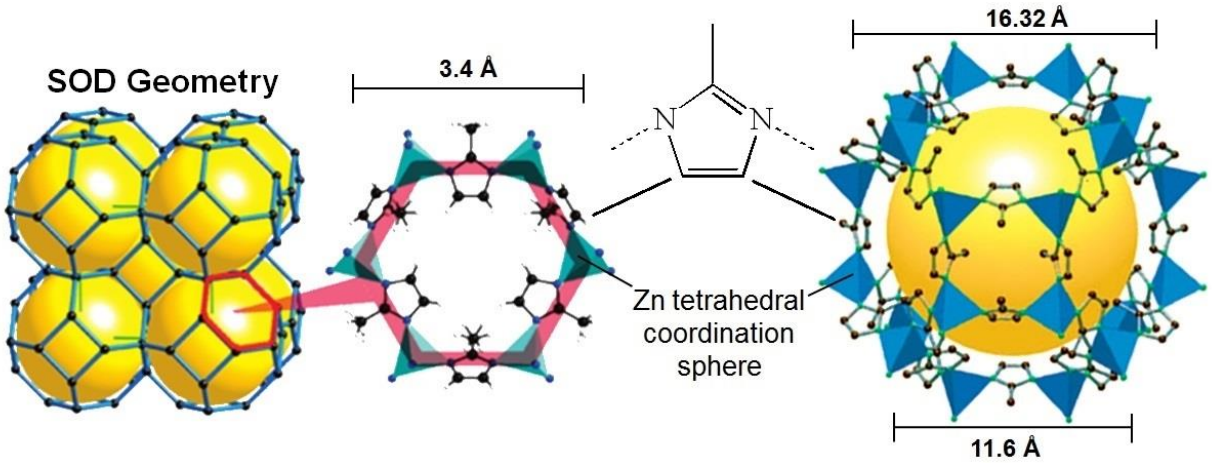

Figure 2.6 The SOD geometry of ZIF-8 showing the 3.4 Å pore aperture of the 6 membered ring, as well as the 11.6 Å pore volume (yellow sphere) and 16.3 Å unit cell size. Zinc tetrahedral coordination sphere (blue) and the organic linker (black).[12,51] (Reprinted (adapted) with permission from K. S. Park, Z. Ni, A. P. Cote, J. Yong, R. Huang, F. J. Uribe-Romo, H. K. Chae, M. O'Keeffe, O. M. Yaghi, *PNAS*, 2006, 103, 10186-10191 and Copyright (2006) PNAS.). (Reprinted (adapted) with permission from H. Bux, F. Liang, Y. Li, J. Cravillon, M. Wiebcke and J. Caro, *J. Am. Chem. Soc*., 2009, **131**, 16000-16001. Copyright (2009) American Chemical Society.)

The versatility of ZIFs lies in their organic linkers allowing a large number of ZIFs to be synthesised from various derivatives of imidazolate ligands (**Figure 2.7, p 19**) with a few listed in (**Table 2.1, p 16**). The use of large substituents can create unstable or metastable ZIFs having large structures, where the pores may be blocked, for example by using purine (pur) imidazolate linkers (**Figure 2.7, p 19**) to synthesise ZIF-20 (**Figure 2.8, p 20**). The pores (2.8 Å in diameter) are too small for even nitrogen to enter and ZIF-20 can thus be regarded as a "nonporous" material.[47,49]

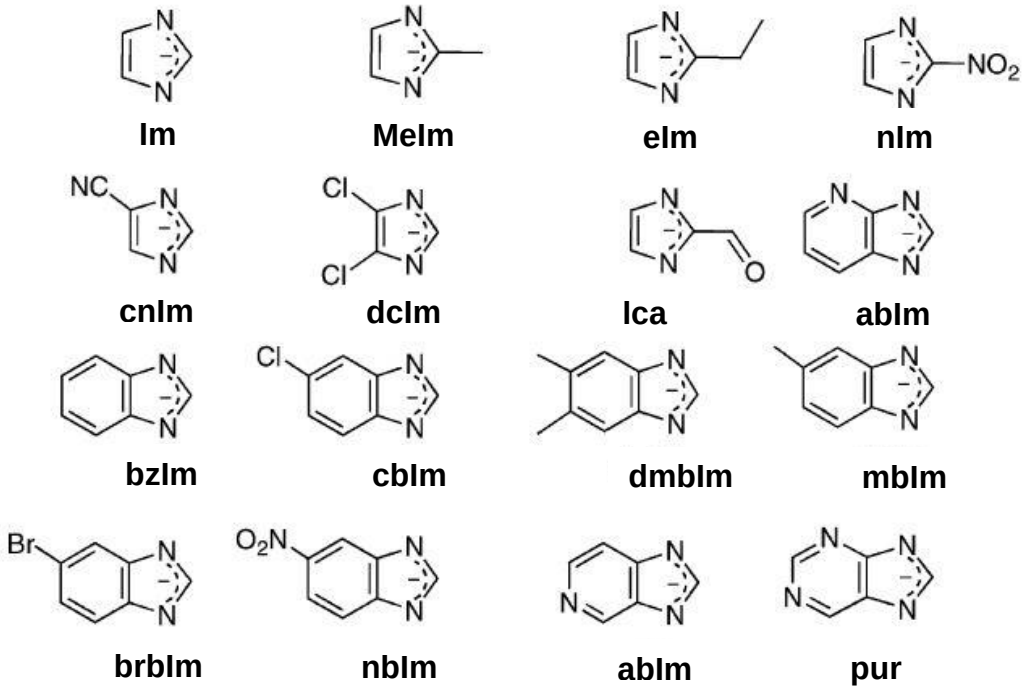

Figure 2.7 Examples of imidazole linkers used to synthesise ZIFs.[44] (Reprinted (adapted) with permission from A. Phan, C.J. Doonan, F. J. Uribe-Romo, C. B. Knobler, M. O'Keeffe, O. M. Yaghi, *Acc. Chem. Res*., 2009, **43**, 58-67. Copyright (2009) American Chemical Society.)

The ZIFs are microporous with an average cavity width of less than 20 Å.[4] ZIF-11, with benzimidazole (bzIm) linkers, is nonporous to nitrogen because the pore aperture is only 3.0 Å. The use of larger linkers such as benzimidazole with substituents on the 4 and 5 position of the benzene ring, prevents the formation of ZIFs with RHO topologies. The use of 5-chlorobenzimidazole (cbIm), shown in (**Figure 2.7, p 19**) lead to the formation of ZIF-95 having a new non zeolite topology named poz (**Figure 2.8, p 20**). The new topology is still tetrahedrally linked Zn nodes in 8, 10 and 12 membered rings. ZIF-95 synthesised in anhydrous conditions, leads to the formation of ZIF-100, a ZIF with a large complex topology called moz (**Figure 2.8, p 20**) with 264 vertices and 7524 atoms (264 metal atoms). ZIF-100 has a larger outer diameter (64.7 Å) than faujasite (18.1 Å) and MIL-101 (46.7 Å).[49] Similarly, ZIF-5 mentioned earlier with multi metals (Zn and In) can have octahedral and tetrahedral coordination metal nodes with the same net structure as the (4,6)-coordinated GAR structure found in $Ca_3Al_2Si_3O_{12}$.[12,44] Having such large variety of different derivatives of imidazolate ligands one is able to synthesise a large variety of single phase materials with different aperture sizes and topologies. Until now, it has become more popular to synthesise mixed metal or multi ligand ZIFs where a few are shown in (**Table 2.1, p 16**) and (**Figure 2.8, p 20**).

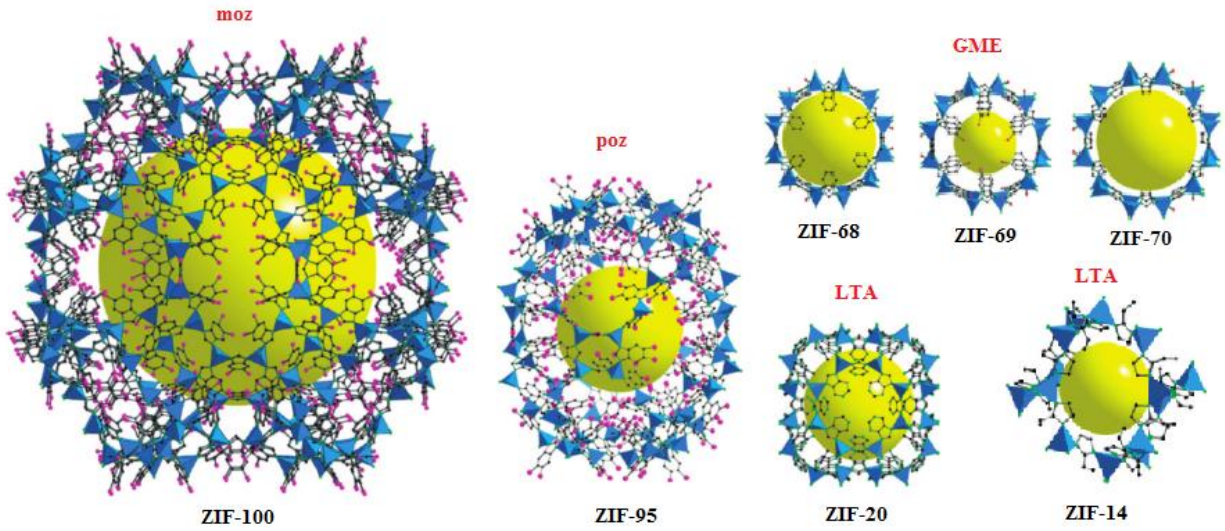

Figure 2.8 Single crystal x-ray structures of selected ZIFs: The topology shown in red. The largest cage is represented by a yellow ball, with ZnN4 tetrahedra shown in blue. H atoms are omitted for clarity.[44] (Reprinted (adapted) with permission from A. Phan, C. J. Doonan, F. J. Uribe-Romo, C. B. Knobler, M. Okeeffe and O. M. Yaghi, *Acc. Chem. Res.*, 2010, **43**, 58–67. Copyright (2009) American Chemical Society.)

2.3.2 Synthesis of ZIF-8

The solvothermal synthesis method mentioned earlier by Park *et al.* remained the most popular way to obtain ZIFs. The high potential for ZIFs in their applications has led to increased efforts to create new methods of producing ZIFs. The use of ultrasonification promotes the nucleation process which in return decreases the synthetic time dramatically, but larger particles were obtained with increasing sonocrystallization time.[52] This is due to Ostwald ripening that occurs when ZIF particles are sonicated and remains stable up to 5 minutes, but begin to form large particles after 10 minutes.[53] Different methods include anodic dissolution in a electrochemical cell giving ZIF particles of less than 1 μm in diameter.[54] Liquid assisted mechanochemistry of ZnO with NH_4^+ ions facilitates the formation of SOD topology ZIF[55], while dry mechanochemistry gave core-shell ZnO particles coated with ZIF-8 with overall particle sizes between 30 to 150 nm.[56] Microwave assisted solvothermal synthesis of ZIF-8 gave particles of 300 μm[51] and an aerosol/spray drying/EISA (Evaporated Induced Self Assembly) method gave particles of ~100 nm.[57,58]

Obtaining environmental friendly synthetic methods has been a challenging task in the synthesis of MOFs. In 2011 Pan *et al*. first devised a method to synthesise nZIF-8 (ZIF-8 nanoparticles) in an aqueous solution with a ratio of 1:70:1238 (Zn^{2+}:MeIm:H_2O) at room temperature. Within 5

minutes a 80 % yield was obtained with a particle size of 70 nm. A further increase in MeIm ratio to 200, reduced the particles to 50 nm.[59] Further investigations determined the minimal MeIm ratio of 40 is necessary to prevent the formation of zinc hydroxides byproducts, because the pH plays an important role in the ZIF-8 crystallization process.[60,61] To greatly reduce the amount of imidazolate (2 times ratio) ligand Yao *et al*. used two additives, ammonium hydroxide and nonionic triblock polymer (Pluronic P123) which deprotonates and attract metal ions respectively, with a yield of 99 %.[62] Cho *et al*. synthesised ZIF-8 via a sonochemical method and a pH study by using different ratios of triethylamine and NaOH as additives. They observed that the yield increased from 22 % to 93 % by increasing the pH from 7.1 to 9.3, but a large particle of ~200 nm was obtained.[63] Surfactants such as cetyltrimethylammonium bromide (CTAB) can be used as capping agents to slow down crystal growth thus obtaining particles of ~100 nm and changings the shape from truncated cubic to rhombic dodecahedron.[64]

Lian *et al*. synthesised ZIF-8 particles with 20 different amino acids as biomimetic crystallization agents. Amino acids, which are highly positive-charged, prevent crystal growth, while non-polar amino acids with increasing hydrophobicity produce particles of 1.5 μm to 0.5 μm. Amino acids with aromatic side chains gave truncated cubic particles (300 nm), while amino acids with hydroxyl groups (polar neutral) gave cubic particles and negatively charged amino acids gave the smallest spherical particles (200 nm).[65]

Recently in 2016, Polyzoidis *et al*. reported that the synthesis of ZIF-8 may be accelerated with a microreactor with a good output of 640 g/day. The study found that reactant concentration affects the morphology and reaction time affect the crystal size ranging from 150 nm to 600 nm for 0.5 h and 25 h respectively. In methanol, a very poor yield of 3 to 10 % was obtained. To improve the yield a saturated 35 % aqueous ammonia solution was added showing a significant increase in yield to 55 % with a ratio of 1:2:41:20 (Zn:Hmim:MeOH:NH_3) with a crystal size of 80 nm. At lower ammonia concentrations a nonporous material was observed due to the presence of water.[66]

A nanoparticle's size is between 1 to 100 nm. Nanoparticles with their large surface areas are useful especially in catalysis. The first nano-sized ZIF-8 or abbreviated as nZIF-8 was synthesised by Cravillon *et al*. by a simple rapid room-temperature colloidal method without any auxiliary stabilizing agents. The optimal ratio of 1:8:700 (Zn^{2+}:MeIm:MeOH) gave a particle size (**Figure 2.9, p 22**) of 40 nm, determined by SEM and HRTEM, and 46 nm, determined by PXRD peak broadening. An excess of MeIm is enough to terminate the crystal growth by

deprotonating the linker and act as neutral stabilizing agent. The lattice fringe of ~1.2 nm corresponds to the (110) face as observed by HRTEM. A stable dispersion in methanol gave a ζ potential of +55 mV.[67] The ligand ratio can control the crystallization rates, with low concentrations leading to slow crystallization rates producing larger particles.[68] During further investigation by Cravillon *et al*. a series of excess modulating ligands were added: sodium formate, 1-methylimidazole and n-butylamine was able to reduce the particle size to ~10 nm (determined by PXRD). Nanocrystal formation is governed by continuous slow nucleation, crystallization and followed by fast crystal growth, thus the modulating ligand act as competitive ligands in coordinating equilibrium together with the deprotonation of 2-methylimidazole linker with a base.[60,69,70] The solvent plays an important role in the synthesis of nZIF-8 by the hydrogen bonding ability between the reagents and solvent, which assists in deprotonation and coordination. Acetone was found to be most effective at synthesising smaller particles with a size of 14.8 nm, but methanol maintained the highest crystallinity.[71] By altering the reagent and solvent ratios it was reported that with a higher solvent ratio the particles decrease in size from ~330 nm (Zn:MeIm:MeOH ratio of 1:7.9:86.7) to ~40 nm (Zn:MeIm:MeOH ratio of 1:7.9:1002).[72] Previous work done by this author has shown that temperature plays a role in controlling the size of nanoparticles. An increase in temperature from -15 ℃ to 60 ℃ reduced the particle size from 78 nm to 26 nm and increased the external surface area from 220 to 336 m^2 g^{-1}. The observation has shown that particle size is directly proportional to external surface area.[73]

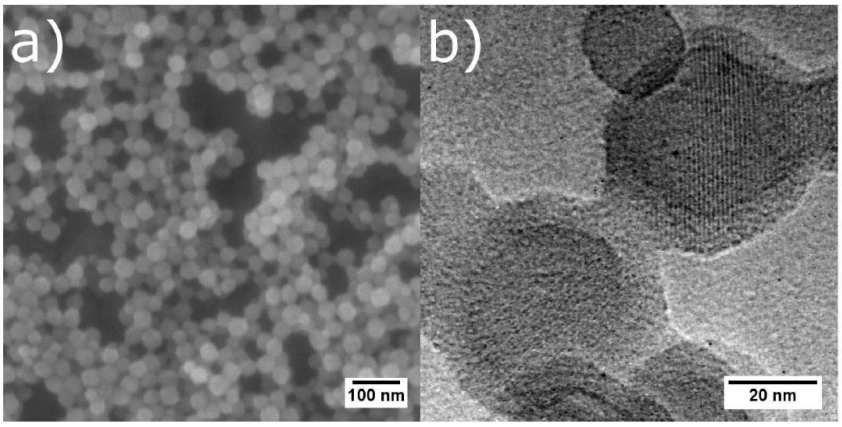

Figure 2.9 ZIF-8 nanoparticles synthesised in methanol at room temperature. a) SEM and b) HRTEM images.[67] (Reprinted (adapted) with permission from J. Cravillon, S. Münzer, K. Huber and M. Wiebcke, *Chem. Mater*., 2009, **21**, 1410-1412. Copyright (2009) American Chemical Society.)

2.3.3 Characterisation of ZIF-8

The ZIF products were characterised by powder X-ray diffraction (PXRD) as well as single crystal X-ray diffraction (XRD). Both X-ray diffraction techniques serve as the basis of characterising ZIFs, since they are able to identify the structure, topology, fingerprint, impurities and identify any structural modifications. Park *et al*. obtained the single crystal X-ray diffraction of ZIF-8, observing that the organic imidazolate linkers can lower the space group symmetry compared to zeolites, while the net between the metal nodes and organic linker still corresponds to zeolites. ZIF-8 Crystallographic details can be found in (**Appendix F**).[12]

In this study, PXRD will serve as an important characterisation tool to identify the topology and crystal size. Simulated PXRD patterns of ZIF-8 (**Figure 2.10, p 23**) obtained by single crystal data having a SOD topology matches those of the as synthesised nano-ZIF-8 pattern, although a slight deviation in peak positions is due to the temperature at which the PXRD was measured. In 1978 Paul Scherrer devised the Scherrer equation (1) where the nano crystallite size smaller than 100 nm can be theoretically determined by the peak broadening of the PXRD pattern. ZIF-8 nanoparticles size can be determined by the Scherrer equation on the (011) peak.[56]

$$D = \frac{K\lambda}{\beta \cos\theta} \qquad (1)$$

Where D = nanoparticle diameter, K = the shape factor a typical value of 0.9, λ = X-ray wavelength, β = line broadening at half the maximum intensity (Full width at half maximum or FWHM) and θ = Bragg angle.[74,75,76]

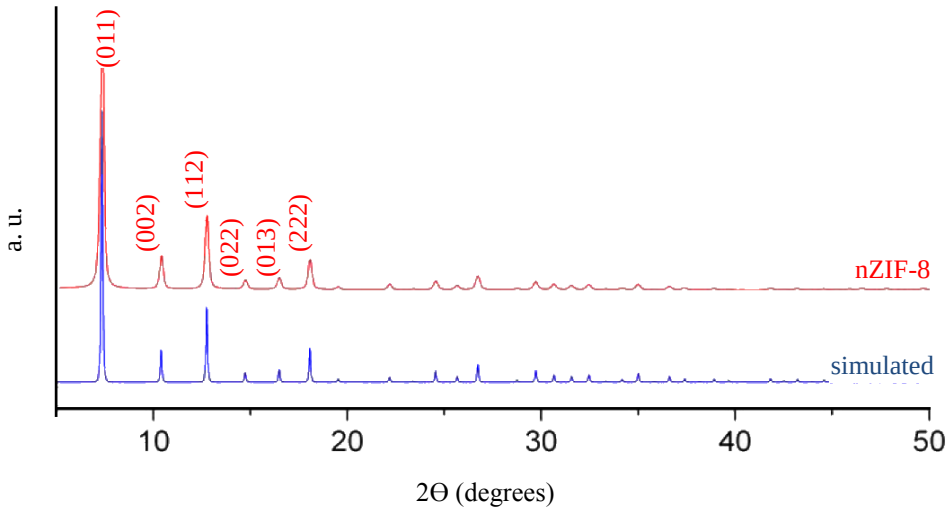

Figure 2.10 PXRD patterns of nano ZIF-8 (red) and simulated ZIF-8 (blue).[67,60] (Reprinted (adapted) with permission from J. Cravillon, S. Münzer, K. Huber and M. Wiebcke, *Chem. Mater.*, 2009, **21**, 1410-1412. Copyright (2009) American Chemical Society.)

The Infrared spectroscopies of ZIF-8 are well-characterised (**Figure 2.11, p 24**) since the measurement by Park *et al*. The disappearance of a broad peak at ~3400 cm^{-1} suggests the substitution of the N-H bond of the MeIm with the Zn metal. The two peaks at ~3130 and ~2930 cm^{-1} represent the stretching frequency of the aromatic C-H and aliphatic C-H bonds respectively. The stretching frequency at 1606 cm^{-1} stretching frequency relates to the C=C bond. Adsorption bands for C-N bonds are between 1400 and 1100 cm^{-1}. Bands between 1350 to 900 cm^{-1} relates to the in plane bending of the ring and lastly the Zn-N stretching frequency is at 421 cm^{-1}.[12,77,78,79]

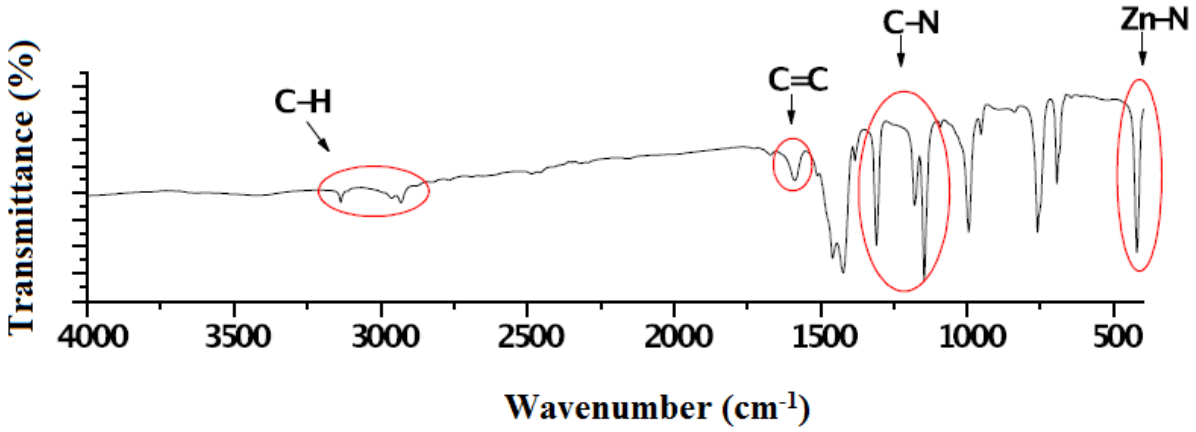

Figure 2.11 Infrared spectrum of ZIF-8 with notable regions mark in red.[77] (Reprinted (adapted) with permission from I. B. Vasconcelos, T. G. da Silva, G. C. G. Militão, T. A. Soares, N. M. Rodrigues, M. O. Rodrigues, N. B. da Costa Jr., R. O. Freire and S. A. Junior, *RSC Adv.*, 2012, **2**, 9437-9442. Copyright (2012) The Royal Society of Chemistry.)

2.3.4 Porosity of ZIF-8

The pores of materials are classified into 3 categories; pores with a diameter of smaller than 20 nm are microporous, pores between 2 and 50 nm are mesoporous and larger than 50 nm are macroporous.[80] Since ZIF-8 is a microporous material its van der Waals adsorption of gasses gives a Type I isotherm (shown in **Figure 2.12**, **p 25**).

Type I: is well known as a Langmuir adsorption isotherm. These materials have extremely small pores of sizes ~20 nm and smaller.

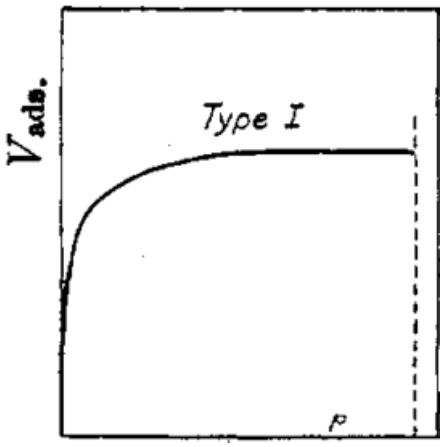

Figure 2.12 General examples of a Type I isotherm.[81] (Reprinted (adapted) with permission from S. Brunauer, L. S. Deming, W. E. Deming and E. Teller, *J. Am. Chem. Soc.*, 1940, **62**, 1723–1732. Copyright (1940) American Chemical Society.)

Materials with micropores, like those encountered in this study, will show the curve initially rising almost vertically then level out until it reaches saturation pressures.[82] The BET theory (2) determines the multilayer adsorption.

$$\frac{P}{V_a(P_0-P)} = \frac{1}{V_m C} + \frac{C-1}{V_m C}\left(\frac{P}{P_0}\right) \quad (2)$$

Where V_a is the amount of gas adsorbed, V_m the gas adsorbed on the surface, P the pressure, P_0 the saturation pressure and C a constant. The equation is then related to the area of nitrogen of 16.2 $Å^2$ to determine the surface area.[81,82,83]

ZIF-8 exhibits a Type-I nitrogen isotherm (**Figure 2.13, p 26**) proving it to be microporous with a Brunauer-Emett-Teller (BET) surface area of ~1630 $m^2 g^{-1}$ and micropore volume of 0.636 $cm^3 g^{-1}$, which correlates to the theoretical values of 1947 $m^2 g^{-1}$ and 0.663 $cm^3 g^{-1}$ respectively, as calculated from single X-ray crystal data.[12] These surface areas are much higher than those of zeolites with similar topology are. ZIF-8 as well as ZIF-11 was capable of reversible hydrogen adsorption (**Figure 2.13, p 26**). ZIF-11 with its RHO topology and benzene rings were more favourable at adsorbing larger quantity of hydrogen. Reaching higher pressures of 760 Torr ZIF-8 adsorbed 145 $cm^3 g^{-1}$ at STP which is close to ZIF-11 (154 $cm^3 g^{-1}$ at STP) because ZIF-8 has a higher surface area and micropore volume than ZIF-11.[12] Gas storage of ZIFs will be discussed later (**Chapter 2.6.4**, **p 45**).

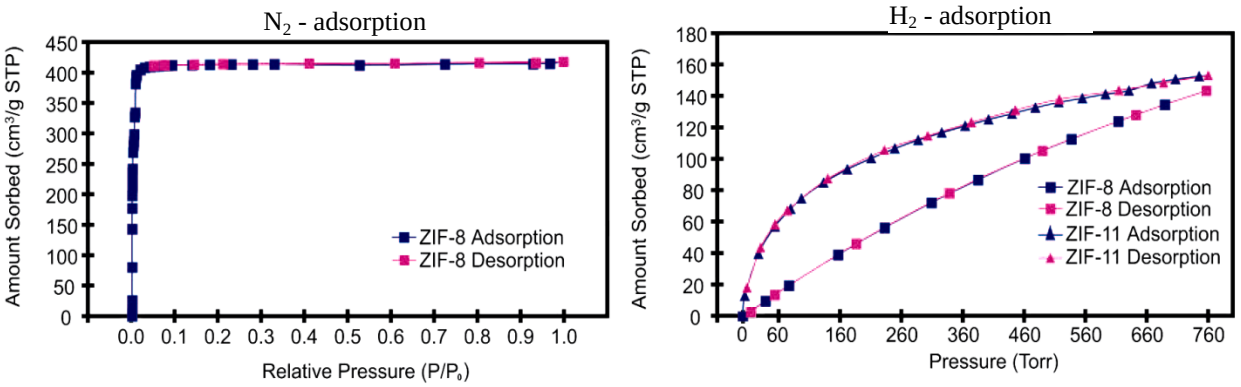

Figure 2.13 ZIF-8 nitrogen isotherms at 77 K (left) with ZIF-8 and ZIF-11 hydrogen isotherms at 77 K (right).[12] (Reprinted (adapted) with permission from K. S. Park, Z. Ni, A. P. Cote, J. Yong, R. Huang, F. J. Uribe-Romo, H. K. Chae, M. O'Keeffe, O. M. Yaghi, *PNAS*, 2006, **103**, 10186-10191. Copyright (2006) PNAS.)

The hydrophobic nature of ZIF-8 was demonstrated by water physisorption isotherms obtained by Küsgens *et al.* showing that only 10 cm^3 g^{-1} of water was adsorbed at $p/p^0 = 0.6$. Water has a molar enthalpy of evaporation of 40.69 KJ mol^{-1} and the heat of adsorption of water is much higher for ZIF-8 at 44.68 KJ mol^{-1}.[8] Zhang *et al*. proved that ZIF-8 is hydrophobic by performing water and alcohol mixture adsorptions. ZIF-8 was able to separate alcohols (*n*-butanol and propanol) from water with high initial adsorptions for alcohols, while smaller alcohols (methanol) show even higher adsorption steps. Compared to ZIF-71 and ZIF-90 the adsorption of alcohols does not depend on the on pore size but rather on the imidazolate linker.[84] The linker and topology plays an important role as ZIF-65 and ZIF-90 were found to be hydrophilic.[85,86]

2.3.5 Thermal and Chemical Stability of ZIF-8

ZIF-8's thermal and chemical stability is comparable to those of zeolites. TGA curves (**Figure 2.14, p 27**) obtained by analysis performed by Park *et al.* for micro sized ZIF-8 showed an initial weight loss of 28.25 % in the region between 25 ℃ and 450 ℃ representing the slow release of guest molecules (solvent) from the pores. This value was less than the estimated amount (36 %) because guest molecules escape slowly out of the pores and at high temperatures carbonization occurs (darker colour) of the guest molecules. The structure fully decomposes at 600 ℃. It is observed with PXRD (**Figure 2.14.b.ii, p 27**) that after heating to 500 ℃ the SOD structure remains intact with the release of guest molecules. The high thermal stability is on par with other highly dense MOFs.[12,59] The final decomposition yields ZnO.[62,77] The TGA thermograms of nano sized ZIF-8 are similar to micro sized ZIF-8.[59]

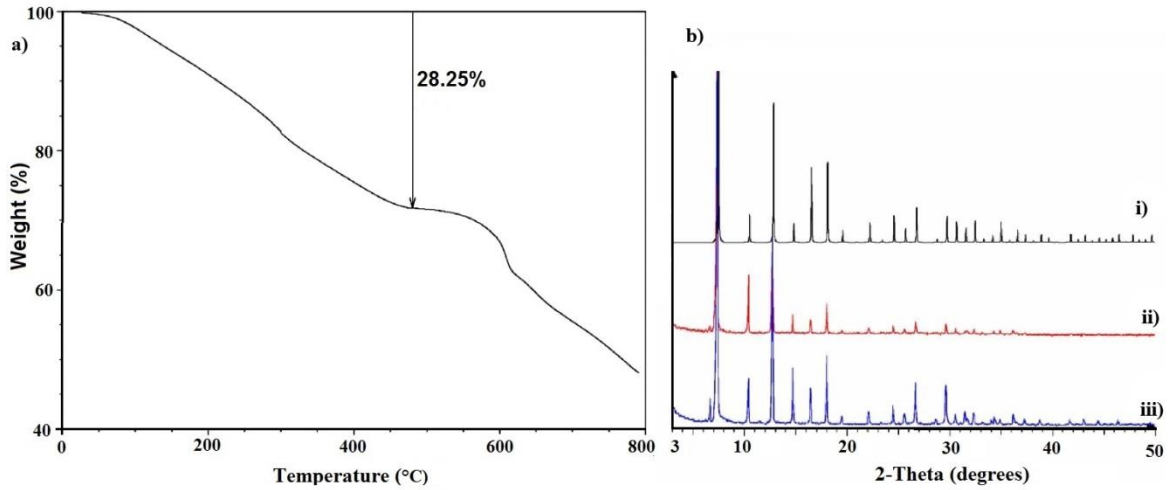

Figure 2.14 a) TGA curves of micro sized ZIF-8 as-synthesised in DMF and b) PXRD patterns of ZIF-8: i) as-synthesised ii) after heating to 500 °C in nitrogen and iii) activated ZIF-8.[12] (Reprinted (adapted) with permission from K. S. Park, Z. Ni, A. P. Cote, J. Yong, R. Huang, F. J. Uribe-Romo, H. K. Chae, M. O'Keeffe, O. M. Yaghi, *PNAS*, 2006, **103**, 10186-10191. Copyright (2006) PNAS.)

The use of high boiling point solvents during synthesis can be difficult to remove from the pores of ZIF-8. Solvent exchange techniques were investigated with THF, acetonitrile, dicholoromethane and methanol. After exchanging the DMF with methanol, the TGA thermogram (**Figure 2.15, p 28**) show a simpler thermogravimetric behaviour with only 7.6 % weight loss compared to 28.25 % (**Figure 2.14.a, p 27**) at 450 °C.

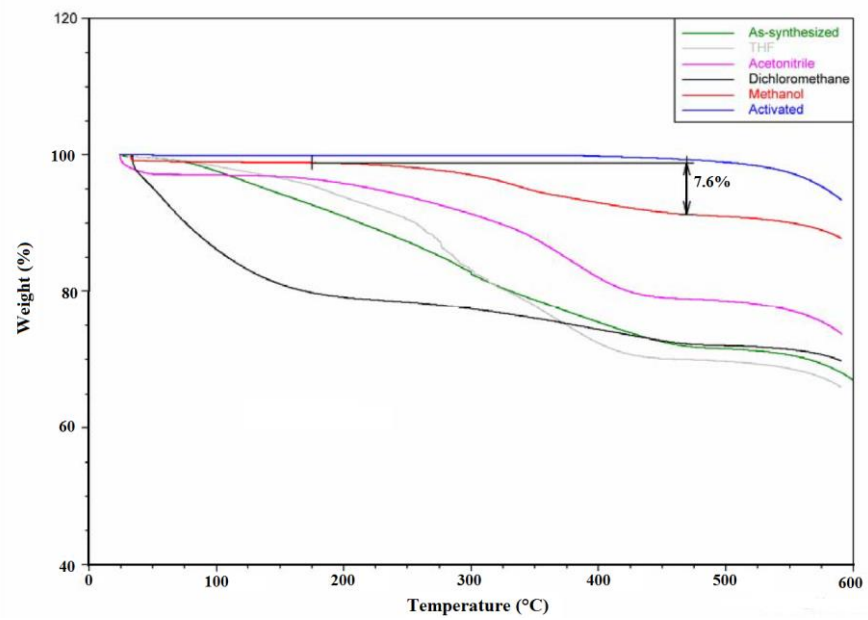

Figure 2.15 ZIF-8 TGA curve after solvent exchange with different solvents: as-synthesised (green), activated (blue) and with methanol (red).[12] (Reprinted (adapted) with permission from K. S. Park, Z. Ni, A. P. Cote, J. Yong, R. Huang, F. J. Uribe-Romo, H. K. Chae, M. O'Keeffe, O. M. Yaghi, *PNAS*, 2006, **103**, 10186-10191. Copyright (2006) PNAS.)

ZIF-8 does not only have high thermal but also high chemical stability in both ambient and harsh conditions in industry. ZIF-8 was tested under similar conditions include boiling in solvents such as benzene, methanol and water as well as in high and low concentrations of aqueous sodium hydroxide. By boiling ZIF-8 in methanol and benzene solvents for 7 days, the PXRD patterns (**Figure 2.16, p 29**) showed that ZIF-8 maintained its full crystallinity. ZIF-8 has great chemical stability in boiling H_2O for 7 days and similarly in 0.1 M and 8 M aqueous sodium hydroxide for 24 hours as shown in (**Figure 2.16, p 29**) PXRD patterns.[12,87] Suspensions of ZIF-8 in ethanol remained stable after 3 weeks, but after 1 month the particles began to aggregate by hydrogen bonding network of the protonated imidazolate linker and the solvent.[88] ZIF-8 was tested in a phosphate buffer saline solution with a pH of 7.4 at 37 °C for 7 days and maintained full crystallinity after 7 days. However, ZIF-8 is highly sensitive to an acidic medium and was completely dissolved after 30 minutes in acetate buffer solution with a pH of 5.0 at 37 °C.[89] Two phenomena describe the stability of ZIF-8 to hydrolysis; firstly, the hydrophobicity prevents dissolution of ZIF-8 and secondly, the ZIF Zn-N bonds improves hydrothermal stability which is similar to covalent solids.[12] Nanoparticles of ZIF-8 also exhibit the same chemical stability as micro sized particles.[59] Hydrothermal stability of ZIF-8 nanoparticles was improved by shell-ligand exchange discussed in (**Chapter 2.4.2, p 32**) with 5,6-dimethylbenzimidazole which

greatly enhance the hydrothermal stability and prevents transformation to ZnO (thermodynamically preferred).[90]

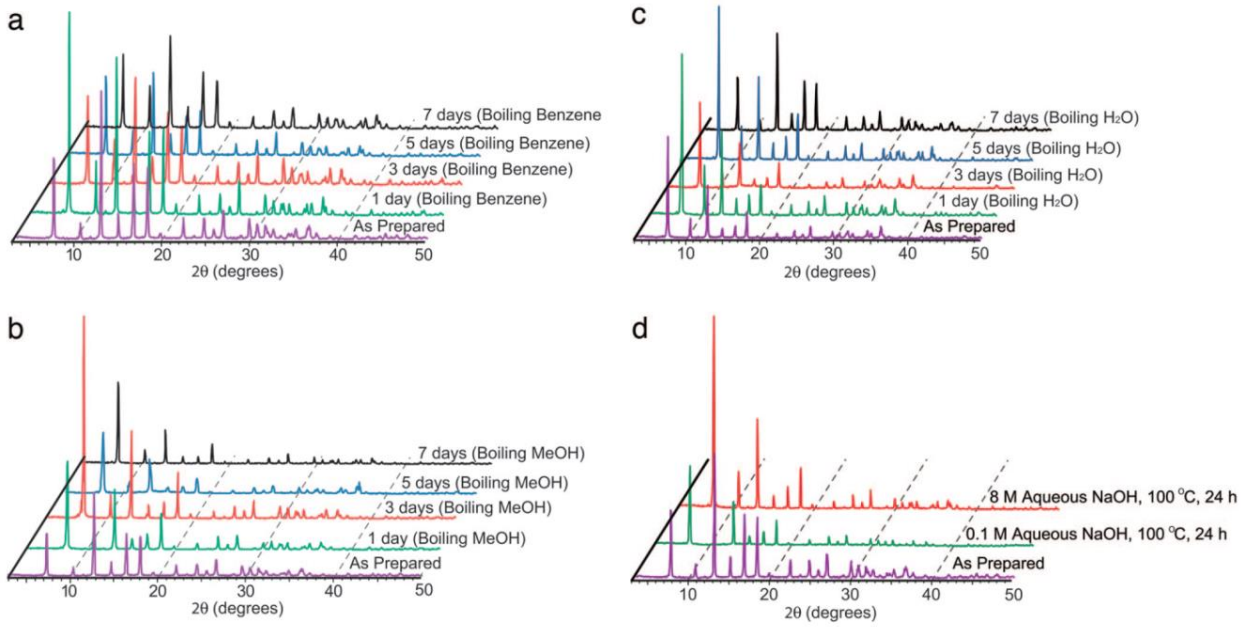

Figure 2.16 PXRD patterns of chemical stability tests of ZIF-8 in a) benzene at 80 °C for 7 days b) methanol at 60 °C for 7 days c) H_2O at 100 °C for 7 days and d) aqueous NaOH (0.1 M and 8 M) at 100 °C for 24 hours.[12] (Reprinted (adapted) with permission from K. S. Park, Z. Ni, A. P. Cote, J. Yong, R. Huang, F. J. Uribe-Romo, H. K. Chae, M. O'Keeffe, O. M. Yaghi, *PNAS*, 2006, **103**, 10186-10191. Copyright (2006) PNAS.)

2.3.6 Pore Flexibility of ZIF-8

The flexibility of pores in MOFs leads to breathing or gate opening effects by external stimuli (**Chapter 2.2, p 8**). Dense nonporous ZnIM material was found to undergo a phase transition from $I\bar{4}cd$ to $I4_1$ space group at 0.8 GPa.[45,91] Recent works by Moggach *et al*. has shown that ZIF-8 also undergoes phase transition at high pressures. At a pressure of 0.18 GPa the volume increased from 4900 $Å^3$ to 4999 $Å^3$. The ZIF-8 crystal underwent a phase transition up to a pressure of 1.47 GPa. The process is reversible after decreasing the pressure. The ZIF-8 maintained a $I\bar{4}3m$ space group but the imidazole ligands twist to increase the accessibility of the pores and the size of 6-ring windows (**Figure 2.17.b, p 30**). A new method, using extreme high pressures can remove guest molecules in the pores or introduce larger molecules within the pores of MOFs.[92] ZIF-8 is capable of withstanding pressures up to 39.15 GPa.[78] Similarly N_2 isotherms of simulated and experimental results shows a two-step isotherm suggesting a rearrangement of

N_2 molecules at the first step and a gate opening effect at the second step that allows 26 % increase uptake of nitrogen. XRD results of ZIF-8 loaded with nitrogen at pressures after the second step (0.4 P/P_0) and ZIF-8 structures at high pressure show little change in structure, thus confirms the twist effect of imidazole ligand.[93] This gate opening phenomenon was further proven by Casco *et al*. using *in situ* inelastic neutron scattering (INS) before and after N_2 adsorption at cryogenic temperatures.[94] Molecular dynamics simulations with CO_2 at high pressure show gate-opening effects. It initially shows a decrease in gate size at low loadings (20 CO_2/cage) which, after the gate opens up, allowed 30 CO_2/cage and still showed diffusion.[95] Interesting, p-Xylene with a kinetic diameter ~6.4 Å was able to transition through the pores rather than hosting the p-Xylene by the tilting of the imidazole ligand.[96] The flexibility (gate opening) of the imidazole ligand can vary between 5.8 – 6.3 Å, while the zinc nodes remained rigid to allow larger molecules to enter.[97,98] ZIF-8 was further tested with solvents with different kinetic diameters *i.e*: *n*-hexane (kinetic diameter 4.3 Å), cyclohexane (kinetic diameter 6.0 Å) and toluene (kinetic diameter 6.1 Å). The solvents are all larger than the 3.4 Å aperture of the framework. TGA-MS showed that only *n*-hexane was released from the pores while cyclohexane and toluene did not enter. Interestingly the *n*-hexane was released at a much higher boiling point which is expected by the higher thermal energy needed for molecules whose size is larger than the aperture size to leave the pores.[12,47] Changing or modifying the imidazole linker will impact the way the pores open and allow molecules to enter which is especially important for understanding the fundamentals molecular sieving.

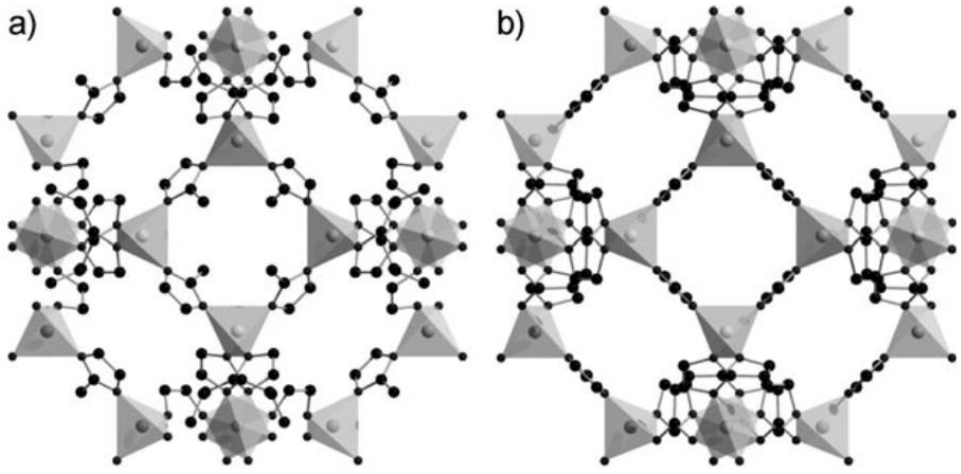

Figure 2.17 ZIF-8 packing a) at ambient pressure and b) at 1.47 GPa.[92] (Reprinted (adapted) with permission from S. A. Moggach, T. D. Bennett and A. K. Cheetham, *Angew. Chemie - Int. Ed*., 2009, **48**, 7087–7089. Copyright (2009) Wiley.)

2.4 Post-Synthetic Modification (PSM)

One key attribute of ZIFs compared to zeolites is that the binding ligands are organic moieties. Organic synthetic modification can thus be performed on these ligands, similar to those MOFs discussed previously, to enhance the properties of the ZIFs.

2.4.1 Modification by direct chemical reactions

The idea "crystals as molecules" comes to mind when crystalline ZIF nanoparticles are seen as organic molecules in typical post synthetic modification organic synthesis. In 2008, Morris *et al*. performed PSM with ZIF-90 having a SOD topology with an aldehyde functional group on the 2-imidazolecarboxaldehyde linker. Two reactions were performed on ZIF-90 as shown in (**Figure 2.18**, **p 31**) which produced two new ZIFs namely: ZIF-91 and ZIF-92. ZIF-91 was synthesised by reducing the aldehyde with $NaBH_4$ into an alcohol and ZIF-92 reacted with ethanolamine. The two reactions gave a good conversion of 80 % while maintaining high crystallinity and the original SOD topology determined by PXRD.[99]

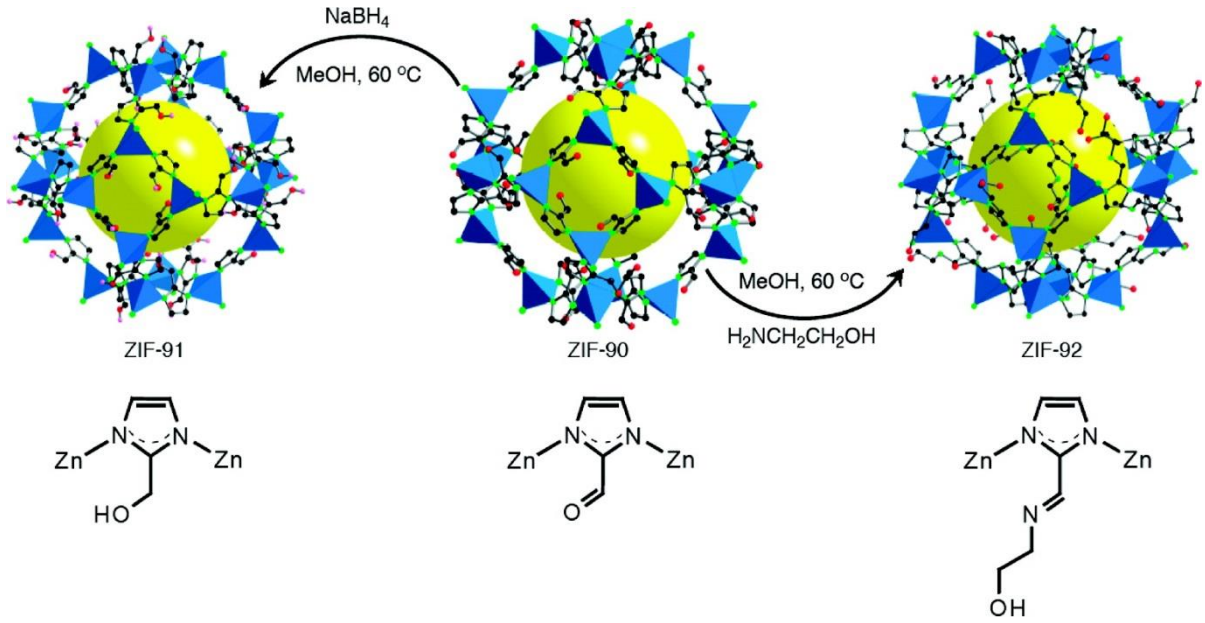

Figure 2.18 Post synthetic modification of ZIF-90 (center) to ZIF-91 (left) by reduction with $NaBH_4$ and to ZIF-92 (right) by reaction with ethanolamine. (carbon, black; nitrogen, green; oxygen, red).[44] (Reprinted (adapted) with permission from A. Phan, C.J. Doonan, F. J. Uribe-Romo, C. B. Knobler, M. O'Keeffe, O. M. Yaghi, *Acc. Chem. Res*., 2009, **43**, 58-67. Copyright (2009) American Chemical Society.)

Recent studies have shown that multi-linker synthesis was possible in a typical reaction where two different imidazolate linkers was added together at different ratio to synthesise ZIFs with two different linkers. The works perform by *Thompson* et al. successfully synthesised two multi-linker ZIFs having different ratio combinations of: 2-methylimidazole with 2-carboxaldehydeimidazole (ZIF-8-90 hybrid) and 2-methylimidazole with benzimidazole (ZIF-8-7 hybrid). Different ratio synthesis shows that the ZIF-8-90 hybrid maintain the cubic space group throughout, while the ZIF-8-7 hybrid show a change in topology from cubic to rhombohedral space group after 79 % benzimidazole ratio. As the exchange percentage increases, an expected drop in porosity is observed for both ZIF-8-90 hybrid and ZIF-8-7 hybrid, because ZIF-90 and ZIF-7 have lower porosity than ZIF-8. A step observed in the isotherm as well as pore width measurements shows different pore widths from the different linkers in the structure.[100] ZIF-78 is a known multi-linker ZIF with a GME topology consisting of 2-nitroimidazolate (nIm) and 5-nitrobenzimidazolate (nbIm). When triethylamine was added as a deprotonating agent, hexagonal microrods were obtained.[101]

Thompson *et al*. were the first to employ 2-aminobenzimidazole and 2-methylimidazole (ZIF-8-NH_2BzIm) in multi-linker synthesis. The ZIF-8-90 was reacted with ethylenediamine by post synthetic modification. The synthesis was performed in H_2O and $NaCO_2H$, as an additive, was stirred for 1 hour at room temperature. Except for ZIF-8-90, the reaction was performed in methanol with $NaCO_2H$ additive and stirred for 2 hours at 50 ℃. After separating, ethylenediamine was added and heated for 24 hours at 80 ℃. Both reactions maintained a crystalline topology similar to that of ZIF-8. The N_2 porosity isotherm of the ZIF-8- NH_2BzIm drops considerably as the ratio is increased from 1640 $m^3 g^{-1}$ (9.5 % linker substitution) to 70 $m^3 g^{-1}$ (47 % linker substitution). ZIF-8-90 maintained its original porosity and after PSM the porosity drop to 860 $m^3 g^{-1}$ (27 % ethylenediamine).[102]

2.4.2 Modification by Solvent Assisted Ligand Exchange

Karagiaridi *et al*. were the first to perform solvent assisted ligand exchange (SALE) on ZIFs. A cadmium ZIF (CdIF-4) with a RHO topology containing a 2-ethylimidazole linker was successfully exchange with 2-nitroimidazole to produce CdIF-9 and with 2-methylimidazole to produce SALEM-1. The two products are characterised by digestive ^{1}H NMR, showing a 100 % conversion. The PXRD identified that the RHO topology was retained, thus prove no structural change during solvent assisted ligand exchange process. The size of particles remained

unchanged while obtaining an exceptional BET surface area. Ligand exchange is a useful method to obtain products which are usually polycrystalline or amorphous.[103]

The same year Karagiaridi *et al*. reported the SALE can be performed in a similar fashion on ZIF-8 (**Scheme 2.3,p 33**), where the 2-methylimidazole linker was exchanged with imidazole to produce SALEM-2 while retaining the original SOD topology (ZIF-8).[47]

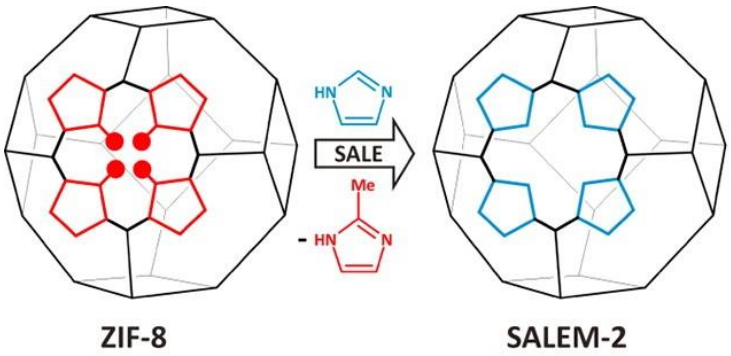

Scheme 2.3 Solvent assisted ligand exchange of ZIF-8 where the 2-methylimidazole (red) was replaced with imidazole (blue) producing SALEM-2.[47] (Reprinted (adapted) with permission from O. Karagiaridi, M. B. Lalonde, W. Bury, A. A. Sarjeant, O. K. Farha and J. T. Hupp, J. Am. Chem. Soc., 2012, **134**, 18790−18796. Copyright (2012) American Chemical Society.)

Characterisation of SALEM-2 with PXRD (**Figure 2.19.a, p 34**) show the spectra is identical to ZIF-8 hinting that the SOD topology is retained, similarly the crystal shape and size maintained its appearance (**Figure 2.19.d, p 34**). A conversion of 85 % was determined with the proton ratio of ^{1}H NMR (**Figure 2.19.b, p 34**) after digesting in acid. However, the nitrogen isotherm (**Figure 2.19.c, p 34**) show a decrease in porosity after SALE from 1080 $m^2 g^{-1}$ for ZIF-8 to 830 $m^2 g^{-1}$ for SALEM-2.[47]

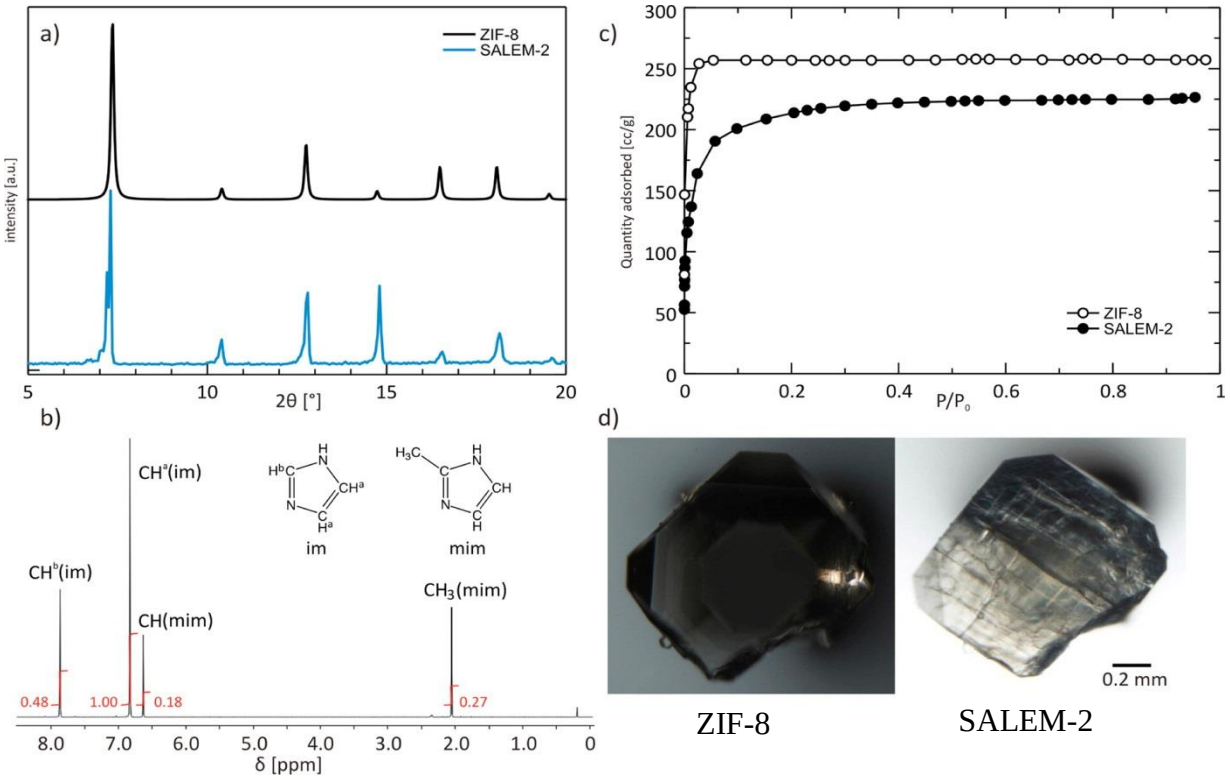

Figure 2.19 a) PXRD patterns of ZIF-8 (black) and SALEM-2 (blue) b) digestive ^{1}H NMR of SALEM-2 in D_2SO_4 and D_2O (9:1) c) Nitrogen isotherm at 77 K of ZIF-8 (top) and SALEM-2 (bottom) d) photographs of ZIF-8 (left) and SALEM-2 (right).[47] (Reprinted (adapted) with permission from O. Karagiaridi, M. B. Lalonde, W. Bury, A. A. Sarjeant, O. K. Farha and J. T. Hupp, J. Am. Chem. Soc., 2012, **134**, 18790−18796. Copyright (2012) American Chemical Society.)

The choice of solvent plays an important role in SALE reactions, simply by using N,N-dimethylformamide and N,N-dimethylacetamide it leads to the degradation of ZIF-8's SOD topology while with *n*-butanol it was highly effective. The excess ligand concentration of the replacing imidazole linker to ZIF-8 play a crucial role, as a ratio higher than 7:1 leads to the loss of SOD topology while a ratio less than 3:1 gave no exchange. SALEM-2 exhibits similar thermal stability of ZIF-8.[47] SALE reactions is able to synthesise ZIFs with topology difficult to obtain through conventional solvothermal procedures for examples by using imidazole leads variety different topology of ZIFs seen in (**Table 2.1, p 16**) but not the SOD topology.

A number of ZIFs with various topologies and linkers were ligand exchanged with promising results. Kim *et al*. were able to ligand exchange ZIF-71 (RHO topology) with 4-bromoimidazole. The reaction was incubated for 5 days at 55 ℃ in methanol with an exchange of 30 % was achieved and the PXRD pattern confirmed the crystallinity was retained.[104] ZIF-8 (40 nm) was

exchanged with 5,6-dimethylbenzimidazole in methanol for 15 hours at 60 ℃. The exchange achieved an exchange ratio of 9.1 % while maintaining the SOD topology and was found to take place only the external surface (core-shell) because the linker might be too large to penetrate the ZIF-8 narrow windows.[90] The works done by Fei *et al*. successfully exchanged ZIF-8 (SOD) with 2-ethylimidazole and ZIF-71 (RHO) with 4-bromoimidazole which gave an exchange of ~20 % and ~35 % respectively without changing the topologies and porosity. Both reactions were performed in methanol solutions at 55 ℃ for 3 days with a linker to ZIF ratio of 3:1.[105] ZIF-8 was exchanged with five times excess 4,5-dichloroimidazole in isopropanol at 100 ℃ for 5 days. After 5 days a 99 % conversion was obtained while maintaining the SOD topology but the particles size increased from 20 nm to 200 nm. Direct synthesis of ZIF-71 with the aid of modulating ligands forms SOD topology but eventually converts to ZIF-72 (lcs topology).[106] Triazole-based ligands similar to imidazole but have 3 nitrogen atoms are found to be difficult or unreactive to use as linker to synthesis ZIFs, but with ligand exchange with ZIF-7 the benzimidazole linker was easily replaced with benzotriazole in DMF at room temperature with a 71 % conversion.[107] The SALE process can also assist in incorporating large molecules such as red sulfur chromophores. ZIF-8 was first exchanged *via* SALE with 4-methyl-5-imidazolecarboxaldehyde in n-butanol for 24 hours and after the product was suspended in a solution with Na_2S_4 and 2-mentylimidazole. The process reverses the SALE product back to ZIF-8, while the 4-methyl-5-imidazolecarboxaldehyde act as a reducing agent for Na_2S_4 to form S_4 red chromophore in the pores of ZIF-8.[108] Another scenario, where ZIF-8 is previously loaded with Pt nanoparticles (Pt@ZIF-8) which then undergo SALE with imidazole in *n*-butanol for 4 days at 100 ℃. The Pt nanoparticle size and distribution remains intact without changes during SALE but the pore apertures are larger than the parent material. The larger aperture was observed by catalytic testing where larger molecules was hydrogenated while the previous Pt@ZIF-8 show 0 % conversion.[109]

ZIF-108 with SOD topology was exchanged with 5 different linkers *i.e.* imidazole (Im), 5-nitrobenzimidazole (nbIm), 5,6-dimethylbenzimidazole (dmbIm), 2-ethylimidazole (eIm) and 2-methylimidazole (mIm) in DMF at 60 ℃ for 52 hours with exchange conversion ranging from 25 – 65 %. The products obtained showed that not all linkers maintain the parent SOD topology, only eIm and mIm maintained the SOD topology while Im and nbIm gave GME topology and dmbIm gave a GIS topology. The ligand exchange happens through a dissolution-heterogeneous nucleation process, therefore allowing different topology to form.[110]

SALE can be selective towards choosing which ligands to exchange in a multi-linker MOF. ZIF-69 with nIm and cbIm linkers was submerged in *n*-butanol with 5-(trifluoromethyl)benzimidazol (fbIm) for 3 days at 120 ℃. The ^{1}H NMR show a result of 95 % exchange on the cbim linker. Investigation of ZIF-78 under similar conditions, found to have an exchange of 90 % replacement of nbIm with fbIm. ZIF-76 produced identical results to ZIF-78 by replacing 90 % of cbIm with fbIm linker. All exchange products maintain their original topology and permanent porosity with ZIF-78 and ZIF-69 having GME and ZIF-76 having LTA topology. Factors that drive the exchange selectivity are governed possibly by pK_a, steric or kinetic factors.[111]

The SALE is not only limited to a solid-liquid solution but can also be performed in a solid-solid solution by having two similar MOFs where the linkers of the two different MOFs interchange with one another.[104]

2.4.3 Modification by Metal-Ion Exchange

The metal nodes of MOFs can also be exchange *via* metal-ion exchange by a reaction in a solution of metal salt in a single crystal to single crystal method similar to SALE.[38] Kim *et al*. recently successfully exchanged metals with different robust MOFs (MIL and UiO) through solid-solid and solid-liquid solutions which produced unique MOFs with the original crystallinity.[104] Fei *et al*. exchange the Zn metal of two different topologies, SOD of ZIF-8 and RHO of ZIF-71, with redox active Manganese. Mn(acetylacetonate)$_2$ was suspended in a 3:1 ratio of ZIF and heated for 24 hours at 55 ℃ yielding a 10 % exchange while maintaining their respective topologies.[105] ZIF-108 with a 2-nitroimidazole linker was exchanged with seven different metals: Cr, Fe, Mn, Co, Ni, Cu and Mg at 60 ℃ for 24 hours in DMF. The SOD topology remained for all the metals except for Cu having a RHO topology. ZIF-108 is less stable having a Zn-N bond of 2.007 Å (ZIF-8 = 1.987 Å and ZIF-7 = 1.984 Å) which is easier for metal exchange. The highest obtained metal/Zn ratio was Co (0.081), Ni (0.17) and Cu (64). Interesting, the Ni produced has a very high CO_2 selectivity.[112]

In this study, the exchange of organic linkers will be the main focus.

2.5 Metallocenes Synthesis and Applications

Metallocenes are compounds or sandwich complexes discovered in the early 1950s. Typically consisting of two cyclopentadienyl ligands (Cp) bound to a metal centre with a valence charge of 2+. A number of different metal centres such as Fe, Ru, Os, V, Cr, Mn, Co and Ni just to name a few can be used.[113,114] In this study Ferrocene with an iron metal centre will be the main focus.

Owing to the cycopentadienyl rings on the ferrocene, various ferrocene derivatives can be prepared by aromatic substitution on the Cp rings using standard Friedel-Craft acylation, Vilsmeier–Haack reaction, metalation, mercuric acetate or sulfonated with examples shown in (**Scheme 2.4, p 38**).[114,115]

Ferrocenylmethylamine can be prepared according to a two-step reaction. Firstly, the ferrocenecarboxaldehyde was reacted with hydroxylamine under reflux to form ferrocenecarboxaldehyde oxime and secondly, in a one-pot synthesis, the oxime was reduced with $LiAlH_4$ in anhydrous THF, producing Ferrocenylmethylamine. The product was easily purified with column chromatography giving a decent yield.[116,117] Knoevenagel condensation of ferrocene derivatives can be easily performed with ferrocenecarboxaldehyde and malononitrile using piperidine as a catalyst under reflux in ethanol with a yield of 50 %.[118]

Ferrocene derivatives have a large variety of applications from rocket propellant catalysts[119], Li-ion redox flow battery[114], industrial catalysts[120,121] and recently in biomedical applications[113,122]. Ferrocene has low toxicity and shows interesting applications in anti-malarial, anti-HIV, anti-cancer, anti-tumour drugs and DNA cleaving or detection ability.[123,124] Well known examples include Ferrocifen which show anti-proliferative effects on breast cancer cells and Ferroquine as an antimalarial agent which is already in phase I clinical trials.[124] Ferrocene derivatives are been connected to water-soluble and biodegradable polymer drug carriers to assist in anti-cancer drug delivery.[125]

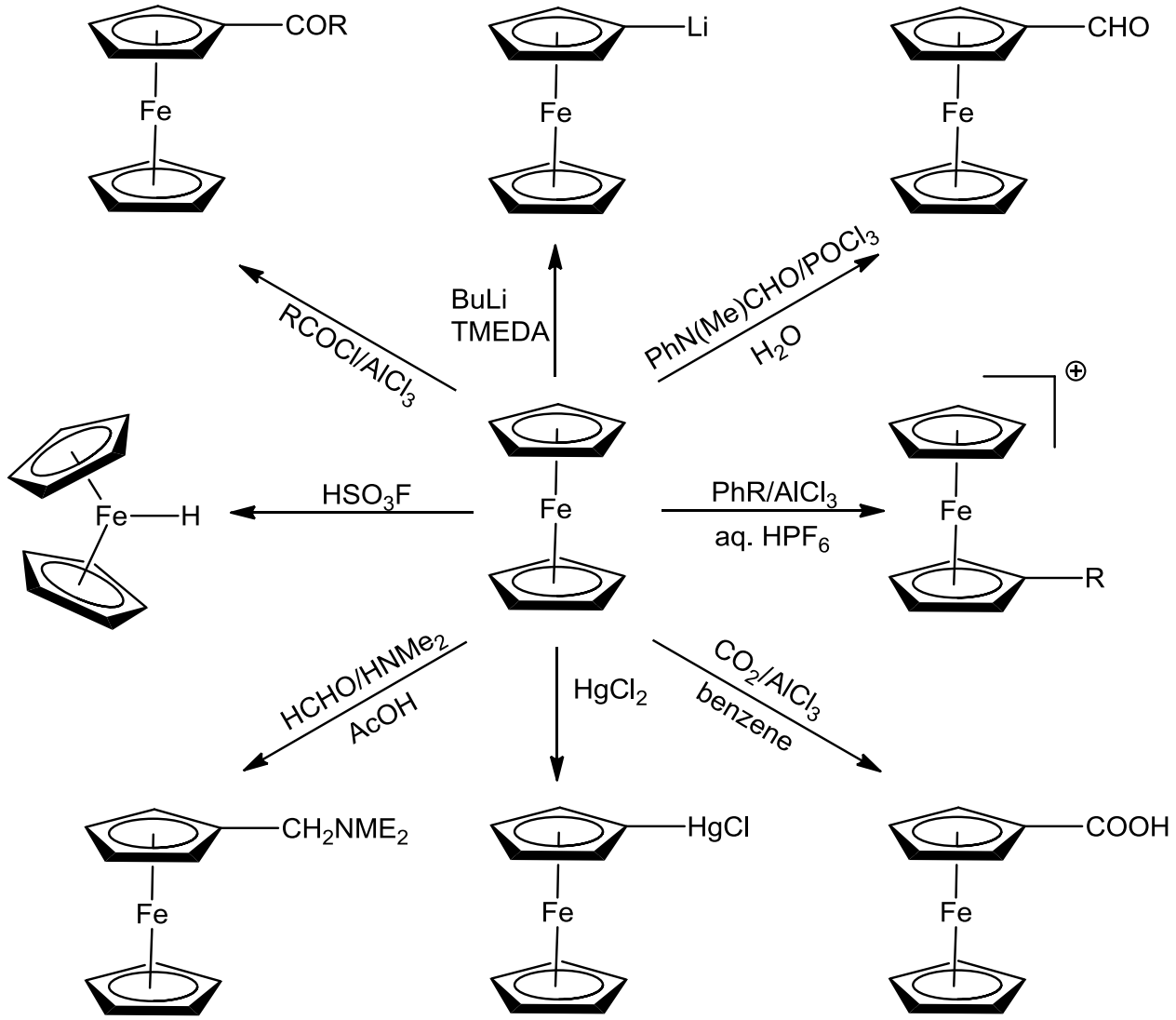

Scheme 2.4 Methods to functionalize ferrocene with different functional groups.[114] (Reprinted (adapted) with permission from Y. Zhao, Y. Ding, Y. Li, L. Peng, H. R. Byon, J. B. Goodenough and G. Yu, *Chem. Soc. Rev.*, 2015, **44**, 7968–7996..)

2.6 Application of ZIFs

2.6.1 Catalysis

The use of metal nanoparticles as catalysts has recently been widely investigated for its unique and quasi-homogeneous effect.[126,127] Gold nanoparticles have been used to catalyse the formation of hydrogen from CO and water.[127,128] These "nanocatalysts" are heterogenized, by linking ferrocenyl homogeneous catalysts onto mesoporous silica supports.[126] Further advancements with nanoparticles, to be used as supports, was to attach functionalized active groups. Abu-Rezig *et al*. successfully modified Fe_3O_4 nanoparticles post synthetically with N-[3-(trimethoxysilyl)propyl]ethylenediamine containing primary and secondary amine groups to catalyse Knoevenagel condensation reaction.[129] ZIFs can be impregnated with various metals e.g. Pd[130,131], Ir[132], Pt[133] and Au[134] for catalysis.

In 2016 Xi *et al*. demonstrated a Metal-*m*SiO_2@ZIF-8 core shell structure. The silica core was initially loaded with metals (Pt, Pd, Ru and Ag). Thereafter, a ZIF-8 shell was grown over the core. The ZIF-8 core-shell prevents the metal particles from leeching out and provides good selectivity towards hydrogenation of alkenes (styrene and cyclohexene) in converting styrene to ethylbenzene. The higher selectivity could be due to the π−π stacking interaction of styrene on ZIF-8 framework to allow gate opening by external stimuli.[135]

Besides modifying ZIFs by loading the pores with metals, the surface of the ZIF-8 itself contains catalytic ability. The works done by Chizallet *et al*. probed the surface with CO adsorption and with the aid of DFT calculations found that ZIF-8 has strong Lewis acid sites from the unsaturated Zn species, strong Brønsted acid sites from the NH groups and basic sites from the N^- moieties and possible OH groups on the external surface.[136] ZIF-8 was found to catalyse various organic reactions such as transesterification[136], Friedel-Craft acylation[137], CO_2 cycloaddition reaction[138] and Knoevenagel condensation[63,79]. Different ZIFs, such as ZIF-9, were also capable of catalysing Knoevenagel condensation.[139] All these catalytic reactions are performed with micro sized ZIF-8. The author has shown that nanoparticles greatly enhance the catalytic activity.[73]

Transesterification of vegetable oils (rapeseed oil) into alkyl esters with a ZIF-8 catalyst proved the existence of acid and basic sites on the external surface. ZIF-8 showed better performance than existing catalysts ($ZnAl_2O_4$) and the reaction allowed the use of different alcohols.[136] ZIF-8 has Lewis acid sites, as experimentally shown in a Friedel-Crafts acylation reaction between

anisole and benzyl chloride heterogeneously catalysed without the need of an inert atmosphere. High selectivity towards the *p*-isomer was observed and using smaller particles enhanced the reaction time.[137]

In this study, the Knoevenagel condensation will be the main focus. Knoevenagel condensation (**Scheme 2.5, p 40**) is a well-known nucleophilic addition of an activated methylene group followed by dehydration to form a carbon-carbon bond. The reaction is normally catalysed with a weak base *e.g*. primary, secondary or tertiary amines where piperidine was found to be the most effective.[140] The amines are often used as homogeneous catalysts which are difficult to recycle, require high mole ratios and are not environmental friendly.[139,118]

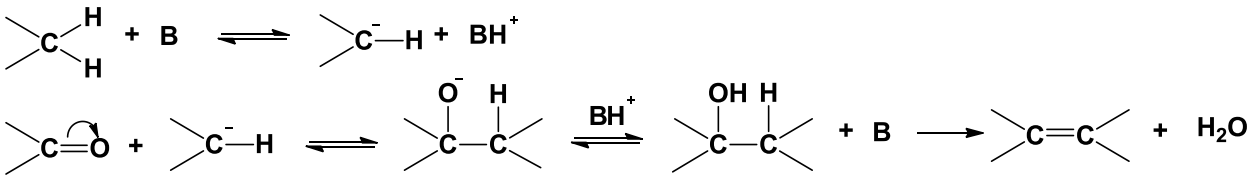

Scheme 2.5 A base (B) catalyzed Knoevenagel condensation reaction between an aldehyde or ketone with a methylene group.[140]

The development of heterogeneous catalysis is important and ZIFs has shown the have great potential. Tran *et al*. in 2011, were the first group to perform Knoevenagel condensation using minute amounts (3 mol %) of ZIF-8 to catalyse benzaldehyde and malononitrile (**Scheme 2.6, p 40**) at room temperature without an inert atmosphere.

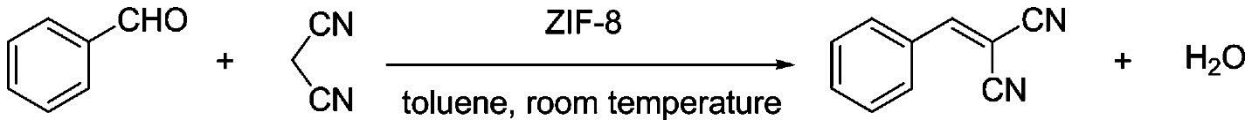

Scheme 2.6 ZIF-8 catalyzed Knoevenagel condensation reaction of benzaldehyde and malononitrile in toluene at room temperature.[79] (Reprinted (adapted) with permission from U. P. N. Tran, K. K. A. Le and N. T. S. Phan , *ACS Catalysis.*, 2011, **1**, 120-127. Copyright (2011) American Chemical Society.)

Solvent studies show that THF performed the best. The use (**Figure 2.20.a, p 41**) of smaller micro size particles (143 μm) achieved full conversion within 4 hours whereas using larger particles (282 μm) only 55 % conversion. Since the catalysis takes place at active sites on the

external surface, smaller particles have better conversion due to their larger external surface areas. The pore diameter of ZIF-8 is only 3.4 Å which prevents larger molecules from entering. ZIF-8 is active (**Figure 2.20.b, p 41**) towards benzaldehyde having substituents of both electron-withdrawing and donating groups. Electron-withdrawing groups such as NO_2 accelerate the reaction to completion within 1 hour as compared to other substituents. ZIF-8 was found to be stable as the leeching test (**Figure 2.20.c, p 41**) performed show that leeching of the catalyst was not observed. The ZIF-8 particles were easily removed and can be reused (**Figure 2.20.d, p 41**) while maintaining high conversions without signs of catalyst poisoning or degradation.[79]

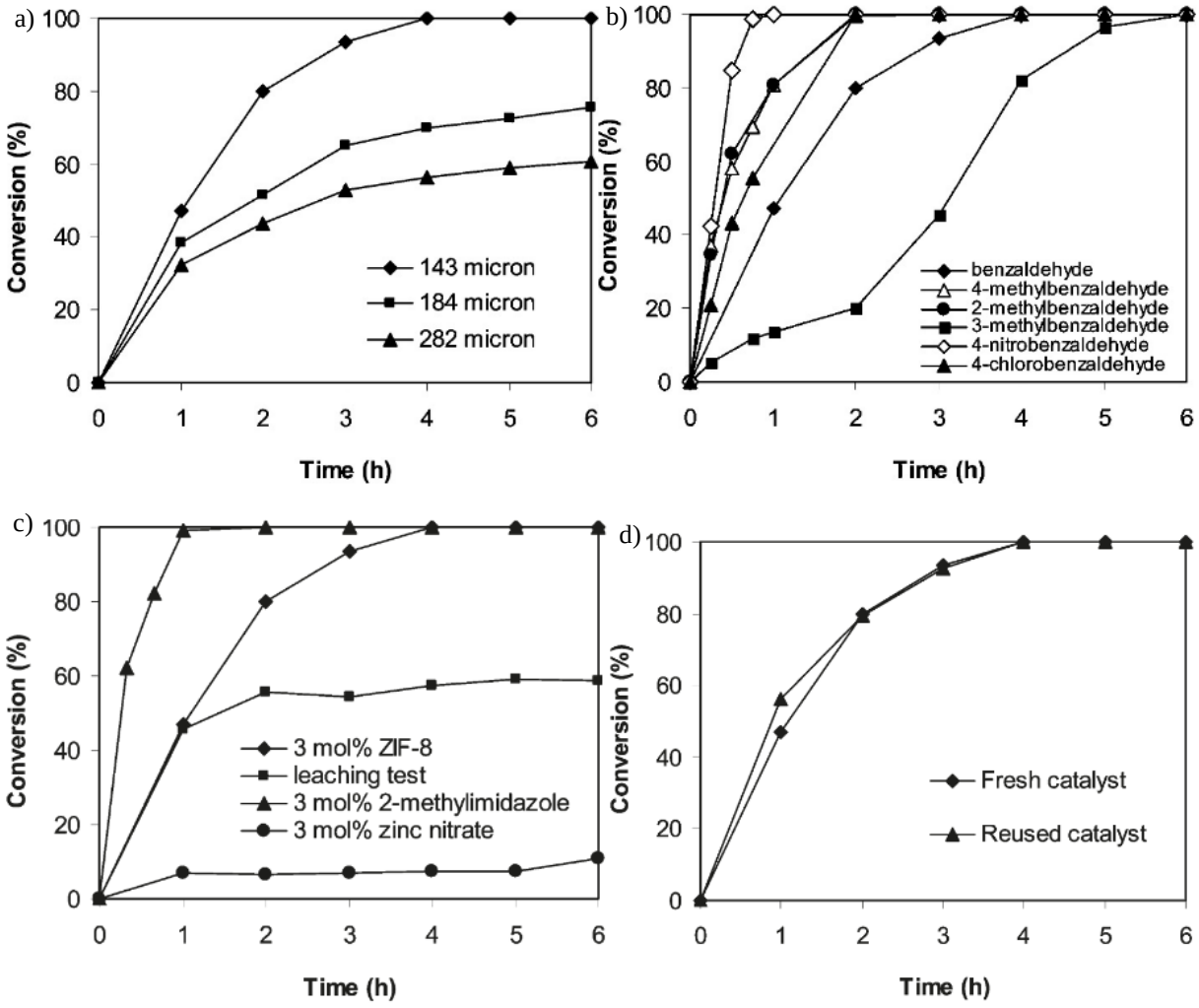

Figure 2.20 Knoevenagel condensation with ZIF-8 determined by GC-MS a) effect of particle size b) effect of substituents c) leeching test and d) catalyst recycle test.[79] (Reprinted (adapted) with permission from U. P. N. Tran, K. K. A. Le and N. T. S. Phan , *ACS Catalysis.*, 2011, **1**, 120-127. Copyright (2011) American Chemical Society.)

ZIF-8 subjected to SALE into SALEM-2 (**Chapter 2.4.2, p 32**), has shown to provide new functionality for catalysis after further post synthetic modification. The C2 position of the

imidazole can be easily lithiated into carbene-like moieties (**Figure 2.21, p 42**). The lithiated species is active towards conjugated addition of alcohols (benzyl alcohol and methanol) on an alkene. Using reagents larger than the pores allow the reaction to take place only on the external surface area. A higher conversion was obtained as compared to homogeneous catalyst (1,3-bis-(2,4,6-trimethylphenyl)imidazole-2-ylidene).[47]

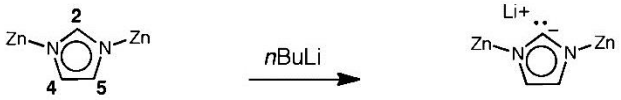

SALEM-2 **SALEM-2-Li**

Figure 2.21 Post synthetic modification of SALEM-2 by lithiation with *n*-BuLi into carbene like moieties.[47] (Reprinted (adapted) with permission from O. Karagiaridi, M. B. Lalonde, W. Bury, A. A. Sarjeant, O. K. Farha and J. T. Hupp, J. Am. Chem. Soc., 2012, **134**, 18790−18796. Copyright (2012) American Chemical Society.)

Amino-based MOFs have been popular *e.g.* IRMOF-3 and NH_2-MIL-53 and were highly effective as heterogeneous catalysts which are more active and behaves similarly to aniline homogeneous catalyst.[141] Modified ZIFs with amino groups will be studied in this work. This study will focus on the Knoevenagel condensation of ferrocene derivatives using ZIF nanoparticles as catalyst. The products of these reactions are used in dye technology, catalysis and medicine (**Chapter 2.5, p 37**).

2.6.2 ZIF Membranes and Separations

ZIFs have great potential to selectively separate mixtures of molecules, gases in particular. *E.g.* separation of CO_2 from CH_4/CO_2, N_2/CO_2, O_2/CO_2 and CO/CO_2, is important in today's industry. ZIFs are able to restrict CO_2 flow, while allowing other gasses to flow through in gas separation columns, because most ZIFs have a high affinity and selectivity for CO_2.[44,142] Multi-linker ZIFs (ZIF-69) have shown great selectivity in separating CO_2/CO mixtures.[48] ZIF-8 membranes gave good selectivity for H_2/CH_4 and H_2/N_2 mixtures favouring smaller molecules. O_2 has a higher affinity in the framework than CO_2 due to charge transfer in the ZIF-8 framework.[143]

Peralta *et al,* performed separations of hydrocarbon solvent mixtures, using ZIFs without any functional groups which behave like a-polar adsorbents and have an affinity for solvents in the following order: alkanes > alkene > aromatics solvents.[96] ZIF-8 acts as a molecular sieve and can be coated on capillaries. Linear alkanes easily flow through the pores where branched alkanes

are restricted by the pore size and hydrophobicity. Alkanes are eluted in the following order where branched alkanes elute faster than linear alkanes and short chains elute faster than longer chains.[144,145]

In 2010 Huang *et al*. successfully formed covalent bonds by coating a Al_2O_3 support with ZIF-90. Firstly, by reacting the hydroxyl group on Al_2O_3 with 3-aminopropyltriethoxysilane, then imine condensation of the amino groups with the aldehyde group of the imidazolate-2-carboxyaldehyde ligand and lastly by the nucleation and crystal growth of ZIF-90 on the modified Al_2O_3 surface during a solvothermal reaction (**Scheme 2.7**, p **43**). The membrane shows good thermal stability up to 200 ℃ and H_2 permselectivity from gas mixtures.[146]

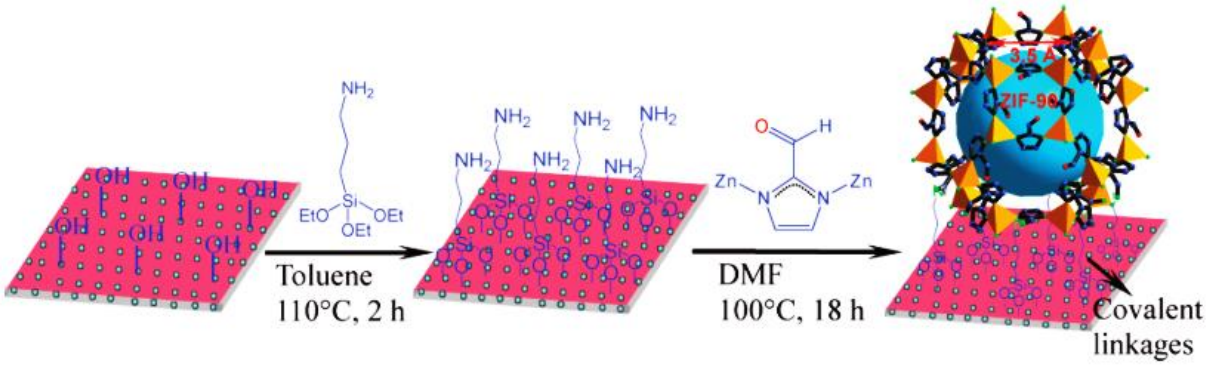

Scheme 2.7 Scheme of ZIF-90 formation and covalent bond on Al_2O_3 support by imine condensation with 3-aminopropyltriethoxysilane.[146] (Reprinted (adapted) with permission from A. Huang, W. Dou and J. Caro, *J. Am. Chem. Soc.*, 2010, **132**, 15562–15564. Copyright (2010) American Chemical Society.)

Membranes and Separations are not within the scope of this study but the findings can assist us in understanding the nature of ZIF's and bond formation.

2.6.3 Medical applications

The detection and measurement of nanoparticles was made possible with the development of sophisticated machines which can analyse and detect these particles: *e.g.* Atomic Force Miscroscopy (AFM), X-ray Photoelectron Spectroscopy, high resolution Transmission Electron Microscopy (TEM) or Scanning Electron Microscopy (SEM).[147] Nanotechnology has opened doors to many fields of research, *e.g.* the use of nanoparticles *i.e.* polymeric nanoparticles, carbon nanotubes, liposomes, zeolites in medicine.[148] Direct administrations of drugs usually require high dosages and poor targeting of cells. Nanoparticles can assist in stabilising the drug by encapsulation or surface modifications and assist in targeting specific cells with slow release of drugs and may even breach the blood-brain barrier.[148,149,150]

Recently MOFs have also been feasible candidates in medicine especially as drug carriers. The building blocks of ZIF-8 have low toxicity, suitable for medical applications; Zn has a LD_{50} of 0.35 g/kg and 1-methylimidazole has a LD_{50} of 8.4 g/kg, and is easily removed under physiological conditions, which is important for MOFs that digest in the body. The nanoparticles need to be smaller than 200 nm to move freely in the thinnest blood vessels.[151] ZIFs have shown to be good candidates for drug delivery systems because of their relatively low cytotoxicity.[149,152,153] ZIF-8 has a relatively higher cytotoxicity than other MOFs since the Zn ions are known to induce cellular toxicity by competing with Fe and Ca ions thus modifying the metabolism causing cell damage.[152]

In 2012 Liédana *et al*. used ZIF-8 to encapsulate caffeine by *in situ* and *ex situ* methods. The *in situ* method, by synthesising ZIF-8 in the presence of caffeine, gave a loading of 28 % within two hours. With *ex situ* methods, mixing pre synthesised ZIF-8 with caffeine, the process was much slower and took over 3 days to reach 28 % loading. Both encapsulating methods show slow drug release of up to 27 days with little damage to the ZIF-8 crystallinity.[154] Sun *et al*. were the first researchers to use ZIF-8 as a drug carrier for anticancer drugs. The anticancer agent used was 5-fluorouracil (5-FU) and achieved a loading of 660 mg g^{-1} in ZIF-8. ZIF-8, which have a low pH sensitivity, (**Chapter 2.3.5, p 26**) is suitable as a pH responsive drug release. Experiments was performed at a pH of 7.0, where 50 % 5-FU was released within 12 hours; where as a pH of 5.0, 45 % 5-FU was released in 1 hour as opposed to 17 % at pH 7.0.[89] The anti-cancer drug doxorubicin (DOX) incorporated in ZIF-8 has a loading of 0.049 g of doxorubicin per gram of ZIF-8. The therapeutic profile was improved to give a slow release up to 30 days. The slow release allowed the drugs to show lower cytotoxicity compared to pure doxorubicin.[77] The loading of DOX was further improved by modifying the zinc metal nodes with poly acrylic acid after ZIF-8 formation with 2-methylimidazole. The new PAA@ZIF-8 has a loading of 1.9 g DOX per gram of PAA@ZIF-8 with low toxicity and effective drug release.[155] Small molecules, namely fluorescein and the anti-cancer drug camptothecin, were also encapsulated with ZIF-8 showing effectiveness towards MCF-7 breast cancer cells, with an EC_{50} of 45 µg/ml with successful drug delivery and release of cytotoxic camptothecin in cells. Further studies showed that camptothecin@ZIF-8 leads to faster cell deaths than free camptothecin.[149] ZIF-8 is a good sorbent for acidic drugs (Ibuprofen, Naproxen and Ketoprofen) at low concentrations.[156] Multi-functional ZIF-8 drug carriers and imaging agents for cancer cells were synthesised in a two-step reaction: encapsulation of carbon nanodots in ZIF-8 (C-dots@ZIF-8) followed by incorporation of 5-FU anticancer drug. The pH responsive C-dots@ZIF-8 can

effectively deliver C-dots fluorescence imaging agent and 5-FU anticancer drug simultaneously.[157]

The use of pH sensitive material to deliver and release drugs is a useful technique.[158] The acid sensitivity of ZIF-8 enables the release of drugs to target cancer cells which are more acidic than normal cells. The ZIF-8 structure is thus able to hold the drugs for a reasonable time in the body before it reaches the cancer cells.[89,149] ZIF-8 is used in biomimetic mineralization as a protective coating for biomacromolecules (proteins, enzymes and DNA) to enhance stability in extreme conditions such as boiling water where the enzyme completely loses its bioactivity. For example, Urease denatures at 45° C which after ZIF-8 coating is protected up to 80 °C.[159]

Combing ZIF-8 nanoparticles with selected Metallocenes (anticancer drugs), it is possible to achieve effective drug delivery. In this study, ZIF-8 nanoparticles will undergo solvent assisted ligand exchange and then post-synthetical modification with ferrocene.

2.6.4 Gas Storage

Gas storage has become very important in today's world especially hydrogen and carbon dioxide storage. Hydrogen is one of the most important energy carriers with the ability to provide clean energy with a huge positive environmental impact and a high power density (33.3 kWh kg^{-1}) compared to methane (13.9 kWh kg^{-1}) and gasoline (23.5 kWh kg^{-1}).[160] A rising amount of greenhouse gas, especially carbon dioxide, has a negative effect on climate change and it is important to capture and store CO2. Materials such as MOFs can be adapted to safely store gasses. ZIFs requires pores sizes large enough to allow gases to enter for instance H_2 kinetic diameter is ~2.9 Å , CO_2 kinetic diameter is 3.3 Å and N_2 kinetic diameter is 3.6 Å .[146]

Three important factors contribute greatly to hydrogen adsorption *i.e.* surface area, free volume and heat of adsorption. The higher the surface area, the higher the H_2 excess uptake in MOFs. Together with the free volume one can estimate the potential of H_2 adsorption.[161] Various methods or modifications on MOFs like: open metal sites, guest metal ions, metal nanoparticles, different ligand bonds and ligand functionalization has been employed to improve hydrogen storage.[162] Computational studies of H_2 adsorption in MOFs correlates well with experimental values.[163,160] Wu *et al.* and others, using neutron powder diffraction and computational simulations, have shown that the strongest attraction site for H_2 in ZIFs is on the imidazolate organic linker itself (**Figure 2.22, p 46**) rather than on the metal tetrahedral ZnN_4 triangular

faces. The hydrogen adsorbs mainly on the sp^2 hybridized C=C bond with and adsorption energy of 8.6 kJ mol^{-1} and on both sides of the imidazole organic linker and then forms secondary adsorption site in the pore channel with an adsorption energy of 6.9 kJ mol^{-1}.[164,165] The presence of oxygen (electronegativity effects) atoms or COO groups in MOFs also play an important role in hydrogen adsorption. The difference in adsorption results between calculations and experimental results is due to: a) ZIF-8 undergoes structural change at high loadings b) ZIF-8 may have kinetically inaccessible areas.[166]

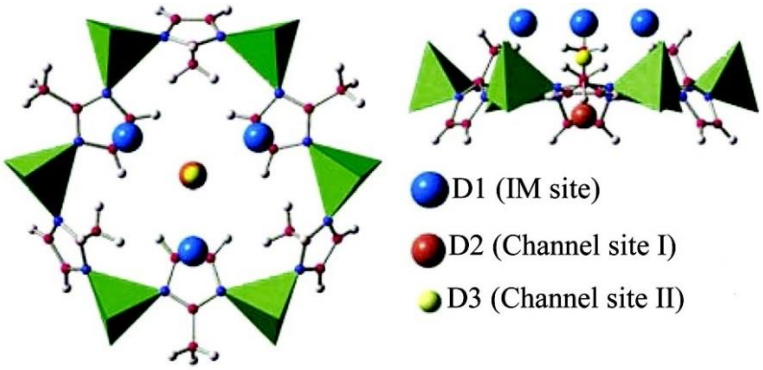

Figure 2.22 Hydrogen adsorption sites on the C=C bond of 2-methylimidazole of ZIF-8 obtained from Fourier difference analysis. Hydrogen atoms represented by blue (D1), red (D2) and green (D3) balls. Zinc metal tetrahedral coordination is represented by the green pyramids.[164] (Reprinted (adapted) with permission from H. Wu, W. Zhou, T. Yildirim, *J. Am. Chem. Soc.*, 2007, **129**, 5314-5315. Copyright (2007) American Chemical Society.)

Hydrogen storage at low pressure, as shown by the works of Rowsell *et el*., showed a slight improvement to hydrogen uptake on functional groups of IRMOF with $-C_2H_4-$ > $-NH_2$ > -Br on the benzene rings. Catenation (interpenetration of two or more framework) to reduce the pore dimensions lead to a higher uptake. Unsaturated metal sites found on HKUST-1 and MOF-74 provide attractive binding sites and enhanced physisorption which aids in the increased uptake of hydrogen at low pressures.[13] The pore dimensions are a major factor for adsorption of hydrogen with large pore volumes being essential for total hydrogen uptake. The well-known Chahine rule for hydrogen adsorption, states that every 1 wt % of excess hydrogen adsorption requires a surface of 500 m^2 g^{-1}. The microporous volume has a correlation of 5 wt % per cm^{-3} g^{-1}. Materials with a median pore size of 0.7 nm was found to perform better than the Chahine rule, which shows the importance of pore size. Materials with mircopore volumes less than 0.8 g cm^{-3} have similar density to liquid hydrogen.[167]

Initial reports on ZIF-8 have found it to have high potential in H_2 adsorption although the adsorption is lower in than other MOFs due to the smaller pore volume and surface area. ZIF-8 adsorbs 4.4 wt % excess hydrogen at 30 K, while at 77 K the maximum excess adsorption is 3.3 wt % at 30 bar (**Figure 2.23, p 47**). The excess isosteric heat of adsorption modified from the Clausius-Clapeyron equation for ZIF-8 is ~12.0 kJ mol^{-1}, is comparable to that of carbon materials. The low energy means the adsorption is mainly physisorption although a higher heat of adsorption of ~20 kJ mol^{-1} is preferred for practical use.[168] ZIF-7 (Zn) and ZIF-9 (Co) with benzimidazole linker was seen to have unusual gate opening effects (**Figure 2.23, p 47**) with a maximum adsorption of 1.43 and 1.37 wt % respectively. ZIF-11(Zn) and ZIF-12 (Co) with RHO topology has an adsorption of 2.53 and 2.63 wt % respectively. This shows that metal centres do not play a role in hydrogen adsorption but the RHO topology has roughly doubled the adsorption.[167]

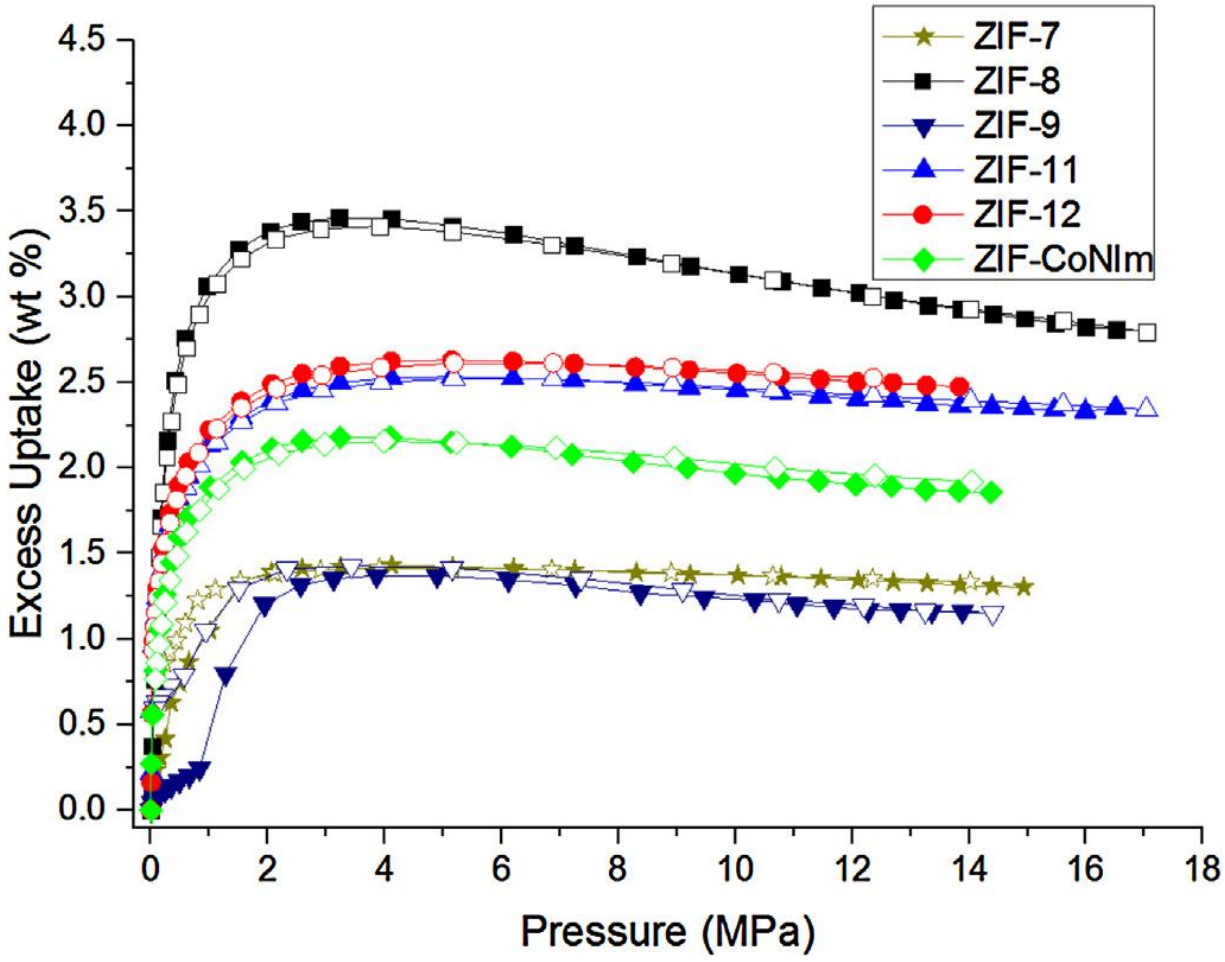

Figure 2.23 Various ZIF higher pressure isotherms of hydrogen adsorption at 77 K. Open symbols represent desorption isotherms.[167] (Reprinted (adapted) with permission from A. Noguera-Díaz, N. Bimbo, L. T. Holyfield, I. Y. Ahmet, V. P. Ting and T. J. Mays, *Colloids Surfaces A Physicochem. Eng. Asp.*, 2016, **496**, 77–85. Copyright (2015) Elsevier B.V.)

ZIFs are good candidates for CO_2 adsorption with ZIF-8 having a capacity of 0.53 mmol CO_2/ g.[72] One of the best performing ZIFs, ZIF-69 (gme topology), reversibly adsorbs 82.6 litres of CO_2 in 1 litre of material at 273 K (40.6 $cm^3 g^{-1}$) which is a significant improvement to industrial BPL carbon or even MOF-177.[44] ZIF-78 with a multi-linker structure has a CO_2 adsorption of ~30 $cm^3 g^{-1}$.[101] The ZIF-8- NH_2BzIm discussed in (**Chapter 2.4.1, p 31**) shows an improvement in CO_2 adsorption (12.2 mmol cm^{-3}) but as the percentage of NH_2BzIm linker increases to 47% a significant decrease of CO_2 adsorption (3.5 mmol cm^{-3}) was observed due to the shrinking pore size of the new NH_2BzIm linker.[102] ZIF-8 high-pressure CO_2 adsorption of both experimental and simulation shows an adsorption of ~5.5 mmol g^{-1} at 30 bar. Amine modified ZIF-8 shows an increase of CO_2 adsorption. The additional amine groups increases the mass of the ZIF-8, thus showing that even with an increasing mass the uptake (mmol) improves.[169]

A different approach to improve CO_2 adsorption is by modification of MOFs with amines. Amine groups have been used to effectively enhance CO_2 adsorption in materials.[170,171] The concept has been performed on Mg-MOF-74 where ethylenediamine was grafted in the pores and showed a significant improvement of about 50 % increase in CO_2 uptake.[172] Ethylenediamine was later PSM on ZIF-8-90 multi-linker and a significant increase of CO_2 uptake was observed.[102]

2.7 References

1 E. M. Flanigen, R. W. Broach and S. T. Wilson, *Zeolites in Industrial Separation and Catalysis*, John Wiley & Sons, 2010, 2010.

2 C. S. Cundy and P. A. Cox, *Chem. Rev.*, 2003, **103**, 663–701.

3 B. Yilmaz and U. Muller, *Top. Catal.*, 2009, **52**, 888–895.

4 J. Scherzer, *Catal. Rev.- Sci. Eng*, 1989, **31**, 215–354.

5 M. Schröder, *Functional Metal-Organic Frameworks: Gas Storage, Separation and Catalysis*, Springer, 2010.

6 D. Farrusseng, S. Aguado and C. Pinel, *Angew. Chemie - Int. Ed.*, 2009, **48**, 7502–7513.

7 M. Fujita, *METAL-ORGANIC FRAMEWORKS: Design and Application*, John Wiley & Sons, 2010, 2010.

8 P. Küsgens, M. Rose, I. Senkovska, H. Fröde, A. Henschel, S. Siegle and S. Kaskel, *Microporous Mesoporous Mater.*, 2009, **120**, 325–330.

9 A. R. Millward and O. M. Yaghi, *J. Am. Chem. Soc.*, 2005, **127**, 17998–17999.

10 S. R. Miller, D. Heurtaux, T. Baati, P. Horcajada, J.-M. Grenèche and C. Serre, *Chem.*

Commun. (Camb)., 2010, **46**, 4526–4528.

11 O. Farha, I. Eryazici, N. C. Jeong, B. Hauser, C. Wilmer, A. Sarjeant, R. Snurr and S. Nguyen, *J. Am. Chem. Soc.*, 2012, **134**, 15016–15021.

12 K. S. Park, Z. Ni, A. P. Côté, J. Y. Choi, R. Huang, F. J. Uribe-Romo, H. K. Chae, M. O'Keeffe and O. M. Yaghi, *Proc. Natl. Acad. Sci. U. S. A.*, 2006, **103**, 10186–10191.

13 J. L. C. Rowsell and O. M. Yaghi, *J. Am. Chem. Soc.*, 2006, **128**, 1304–1315.

14 A. Kuc, A. Enyashin and G. Seifert, *J. Phys. Chem. B*, 2007, **111**, 8179–8186.

15 E. Y. Lee, S. Y. Jang and M. P. Suh, *J. Am. Chem. Soc.*, 2005, **127**, 6374–6381.

16 F. X. Coudert, M. Jeffroy, A. H. Fuchs, A. Boutin and C. Mellot-Draznieks, *J. Am. Chem. Soc.*, 2008, **130**, 14294–14302.

17 B. F. Hoskin and R. Robson, *J. Am. Chem. Soc.*, 1990, **112**, 1546–1554.

18 U. Schubert, N. Huesing and A. Lorenz, *Chem. Mater.*, 1995, **7**, 2010–2027.

19 M. H. Lim, C. F. Blanford and A. Stein, *Chem. Mater.*, 1998, **4756**, 467–470.

20 F. Diaz, K. J. Balkus, F. Bedioui, V. Kurshev, L. Kevan and J. F. Diaz, *Chem. Mater.*, 1997, **9**, 61–67.

21 M. Schroeder, *Functional Metal-Organic Frameworks: Gas Storage, Separation and Catalysis*, Springer, 2010, vol. 293.

22 K. K. Tanabe, Z. Wang and S. M. Cohen, *J. Am. Chem. Soc.*, 2008, **130**, 8508–8517.

23 E. Dugan, Z. Wang, M. Okamura, A. Medina and S. M. Cohen, *Chem. Commun. (Camb).*, 2008, **7345**, 3366–3368.

24 M. J. Ingleson, J. P. Barrio, J.-B. Guilbaud, Y. Z. Khimyak and M. J. Rosseinsky, *Chem. Commun. (Camb).*, 2008, 2680–2682.

25 C. Volkringer and S. M. Cohen, *Angew. Chemie - Int. Ed.*, 2010, **49**, 4644–4648.

26 T. Ahnfeldt, D. Gunzelmann, T. Loiseau, D. Hirsemann, J. Senker, G. Férey and N. Stock, *Inorg. Chem.*, 2009, **48**, 3057–3064.

27 M. Savonnet, D. Bazer-Bachi, N. Bats, J. Perez-Pellitero, E. Jeanneau, V. Lecocq, C. Pinel and D. Farrusseng, *J. Am. Chem. Soc.*, 2010, **132**, 4518–4519.

28 D. Britt, C. Lee, F. J. Uribe-Romo, H. Furukawa and O. M. Yaghi, *Inorg. Chem.*, 2010, **49**, 6387–6389.

29 A. D. Burrows, C. G. Frost, M. F. Mahon and C. Richardson, *Chem. Commun.*, 2009, 4218–4220.

30 K. K. Tanabe and S. M. Cohen, *Chem. Soc. Rev.*, 2011, **40**, 498–519.

31 T. Gadzikwa, O. K. Farha, C. D. Malliakas, M. G. Kanatzidis, J. T. Hupp and S. T. Nguyen, *J. Am. Chem. Soc.*, 2009, **131**, 13613–13615.

32 T. Yamada and H. Kitagawa, *J. Am. Chem. Soc.*, 2009, **131**, 6312–6313.

33 M. Meilikhov, K. Yusenko and R. A. Fischer, *Dalt. Trans.*, 2010, **39**, 10990–10999.

34 M. Wehring, P. C. M. M. Magusin, S. Amirjalayer, R. Schmid and F. Stallmach, *Microporous Mesoporous Mater.*, 2014, **186**, 130–136.

35 M. Meilikhov, K. Yusenko and R. A. Fischer, *J. Am. Chem. Soc.*, 2009, **131**, 9644–9645.

36 J. E. Halls, A. Hernán-Gómez, A. D. Burrows and F. Marken, *Dalton Trans.*, 2012, **41**, 1475–80.

37 A. D. Burrows, L. C. Fisher, T. J. Mays, S. P. Rigby, S. E. Ashbrook and D. M. Dawson, *J. Organomet. Chem.*, 2015, **792**, 134–138.

38 P. Deria, J. E. Mondloch, O. Karagiaridi, W. Bury, J. T. Hupp and O. K. Farha, *Chem Soc Rev*, 2014, **43**, 5896–5912.

39 M. Kondo, S. Furukawa, K. Hirai and S. Kitagawa, *Angew. Chemie - Int. Ed.*, 2010, **49**, 5327–5330.

40 O. Karagiaridi, W. Bury, E. Tylianakis, A. A. Sarjeant, J. T. Hupp and O. K. Farha, *Chem. Mater.*, 2013, **25**, 3499–3503.

41 M. Schröder, *Functional Metal-Organic Frameworks: Gas Storage, Separation and Catalysis*, Springer, 2010.

42 H. Deng, C. J. Doonan, H. Furukawa, R. B. Ferreira, J. Towne, C. B. Knobler, B. Wang and O. M. Yaghi, *Science (80-.).*, 2010, **327**, 846–850.

43 J. P. Zhang, Y. B. Zhang, J. Bin Lin and X. M. Chen, *Chem. Rev.*, 2012, **112**, 1001–1033.

44 A. Phan, C. J. Doonan, F. J. Uribe-Romo, C. B. Knobler, M. Okeeffe and O. M. Yaghi, *Acc. Chem. Res.*, 2010, **43**, 58–67.

45 R. Lehnert and F. Seel, *Zeitschrift für Anorg. und Allg. Chemie*, 1980, **464**, 187–194.

46 X. Huang, J. Zhang and X. Chen, *Chinese Sci. Bull.*, 2003, **48**, 1531–1534.

47 O. Karagiaridi, M. B. Lalonde, W. Bury, A. A. Sarjeant, O. K. Farha and J. T. Hupp, *J. Am. Chem. Soc.*, 2012, **134**, 18790–18796.

48 R. Banerjee, A. Phan, B. Wang, C. Knobler, H. Furukawa, M. O'Keeffe and O. M. Yaghi, *Science*, 2008, **319**, 939–943.

49 B. Wang, A. P. Côté, H. Furukawa, M. O'Keeffe and O. M. Yaghi, *Nature*, 2008, **453**, 207–211.

50 M. Eddaoudi and J. F. Eubank, *METAL-ORGANIC FRAMEWORKS: Design and Application*, John Wiley & Sons, 2010, 2010.

51 H. Bux, F. Liang, Y. Li, J. Cravillon and M. Wiebcke, *J. Am. Chem. Soc.*, 2009, **131**, 16000–16001.

52 B. Seoane, J. M. Zamaro, C. Tellez and J. Coronas, *CrystEngComm*, 2012, **14**, 3103.

53 J. A. Thompson, K. W. Chapman, W. J. Koros, C. W. Jones and S. Nair, *Microporous*

Mesoporous Mater., 2012, **158**, 292–299.

54 A. M. Joaristi, J. Juan-alcan, P. Serra-crespo, F. Kapteijn and J. Gascon, *Cryst. Growth Des.*, 2012, **12**, 3489–3498.

55 P. J. Beldon, L. Fábián, R. S. Stein, a. Thirumurugan, A. K. Cheetham and T. Friščić, *Angew. Chemie - Int. Ed.*, 2010, **49**, 9640–9643.

56 S. Tanaka, K. Kida, T. Nagaoka, T. Ota and Y. Miyake, *Chem. Commun.*, 2013, **49**, 7884–7886.

57 A. Carné-Sánchez, I. Imaz, M. Cano-Sarabia and D. Maspoch, *Nat. Chem.*, 2013, **5**, 203–11.

58 A. Garcia Marquez, P. Horcajada, D. Grosso, G. Ferey, C. Serre, C. Sanchez and C. Boissiere, *Chem. Commun. (Cambridge, United Kingdom)*, 2013, **49**, 3848–3850.

59 Y. Pan, Y. Liu, G. Zeng, L. Zhao and Z. Lai, *Chem. Commun. (Camb).*, 2011, **47**, 2071–2073.

60 S. R. Venna, J. B. Jasinski and M. A. Carreon, *J. Am. Chem. Soc.*, 2010, **132**, 18030–18033.

61 K. Kida, M. Okita, K. Fujita, S. Tanaka and Y. Miyake, *CrystEngComm*, 2013, **15**, 1794.

62 J. Yao, M. He, K. Wang, R. Chen, Z. Zhong and H. Wang, *CrystEngComm*, 2013, **15**, 3601.

63 H. Y. Cho, J. Kim, S. N. Kim and W. S. Ahn, *Microporous Mesoporous Mater.*, 2013, **169**, 180–184.

64 Y. Pan, D. Heryadi, F. Zhou, L. Zhao, G. Lestari, H. Su and Z. Lai, *CrystEngComm*, 2011, **13**, 6937.

65 K. Liang, R. Ricco, C. M. Doherty, M. J. Styles and P. Falcaro, *CrystEngComm*, 2016, **18**, 4264–4267.

66 A. Polyzoidis, T. Altenburg, M. Schwarzer, S. Loebbecke and S. Kaskel, *Chem. Eng. J.*, 2016, **283**, 971–977.

67 J. Cravillon, S. Münzer, S. J. Lohmeier, A. Feldhoff, K. Huber and M. Wiebcke, *Chem. Mater.*, 2009, **21**, 1410–1412.

68 I. H. Lim, W. Schrader and F. Schüth, *Chem. Mater.*, 2015, **27**, 3088–3095.

69 J. Cravillon, R. Nayuk, S. Springer, A. Feldhoff, K. Huber and M. Wiebcke, *Chem. Mater.*, 2011, **23**, 2130–2141.

70 J. Cravillon, C. A. Schröder, R. Nayuk, J. Gummel, K. Huber and M. Wiebcke, *Angew. Chemie - Int. Ed.*, 2011, **50**, 8067–8071.

71 E. L. Bustamante, J. L. Fernández and J. M. Zamaro, *J. Colloid Interface Sci.*, 2014, **424**, 37–43.

72 L. S. Lai, Y. F. Yeong, N. C. Ani, K. K. Lau and A. M. Shariff, *Part. Sci. Technol.*, 2014, **32**, 520–528.

73 C. W. Tsai and E. H. G. Langner, *Microporous Mesoporous Mater.*, 2016, **221**, 8–13.

74 P. Scherrer, *Nachrichten von der Gesellschaft der Wissenschaften zu Göttingen, Math. Klasse*, 1918, **2**, 98–100.

75 J. I. Langford and A. J. C. Wilson, *J. Appl. Crystallogr.*, 1978, **11**, 102–113.

76 A. Monshi, *World J. Nano Sci. Eng.*, 2012, **02**, 154–160.

77 I. B. Vasconcelos, T. G. Da Silva, G. C. G. Militão, T. a. Soares, N. M. Rodrigues, M. O. Rodrigues, N. B. Da Costa, R. O. Freire and S. a. Junior, *RSC Adv.*, 2012, **2**, 9437.

78 Y. Hu, H. Kazemian, S. Rohani, Y. Huang and Y. Song, *Chem. Commun.*, 2011, **47**, 12694.

79 U. P. N. Tran, K. K. A. Le and N. T. S. Phan, *ACS Catal.*, 2011, **1**, 120.

80 P. A. Webb and C. Orr, *Analytical Methods in Fine Particle Technology*, Micromeretics Instrument Corp, First edit., 1997.

81 S. Brunauer, L. S. Deming, W. E. Deming and E. Teller, *J. Am. Chem. Soc.*, 1940, **62**, 1723–1732.

82 P. A. Webb and C. Orr, *Analytical Methods in Fine Particle Technology*, Micromeretics Instrument Corp, First edit., 1997.

83 K. W. Kolasinski, *Surface science: foundations of catalysis and nanoscience*, John Wiley & Sons, Second edi., 2012.

84 K. Zhang, R. P. Lively, M. E. Dose, A. J. Brown, C. Zhang, J. Chung, S. Nair, W. J. Koros and R. R. Chance, *Chem. Commun. (Cambridge, United Kingdom)*, 2013, **49**, 3245–3247.

85 A. U. Ortiz, A. P. Freitas, A. Boutin, A. H. Fuchs and F.-X. Coudert, *Phys. Chem. Chem. Phys.*, 2014, **16**, 9940–9.

86 I. Khay, G. Chaplais, H. Nouali, G. Ortiz, C. Marichal and J. Patarin, 2016, 4392–4400.

87 K. a. Cychosz and A. J. Matzger, *Langmuir*, 2010, **26**, 17198–17202.

88 A. Demessence, C. Boissière, D. Grosso, P. Horcajada, C. Serre, G. Férey, G. J. a. a. Soler-Illia and C. Sanchez, *J. Mater. Chem.*, 2010, **20**, 7676.

89 C.-Y. Sun, C. Qin, X.-L. Wang, G.-S. Yang, K.-Z. Shao, Y.-Q. Lan, Z.-M. Su, P. Huang, C.-G. Wang and E.-B. Wang, *Dalt. Trans.*, 2012, **41**, 6906.

90 X. Liu, Y. Li, Y. Ban, Y. Peng, H. Jin, H. Bux, L. Xu, J. Caro and W. Yang, *Chem. Commun. (Camb).*, 2013, **49**, 9140–2.

91 E. C. Spencer, R. J. Angel, N. L. Ross, B. E. Hanson and J. A. K. Howard, *J. Am. Chem. Soc.*, 2009, **131**, 4022–4026.

92 S. A. Moggach, T. D. Bennett and A. K. Cheetham, *Angew. Chemie - Int. Ed.*, 2009, **48**, 7087–7089.

93 D. Fairen-Jimenez, S. A. Moggach, M. T. Wharmby, P. A. Wright, S. Parsons and T. Düren, *J. Am. Chem. Soc.*, 2011, **133**, 8900–8902.

94 M. Casco, Y. Cheng, L. L. Daemen, D. Fairen-Jimenez, E. V. Ramos Fernandez, A. J. Ramirez-Cuesta and J. Silvestre-Albero, *Chem. Commun.*, 2016, 3639–3642.

95 T. Chokbunpiam, S. Fritzsche, C. Chmelik, J. Caro, W. Janke and S. Hannongbua, *Chem. Phys. Lett.*, 2016, **648**, 178–181.

96 D. Peralta, G. Chaplais, A. Simon-Masseron, K. Barthelet, C. Chizallet, A. A. Quoineaud and G. D. Pirngruber, *J. Am. Chem. Soc.*, 2012, **134**, 8115–8126.

97 A. F. P. Ferreira, M. C. Mittelmeijer-Hazeleger, M. A. Granato, V. F. D. Martins, A. E. Rodrigues and G. Rothenberg, *Phys. Chem. Chem. Phys.*, 2013, **15**, 8795–804.

98 E. Haldoupis, T. Watanabe, S. Nair and D. S. Sholl, *ChemPhysChem*, 2012, **13**, 3449–3452.

99 W. Morris, C. J. Doonan, H. Furukawa, R. Banerjee and O. M. Yaghi, *J. Am. Chem. Soc.*, 2008, **130**, 12626–12627.

100 J. A. Thompson, C. R. Blad, N. A. Brunelli, R. P. Lively, M. E. Lydon, W. Jones and S. Nair, *Langmuir*, 2012, 1–8.

101 Y. Ban, Y. Li, X. Liu, Y. Peng and W. Yang, *Microporous Mesoporous Mater.*, 2013, **173**, 29–36.

102 J. A. Thompson, N. A. Brunelli, R. P. Lively, J. R. Johnson, C. W. Jones and S. Nair, *J. Phys. Chem. C*, 2013, **117**, 8198–8207.

103 O. Karagiaridi, W. Bury, A. A. Sarjeant, C. L. Stern, O. K. Farha and J. T. Hupp, *Chem. Sci.*, 2012, **3**, 3256.

104 M. Kim, J. F. Cahill, H. Fei, K. A. Prather and S. M. Cohen, *J. Am. Chem. Soc.*, 2012, **134**, 18082–18088.

105 H. Fei, J. F. Cahill, K. A. Prather and S. M. Cohen, *Inorg. Chem.*, 2013, **52**, 4011–4016.

106 M. E. Schweinefuß, S. Springer, I. A. Baburin, T. Hikov, K. Huber, S. Leoni and M. Wiebcke, *Dalt. Trans.*, 2014, **43**, 3528–3536.

107 J. Q. Jiang, C. X. Yang and X. P. Yan, *Chem Commun*, 2015, **51**, 6540–6543.

108 S. A. Basnayake, K. Tan, M. Leonard, Y. Chabal and K. J. Balkus, *Microporous Mesoporous Mater.*, 2016, **219**, 172–177.

109 C. J. Stephenson, J. T. Hupp and O. K. Farha, *Inorg. Chem.*, 2016, **55**, 1361–1363.

110 Y. Ban, Y. Peng, Y. Zhang, H. Jin, W. Jiao, A. Guo, P. Wang, Y. Li and W. Yang, *Microporous Mesoporous Mater.*, 2016, **219**, 190–198.

111 M. B. Lalonde, J. E. Mondloch, P. Deria, A. A. Sarjeant, S. S. Al-Juaid, O. I. Osman, O. K. Farha and J. T. Hupp, *Inorg. Chem.*, 2015, **54**, 7142–7144.

112 Y. Ban, Y. Li, Y. Peng, H. Jin, W. Jiao, X. Liu and W. Yang, *Chemistry*, 2014, **20**, 11402–11409.

113 N. Metzler-Nolte and M. Salmain, *Ferrocenes Ligands, Mater. Biomol.*, 2008, 499–639.

114 Y. Zhao, Y. Ding, Y. Li, L. Peng, H. R. Byon, J. B. Goodenough and G. Yu, *Chem. Soc. Rev.*, 2015, **44**, 7968–7996.

115 M. D. Rausch, E. O. Fischer and H. Grubert, *J. Am. Chem. Soc.*, 1960, **82**, 76–82.

116 J. C. Spiteri, J. S. Schembri and D. C. Magri, *New J. Chem.*, 2015, **39**, 3349–3352.

117 D. A. Links, 2011, 1732–1736.

118 A. M. Asiri, *Appl. Organomet. Chem.*, 2001, **15**, 907–915.

119 W. L. Davis, R. F. Shago, E. H. G. Langner and J. C. Swarts, *Polyhedron*, 2005, **24**, 1611–1616.

120 D. R. Burri, I. R. Shaikh, K. Choi and S. Park, *Catal. Commun.*, 2007, **8**, 731–735.

121 R. C. J. Atkinson, V. C. Gibson and N. J. Long, *Chem. Soc. Rev.*, 2004, **33**, 313–328.

122 G. Jaouen, S. Top and A. Vessières, *Organometallics Targeted to Specific Biological Sites: The Development of New Therapies*, 2006.

123 A. Kaasik, V. Veksler, E. Boehm, M. Novotova and R. Ventura-Clapier, *FASEB J.*, 2003, **17**, 708–710.

124 M. F. R. Fouda, A.-E. M. and R. A. Abdelsamaia, *Appl. Organomet. Chem.*, 2007, **21**, 613–625.

125 E. W. Neuse, *J. Inorg. Organomet. Polym.*, 2005, **15**, 3–32.

126 B. F. G. Johnson, *Top. Catal.*, 2003, **24**, 147–159.

127 B. R. Cuenya, *Thin Solid Films*, 2010, **518**, 3127–3150.

128 D. T. Thompson, *Nano Today*, 2007, **2**, 40–43.

129 R. Abu-Reziq and H. Alper, *Appl. Sci.*, 2012, **2**, 260–276.

130 B. Yuan, Y. Pan, Y. Li, B. Yin and H. Jiang, *Angew. Chemie - Int. Ed.*, 2010, **49**, 4054–4058.

131 T. T. Dang, Y. Zhu, J. S. Y. Ngiam, S. C. Ghosh, A. Chen and A. M. Seayad, 2013, **5**.

132 M. Zahmakiran, *Dalt. Trans.*, 2012, **41**, 12690.

133 P. Wang, J. Zhao, X. Li, Y. Yang, Q. Yang and C. Li, *Chem. Commun. (Camb).*, 2013, **49**, 3330–2.

134 D. Esken, S. Turner, O. I. Lebedev, G. Van Tendeloo and R. a. Fischer, *Chem. Mater.*, 2010, **22**, 6393–6401.

135 B. Xi, Y. C. Tan and H. C. Zeng, *Chem. Mater.*, 2016, **28**, 326–336.

136 C. Chizallet, S. Lazare, D. Bazer-Bachi, F. Bonnier, V. Lecocq, E. Soyer, A. A. Quoineaud and N. Bats, *J. Am. Chem. Soc.*, 2010, **132**, 12365–12377.

137 L. T. L. Nguyen, K. K. A. Le and N. T. S. Phan, *Chinese J. Catal.*, 2012, **33**, 688–696.

138 M. Zhu, D. Srinivas, S. Bhogeswararao, P. Ratnasamy and M. a. Carreon, *Catal. Commun.*, 2013, **32**, 36–40.

139 L. T. L. Nguyen, K. K. A. Le, H. X. Truong and N. T. S. Phan, *Catal. Sci. Technol.*, 2012, **2**, 521.

140 A. I. Vogel, *A Text-book of Practical Organic Chemistry Including Qualitative Organic Analysis*, Longmans Green and Co, Third edit., 1961.

141 J. Gascon, U. Aktay, M. D. Hernandez-Alonso, G. P. M. van Klink and F. Kapteijn, *J. Catal.*, 2009, **261**, 75–87.

142 C. Chmelik, J. van Baten and R. Krishna, *J. Memb. Sci.*, 2012, **397–398**, 87–91.

143 M. C. McCarthy, V. Varela-Guerrero, G. V. Barnett and H. K. Jeong, *Langmuir*, 2010, **26**, 14636–14641.

144 D. Peralta, G. Chaplais, A. Simon-Masseron, K. Barthelet and G. D. Pirngruber, *Ind. Eng. Chem. Res.*, 2012, **51**, 4692–4702.

145 N. Chang, Z. Y. Gu and X. P. Yan, *J. Am. Chem. Soc.*, 2010, **132**, 13645–13647.

146 A. Huang, W. Dou and J. Caro, *J. Am. Chem. Soc.*, 2010, **132**, 15562–15564.

147 K. W. Kolasinski, *Surface science: foundations of catalysis and nanoscience*, Second Edi., 2012.

148 A. H. Faraji and P. Wipf, *Bioorganic Med. Chem.*, 2009, **17**, 2950–2962.

149 J. Zhuang, C. Kuo, L. Chou, D. Liu, E. Weerapana, C. Tsung, C. Hill, U. States, S. Barbara and U. States, 2014, 2812–2819.

150 G. Kong, R. D. Braun and M. W. Dewhirst, *Cancer Res.*, 2000, **60**, 4440–4445.

151 P. Horcajada, R. Gref, T. Baati, P. K. Allan, G. Maurin and P. Couvreur, 2012, 1232–1268.

152 C. Tamames-Tabar, D. Cunha, E. Imbuluzqueta, F. Ragon, C. Serre, M. J. Blanco-Prieto and P. Horcajada, *J. Mater. Chem. B*, 2014, **2**, 262–271.

153 W.-S. Lo, S.-M. Liu, S.-C. Wang, H.-P. Lin, N. Ma, H.-Y. Huang and F.-K. Shieh, *RSC Adv.*, 2014, **4**, 52883–52886.

154 N. Liedana, A. Galve, C. Rubio, C. Tellez and J. Coronas, *ACS Appl. Mater. Interfaces*, 2012, **4**, 5016–5021.

155 H. Ren, L. Zhang, J. An, T. Wang, L. Li, X. Si, L. He, X. Wu, C. Wang and Z. Su, *Chem. Commun. (Camb).*, 2014, **50**, 1000–2.

156 D. Ge and H. K. Lee, *J. Chromatogr. A*, 2012, **1263**, 1–6.

157 L. He, T. Wang, J. An, X. Li, L. Zhang, L. Li, G. Li, X. Wu, Z. Su and C. Wang, *CrystEngComm*, 2014, **16**, 3259.

158 J. Jung, I.-H. Lee, E. Lee, J. Park and S. Jon, *Biomacromolecules*, 2007, **8**, 3401–3407.

159 K. Liang, R. Ricco, C. M. Doherty, M. J. Styles, S. Bell, N. Kirby, S. Mudie, D. Haylock, A. J. Hill, C. J. Doonan and P. Falcaro, *Nat. Commun.*, 2015, **6**, 7240.

160 Y. Basdogan and S. Keskin, *CrystEngComm*, 2014, **17**, 261–275.

161 H. Frost, T. Düren and R. Q. Snurr, *J. Phys. Chem. B*, 2006, **110**, 9565–9570.

162 H. W. Langmi, J. Ren, B. North, M. Mathe and D. Bessarabov, *Electrochim. Acta*, 2013, **128**, 368–392.

163 B. Assfour and G. Seifert, *Int. J. Hydrogen Energy*, 2009, **34**, 8135–8143.

164 H. Wu, W. Zhou and T. Yildirim, *J. Am. Chem. Soc.*, 2007, **129**, 5314–5315.

165 B. Assfour, S. Leoni and G. Seifert, *J. Phys. Chem. C*, 2010, **114**, 13381–13384.

166 M. Zhou, Q. Wang, L. Zhang, Y. C. Liu and Y. Kang, *J. Phys. Chem. B*, 2009, **113**, 11049–11053.

167 A. Noguera-Díaz, N. Bimbo, L. T. Holyfield, I. Y. Ahmet, V. P. Ting and T. J. Mays, *Colloids Surfaces A Physicochem. Eng. Asp.*, 2016, **496**, 77–85.

168 W. Zhou, H. Wu, M. R. Hartman and T. Yildirim, *J. Phys. Chem. C*, 2007, **111**, 16131–16137.

169 D. Liu, Y. Wu, Q. Xia, Z. Li and H. Xi, *Adsorption*, 2013, **19**, 25–37.

170 S. Choi, J. H. Drese and C. W. Jones, *ChemSusChem*, 2009, **2**, 796–854.

171 P. Bollini, S. A. Didas and C. W. Jones, *J. Mater. Chem.*, 2011, **21**, 15100.

172 S. Choi, T. Watanabe, T. H. Bae, D. S. Sholl and C. W. Jones, *J. Phys. Chem. Lett.*, 2012, **3**, 1136–1141.

3 Results and Discussion

3.1 Introduction

In this chapter, the synthesis and characterisation of nano-sized Zeolitic Imidazolate Framework -8 (nZIF-8) with different solvent ratio and additives to improve molecular yields are described first, followed by the synthesis of imidazolate ligands via *S*-alkylation and ferrocene derivatives. Time resolved solvent assisted ligand exchange (SALE) reactions of nZIF-8 with various imidazolate linkers as well as further post synthetic modification on the exchanged linkers is discussed.

Characterisations of the above ZIFs include Fourier transform infrared (FT-IR) spectroscopy, Powder X-ray diffraction (PXRD), surface area and porosity analysis via gas sorption, Transmission Electron Microscopy (TEM) with Energy-dispersive X-ray spectroscopy (EDS), Thermo-gravimetric analyse (TGA), X-ray Photoelectron Spectroscopy (XPS), inductively coupled plasma – optical emission spectrometry (ICP-OES), Liquid and Solid-state Nuclear magnetic resonance (NMR) spectroscopy where appropriate.

Lastly, applications in catalysis of the Knoevenagel condensation reaction and gas storage of CO_2 and H_2 by SALE ZIFs will be discussed.

3.2 Synthesis

3.2.1 Synthesis of nZIF-8 at increasing solvent ratio

ZIF-8 nanoparticles were synthesised by a rapid isothermal bench top reaction in ambient atmosphere conditions. In a typical reaction $Zn(NO_3).4H_2O$ (5 mmol) and 2-methylimidazole (MeIm) (40 mmol) was dissolved separately in methanol (100 cm^3) and heated to 60 ℃ before mixing the two solutions together. To determine the effect of various reagent concentrations, the Zn^{2+}:MeIm molar ratio of 1:8 was kept constant, while changing the methanol solvent molar ratios (1000, 1500 and 2000 - investigated in triplicate). During the addition of the $Zn(NO_3)_2$

solution into the MeIm solution, the solution turned milky immediately while stirring rapidly at 60 ℃ for 1 hour (**Scheme 3.1**, **p 58**). As the solvent ratios were increased the reactions turned milky much slower. During the synthesis, the deprotonated MeIm coordinates with the Zn^{2+} ion in a tetrahedral manner while the excess neutral MeIm acts as a surfactant preventing particle size growth.

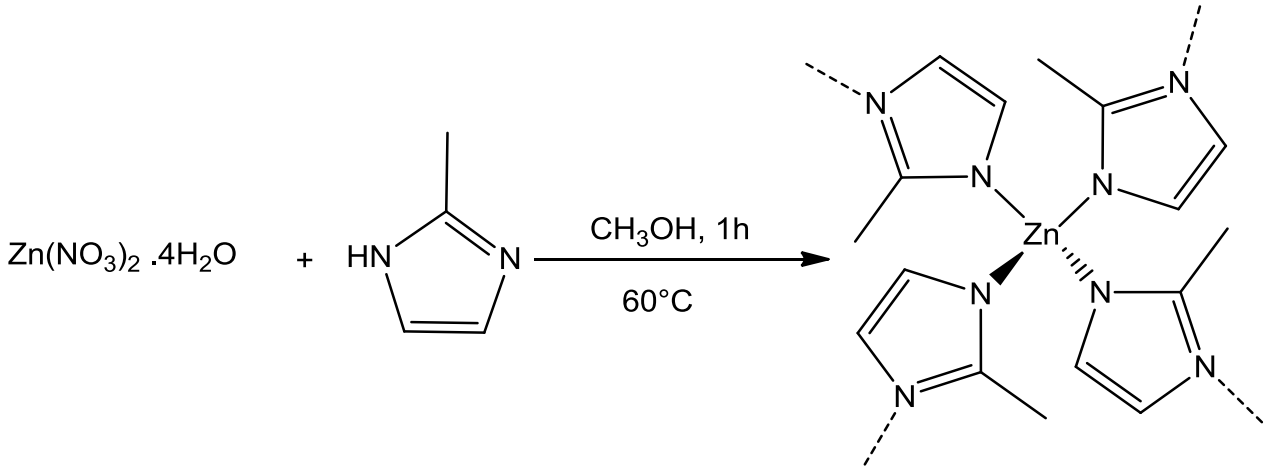

Scheme 3.1 General synthesis of ZIF-8 nanoparticles by rapid isothermal mixing of zinc nitrate and 2-methylimidazole in methanol.

The particles were isolated by centrifugation at 8500 rpm at 10 ℃, but for the methanol ratio of 1500 the suspension remained milky at lower centrifugation force, showing that the particles were unable to separate. For the methanol ratio of 2000, the suspension remained milky even after increasing the centrifugation speed to 9500 rpm. Dialysis (12000 MWCO tubes) followed by freeze-drying was used to isolate the nanoparticles and remove the water. Thereafter the particles were activated under vacuum at 100 ℃ to remove excess solvent or reagents in the pores to obtain a white powder or flakes. Reasonable yields of about 45 % were obtained, except for the high methanol ratio (2000) which gave a yield of 35 %, possibly due to ineffective centrifugation or dialysis.

The samples synthesised at different methanol ratios were characterised by FTIR as seen in **Figure 3.1 (p 59)**. In all the spectra, the absence of a broad N-H stretching frequency between 3000 and 3500 cm^{-1} shows that the 2-methylimidazole is bound to Zn in nZIF-8. The spectra of nZIF-8_{1000} (**d**) and nZIF-8_{1500} (**c**) are identical to ZIF-8 spectra in literature. A weak stretching frequency at 3134 cm^{-1} together with the out-of-plane bending frequency at 1145 cm^{-1} for CH_3, the aliphatic C-C stretching frequency band at 1572 cm^{-1}, the sp^3 C-H bend frequency at 1420 cm^{-1} and the C-N stretching frequency between 1150 – 1350 cm^{-1} are all in agreement to

literature.[1,2] The nZIF-8_{2000} after dialysis for 1 day (**b**) shows an additional peaks at 827 cm^{-1}, which shows that the short dialysis is insufficient to purify the sample.

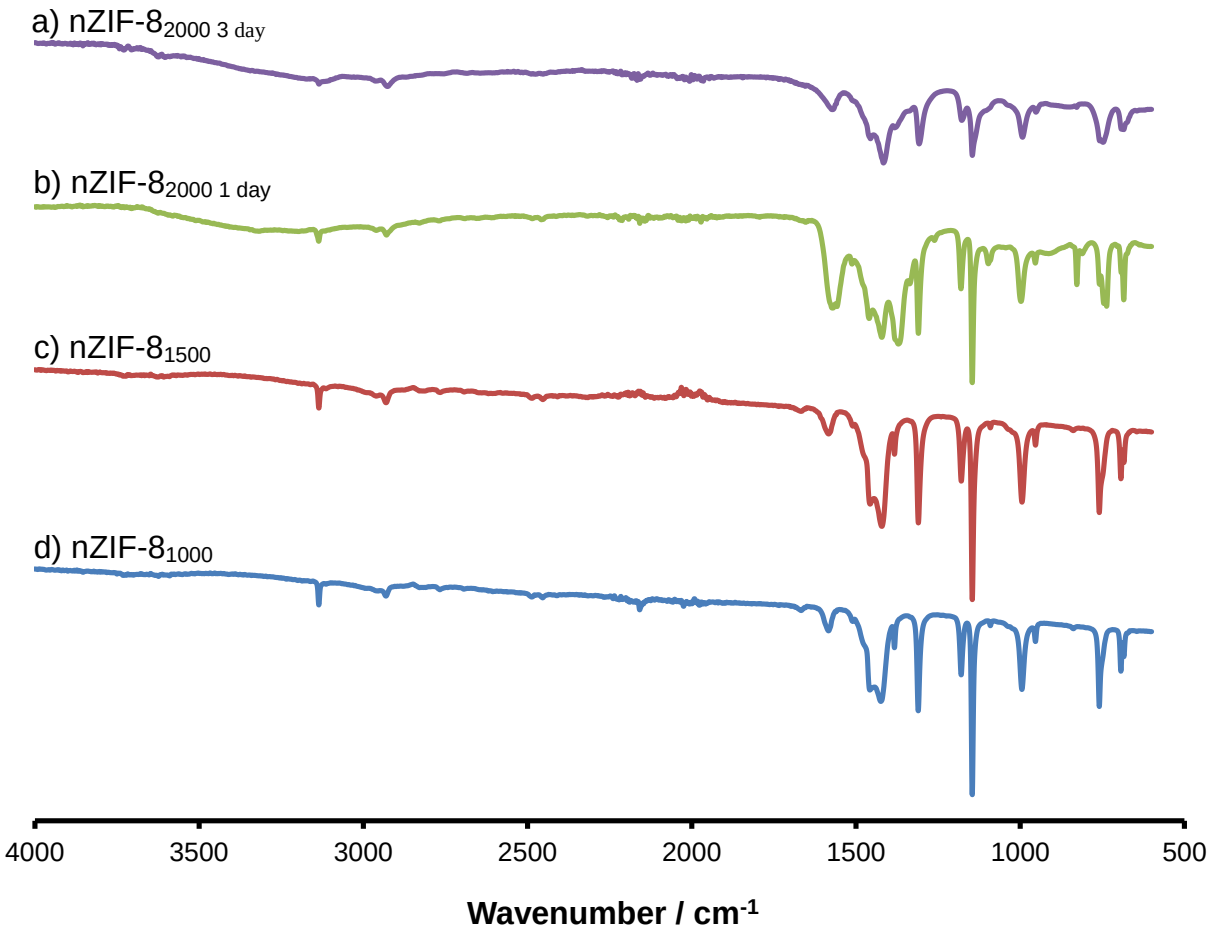

Figure 3.1 FTIR spectra of nZIF-8 synthesised with different methanol molar ratios (2000, 1500 and 1000 with respect to Zn): a) nZIF-8_{2000} after 3 day of dialysis, b) nZIF-8_{2000} after 1 day of dialysis, c) nZIF-8_{1500} and d) nZIF-8_{1000}.

Table 3.1 Summary of nZIF-8 synthesised from $Zn(NO_3)_2.4H_2O$ (5 mmol) and 2-methylimidazole (40 mmol) at 60 ℃, at different methanol solvent ratios. Syntheses were performed in triplicate to obtain average values. Particle sizes were measured statically from TEM images (by measuring 100 random particles) and calculated from selected PXRD peaks.

Name:		**nZIF-8_{1000}**	**nZIF-8_{1500}**	**nZIF-8_{2000}**
Methanol ratio		**1000**	**1500**	**2000**
Zn:MeIm ratio		1:8	1:8	1:8
Yield/ %		47	45	35
TEM Particle Size/ nm	**Average/ nm**	31	23	14[#]
	Std dev.	4.16	3.30	2.77
	Minimum	21	15	9
	Maximum	45	34	24
PXRD Particle Size/ nm	**Average/ nm**	28.95	21.58	15.12[*]
	Std dev.	0.75	0.81	4.03

[#]without dialysis (crude sample)

[*]after 3 days of dialysis

The transmission electron microscopy (TEM) images in (**Figure 3.2, p 61**) were taken at 64000x magnification and provide a direct method for determining particle size, shape and certain impurities. The nanoparticles have a spherical shape. The particle sizes are summarised in **Table 3.1** (**p 60**) and shows a slight a slight decrease in size from 31 to 23 nm (average of triplicate experiments) as the solvent ratio increases from nZIF-8_{1000} to nZIF-8_{1500}. TEM images of a crude, as-synthesised nZIF-8_{2000} suspension revealed (**Figure 3.2.c**) the particles to be 14.39 nm with no distinct particle shape. The grainy observation is possibly caused by unreacted MeIm or the limitations of the TEM to observe particles < 20 nm. When the dialysis time was reduced to 1 day the TEM images (**Figure 3.2.d, p 61**) revealed a minute increase in particle size to 22 nm, relatively the same as nZIF-8_{1500} which is easily obtained by centrifugation. A shorter dialysis time also prevented particle agglomeration.

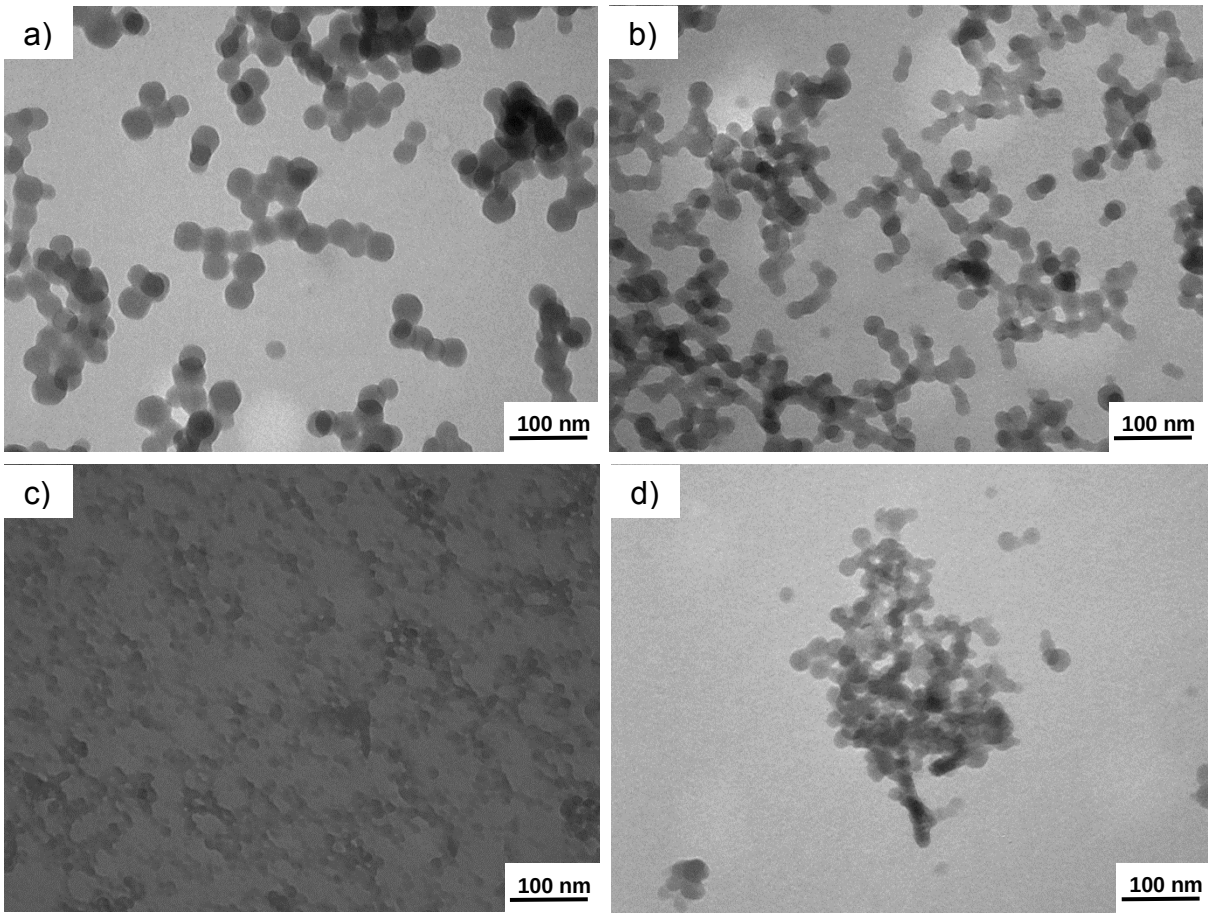

Figure 3.2 TEM images of nZIF-8 synthesised with different methanol ratios (1000, 1500 and 2000 with respect to Zn: a) nZIF-8_{1000} b) nZIF-8_{1500} c) nZIF-8_{2000} before dialysis and d) nZIF-8_{2000} after 1 day of dialysis.

It is possible that higher solvent ratio (lower reagent concentrations) causes the formed particle concentration to be lower thus preventing particle aggregation and inhibiting crystal growth, resulting in smaller particles. A lower concentration of the reagents, zinc nitrate and 2-methylimidazole, causes the nucleation and crystal growth rate to decrease. Within a one-hour reaction time it is still optimal to obtain a reasonable ~45 % yield for nZIF-8_{1000} and nZIF-8_{1500}, however when the methanol ratio reaches 2000 a much lower yield of 35 % was obtained for nZIF-8_{2000}. A diluted solution thus slows down the formation of nZIF-8.

The purity and structural integrity of nZIF-8 was characterised with powder X-ray diffraction (PXRD) (**Figure 3.3, p 62**). For nZIF-8_{1000} (a) and nZIF-8_{1500} (b), the main diffraction peaks are found at 2θ 7.45, 10.46, 12.82, 14.80, 16.54 and 18.13 °, identical to the PXRD patterns obtained in literature and simulation (**Appendix F.2**) with a CCDC code of FAWCEN, representing the SOD topology of nZIF-8.[1] The patterns of nZIF-8_{2000} (**Figure 3.3.c and d, p 62)** contain the peaks of nZIF-8. After 1 day of dialysis, additional peaks at 10.94 (i) and 18.9 (ii) ° 2Θ show that

impurities will still present in the sample. These peaks gradually disappeared after 3 days of dialysis. A similar trend was observed with FTIR spectroscopy where the C-C and C-N stretching frequencies diminished after performing dialysis for 3 days, a confirmation of the unreacted reagents initially present in the nZIF-8 products after synthesis.

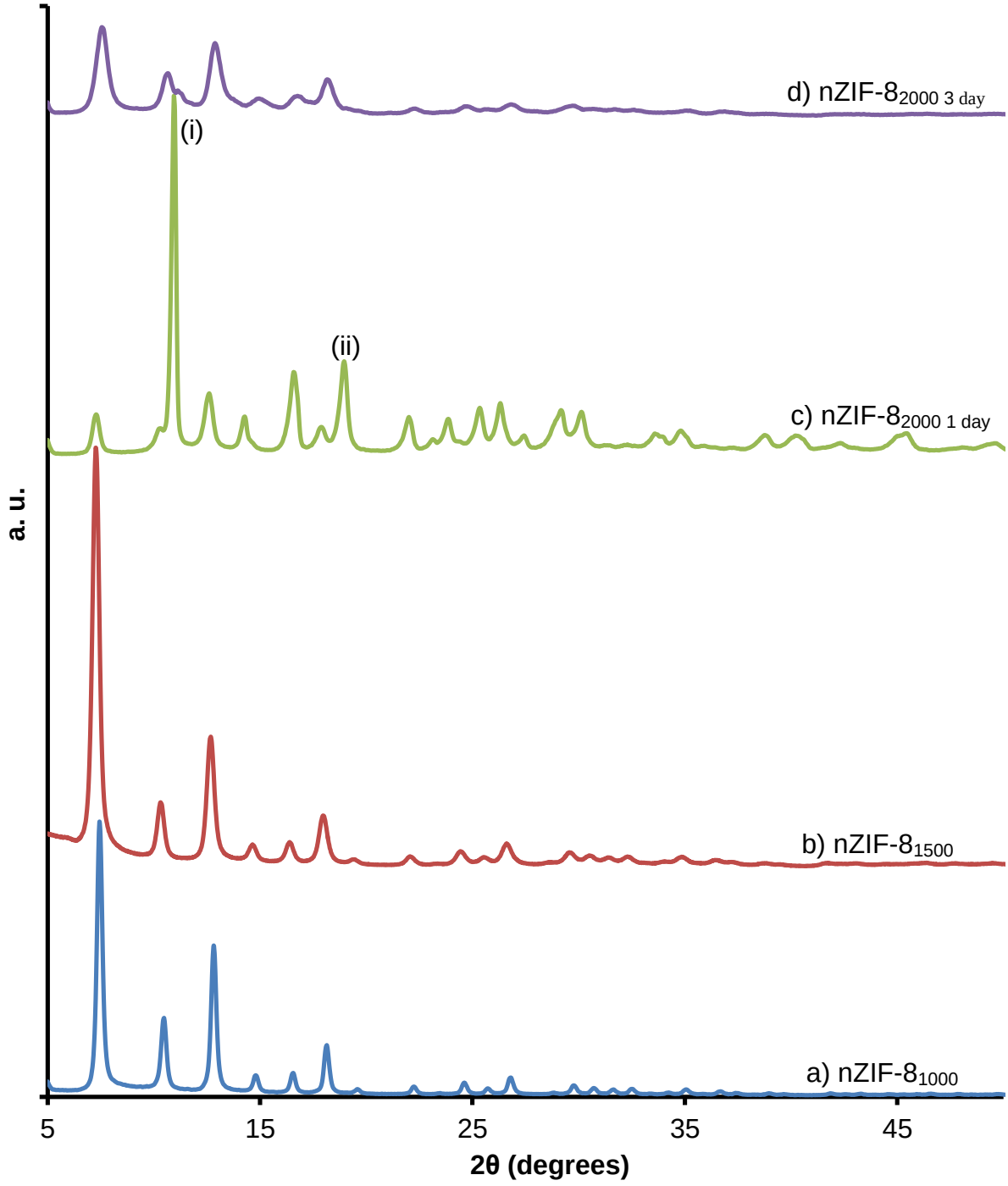

Figure 3.3 PXRD patterns of nZIF-8 synthesised with different methanol ratio (1000, 1500 and 2000 with respect to Zn): a) nZIF-8_{1000}, b) nZIF-8_{1500}, c) nZIF-8_{2000} after 1 day of dialysis and d) nZIF-8_{2000} after 3 day dialysis.

The intensity of the PXRD patterns for nZIF-8_{1500} is due to its high crystallinity, where the signal for nZIF-8_{2000} is five times weaker due to the formation of amorphous material. The Scherrer equation (**Chapter 2.3.3**) was used to determine the minimum particle size from the peak broadening of selected PXRD peaks. The particle sizes for nZIF-8_{1000} and nZIF-8_{1500} were calculated to be ~29 nm ~22 nm respectively, similar to the values obtained by TEM (**Table 3.1, p 60**). For nZIF-8_{2000} (1 day dialysis) the peak at 7.28 ° gave a particle size of 21 nm, while the 3 days dialysis resulted in nZIF-8 particles of ~15 nm in diameter.

The nZIF-8 batches synthesised at different methanol ratios were activated at 150 ℃ for 16 hours prior to porosity analyse. The Type-1 isotherms (shown in **Figure 3.4, p 64**) are proof that the materials are microporous. The amount of nitrogen adsorbed is at 469 and 512 $cm^3\ g^{-1}$ for the nZIF-8_{1000} (a) and nZIF-8_{1500} (b) products respectively. The nanoparticles obtained from the lowest concentration, nZIF-8_{2000}, showed decrease nitrogen adsorption. Dialysis for 1 day (c) and 3 days (d), resulted in nitrogen adsorption of 122 and 233 $cm^3\ g^{-1}$ respectively. nZIF-8_{2000} after 1 day of dialysis still contained a large amount of nonporous impurities as confirmed by PXRD analysis. The PXRD of nZIF-$8_{2000\ 3day}$ showed a significant decrease in crystallinity, observed by its weaker peak intensities, compared to nZIF-8_{1500}, giving rise to the ~50 % decrease in porosity. The dialysis process in water thus causes the nZIF-8 nanoparticles to become more amorphous.

The BET surface area of nZIF-8_{1500} at 1606 $m^2\ g^{-1}$ is smaller than that of nZIF-8_{1000} 1656 $m^2\ g^{-1}$ (**Table 3.2, p 64**). The t-plot analysis, using the Harkins and Jura thickness curve, was used to determine the t-plot external surface area, which increased from 315 $m^2\ g^{-1}$ (nZIF-8_{1000}) to 321 (nZIF-8_{1500}) $m^2\ g^{-1}$, corresponding to the smaller particle size as determined by TEM measurements. The dialysed samples had low BET surface areas. After 1 day of dialysis, the BET surface area of nZIF-8_{2000} was 339 $m^2\ g^{-1}$ and its micropore volume 0.085 $cm^3\ g^{-1}$. The low micropore volume is a clear indication of nonporous material within the bulk of the sample. After a 3 day dialysis, the micropore volume of nZIF-8_{2000} increased to 0.325 $cm^3\ g^{-1}$, and the BET surface area increased from 339 to 940 $m^2\ g^{-1}$. As observed by TEM, with longer dialysis the nanoparticles agglomerate to form larger particles, causing the t-plot external surface area to decrease by ~50 % from 126 to 66 $m^2\ g^{-1}$.

The activated nZIF-8_{1500} product will be used as starting material for all the Solvent Assisted Ligand Exchange (SALE) and Post Synthetic Modification (PSM) reactions in thus study.

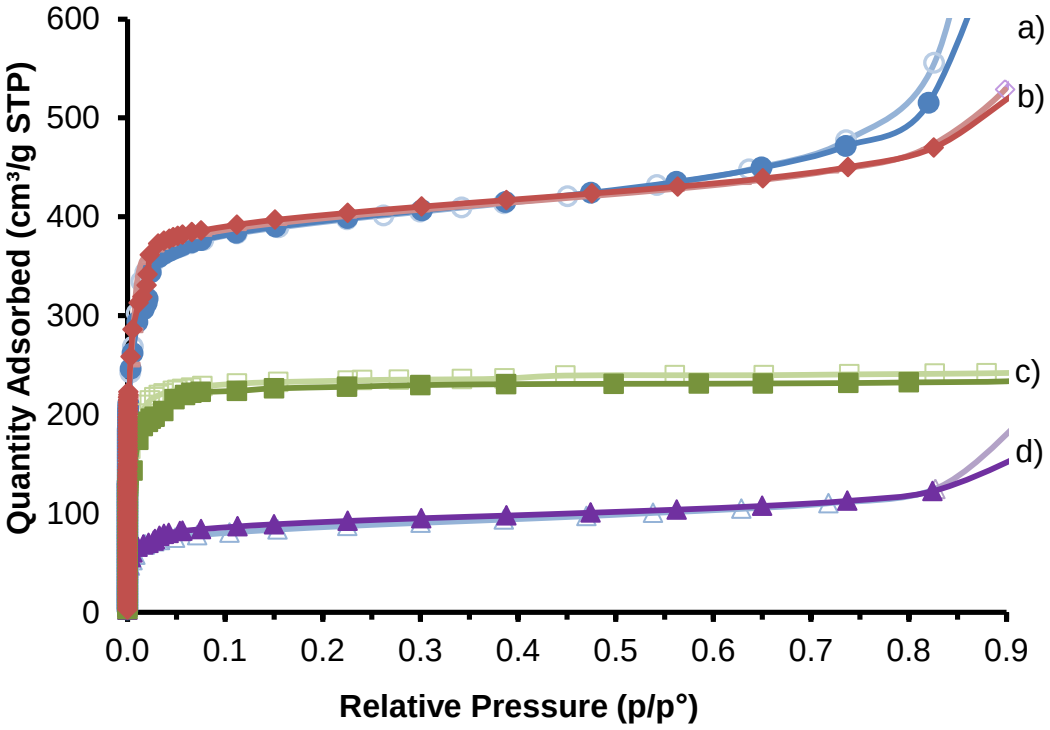

Figure 3.4 N_2 isotherms of nZIF-8 at 77 K, synthesised with different methanol ratio (1000, 1500 and 2000 with respect to Zn): a) nZIF-8_{1000}, b) nZIF-8_{1500}, c) nZIF-8_{2000} after 3 day of dialysis and d) nZIF-8_{2000} after 1 day dialysis. Adsorption marked as solids and desorption as hollow symbols.

Table 3.2 N_2 porosity analyses at 77 K for nZIF-8 synthesised at various solvent ratios (1000, 1500 and 2000 with respect to Zn). Quantities adsorbed were measured at 0.8 p/p°.

Compound	Quantity Adsorbed/ $cm^3\ g^{-1}$	BET Surface Area/ $m^2\ g^{-1}$	t-plot External Surface Area/ $m^2\ g^{-1}$	Micropore volume/ $cm^3\ g^{-1}$
nZIF-8_{1000}	469	1656	315	0.486
nZIF-8_{1500}	515	1605	321	0.471
nZIF-$8_{2000\ 1day}$	122	339	126	0.085
nZIF-$8_{2000\ 3day}$	233	940	66	0.325

The TGA thermograms in (**Figure 3.5, p 65**) show that both nZIF-8_{1000} (a) and nZIF-8_{1500} (b) are stable up to 450 °C, before the initial mass loss of ~25 % followed by a gradual continuous mass loss after 600 °C as nZIF-8 structure collapses. The product (nZIF-8_{2000}) of the 1 day dialysis gave a 2-step thermogram (c) with the first mass loss of 24 % after 333 °C and a second loss of

25 % after 578 °C. The lower thermal stability is due to the impurities that remain after 1 day of dialysis. Further dialysis for 3 days also gave a 2-step thermogram, with the first step after 119 °C, a loss of 9.2 % of water and decomposed impurities formed during the extended dialysis process. The second step after 417 °C is the decomposition of nZIF-8.

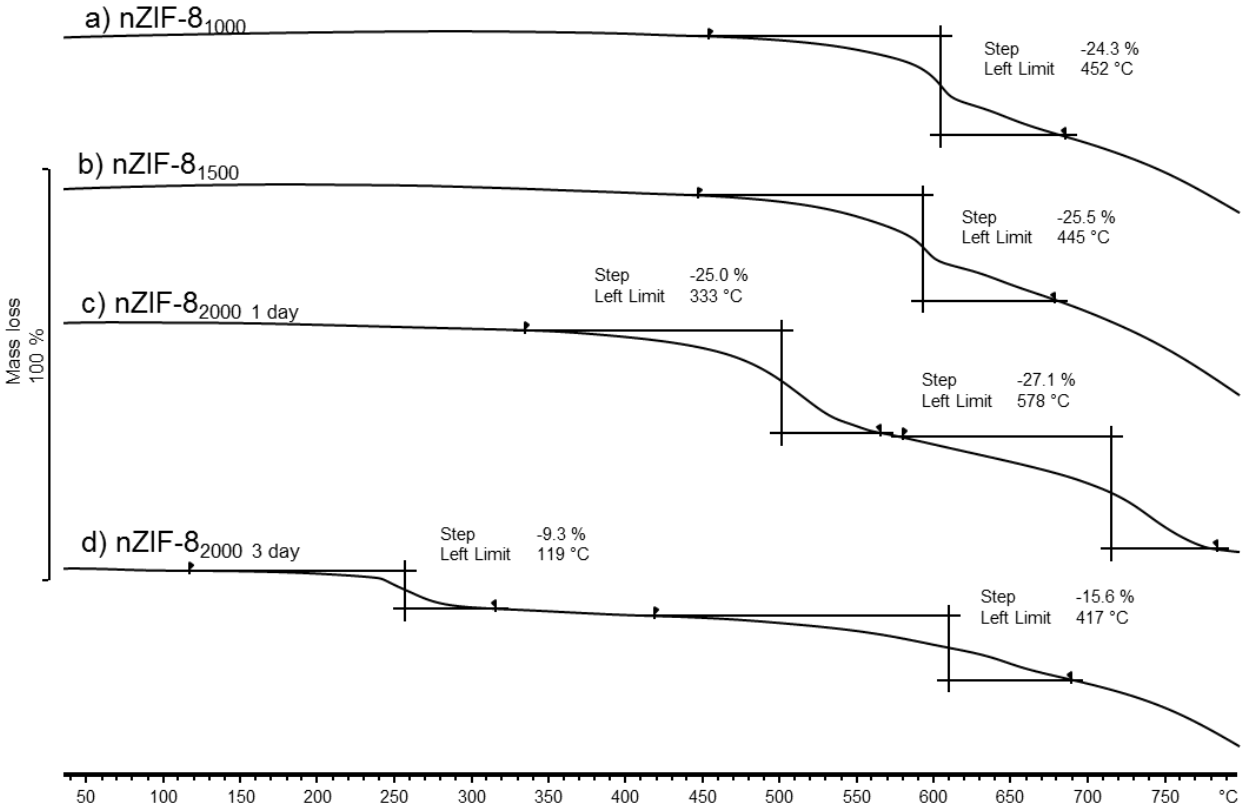

Figure 3.5 TGA thermograms in N_2 of a) nZIF-8_{1000}, b) nZIF-8_{1500}, c) nZIF-8_{2000} after 1 day of dialysis and d) nZIF-8_{2000} after 3 day dialysis.

3.2.2 Synthesis of nZIF-8 at different Triethylamine concentration

The synthesis of ZIF-8 nanoparticles in large quantities is still a challenge (see **Chapter 2**). Although micro-sized ZIF-8, known as Basolite Z1200, is commercially available, nanoparticles of ZIF-8 are not, due to the difficulty of controlling particle size during synthesis. In this section, the yield of nZIF-8 by adding triethylamine as a deprotonating agent and modulating ligand will be investigated. The reaction conditions will be similar to that of nZIF-8_{1500} (**Chapter 3.2.1**) at 60 °C. nZIF-8 was synthesised by the addition of 5 different molar ratios of triethylamine (TEA) according to (**Scheme 3.2, p 66**).

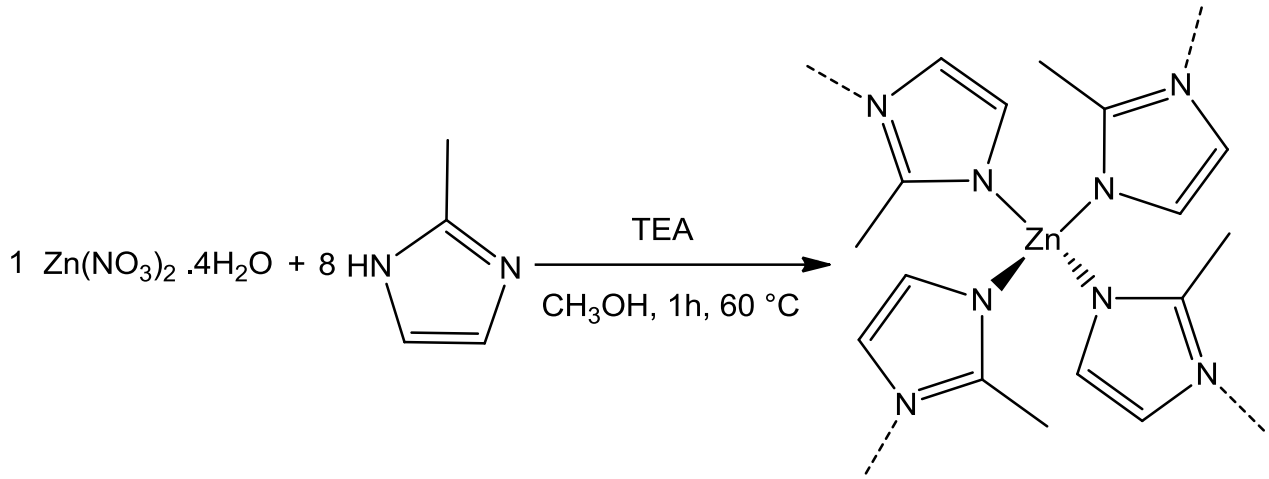

Scheme 3.2 General syntheses of ZIF-8 nanoparticles by rapid isothermal reaction between zinc nitrate and 2-methylimidazole in methanol with the addition of triethylamine at 5 different ratios (1, 2, 3, 4 and 8).

In a typical synthesis $Zn(NO_3)_2.4H_2O$: 2-methylimidazole: triethylamine (TEA) (1:8:8) was mixed together in 300 cm^3 methanol at 60 ℃ for 1 hour. The nanoparticles of the product, denoted as nZIF-8_{T8} (T = triethylamine at molar ratio of 8) were isolated by centrifugation, dried in air and activated at 100 ℃ under vacuum. Identical reactions were performed with 4 different molar ratios of triethlyamine: 4 (nZIF-8_{T4}), 3(nZIF-8_{T3}), 2 (nZIF-8_{T2}) and 1 (nZIF-8_{T1}). The reaction mixtures turned milky instantaneously, except for nZIF-8_{T1} and nZIF-8_{T2} where the milky suspension was less intense.

^{1}H NMR and FTIR spectroscopy were employed to determine whether the TEA remains within the pores of the nZIF-8. For ^{1}H NMR nZIF-8_T was digested in D_2O/D_2SO_4 (9:1). The ^{1}H NMR spectrum of the nZIF-8_{T8} product (**Figure 3.6.a, p 67**) also represents that of the nZIF-8_{T1-4} products (**Appendix B.1**). The singlet at 1.75 ppm represents the CH_3 protons and the peak at 6.42 ppm the CH=CH protons of the 2-methylimidazolate linker. The ^{1}H NMR shows that the TEA was removed from the pores during centrifugation without the need for further activation, except for nZIF-8_{T8} where ~2 % TEA remained in the sample. The FTIR spectrum of nZIF-8_{T8} (**Figure 3.6.b, p 67)** is identical to that of nZIF-8_{T1-4} (**Appendix A.1**) and the FTIR spectrum of to nZIF-8_{1500} (**Chapter 3.2.1**), showing no broad peaks between 2500 to 3000 cm^{-1} representing free N-H of unreacted 2-metylimidazole. The finger print region below 1500 cm^{-1} is identical for all nZIF-8_T samples.

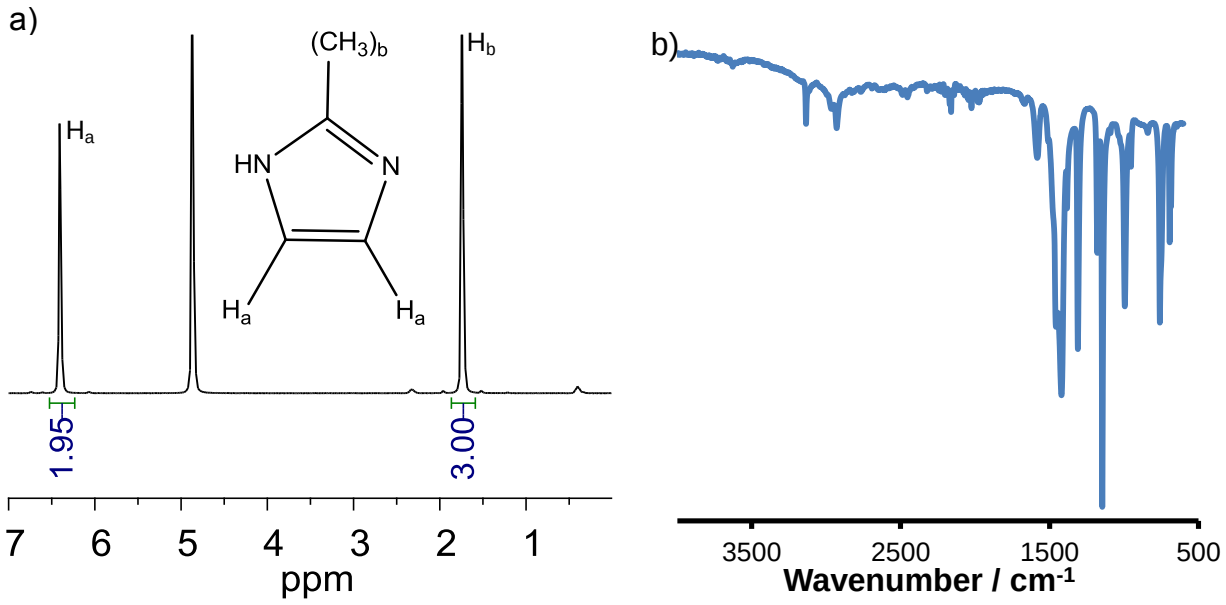

Figure 3.6 Spectra of nZIF-8_{T8} a) ^{1}H NMR in D_2O/D_2SO_4 (9:1) and b) FTIR.

Table 3.3 Summary of nZIF-8 synthesised from $Zn(NO_3)_2.4H_2O$ (5 mmol) and 2-methylimidazole (40 mmol) at 60 °C with the addition of triethylamine (TEA) at different molar ratios. Particle sizes were measured statically from TEM images (by measuring 100 random particles) and calculated from selected PXRD peaks.

Name:		**nZIF-8_{T1}**	**nZIF-8_{T2}**	**nZIF-8_{T3}**	**nZIF-8_{T4}**	**nZIF-8_{T8}**
Triethylamine molar ratio		**1**	**2**	**3**	**4**	**8**
Zn:MeIm molar ratio		1:8	1:8	1:8	1:8	1:8
Yield/ %		40	41	85	83	84
TEM Particle Size/ nm	**Average/ nm**	19	23	22	16	16
	Std dev.	2.14	4.78	4.01	2.67	2.87
	Minimum	16	12	13	12	10
	Maximum	25	34	31	23	23
PXRD Particle Size/ nm	**Average/ nm**	16.10	12.90	16.08	11.82	13.47
	Std dev.	0.38	1.58	0.59	1.11	0.40

The reagent concentration, solvent, temperature and time was kept constant, while the effect of TEA concentration was investigated. After activation, the yields of the nanoparticles were determined and summarized (**Table 3.3, p 67**) and graphically represented (**Figure 3.7, p 68**). The yield of nZIF-8_{T1} and nZIF-8_{T2} is similar to nZIF-8_{1500} (without the addition of TEA) between 40 and 50 %. However, as the TEA is increased to 3 (nZIF-$8T_3$) the doubles to 85 %. A further increase in TEA molar concentration had no further effect on the yield, showing that the lowest TEA molar ratio concentration of 3 is required to increase the yield two fold.

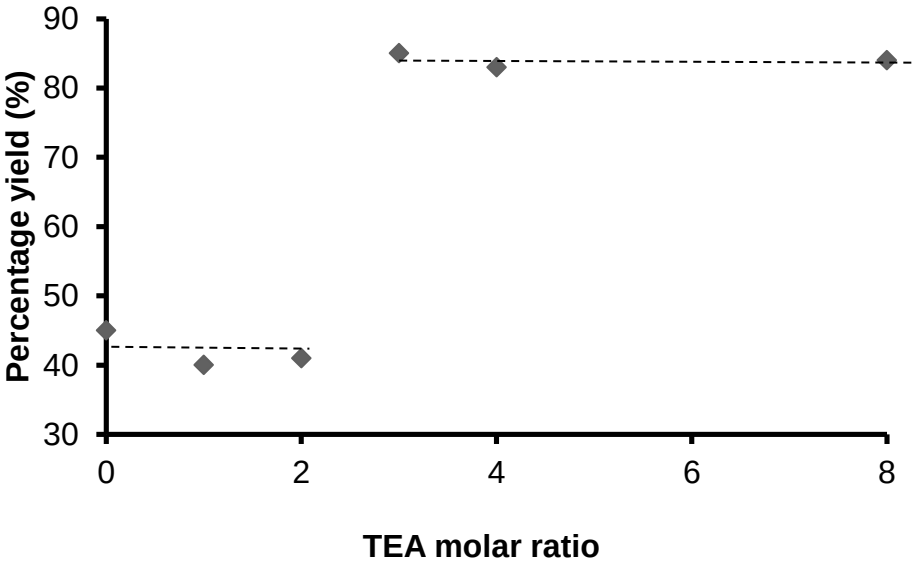

Figure 3.7 Graph of Percentage yield *vs.* TEA molar ratio during the synthesis of nZIF-8 in a 1:8:1500 (Zn:MeIm:MeOH) ratio at 60 ℃ for 1 hour.

Transmission electron microscopy (TEM) of the nZIF-8_T samples provides a direct and physical approach in observing the exact particle size, which was determined statistically by randomly measuring 100 particles as summarised in (**Table 3.3, p 67**). nZIF-8_{T1} and nZIF-8_{T2} have particle sized of 19 and 23 nm respectively without any change in particle shape as compared to the original nZIF-8. As the TEA molar ratio was increased, the particle size decreased (**Figure 3.8,f, p 69**). The addition of TEA did not affect the spherical shape of the particle, and the particle size is maintained within the nanometre region (<100 nm). With the addition of TEA the particles can be synthesised much smaller with a twofold increase in yields.

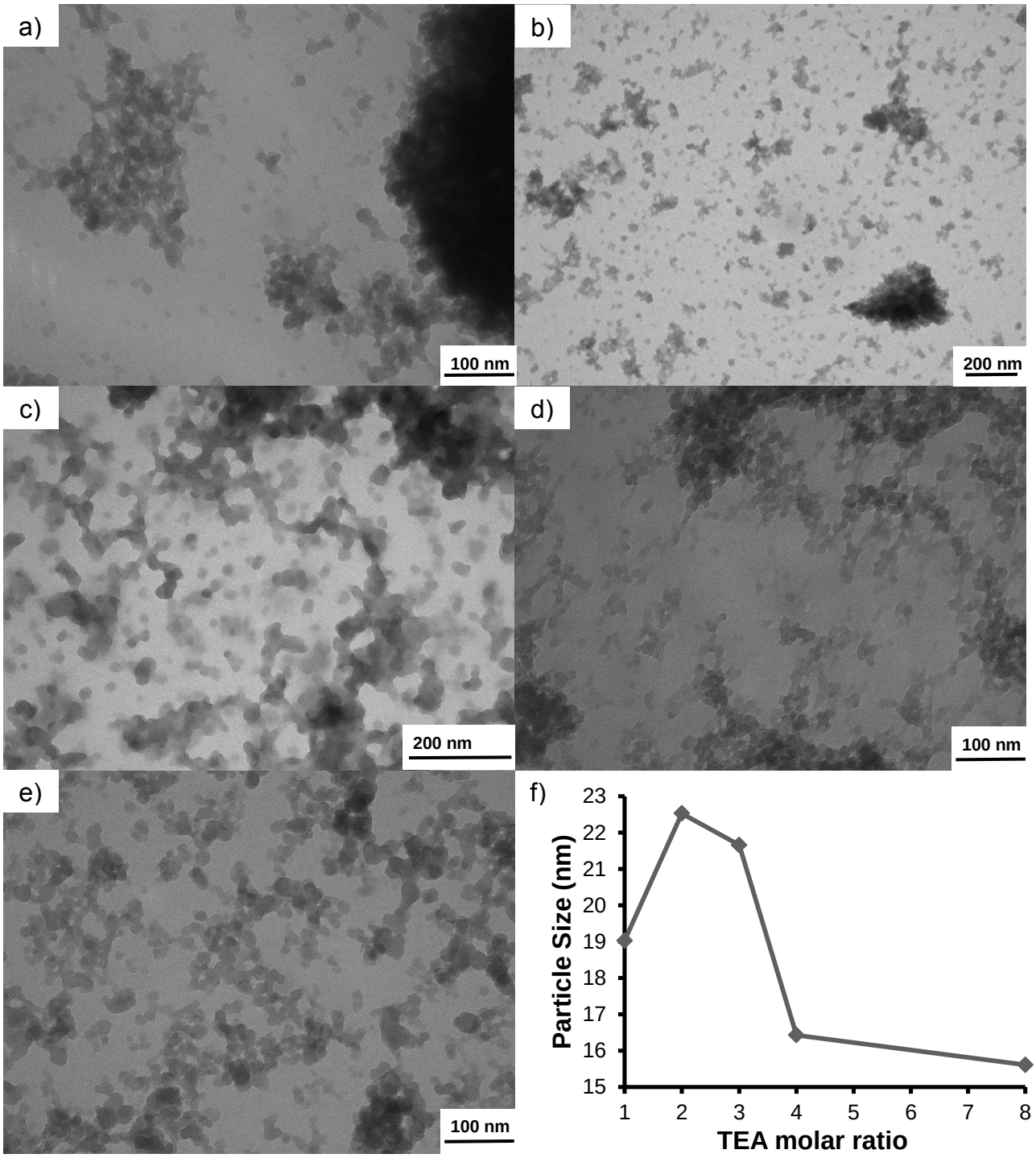

Figure 3.8 TEM images of nZIF-8_T synthesised with TEA at different molar ratios: a) 1, b) 2, c) 3, d) 4, e) 8 and f) graph of particle size *vs.* TEA molar ratio.

The PXRD patterns of nZIF-8 synthesised at different TEA molar ratios are identical to nZIF-8 synthesised without additives (**Figure 3.9**, **p 70**). The peaks are well defined for all the different TEA ratios, an indication of the products' high crystallinity and their SOD topology of ZIF-8 without any structural change. This confirms that TEA has no influence on structural topology during the synthesis of nZIF-8. The 6 main PXRD peaks of nZIF-8 at 2θ = 7.4, 10.5, 12.9, 14.9, 16.7 and 18.2 ° are present for nZIF-8_{T1} to nZIF-8_{T8}. The average minimum particle sizes (**Table 3.3, p 67**) were determined with the Scherrer equation from the first 5 peaks. nZIF-8_{T4} have the smallest particles (11.8 nm) and nZIF-8_{T1} having the largest particles (16.1 nm), correlating well with the minimum particle sizes obtained by TEM.

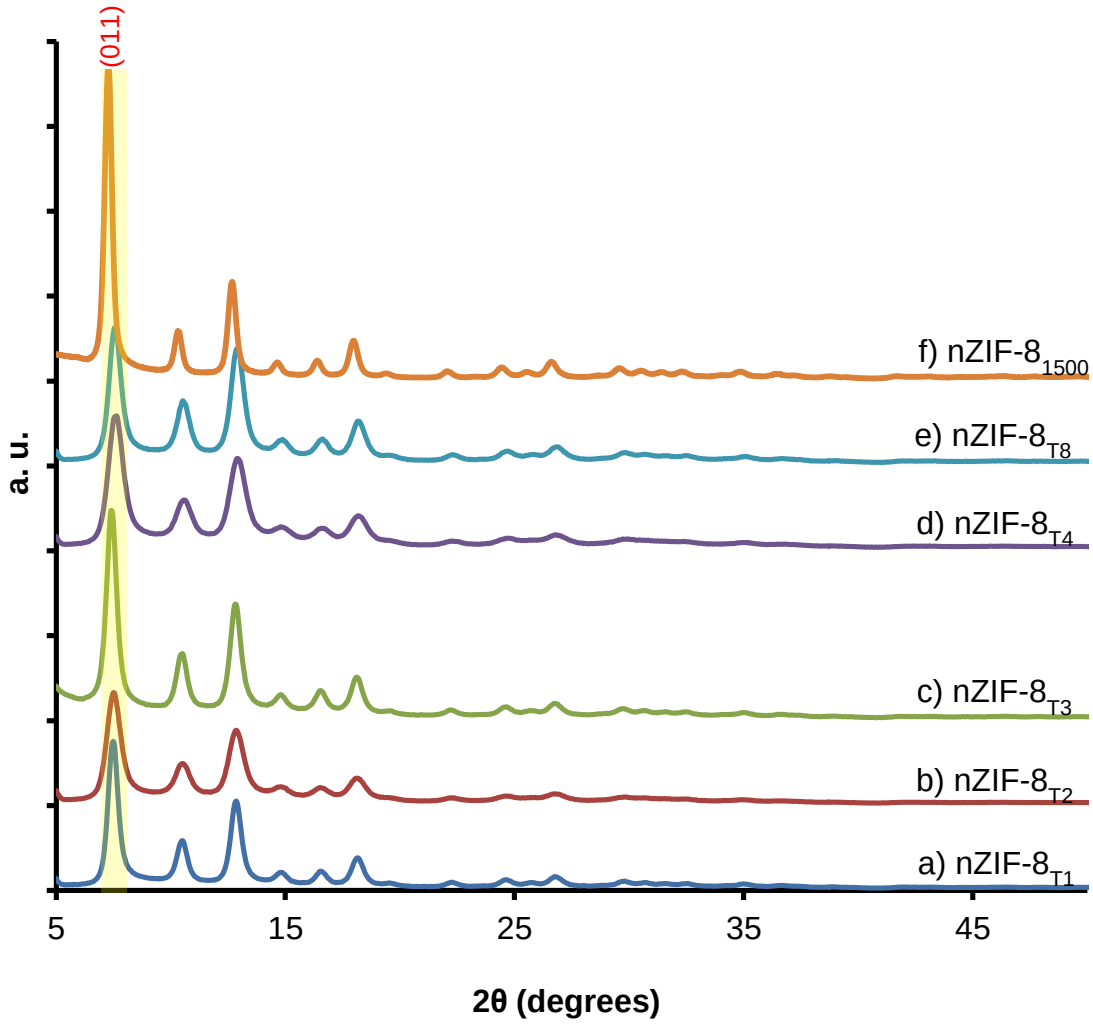

Figure 3.9 PXRD patterns of nZIF-8 synthesised with TEA at different molar ratios: a) 1, b) 2, c) 3, d) 4, and e) 8.

The TEA acts as a basic deprotonating agent on the methyl imidazole ligands and as previously reported in literature, the excess 2-methylimidazole linkers act as free ligands thus a higher concentration of deprotonating agent is required to facilitate nucleation to occur.[3] A basic solution, as with the addition of TEA, increases the nucleation rate and allow the formation of

smaller crystals.[4] This was observed with the TEA molar ratios was 3, as confirmed by the TEM images. The excess TEA can also act as a modulating ligand to control particle size as observed from TEM images for nZIF-8_{T8} with particles reaching 16 nm. An optimal pH of approximately 9.0 is required to improve yield of ZIF-8.[5,6] Therefore, as the TEA molar concentration rose above 3, the pH reached the optimum level to double the yield, as the pH for nZIF-8_{T3}, nZIF-8_{T4} and nZIF-8_{T8} were 9.80, 9.85 and 9.95 respectively. The pH for nZIF-8_{T1} and nZIF-8_{T2} were 6.84 and 7.41 respectively, without any effect on the yield. At these lower pH levels, a rise in particle size was observed due to fast nucleation and particle growth within the 1-hour synthesis time. Synthesis in 1500 methanol molar ratio at 60 ℃, nanoparticles of ~20 nm were obtained within 1 hour and with improved yields due to the added TEA (> molar ratio of 3).

For porosity analysis of the nZIF-8 (synthesised at various TEA molar ratios) it was activated at 150 ℃ for 16 hours. The isotherms of nZIF-8_{T1} shown in (**Figure 3.10, p 71**) and nZIF-$8_{T2\text{-}8}$ in (**Appendix G.1**), are all typical Type-1 isotherms. The amount of nitrogen adsorbed (between at 447 and 525 $cm^3\ g^{-1}$) remains comparable (**Chapter 3.2.1**) to that of nZIF-8.

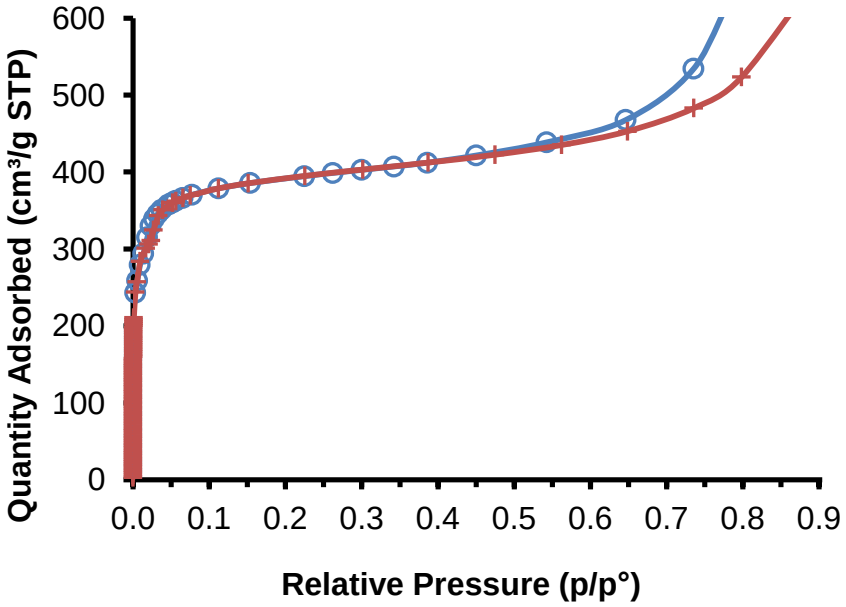

Figure 3.10 N_2 isotherms at 77 K of nZIF-8_{T1} synthesised with a TEA molar ratio of 1. Adsorption marked as crosses and desorption as circles.

The BET surface area, t-plot external surface area and micropore volume for each TEA molar ratio are summarized in (**Table 3.4, p 72)**, with the BET surface area decreasing from 1511 $m^2\ g^{-1}$ to 1365 $m^2\ g^{-1}$ as the TEA ratio increases from 1 to 4 respectively. Similarly, the micropore volume decreased from 0.462 to 0.392 $cm^3\ g^{-1}$. With a molar ratio of 8 the BET surface area and micropore volume increased to 1457 $m^2\ g^{-1}$ and 0.420 $cm^3\ g^{-1}$ respectively. The

drop in porosity could be due to the formation of low crystalline nZIF-8 within the structure, which would also explain the decrease in micropore volume. The t-plot external surface area as determined from the Harkins and Jura thickness curve correlates to the particle size determined by TEM. As the particle size increased the external surface area decreased from 327 to 308 $m^2 g^{-1}$. After a TEA molar ratio of 3 the particle size decreases and the external surface area increases to a maximum of 383 $m^2 g^{-1}$ (TEA molar ratio of 8).

Table 3.4 N_2 porosity analyses of nZIF-8_T at 77 K at various TEA molar ratios (1, 2, 3, 4 and 8). Quantities adsorbed were measured at 0.8 p/p°.

Compound	Quantity Adsorbed/ $cm^3 g^{-1}$	BET Surface Area/ $m^2 g^{-1}$	t-plot External Surface Area/ $m^2 g^{-1}$	Micropore volume/ $cm^3 g^{-1}$
nZIF-8_{T1}	523	1511	327	0.462
nZIF-8_{T2}	503	1444	302	0.442
nZIF-8_{T3}	454	1320	308	0.403
nZIF-8_{T4}	447	1365	344	0.392
nZIF-8_{T8}	525	1457	383	0.420

The TGA thermograms of nZIF-8_T (synthesised with TEA additive at different ratio) obtained under a nitrogen atmosphere (**Figure 3.11, p 73**) show 2 steps with an initial mass loss of ~2-3 % at 250 ℃. This can be associated for the thermal degradation of TEA still present within the pores. All nZIF-8_T are stable up to 400 ℃, similar to nZIF-8 without additives. A steep mass loss of 15-20 % after 400 ℃ followed by a continuous mass loss after 600 ℃, is due to the slow thermal degradation of the organic linker in the nZIF-8 structure after 650 ℃.

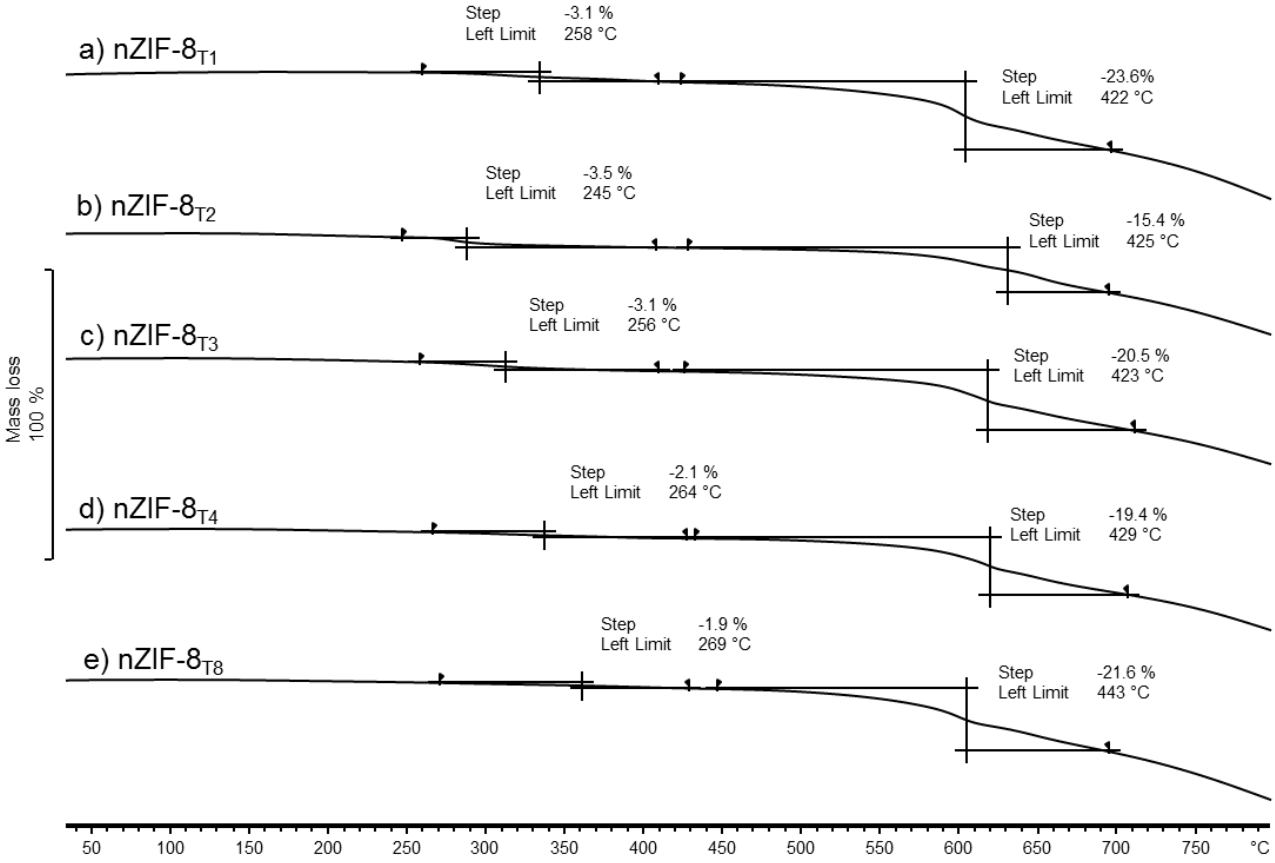

Figure 3.11 TGA thermogram in N_2 of nZIF-8 synthesised with TEA at different molar ratios: a) 1, b) 2, c) 3, d) 4, and e) 8.

3.2.3 Synthesis of Imidazolate Ligands via *S*-Alkylation

A series of benzimidazole-thioesters was synthesised during the Pre Synthetic Modification (PSE) of imidazolate organic linkers *via S*-alkylation on 2-mercaptobenzimidazole (MbIm) (**Scheme 3.3, p 74**).[7] In a typical reaction, the substrate 2-mercaptobenzimidazole was reacted with a suitable bromo-ester in strong basic conditions. The product with the shortest alkyl chain (n = 1) methyl benzimidazole-2-ylthio acetate, was obtained from 2-mercaptobenzimidazole and methylbromoacetate reacting in a potassium hydroxide ethanol solution at 25 ℃. The crude product was purified by recrystallization from dichloromethane and *n*-hexane to give a 72 % yield as white crystals. Reactions where methylbromoacetate was replaced by ethylbromoacetate gave no product under various conditions.

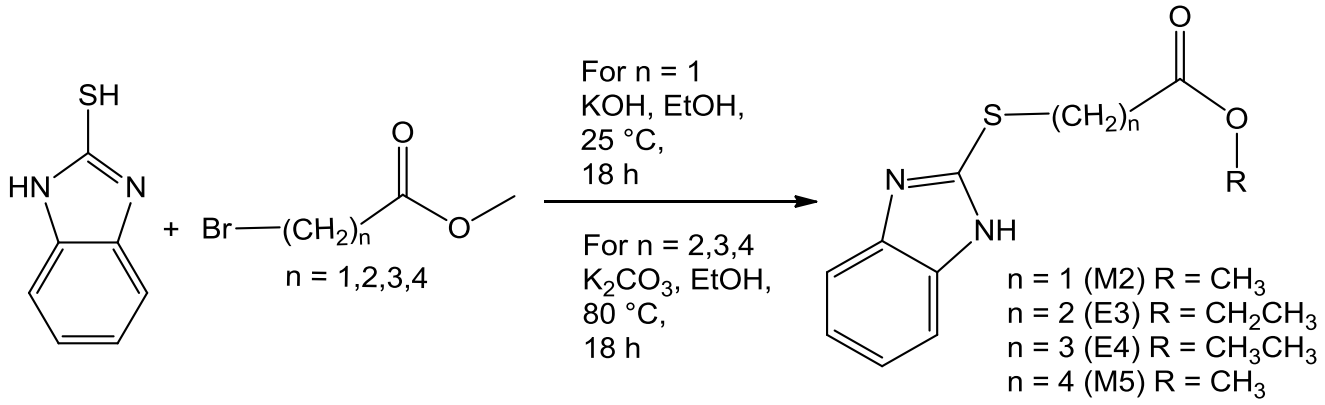

Scheme 3.3 Synthesis of methyl benzimidazole-2-ylthio acetate (n = 1), ethyl benzimidazole-2-ylthio propionate (n = 2), ethyl benzimidazole-2-ylthio butyrate (n = 3) and methyl benzimidazole-2-ylthio valerate (n = 4).

With the synthesis of benzimidazole-thioesters derivatives having longer chains (where n = 2, 3 and 4) (**Scheme 3.3, p 74**), the exact opposite was true. Synthesis in potassium hydroxide ethanol solution gave no product at all. A modified literature procedure with K_2CO_3 instead of KOH was used.[8] Ethyl-3-bromopropionate was used as a different substrate to give ethyl benzimidazole-2-ylthio propionate (n = 2) a 73 % yield as white crystals. The same method with ethyl-4-bromobutyrate (n = 3) and methyl-5-bromovalerate (n = 4) gave ethyl benzimidazole-2-ylthio butyrate (84 % yield) and methyl benzimidazole-2-ylthio valerate (92 % yield) respectively, both as white crystals. During the synthesis of all three compounds in K_2CO_3 ethanol solutions a milky solution was observed which turned light brown when reaching 80 ℃. Ethanol was removed, the solution quenched with water and extracted with chloroform. The unreacted 2-mercaptobenzimidazole is insoluble in chloroform and was be filtered off. The crude product was recrystallized with dichloromethane and *n*-hexane. As the chain length increases (where n > 2), the alkoxy group of the ester did not influence the synthesis as it did for n ≤ 2. The yield of the products to improve as the chain length increases, when n = 2 a yield of 72 % increased to 92 % where n = 4. The melting point of the compounds decrease from 114 ℃ (n = 2) to 88 ℃ (n = 4) as the chain length increases.

The FTIR spectra of benzimidazole-thioesters derivatives (**a** to **d**) are compared in (**Figure 3.12, p 75**). The weak S-H stretching frequency at ~2500 cm^{-1} of 2-mercaptobenzimidazole (**e**) overlaps with the broad N-H peaks. The N-H stretching frequency is observed for all compounds at a broad peak between 2500 and 3200 cm^{-1} with the N-H peaks shifted to a lower frequency after *S*-alkylation. This is an indication that the alkylation occurred only on the sulphur atom.

The aromatic C-H stretching frequency is observed for all compounds at ~3040 cm^{-1}. The additional peak at ~740 cm^{-1} (i) corresponds to the C-S-C frequency. The peaks at 1618 cm^{-1} (ii) are attributed to the C=N stretching frequency for in all the compounds. Except for 2-mercaptobenzimidazole (**e**), there is a sharp peak for carbonyl stretching. For methyl benzimidazole-2-ylthio acetate (**a**) and methyl benzimidazole-2-ylthio valerate (**d**), the strong C=O stretching frequencies are at 1739 cm^{-1} and 1732 cm^{-1} respectively, While the C=O bond for the ethyl esters, ethyl benzimidazole-2-ylthio propionate (**b**) and ethyl benzimidazole-2-ylthio butyrate (**c**), resonate at 1717 and 1719 cm^{-1} respectively. Ethyl groups are more electron donating than methyl groups which cause the C=O stretching to shift ~20 cm^{-1} lower.

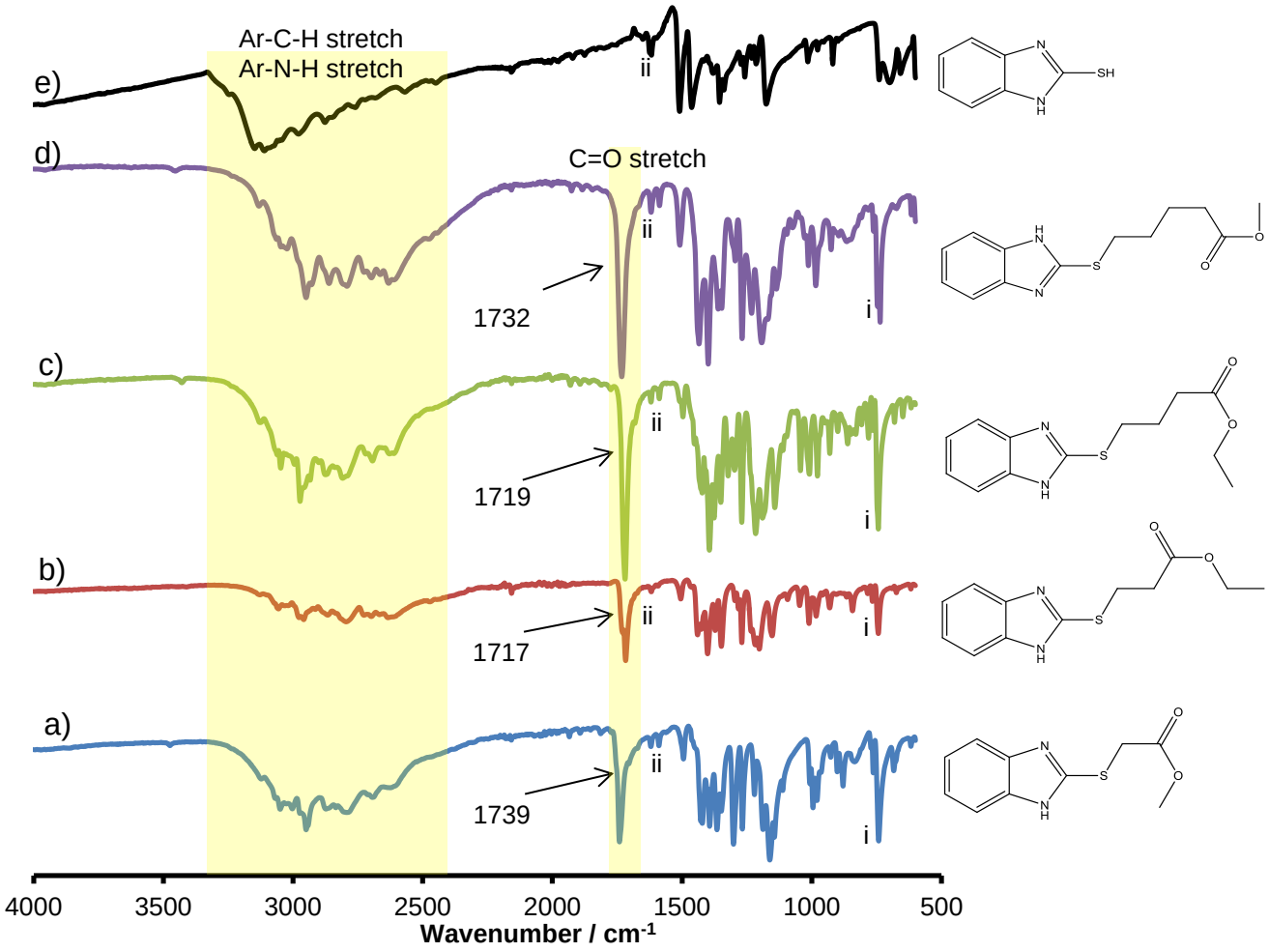

Figure 3.12 FTIR Spectra of a) methyl benzimidazole-2-ylthio acetate, b) ethyl benzimidazole-2-ylthio propionate, c) ethyl benzimidazole-2-ylthio butyrate, d) methyl benzimidazole-2-ylthio valerate and e) 2-mercaptobenzimidazole.

The ^{1}H NMR spectra of benzimidazole-thioesters are compared in (**Figure 3.13, p 77**). The N-H proton of all the derivatives resonates as a broad signal between 11 and 9 ppm. The peaks for the protons in the benzene ring resonate between 7.4 and 7.1 ppm.

RESULTS AND DISCUSSION

For methyl benzimidazole-2-ylthio acetate (**a**) and methyl benzimidazole-2-ylthio valerate (**d**), the methyl alkoxy protons resonate at 3.7 and 3.6 ppm respectively.

For ethyl benzimidazole-2-ylthio propionate (**b**) and ethyl benzimidazole-2-ylthio butyrate (**c**), the ethyl alkoxy protons of both compounds resonate at 4.1 ppm (multiplet) and 1.2 ppm (triplet) for CH_2 and CH_3 respectively.

The CH_2 alkyl protons of all derivatives adjacent to the carbonyl group resonate at 3.9 ppm (**a** marked 1), 3.4 ppm (**b** marked 2), 3.2 ppm (**c** marked 3) and 3.2 ppm (**d** marked 4).

The CH_2 alkyl protons (where $n \geq 2$) adjacent to the thio group resonates at 2.8 ppm (**b** marked 1), 2.5 ppm (**c** marked 1) and 2.3 pm (**d** marked 1). The electron withdrawing effect of the C=O bonds deshields the protons on the adjacent methylene group which cause the protons to resonate at a higher ppm as compared to sulphur which is electron donating.

For (**d**) and (**c**) the protons of the central CH_2 groups resonates at 2.1 ppm (**c** marked 2) and at 1.7 ppm (**d** marked 2 and 3) ppm.

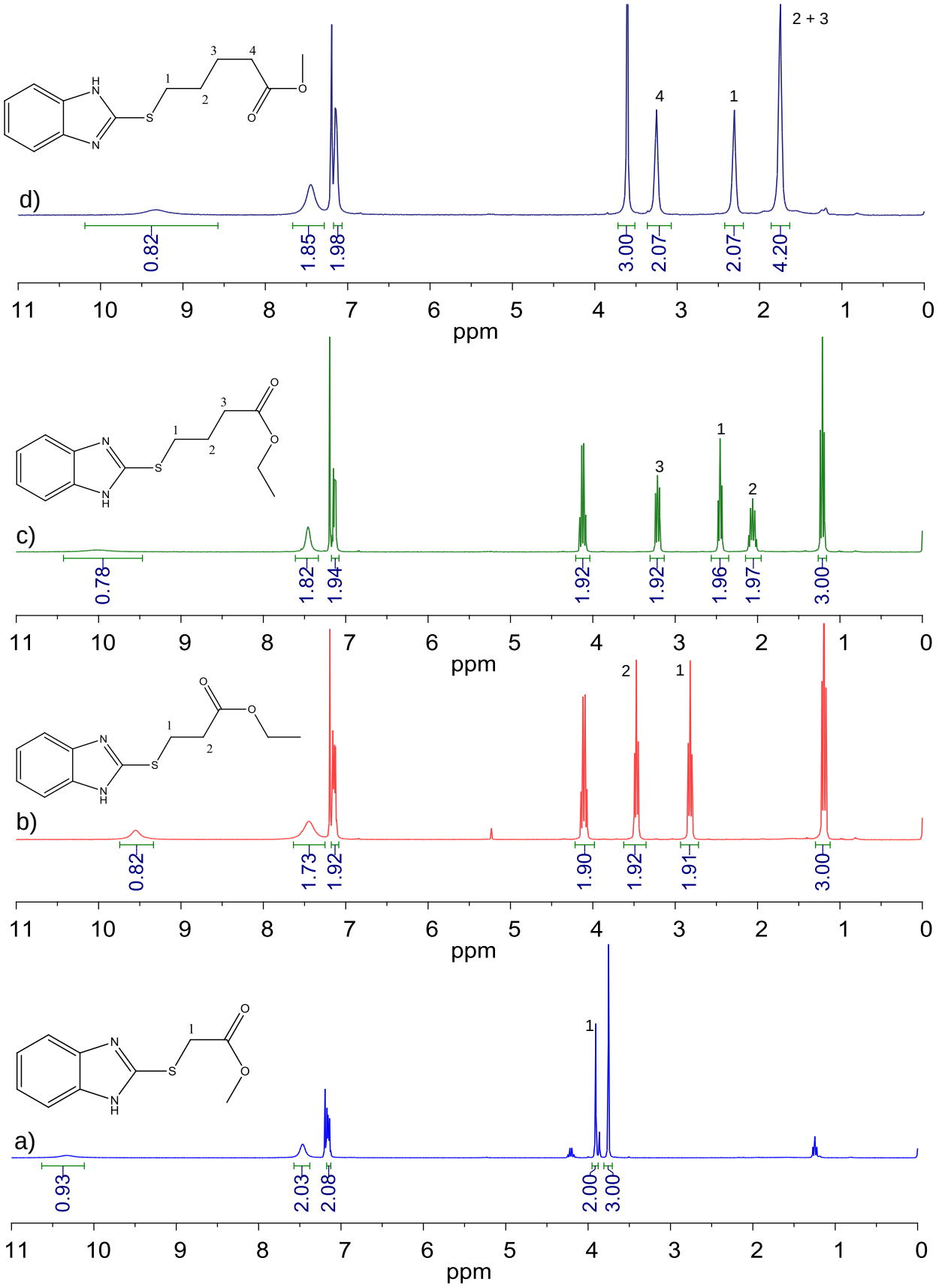

Figure 3.13 ^{1}H NMR Spectra of a) methyl benzimidazole-2-ylthio acetate, b) ethyl benzimidazole-2-ylthio propionate, c) ethyl benzimidazole-2-ylthio butyrate and d) methyl benzimidazole-2-ylthio valerate in $CDCl_3$.

3.2.4 Synthesis of Ferrocenecarboxylaldehyde and Ferrocenemethylamine

The Ferrocene derivatives (ferrocenecarboxylaldehyde and ferrocenemethylamine) that are not easily obtained commercially and are required for catalytic testing as well as post synthetic modification (PSM) after solvent assisted ligand exchange (SALE) in this study.

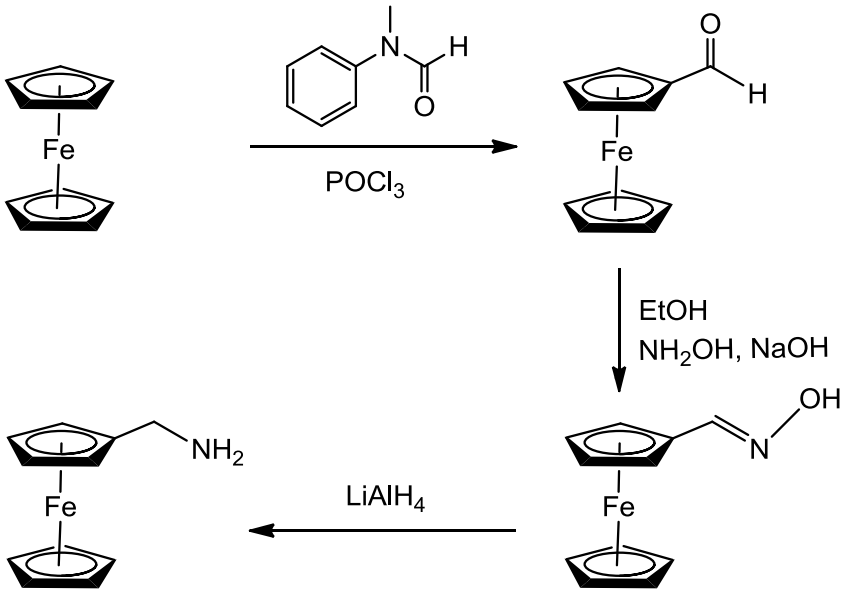

Scheme 3.4 Synthesis of ferrocenecarboxylaldehyde and ferrocenemethylamine.

Ferrocenecarboxylaldehyde was required as a precursor to ferrocenemethylamine (**Scheme 3.4, p 78**) and for Knoevenagel condensation with malononitrile in (**Section 3.5, p 153)**. Ferrocencecarboxaldehyde was synthesised *via* the Vilsmeier formylation reaction (**Scheme 3.4, p 78**) of ferrocene with *n*-methylformanilide and phosphorus oxychloride. The crude product was purified by column chromatography (hexane:ether) to obtain ferrocencecarboxaldehyde, 55 % in yield as red crystals. The method only yielded mono-substituted product as observed in ^{1}H NMR (**Figure 3.15.a, p 80**). To synthesise ferrocenemethylamine, ferrocenecarboxylaldehyde was reacted with hydroxylamine chlorohydrate and sodium hydroxide in an ethanol solution, to give an orange solid as ferrocenecarboxylaldehyde oxime as intermediate after 3 hours of reflux. The crude intermediate product showed no sign of ferrocenecarboxylaldehyde starting material as observed by ^{1}H NMR (**Figure 3.2.b, p 61**). The product was then reduced with $LiAlH_4$ in dry tetrahydrofuran after 16 hours of reflux under argon, the ferrocenemethylamine was obtained as a viscous orange oil.

The FTIR spectra of the snythesised derivatives are shown in (**Figure 3.14, p 79**). For ferrocenecarboxylaldehyde (**a**) a sharp C=O stretching frequency at 1656 cm^{-1} and a C-H

stretching frequency at 3086 cm^{-1} is observed. For ferrocenecarboxylaldehyde oxime (**b**), the C=O stretching frequency is now absent, with a broad O-H peak between 2500 and 3400 cm^{-1} and a C=N stretching frequency at 1627 cm^{-1} is observed. After reduction, ferrocenemethylamine (**c**) gives two peaks at 3360 and 3289 cm^{-1} for 1° N-H_2 stretching with the N-H bending frequency at 1581 cm^{-1}, the aliphatic C-H stretching frequency at 2842 cm^{-1} and the aromatic C-H stretching frequency at 2913 -3082 cm^{-1}.

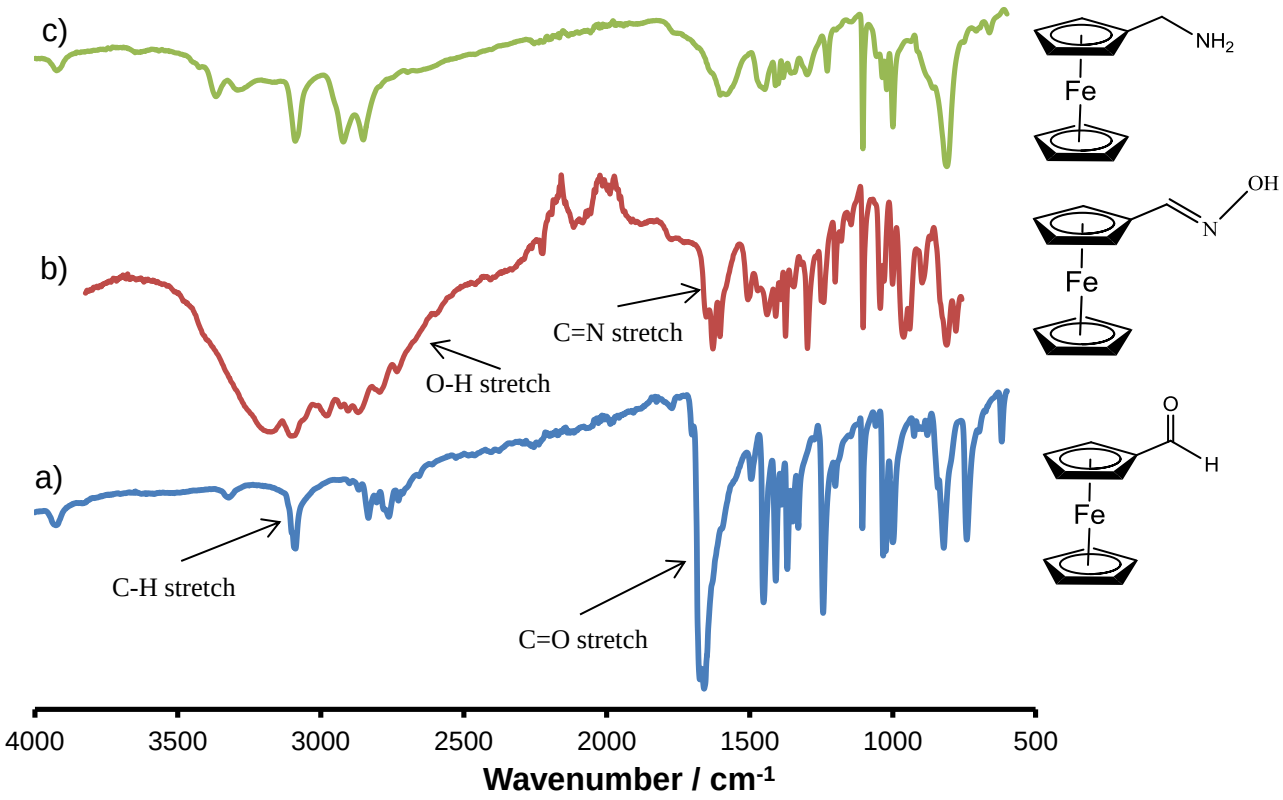

Figure 3.14 Infrared Spectra of a) ferrocenecarboxylaldehyde b) ferrocenecarboxylaldehyde oxime (crude) and c) ferrocenemethylamine.

The ^{1}H NMR spectra for the synthesised ferrocene derivatives are shown in (**Figure 3.13, p 77**). For ferrocenecarboxylaldehyde (**a**), the electron withdrawing power of the carbonyl functionality can be easily observed by the strong deshielding of the aldehyde proton resonating at 9.9 (ix) ppm. The carbonyl groups also deshields the four protons on the substituted cyclopentadienyl ring causing them to resonate at 4.8 (xi) and 4.6 (x) ppm while the unsubstituted cyclopentadienyl ring resonate at 4.3 (xii) ppm. After the reactions with hydroxylamine chlorohydrate to give ferrocenecarboxyl-aldehyde oxime (**b**), the methylene proton's resonance shifted to 7.98 (vi) ppm indicating the replacement of the aldehyde with an imine. The imine is not as highly electron withdrawing as the carbonyl resulting in less deshielding of the substituted cyclopentadienyl ring protons which now resonates at 4.53 (viii) and 4.36 (vii) ppm, while the unsubstituted ring's protons still resonate at 4.22 (v) ppm. After reduction with $LiAlH_4$,

ferrocenemethylamine (**c**) was obtained, with the amine protons resonating as a broad peak at 1.41 ppm and the methylene peak at 3.55 (iv) ppm. The electron donating effect of the methylene group shifted the resonance of both sets of equivalent protons of the substituted cyclopentadienyl ring to 4.18 (iii) and 4.12 (ii) ppm as triplets. The unsubstituted cyclopentadienyl ring's protons resonate at 4.16 (i) ppm.

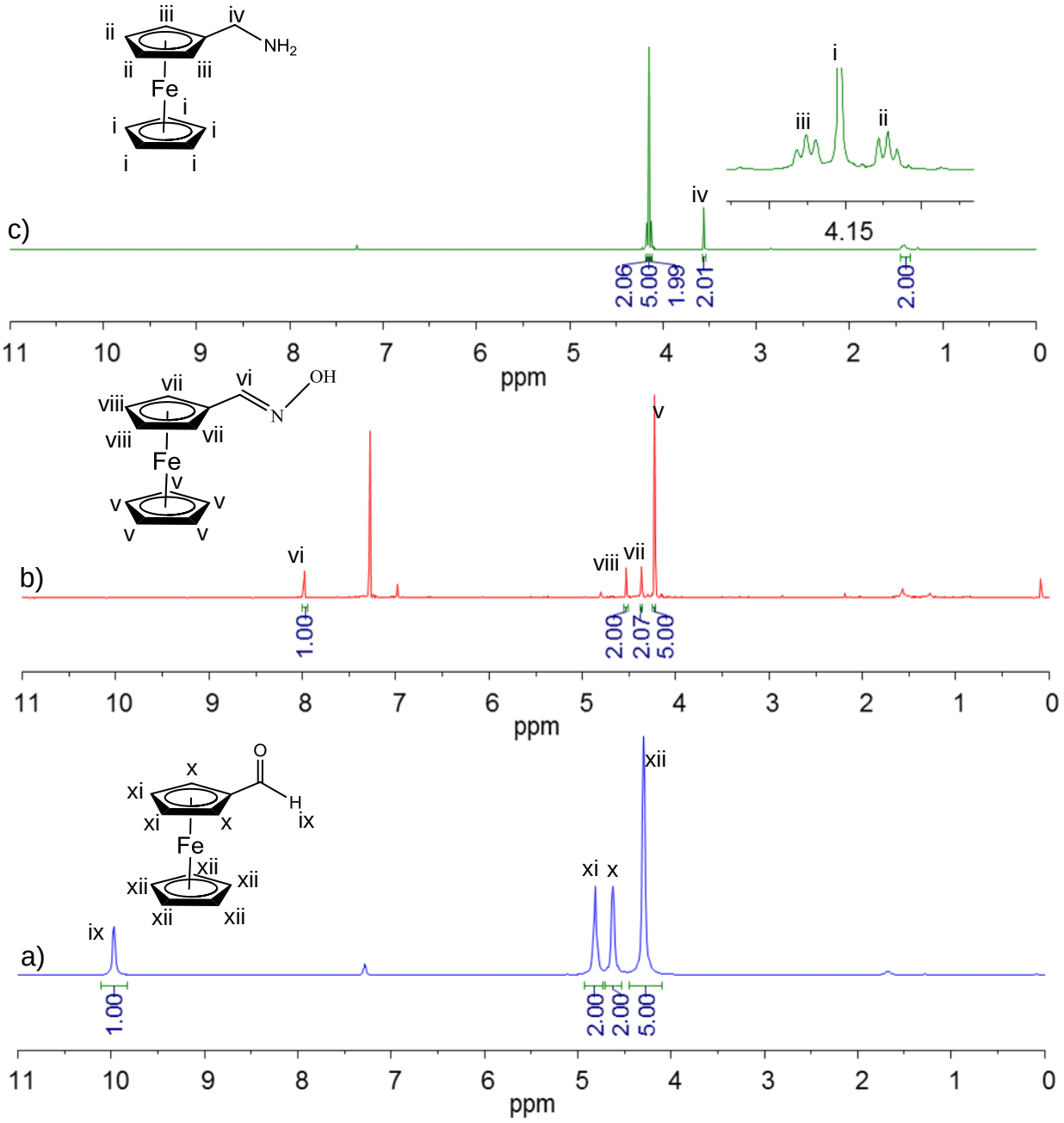

Figure 3.15 ^{1}H NMR Spectra of a) ferrocenecarboxylaldehyde b) ferrocenecarboxylaldehyde oxime (crude) and c) ferrocenemethylamine in $CDCl_3$.

3.3 Solvent Assisted Ligand Exchange (SALE) of nZIF-8

In this section, the 2-methylimidazolate linkers of nZIF-8 will be replaced by differently functionalised imidazole derivatives (**Scheme 3.5, p 81**). In general, the process involved: imidazole, benzimidazole-thioesters (-COOR), 2-mercaptobenzimidazole (-SH), 2-aminobenzimidazole (-NH_2), 2-nitroimidazole (-NO_2) and 2-phenylimidazole (-C_6H_5) will be exchanged in a suitable solvent: methanol or ethanol or *n*-butanol or dimethylformamide.

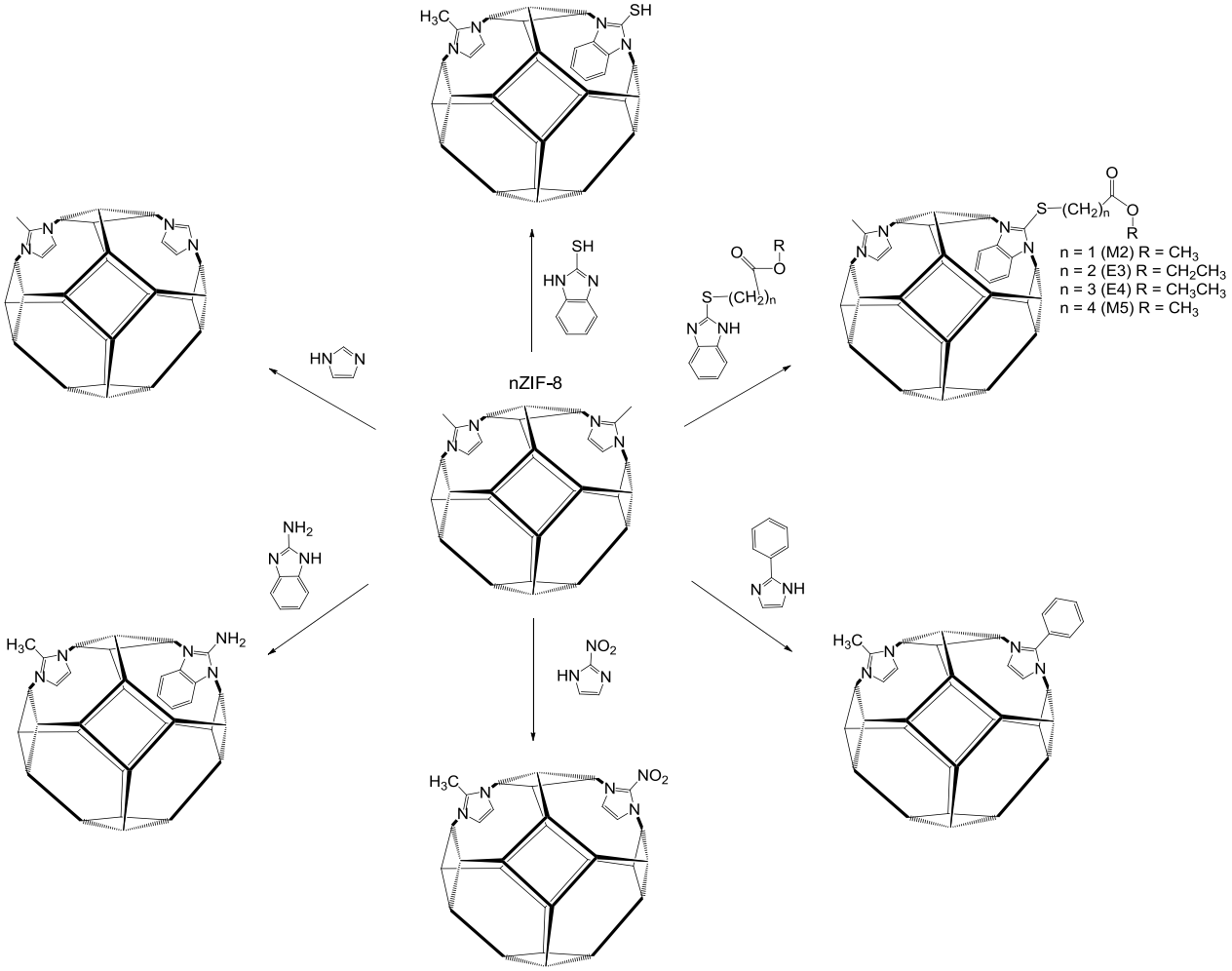

Scheme 3.5 General grand schematic representation of all solvent assisted ligand exchange (SALE) discussed in this study.

The exchange process occurs by the deprotonating of the 2-metyhlimidazolate linkers by the added imidazole derivatives, which then allow 2-methylimidazole to dissociate from the Zn metal nodes and the new imidazole ligands to coordinate on the Zn metal nodes.

3.3.1 Time Resolved SALE of Imidazole

The simplest imidazolate ligand, imidazole, will first be used to replace the 2-methylimidazole linkers of the ZIF-8 nanoparticles synthesised in **Chapter 3.2.1** as shown in (**Scheme 3.6, p 82**). The Solvent Assisted Ligand Exchange (SALE) used in a modified procedure by Karagiaridi *et al.* for micro-sized ZIF-8.

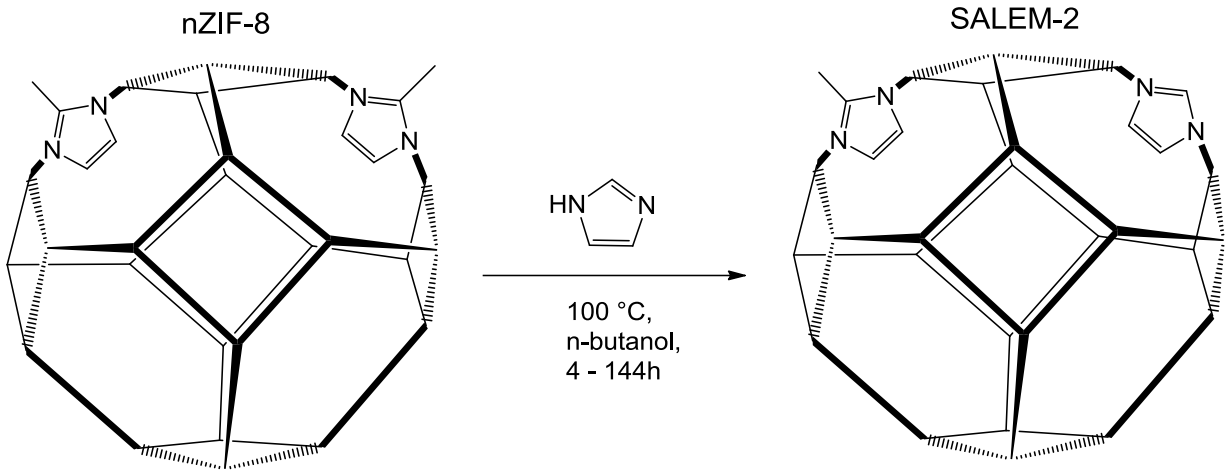

Scheme 3.6 General schematic representation of time resolved solvent assisted ligand exchange (SALE) of nZIF-8 with imidazole at different time intervals (t = 4, 16, 24, 72, 168 hours).

Activated nZIF-8 particles were suspended in *n*-butanol by ultrasonication, before transferring it to a Teflon tube and adding ~7 times excess imidazole also suspended in *n*-butanol. The tube was closed and kept isothermally at 100 ℃, below the boiling of *n*-butanol to prevent a build-up of pressure within the tube. Five different time intervals were employed: 4, 16, 24, 72 and 168 hours. The different SALEM-2 products were isolated, washed, dried and activated at 100 ℃ under vacuum. Over ~70 % of the nanoparticles were recovered. The product loss was mainly due to washing and centrifuging. The SALEM-2 products are highly stable in open atmosphere and no additional precautions were needed for storage.

ZIF-8 nanoparticles and all the ligand exchanged (*e.g.* SALEM-2) are insoluble. In order to determine the amount of 2-mentylimidazole exchanged with imidazole, a different approach is required. Digestive Liquid ^{1}H NMR is an effective technique to determine the ratio of two different ligands, since the SALEM-2 products, like nZIF-8, can be digested in an acidic medium. A 9:1 ratio of D_2O:D_2SO_4 was used in this study to fully digest the SALEM-2 products and liberate the organic ligands in solution to be measured by ^{1}H NMR directly. The ^{1}H NMR spectra of the 5 different SALEM-2 products (**Figure 3.16, p 83**) shows the following 4 singlet peaks: 1.75 (a) and 6.41 (b) ppm represent the CH_3 and CH=CH protons of 2-methylimidazole respectively; 6.61 (d) and 7.82 (c) ppm represent the CH=CH and CH protons of imidazole respectively.

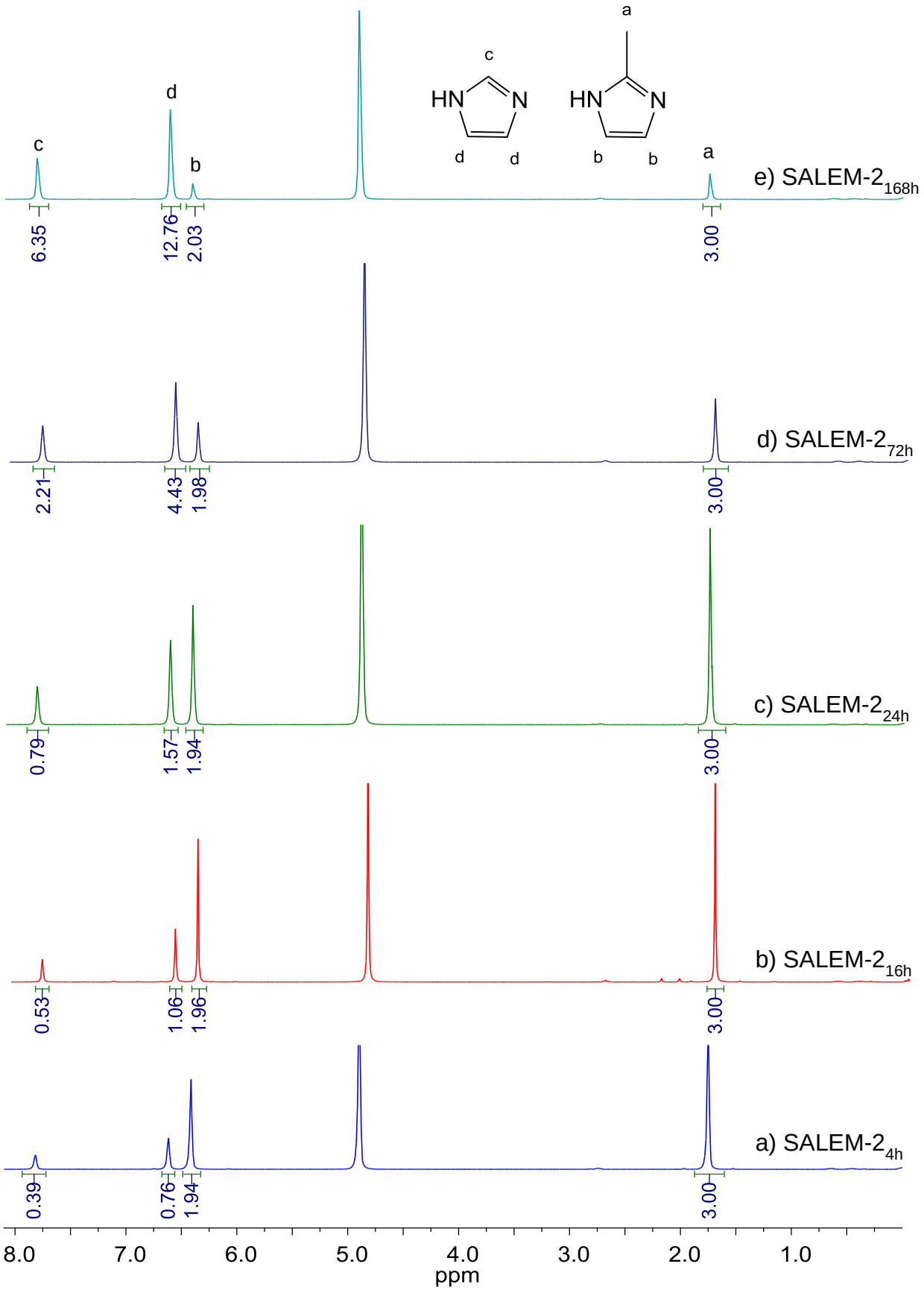

Figure 3.16 ^{1}H NMR spectra in D_2O/D_2SO_4 (9:1) of SALEM-2 products from SALE of nZIF-8 and imidazole in *n*-butanol at different exchange times: a) 4h, b) 16h c), 24h, d) 72h and e) 168h.

The ^{1}H NMR spectra show that the relative peak intensity (peaks a and b) of the 2-methylimidazole decrease as the synthesis time increases while the relative intensity of imidazole peaks (c and d) increase. The integration ratio between the CH=CH protons of 2-methylimidazole and imidazole was used to calculate the exchange %, summarized in **Table 3.5, (p 84**). The exchange to SALEM-2 reached 28 % within the first 4 hours and gradually increased to 86 % after 168 hours. The same process for micro-sized ZIF-8 showed that the initial SALE rate is much slower reaching 14 % within 24 hours as compared to 45 % for nZIF-8. After 72 hours the SALE rate equalized as both micro and nano ZIF-8 gave an exchange of 73 and 69 % respectively. The SALE is driven by the large excess of imidazole ligands in the solution with both imidazole and 2-methylimdiazole having similar pKa values 6.97 and 7.52 respectively.[9] The initial fast SALE rate, as shown in **Figure 3.17 (p 85**), is due to the larger external surface area of nZIF-8 nanoparticles that can interact with the introduced imidazole. The SALE rate slows down after 24 hours, since the imidazole needs to diffuse to the centre of the particle to exchange the remaining 50 %.

Table 3.5 Summary of SALEM-2 synthesised by SALE of nZIF-8 (1.31 mmol) by imidazole (8.86 mmol) in *n*-butanol at various exchange times. Exchange percentages were determined by ^{1}H NMR in D_2O/D_2SO_4 (9:1).

Compound	Exchange time/ h	Yield/ %	Exchange/ %
SALEM-2$_{168h}$	168	68	86.3
SALEM-2$_{72h}$	72	82	69.1
SALEM-2$_{24h}$	24	71	45.7
SALEM-2$_{16h}$	16	69	35.0
SALEM-2$_{4h}$	4	87	28.1

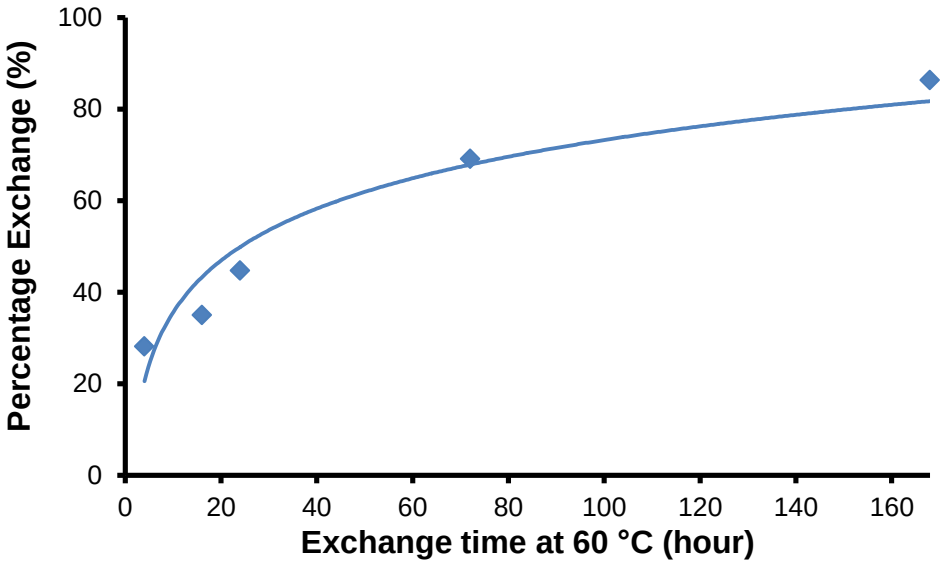

Figure 3.17 Percentage exchange *vs.* exchange time of SALEM-2.

The Solid-state NMR (^{13}C SSNMR) spectra of SALEM-2_{16h} and SALEM-2_{168h} (**Figure 3.18, p 86**) show sharp and distinct peaks for both compounds, meaning that they remain highly crystalline after SALE. For SALEM-2_{16h} (**Figure 3.18.a**), three peaks are observed: at 13.7, 124.1 and 151.1 ppm for to the CH_3, CH=CH and N-C-N carbon atoms of 2-methylimidazole (65 %) respectively. The shoulder at 128.1 ppm and the peak at 142.2 ppm represents to the N-C-N carbon of imidazole. A shoulder was observed at 124.1 ppm which represents the CH=CH carbon atoms of the imidazolate linker (35 %) respectively. After performing SALE for 168 hours (SALEM-2_{168h}) the three peaks if the imidazolate linker became much more dominant since it now represents (86 %) of the compounds linkers.

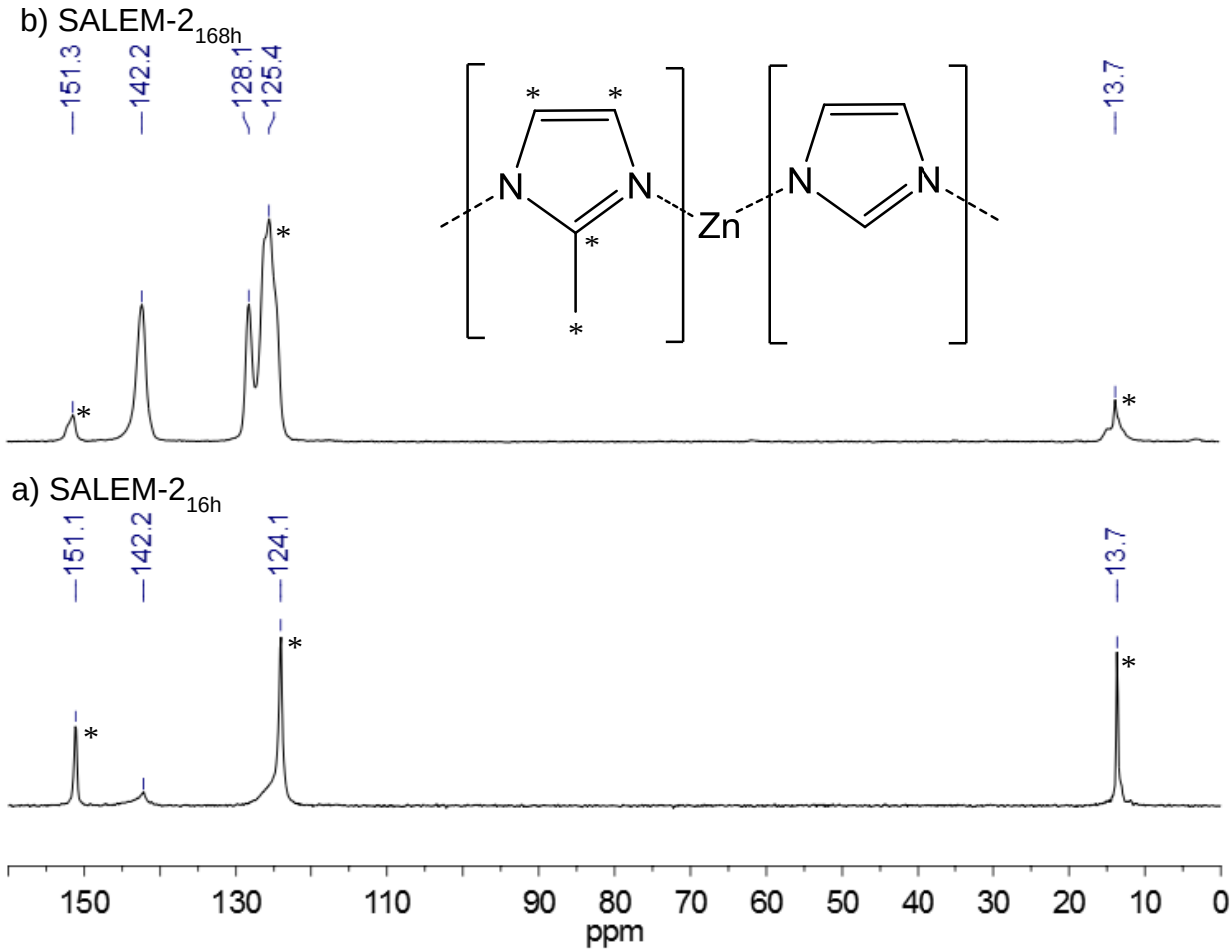

Figure 3.18 Solid State ^{13}C NMR spectrum of SALEM-2 after a) 16 and b) 168 hours of SALE. 2-Methylimidazole makerd with (*).

The SALEM-2 products were further characterised by Fourier transformed infrared spectroscopy (FTIR) (**Figure 3.19, p 87**) with nZIF-8 as reference. The addition of imidazole into the nZIF-8 structure can be observed in the spectrums. A broad N-H stretching frequency between 2500 to 3200 cm^{-1} is absent in all the SALEM-2 products, as proof that no free imidazole is present in the pores of nZIF-8 but is rather bound directly to zinc in the nZIF-8 structure. The weak stretching frequency for CH_3 of nZIF-8 at 3131 cm^{-1} (i) gradually disappears as imidazole replaces the 2-methylimidazole. The sp^2 CH_3 out of plane bending resonating at 1145 cm^{-1} (ii) decreases as it is being replaced by the imidazole C-H out of plane bending frequency at 1087 cm^{-1} (iii). The sp^3 C-H bend frequency at 1415 cm^{-1} (iv) for 2-metylimdiazole decreased as it is replaced with a prominent peak at 1494 cm^{-1} (e) for the imidazole.

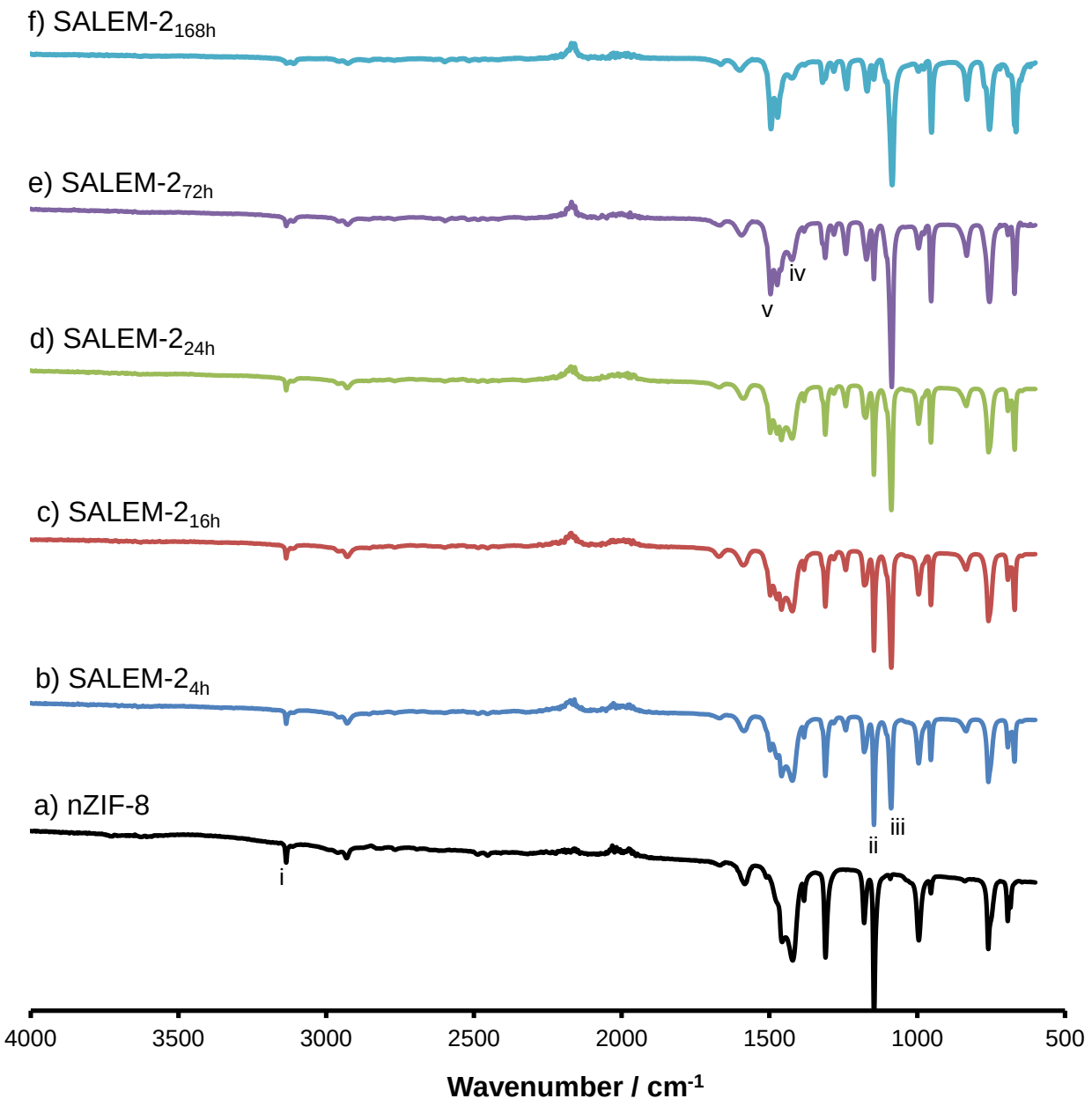

Figure 3.19 FTIR spectra of SALEM-2 products from nZIF-8 and imidazole in *n*-butanol at different exchange times: a) 0h, b) 4h c), 16h, d) 24h, e) 72h and f) 168h.

Powder X-ray diffraction patterns (PXRD) can easily determine the structural integrity of the SALEM-2 products. The PXRD patterns of SALEM-2 for 4 – 168 hours as shown in **Figure 3.20 (p 89**) it can be seen that after 72 hours of exchange, the typical PXRD patterns of the SOD structure of nZIF-8, as observed for SALEM-2_{16h} and SALEM-2_{24h}, starts to change. This is an indication that the integrity of the SOD structure of nZIF-8 begins to change with an exchange of 69 % of the 2-methylimdiazole with imidazole. From the series of SALEM-2 patterns the peaks: i) 7.4, ii) 10.5, iii)12.8, iv)15, v)16.7 and vi) 18 ° are present for all SALEM-2 compounds which is in agreement with the simulated SOD topology PXRD patterns of nZIF-8

(see **Appendix F.2**). The SOD topology was maintained for SALEM-2 exchange at 4, 16 and 24 hours, although a slight decrease in crystallinity is observed. After 72 hours of exchange (69 %) an additional peak at 17.3 ° (vii) was observed and the peak at 15 ° (iv) rose intensely. This is evidence of new crystal faces co-existing with the SOD topology in structure of SALE-2_{72h}. After 168h of exchange (86 %) the peaks (i, ii, iii, v, vi and vii) of the SOD topology diminished and a prominent peak 15 (iv) represents a new dominant topology, identical to the ZNI topology of $Zn(Im)_2$, a nonporous material (see **Appendix F.3**).[10,11,12] The exchange ratio between imidazole and 2-methylimidazole thus plays a crucial role in maintaining the SOD topology. The minimum particle size calculated with the Scherrer equation are as follows: 23, 20, 22, 23, and 33 nm for synthesis times of 4, 16, 24, 72 and 168 hours respectively. The particle size thus stayed constant while the SOD topology was maintained and increased when the ZNI topology became dominant.

From the Transmission electron microscopy (TEM) images of the SALEM-2 products in **Figure 3.21 (p 90**), the particles all remained within the nano particle range (< 100 nm) as seen in the graph of average particles *vs.* synthesis time (**Figure 3.21.f, p 90**). There is an increase in particle size as the exchange time increased. The SALEM-2_{4h} (28 % exchange) has an average particle size of ~24 nm, but as the exchange reached nearly 50 % for SALEM-2_{24h} the average particle increased to ~33 nm, to reach a maximum of ~43 nm after 86 % exchange. The increase in particle size is in agreement with the minimum particle size obtained by PXRD. The shape of the particles gradually changed from spherical (as for nZIF-8) to an irregular shape for SALEM-2 which became more distinct as the exchange time increased. This change could be associated with the change in topology of nZIF-8 from SOD to ZNI during SALE, as confirmed by PXRD analyses. The increase in particles size may be due to Ostwald ripening effects during structural changes.

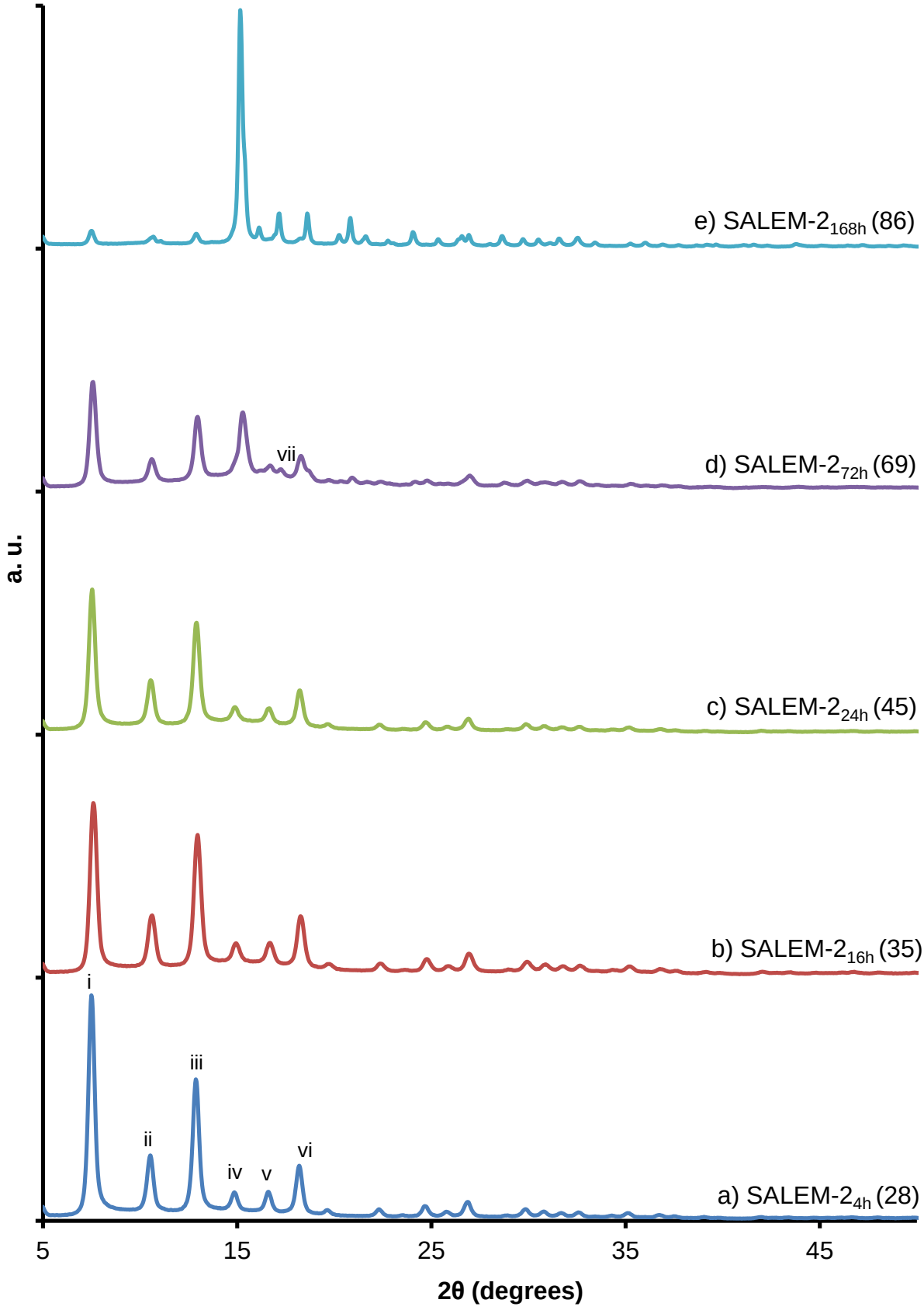

Figure 3.20 PXRD patterns of SALEM-2 products from SALE of nZIF-8 with imidazole in n-butanol for different exchange times: a) 4h, b) 16h c), 24h, d) 72h and e) 168h. The exchange percentages are given in brackets.

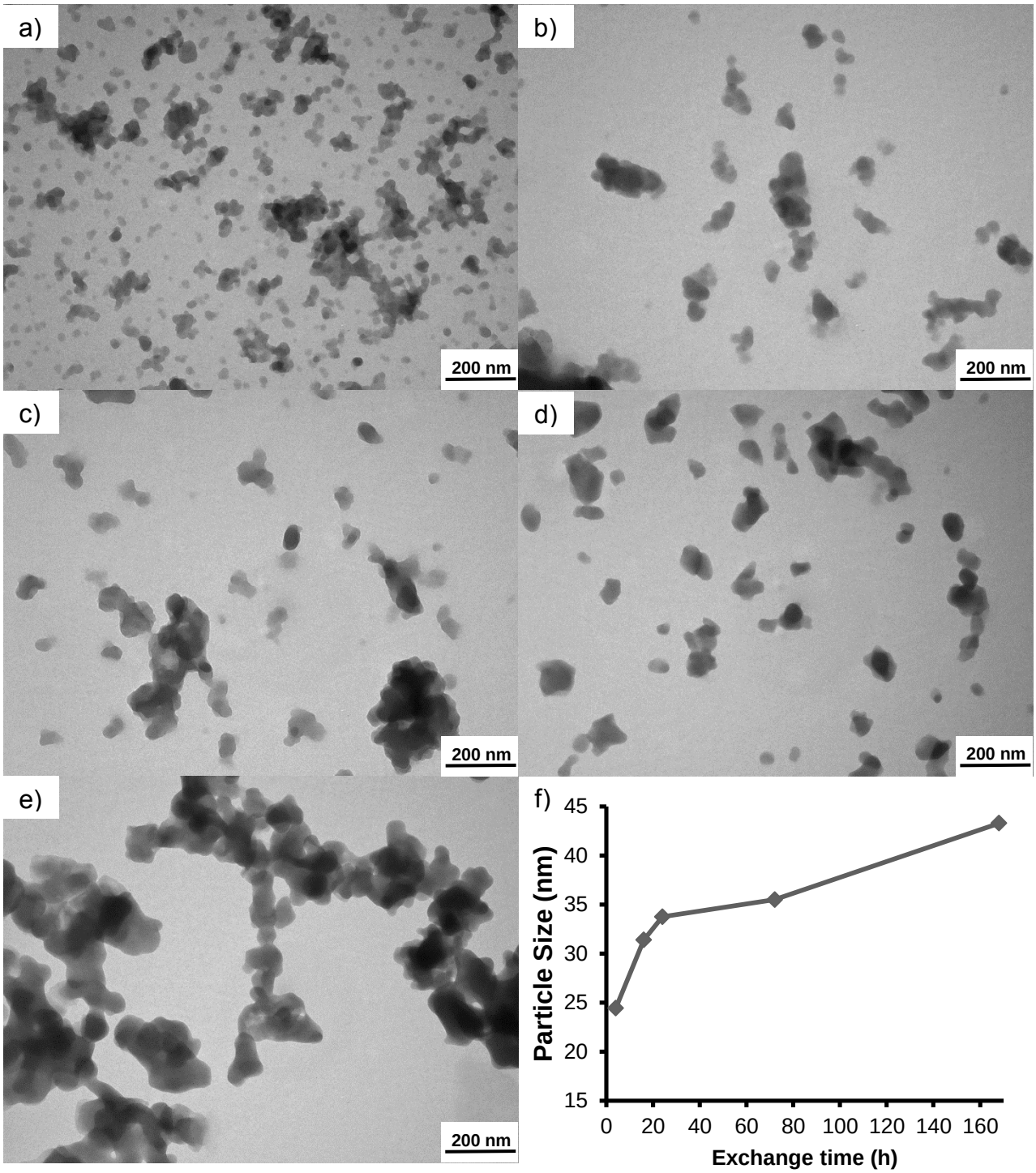

Figure 3.21 TEM images of SALEM-2 products from SALE of nZIF-8 with imidazole in *n*-butanol for different exchange times: a) 4, b) 16, c) 24, d) 72, e) 168 hours and f) graph of particle size *vs.* Synthesis time.

The SALEM-2 materials were activated at 150 ℃ for 16 hours prior to porosity analysis to give the isotherms in **Figure 3.22 (p 91**) for SALEM-2 4 to 168 hours. These Type-1 isotherms show that the materials are microporous and remain porous after SALE. The quantity of nitrogen adsorbed remains high even after 45 % exchange (**c**) with a maximum adsorption of 394 cm^{-3} g^{-1}

at 0.9 p/p°. An exchange of 69 % (after 72 hours) (**d**) with the appearance of the ZNI topology as observed by PXRD, led to a severe decrease in porosity by nearly 50 % as only 215 $cm^{-3}\,g^{-1}\,N_2$ was adsorbed at 0.9 p/p°. With the new ZNI topology being dominant after 168 hours, the isotherm shows an adsorption of only 45 $cm^{-3}\,g^{-1}$ at 0.9 p/p° (**e**), proof that this material is almost non-porous.

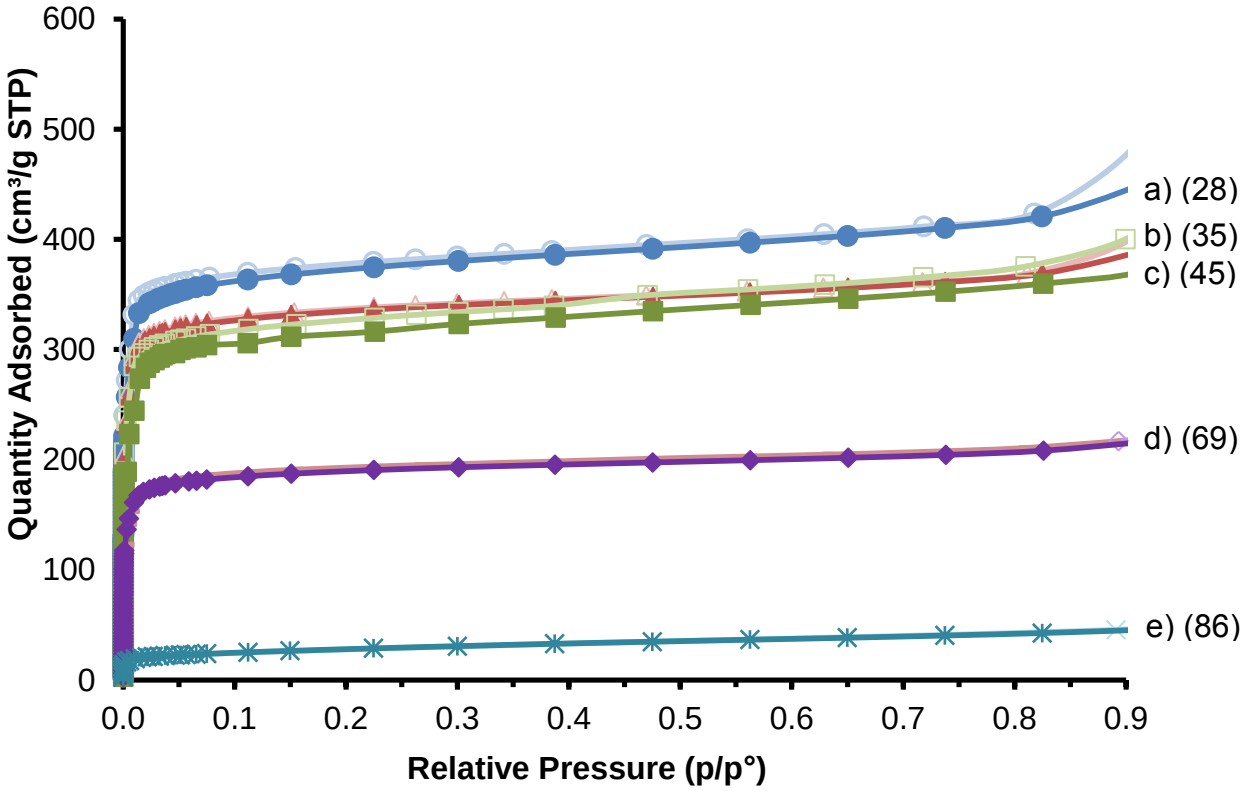

Figure 3.22 Nitrogen adsorption and desorption isotherms at 77 K of SALEM-2 products from SALE of nZIF-8 with imidazole in *n*-butanol for different exchange times: a) 4 (red), b) 16 (blue), c) 24 (green), d) 72 (purple), and e) 168 (turquoise) hours. Adsorption marked as solids and desorption as hollow symbols. The exchange percentages are given in brackets.

The BET surface areas of SALEM-2 products remain above 1200 $m^2\,g^{-1}$ as seen in **Table 3.6 (p 92**) with exchange percentages of 45 and less. As the exchange increased to 69 % and the ZNI topology began to form, the BET surface area dropped to 756 $m^2\,g^{-1}$ and further to 96. $m^2\,g^{-1}$ after a 86 % exchange (**Figure 3.23, p 92**).

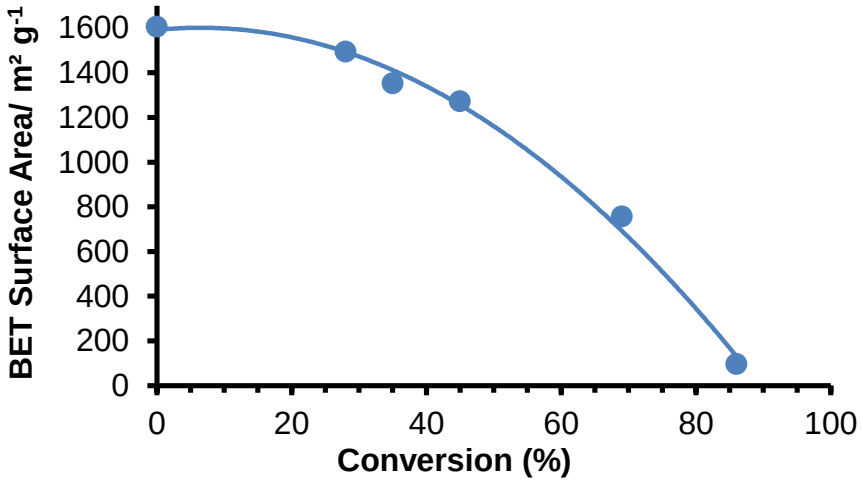

Figure 3.23 BET surface area ($m^2\ g^{-1}$) *vs.* conversion (%) of SALEM-2 products obtained by solvent assisted ligand exchange (SALE) of nZIF-8 with imidazole.

The t-plot external surface area of the SALEM-2 products decreased from 267 to 74 $m^2\ g^{-1}$ as the exchange time increased from 4 to 168 hours. This trend directly correlates to the particle sizes obtained by TEM. As the particle size increased (from 24 to 43 nm) the external surface decreased. Where the materials have a mixture of porous and non-porous topologies, the micropore volumes shrank from 0.375 to 0.011 $cm^3\ g^{-1}$ for 45 to 86 % exchange. This confirms that after SALE exceeding a conversion of 45 % with imidazole, the original porosity cannot be maintained due to the mixture of topologies within the structure.

Table 3.6 N_2 porosity analyses at 77 K of SALEM-2 products from SALE of nZIF-8 with imidazole. Percentage exchange are given in brackets. Quantities adsorbed were measured at 0.9 p/p°.

Exchange (%)	Quantity Adsorbed/ $cm^3\ g^{-1}$	BET Surface Area/ $m^2\ g^{-1}$	t-plot External Surface Area/ $m^2\ g^{-1}$	Micropore volume/ $cm^3\ g^{-1}$
nZIF-8	469	1606	321	0.471
SALEM-2_{4h} (28)	448	1494	267	0.461
SALEM-2_{16h} (35)	388	1353	243	0.415
SALEM-2_{24h} (45)	394	1272	282	0.375
SALEM-2_{72h} (69)	215	756	204	0.211
SALEM-2_{168h} (86)	45	96	74	0.011

TGA thermograms of all the SALEM-2 compounds show high thermal stability up to 400 ℃ (**Figure 3.24, p 93**). Thereafter a mass loss of ~5-7 % was followed by a continued gradual loss of mass after 600 ℃ due to the thermal collapse of the nZIF-8 structure. The thermal stability remains identical to unexchanged nZIF-8 structures. For SALEM-2_{24h} an early mass loss of 9.6 % after 183 ℃ was followed by a larger mass loss of 24 % after 400 ℃. SALEM-2_{24h} has 45 % conversion and can be regarded as a transition phase towards the new ZNI topology (by PXRD) causing the structure to be less thermally stable than the rest.

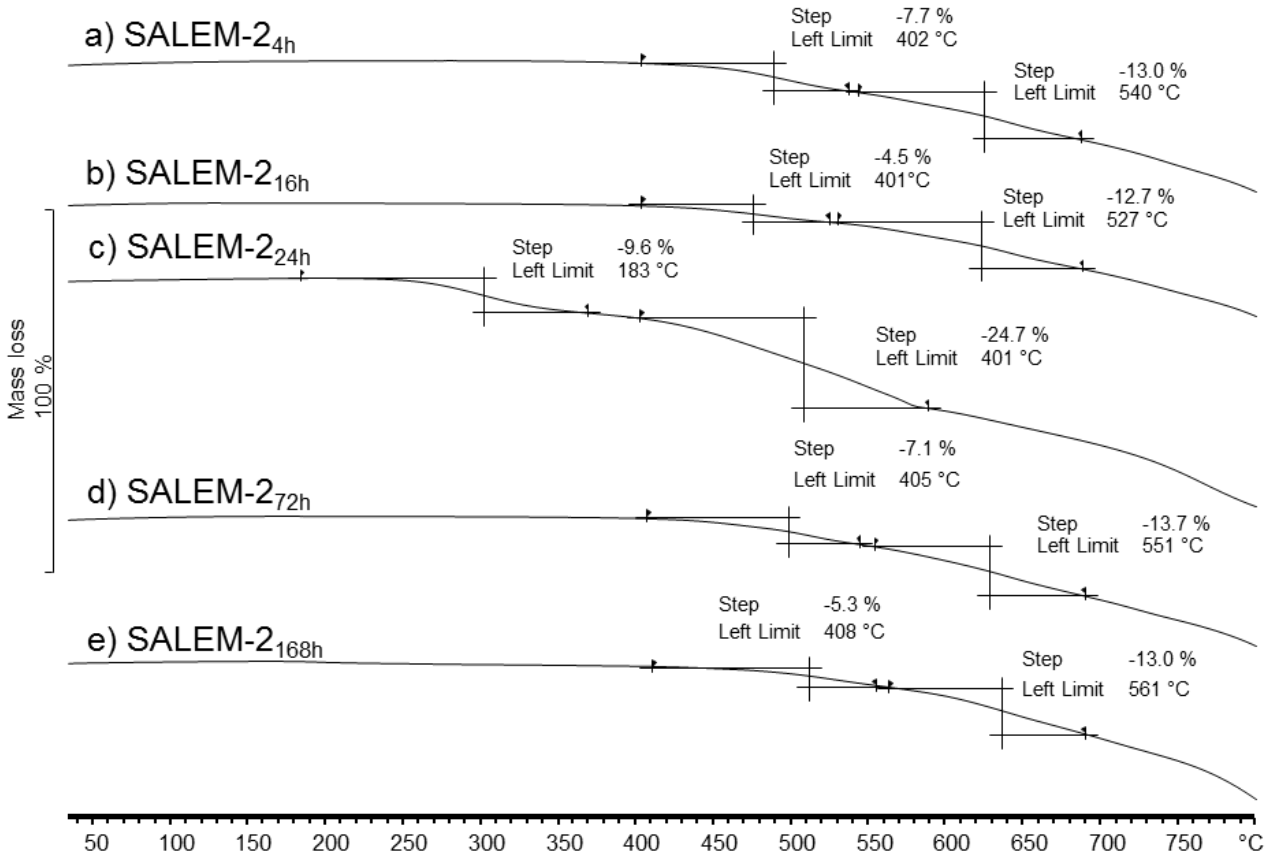

Figure 3.24 TGA thermogram in N_2 of SALEM-2 products from SALE of nZIF-8 with imidazole in *n*-butanol for different exchange times: a) 4, b) 16, c) 24, d) 72, and e) 168 hours.

3.3.2 SALE of Benzimidazole-thioesters

3.3.2.1 2-Mercaptobenzimidazole (nZIF8-SHBzIm)

Solvent assisted ligand exchange (SALE) of nZIF-8 with 2-Mercaptobenzimidazole was first investigated (**Scheme 3.7, p 94**), before attempting Post Synthetic Modification (PSM) via *S*-Alkylation.

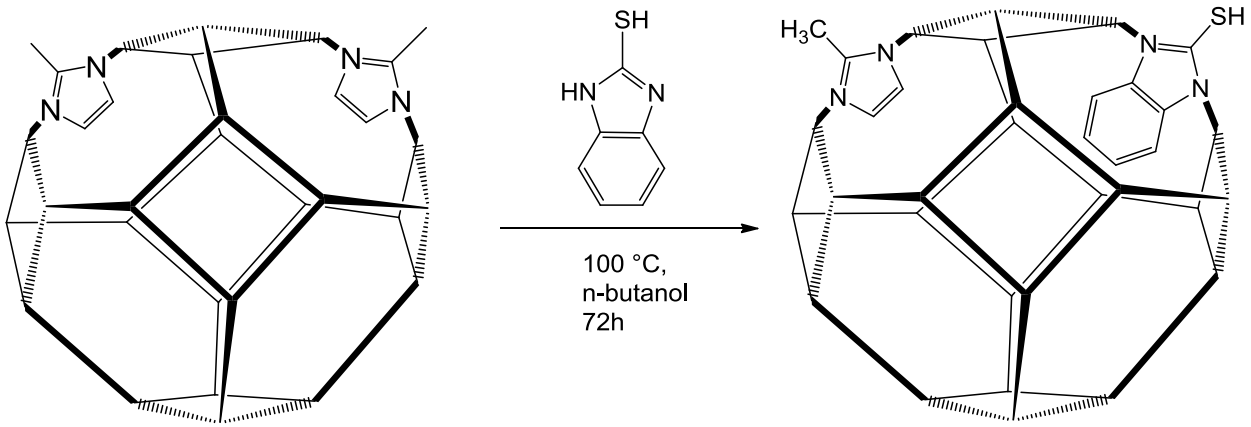

Scheme 3.7 Solvent assisted ligand exchange of nZIF-8 with 2-mercaptobenzimdazole at 60 ℃ for 72 hours.

The SALE was performed as described earlier (**Section 3.3.1, p 82**) at 100 ℃ for 72 hours. The activated product denoted as nZIF8-SHBzIm$_{72h}$, was obtained as a light yellow powder (23 % yield) and is stable in atmospheric conditions. The low yield was due to the acidity the thiol which can digest nZIF-8 during the SALE process.

The exchange percentage of the SALE process was determined by digestive liquid ^{1}H NMR as previously described (**Section 3.3.1, p 82**) giving a spectrum of LeZIF8-SHBzIm$_{72h}$ (**Figure 3.25.a, p 95**) with 4 distinct peaks for both linkers (2-methylimidazole and 2-mercaptobenzimidazole). The peaks at 1.84 and 6.71 ppm represent the CH_3 and CH=CH protons for the 2-methylimidazole respectively. The peaks at 6.72 and 6.82 ppm originates from the protons on the benzyl ring of 2-mercaptobenzimidazole. The exchange percentage (12.5 %) was determined from the proton ratios of the benzyl ring of the 2-mercaptobenzimidazole linker and the CH=CH bond of the 2-mehtylimdiazole linker. The distinct peaks of the Solid-state ^{13}C NMR spectrum of LeZIF8-SHBzIm$_{72h}$ (**Figure 3.25.b, p 95**) is proof that the particles maintained their crystallinity throughout the SALE process. From the spectrum the peaks for 2-methylimidazole is clearly present at 17.2, 127.6 and 154.6 ppm for the CH_3, CH=CH and N-C-N carbon atoms respectively.

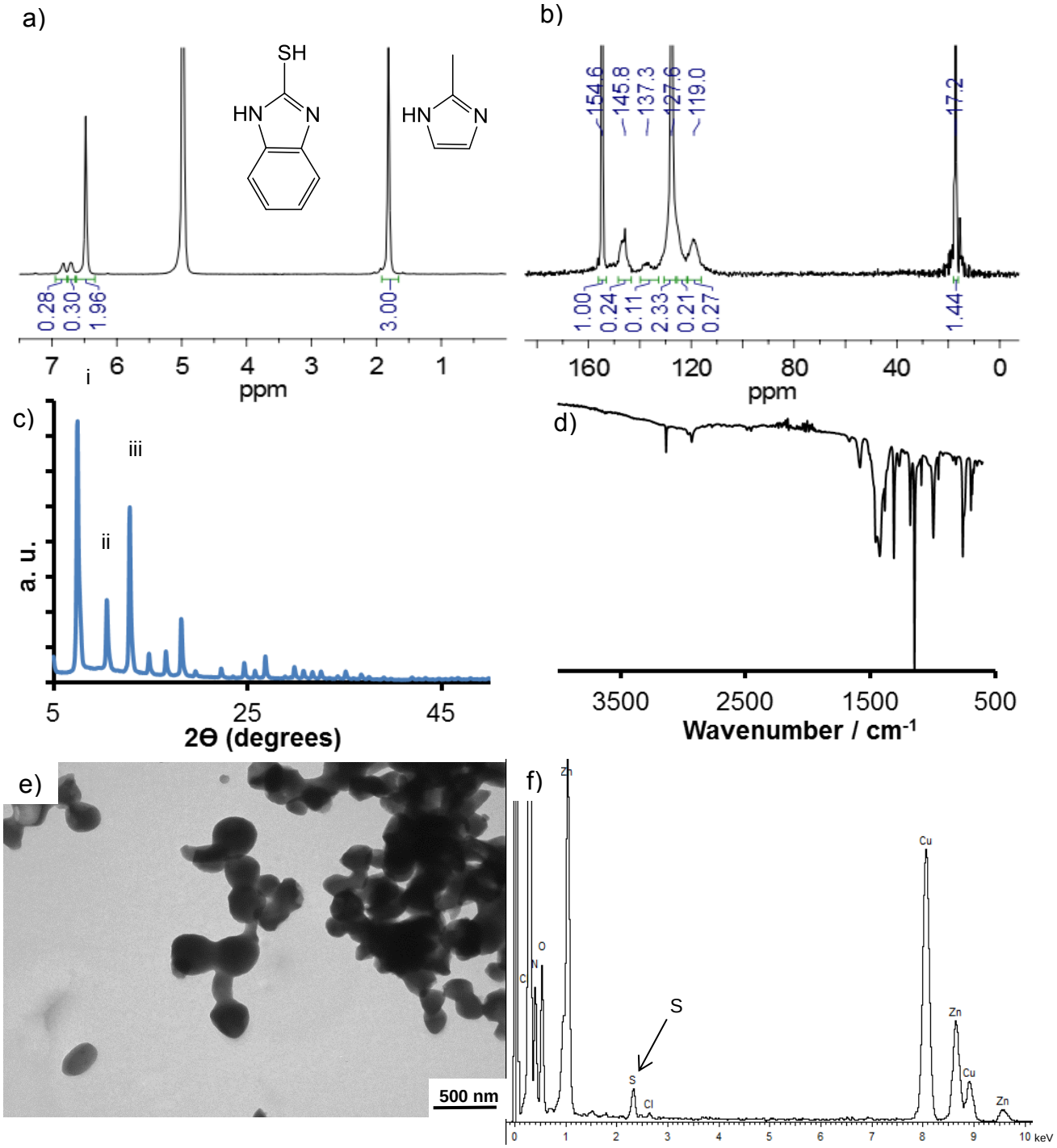

Figure 3.25 Characterisation of LeZIF8-SHBzIm$_{72h}$: a) ^{1}H NMR (digested in D_2O/D_2SO_4 (9:1)) b) Solid-state ^{13}C NMR spectrum c) PXRD pattern d) Infrared spectrum e) TEM and f) EDS spectra of TEM image.

For 2-mercaptobenzimidazole three distinct peaks at 119, 137.3 and 145.8 ppm was identified as the aromatic ring and N-C-N carbon atoms respectively. A shoulder observed at 124 ppm represents the C=C aromatic carbon atoms of the imidazole ring of 2-mercaptobenzimidazole. The FTIR of LeZIF8-SHBzIm$_{72h}$ (**Figure 3.25.d, p 95**) is similar to that of nZIF-8 since the weak S-H frequency is difficult to observe due to the low exchange percentage (12.5 %). The

PXRD pattern for LeZIF8-SHBzIm$_{72h}$ (**Figure 3.25.c, p 95**) is identical to the pattern of nZIF-8 with the 3 main peaks at 7.48 (i), 10.5 (ii) and 12.8 (iii) °, showing that the structure maintained the SOD topology and structural integrity during the harsh SALE process. From the peaks width and with the aid of the Scherrer equation a minimum particle size of 40 nm was determined. From TEM images (**Figure 3.25.e, p 95**), the average particle size of nZIF8-SHBzIm$_{72h}$ was determined as 174 nm. The particles have a spherical shape and are larger than the nZIF-8 starting material due to Ostwald ripening during the lengthy SALE with 2-mercaptobenzimdazole. The EDS spectrum (**Figure 3.25.f, p 95**) shows that sulphur is present (2.4 keV peak) verifying the presence of 2-mercaptobenzimidazole. The identification of copper is from the copper grids used for TEM analyses.

LeZIF8-SHBzIm$_{72h}$ was activated at 150 ℃ for 16 hours prior to porosity analysis, which gave a typical Type-1 isotherm (**Figure 3.26, p 96**), indicating that the material is microporous. LeZIF8-SHBzIm$_{72h}$ maintained a high porosity after SALE even with the low yield and increased particle size. It adsorbed of 317 $cm^{-3}\,g^{-1}$ of N_2 at 0.8 p/p°, with a BET surface area of 1416 $m^2\,g^{-1}$ (nZIF-8 = 1605 $m^2\,g^{-1}$) and a micropore volume of 0.473 $cm^3\,g^{-1}$ (nZIF-8 = 0.471 $cm^3\,g^{-1}$). The t-plot external surface area of LeZIF8-SHBzIm$_{72h}$ was determined as 114 $m^2\,g^{-1}$ much smaller than the 321 $m^2\,g^{-1}$ of the nZIF-8 starting material. This decrease in external surface area correlates with the increase in particle size from 22 nm (nZIF-8) to 174 nm (LeZIF8-SHBzIm$_{72h}$).

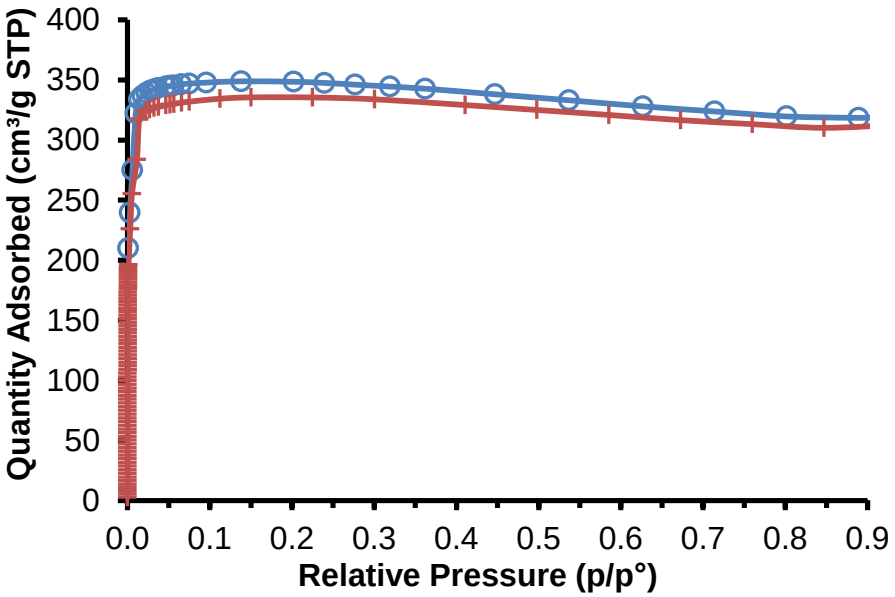

Figure 3.26 Nitrogen adsorption and desorption at 77 K isotherms of LeZIF8-SHBzIm$_{72h.}$ Adsorption marked as crosses and desorption as circles.

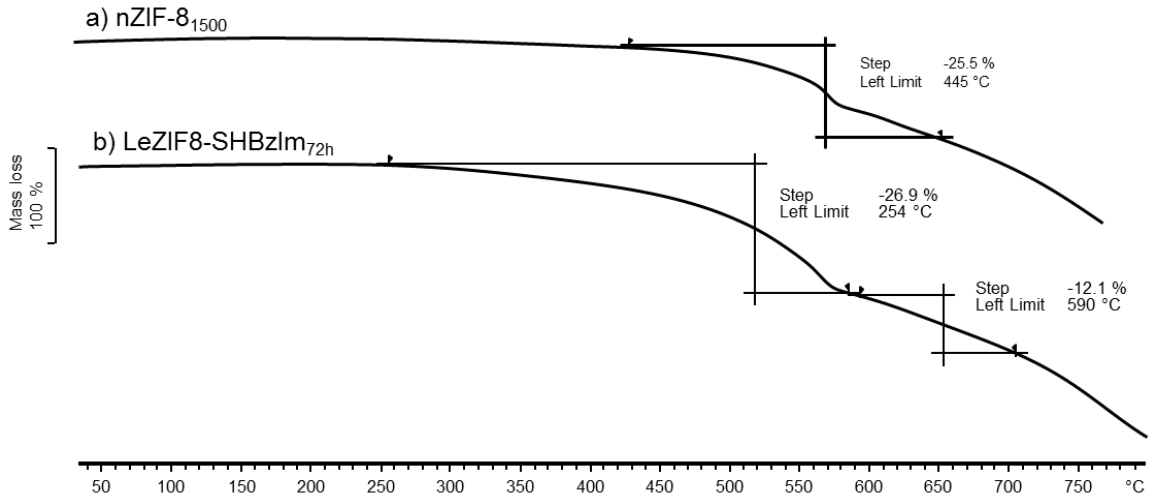

Figure 3.27 TGA thermograms under N_2 of a) nZIF-8 and b) LeZIF8-SHBzIm$_{72h}$.

The thermal stability of LeZIF8-SHBzIm$_{72h}$ has a significant decrease as shown in the thermogram (**Figure 3.27, p 97**). With the new 2-mercaptobenzimidazole linker the thermal stability drop between 450 ℃ to 250 ℃ as seen by the first step with a mass loss of 27 %. Follow by the gradual continuous mass loss after 600 ℃ by the collapse of the nZIF-8 structure.

3.3.2.2 Benzimidazole-thioesters (time resolved)

Since the SALE of nZIF-8 with 2-Mercaptobenzimidazole (**Section 3.3.2.1, p 94**) gave a very low yield of nZIF8-SHBzIm$_{72h}$ (23 %) with an exchange of only 12 %, it is not a viable route to add ester functional groups on the external surface area of nZIF-8. Therefore, Pre-Synthetic Modification was performed by the syntheses of a series of benzimidazole-thioesters (n = 1, 2, 3 and 4) (**Chapter 3.2.3, p 73**) via *S*-Alkylation. nZIF-8 was then subjected to solvent assisted ligand exchang with the pre-synthesised benzimidazole-thioesters (**Scheme 3.8, p 98**). The solvent assisted ligand exchange (SALE) was performed initially with the same procedure as SALEM-2, using *n*-butanol as solvent This, unfortunately, led to ZIF-8 catalysed transesterification[13], between *n*-butanol and the benzimidazole-thioesters (**Appendix B.2**). In order to limit transesterification of the benzimidazole-thioesters with the alcohol solvent, methanol was used for the methyl esters and ethanol for the ethyl esters.

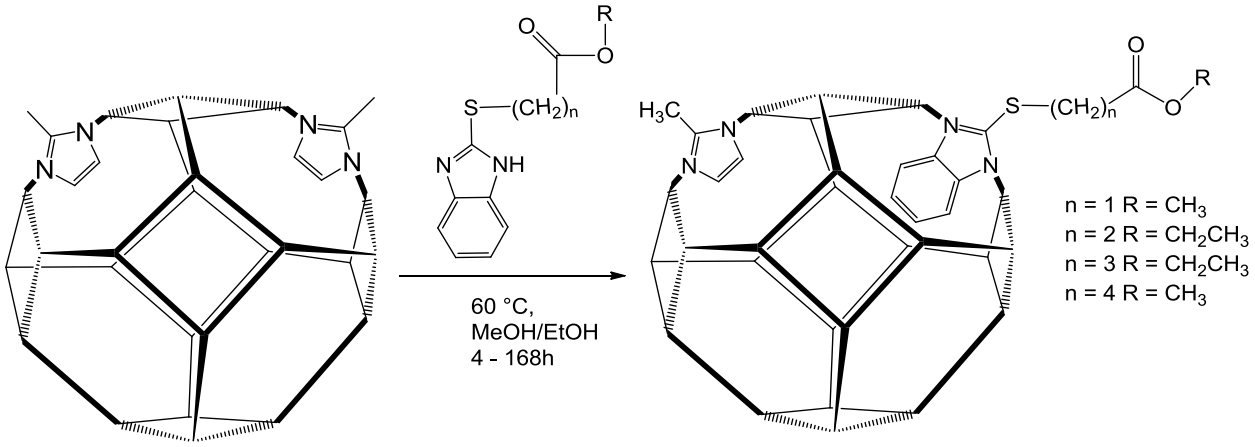

Scheme 3.8 Time resolved solvent assisted ligand exchange of nZIF-8 with a) methyl benzimidazole-2-ylthio acetate (M2), b) ethyl benzimidazole-2-ylthio propionate (E3), c) ethyl benzimidazole-2-ylthio butyrate (E4) and d) methyl benzimidazole-2-ylthio valerate (M5) using different time intervals (t = 4, 16, 24, 72, 168 hours). Methanol was used as solvent for the methyl esters and ethanol for the ethyl esters.

The benzimidazole-thioesters were dissolved in the appropriate solvent to a ~3 times excess and then mixed with suspensions of activated the nZIF-8 nanoparticles. The tubes were sealed and heated at 60 ℃ under isothermal conditions for time intervals of 4, 16, 24, 72 and 168 hours. The products are denoted as: a) LeZIF8-M2, b) LeZIF8-E3, c) LeZIF8-E4 and d) LeZIF8-M5 for the following ligands: methyl benzimidazole-2-ylthio acetate, ethyl benzimidazole-2-ylthio propionate, ethyl benzimidazole-2-ylthio butyrate and methyl benzimidazole-2-ylthio valerate respectively. Each LeZIF8 product was easily isolated, washed, dried and activated at 100 ℃ under vacuum. Except for LeZIF8-E3 where yields between 65 and 85 % were obtained, all the LeZIF8 products had yields above 90 % as summarized in **Table 3.7 (p 99**). The compounds are all stable in atmospheric conditions.

Table 3.7 Products from SALE of nZIF-8 with methyl benzimidazole-2-ylthio acetate (LeZIF8-M2), ethyl benzimidazole-2-ylthio propionate (LeZIF8-E3), ethyl benzimidazole-2-ylthio butyrate (LeZIF8-E4) and methyl benzimidazole-2-ylthio valerate (LeZIF8-M5) at various synthesis times. *Exchange percentages were determined by ^{1}H NMR in D_2O/D_2SO_4 (9:1).

Compound	Exchange time/ h	Yield/ %	*Exchange/ %
LeZIF8-M2$_{168h}$	168	95	13.6
LeZIF8-M2$_{72h}$	72	99	9.5
LeZIF8-M2$_{24h}$	24	96	8.4
LeZIF8-M2$_{16h}$	16	99	7.3
LeZIF8-M2$_{4h}$	4	98	6.5
LeZIF8-E3$_{168h}$	168	65	1.3
LeZIF8-E3$_{72h}$	72	78	1.3
LeZIF8-E3$_{24h}$	24	85	1.9
LeZIF8-E3$_{16h}$	16	77	1.4
LeZIF8-E3$_{4h}$	4	86	0.9
LeZIF8-E4$_{168h}$	168	98	9.1
LeZIF8-E4$_{72h}$	72	97	9.1
LeZIF8-E4$_{24h}$	24	96	8.9
LeZIF8-E4$_{16h}$	16	99	7.6
LeZIF8-E4$_{4h}$	4	93	4.9
LeZIF8-M5$_{168h}$	168	100	11.7
LeZIF8-M5$_{72h}$	72	98	10.0
LeZIF8-M5$_{24h}$	24	90	9.1
LeZIF8-M5$_{16h}$	16	98	8.6
LeZIF8-M5$_{4h}$	4	95	7.0

The SALE exchange percentages were determined by digestive ^{1}H NMR as shown (**Figure 3.28, p 101**) for the products obtained after 168 hours of exchange. The ^{1}H NMR spectra for the other four time intervals can be found in (**Appendix B.3 to B.6**). For all the compounds the peaks for the CH_3 and HC=CH protons can be seen at ~1.8 and ~6.5 ppm respectively. For LeZIF8-M2$_{168h}$ (**a**), the ^{1}H NMR spectrum shows peaks for the methyl benzimidazole-2-ylthio acetate ligand at 6.72 and 6.59 ppm for the benzyl ring and at 3.4 and 2.89 ppm for the alkyl chain (CH_2) and the methyl alkoxy (CH_3) respectively. For LeZIF8-E3$_{168h}$ (**b**), the peaks for the ethyl benzimidazole-2-ylthio propionate ligands resonates at: 6.95 and 6.81 ppm for the benzyl ring, 2.91 and 2.21 ppm for the alkyl chain (CH_2CH_2) and 3.34 and 0.45 ppm for the ethyl alkoxy group (CH_2CH_3). For LeZIF8-E4$_{168h}$ (**c**), the peaks for the ethyl benzimidazole-2-ylthio butyrate ligand are described as follows: peaks at 6.89 and 6.73 ppm for the benzyl ring, 2.91, 2.67 and 1.35 ppm for the alkyl chain ($CH_2CH_2CH_2$) and 3.35 and 0.4 ppm for the ethyl alkoxy group (CH_2CH_3). Lastly, for LeZIF8-M5$_{168h}$ (**d**), the methyl benzimidazole-2-ylthio valerate peaks are easily identified: at 6.89 and 6.73 ppm for the benzyl ring, 2.66, 1.66 and 1.01 ppm for the alkyl chain ($CH_2CH_2CH_2CH_2$) and 2.85 ppm for the methyl alkoxy group (CH_3). The integration ratio between the CH=CH protons of the 2-methylimidazole and the CH=CH (benzyl ring) protons of the benzimidazole-thioesters were used to calculate the exchange percentages summarized in (**Table 3.7, p 99**) with the graphs of exchange percentage *vs* synthesis time next to each relevant ^{1}H NMR spectrums (**Figure 3.28, p 101**). For all the samples, the acidic medium (D_2SO_4 in D_2O) caused slight hydrolysis of the alkoxy groups so that the integration does not show the expected amount of protons, as shown in the proton integration.

The SALE process is relatively fast, reaching a conversion of ~5 % within 4 hours of conversion which then steadily rises to a maximum of ~10 % after 168 hours, for all the esters except for methyl benzimidazole-2-ylthio acetate. This low exchange maximum is due to bulkiness of these ester ligands causing steric preventing them from diffusing into the pores (pore window is ~3.4Å). The exchange thus takes places mainly on the external surface of the nZIF-8 particle.[14] With LeZIF8-E3$_{168h}$, exchange percentage reached only 1.3 % after 168 hours. This could be due to intramolecular cyclization of the ethyl benzimidazole-2-ylthio propionate ester with the NH of the benzimidazole preventing complexation of the NH with the Zn^{2+} metal of the nZIF-8. This type of cyclization process occur with the addition of triethylamine base and form 6 membered rings.[15,16] There is a higher preference of forming 5 membered rings than 6 membered rings, although the latter are formed faster.[17] Although cyclization of five membered rings was not observed with methyl benzimidazole-2-ylthio acetate, this suggest that the methyl alkoxy group could play and important role in the cyclization process. The effect of cyclization of other benzimidazole-thioesters was not part of the scope of this study and was not investigated further.

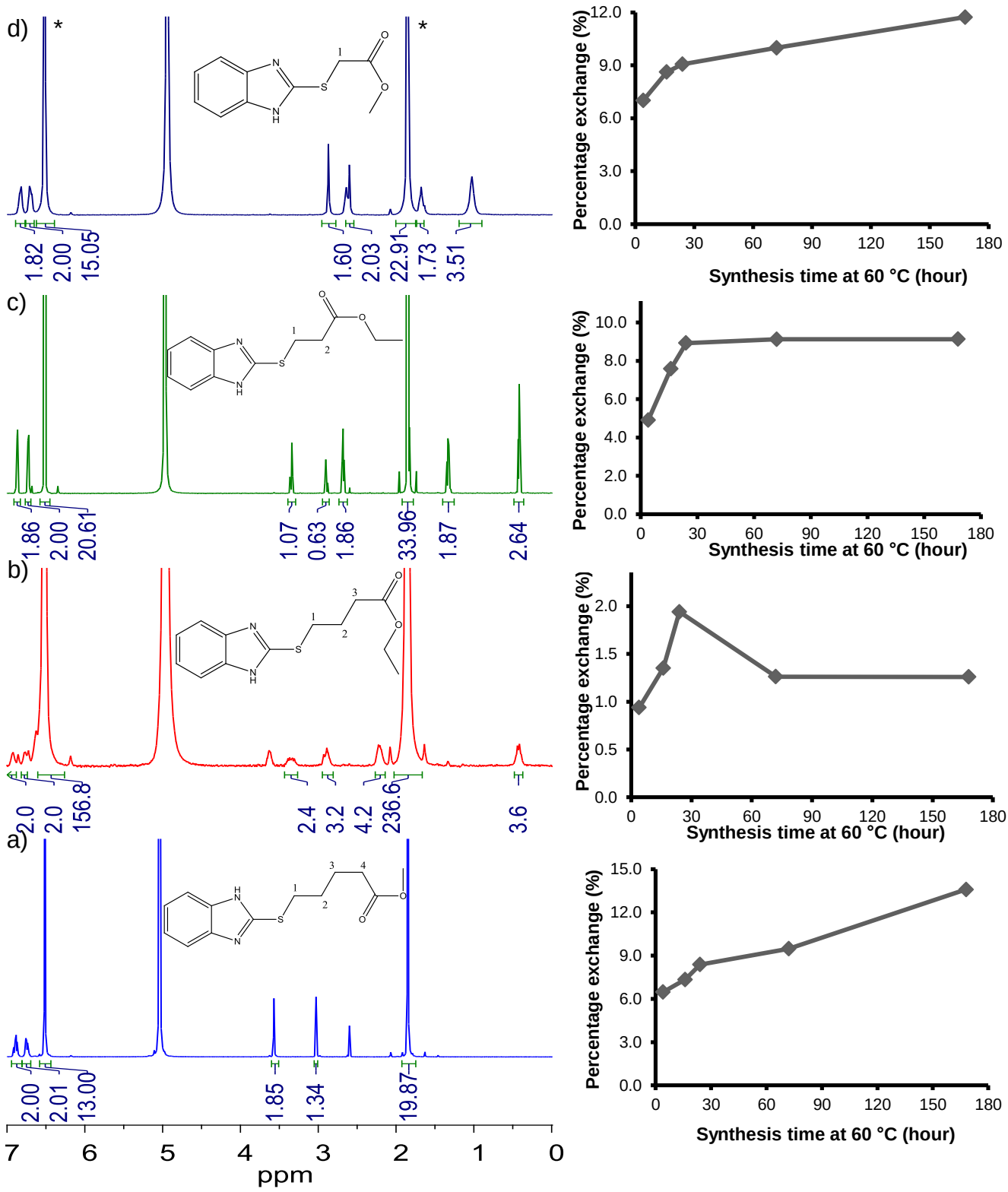

Figure 3.28 Digestive ^{1}H NMR (D_2O/D_2SO_4 (9:1)) Spectra (left) and graphs of exchange percentages vs synthesis time (right) after SALE of nZIF-8 for 168 hours with a) methyl benzimidazole-2-ylthio acetate (LeZIF8-$M2_{168h}$), b) ethyl benzimidazole-2-ylthio propionate (LeZIF8-$E3_{168h}$), c) ethyl benzimidazole-2-ylthio butyrate (LeZIF8-$E4_{168h}$) and d) methyl benzimidazole-2-ylthio valerate (LeZIF8-$M5_{168h}$) in. 2-Methylimidazole protons are marked (*).

Solid-state NMR (^{13}C SSNMR) (**Figure 3.29, p 103**) was performed on **a**) LeZIF8-M2$_{168h}$, **b**) LeZIF8-E3$_{168h}$, **c**) (LeZIF8-E4$_{168h}$ and **d**) LeZIF8-M5$_{168h}$ with an exchange time of 168h (highest exchange percentages) All the peaks are relatively sharp suggesting that the product particles remain crystalline after SALE. All the ^{13}C NMR spectra show the characteristic peaks (marked with *) of the 2-methylimidazolate at 16.87, 127.33 and 154.35 ppm for the CH_3, CH=CH and N-C-N carbon atoms respectively. For each LeZIF-8 compound the exchanged benzimidazole-thioester are present as observed in the spectra. The benzyl group observed as three groups of equivalent carbons for all the spectrums as ~118, ~125 and ~147 ppm. For all the spectrums the C=O carbons resonates 169.07, 172.8, 173.99 and 174.72 ppm for n = 1, 2, 3 and 4 respectively. The longer the alkyl chain the higher the chemical shift was observed. All the N_2-C-S carbons resonates at 160.46, 165.43, 158.89 and 158.87 ppm for n = 1, 2, 3 and 4 respectively.

For LeZIF8-M2$_{168h}$, the overlapping and shoulder peak at 125.62 ppm resonates similarly to the CH=CH bonds of 2-methylimidazole at the same position of benzimidazole fragment. The alkoxy methyl group resonates at 51.36 ppm and the alkyl chain (n = 1) resonates at 39.12 ppm. For LeZIF8-E3$_{168h}$, due to the low conversion of ~1 % as shown in ^{1}H NMR spectroscopy the peaks for E3 ligand is difficult to identify. The peaks at 137.23 as solvent impurities. And the alkoxy ethyl group resonates at 63.5 and 33.13 ppm for (CH_2CH_3) respectively and the alkyl chain (n = 2) resonates between 36 - 46 ppm. For LeZIF8-E4, the alkoxy ethyl group resonates at 62.23 and 27.11 ppm for (CH_2CH_3) respectively and the alkyl chain (n = 3) resonates between 28 - 37 ppm. Distinct peaks for both the alkoxy ethyl carbons could not been seen clearly due to overlapping and having similar frequency as the alkyl chain and also due to transesterification that occur as observed in ^{1}H NMR where part of the alkoxy groups was transesterified. For LeZIF8-M5$_{168h}$, the alkoxy methyl group resonates at 52.83 for (CH_3) and the 4 peaks for the alkyl chain (n = 4) resonates between 26 - 38 ppm.

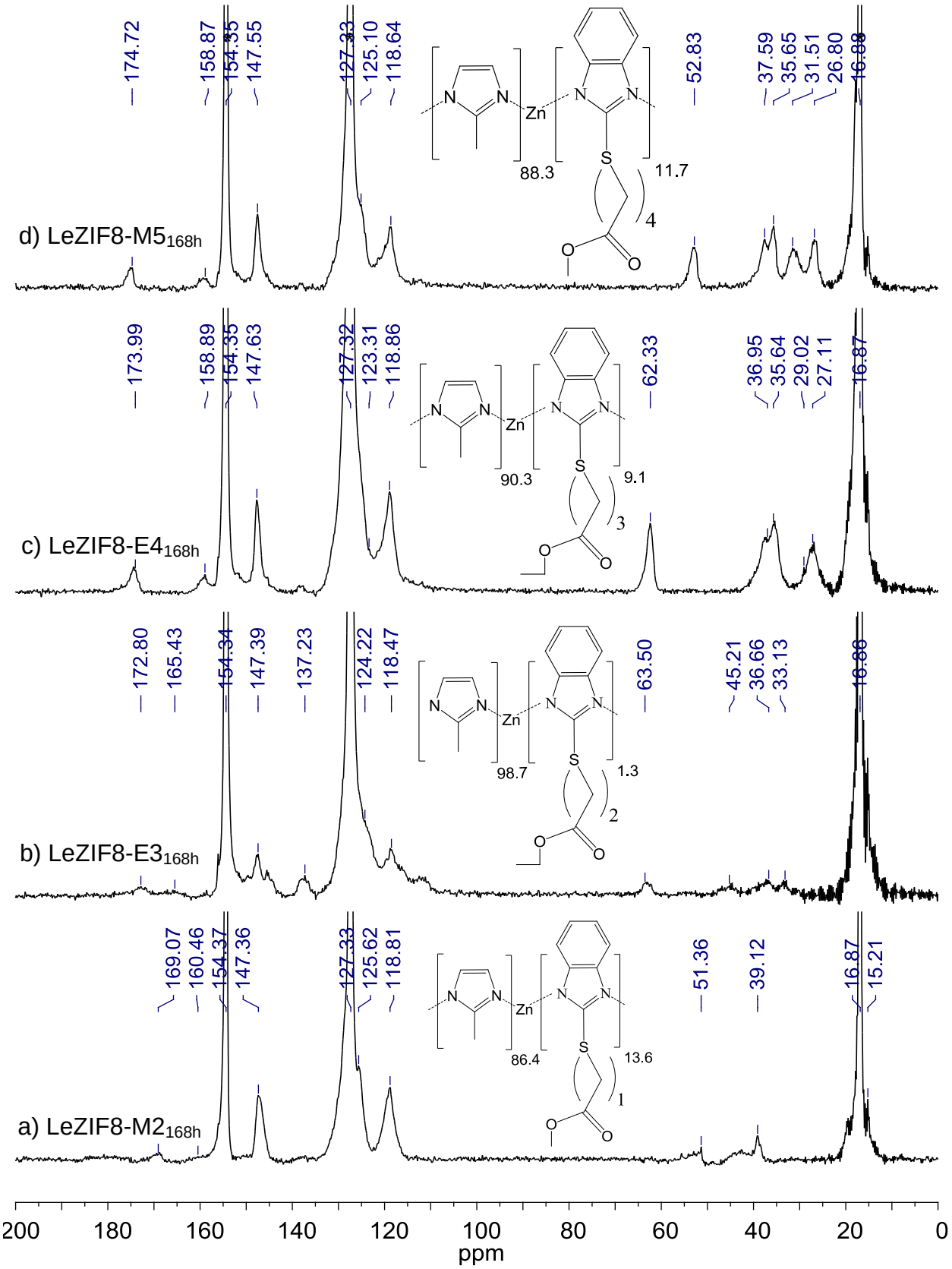

Figure 3.29 Solid-state ^{13}C NMR spectra of a) LeZIF8-M2$_{168h}$, b) LeZIF8-E3$_{168h}$, c) LeZIF8-E4$_{168h}$ and d) LeZIF8-M5$_{168h}$. 2-mehtylimidazole linker peaks are marked as (*).

The FTIR spectra of all the other LeZIF8-esters are found in (**Appendix A.2 to Appendix A.5**) As expected the FTIR spectra of LeZIF-8 esters obtained after 168 hours' exchange (**Figure 3.30, p 104**), show peaks that are similar to the starting material, nZIF-8_{1500} (**Figure 3.1, p 59**). In addition to these peaks are observed for the 2-mercaptobenimidazolate's ester functional groups: of all four compounds the C-O stretching at 1266 cm^{-1} and the C=O stretching frequency at 1738 cm^{-1} and the C-H stretch (~2900 cm^{-1}) for the methyl and ethyl groups as well as the alkyl chains.

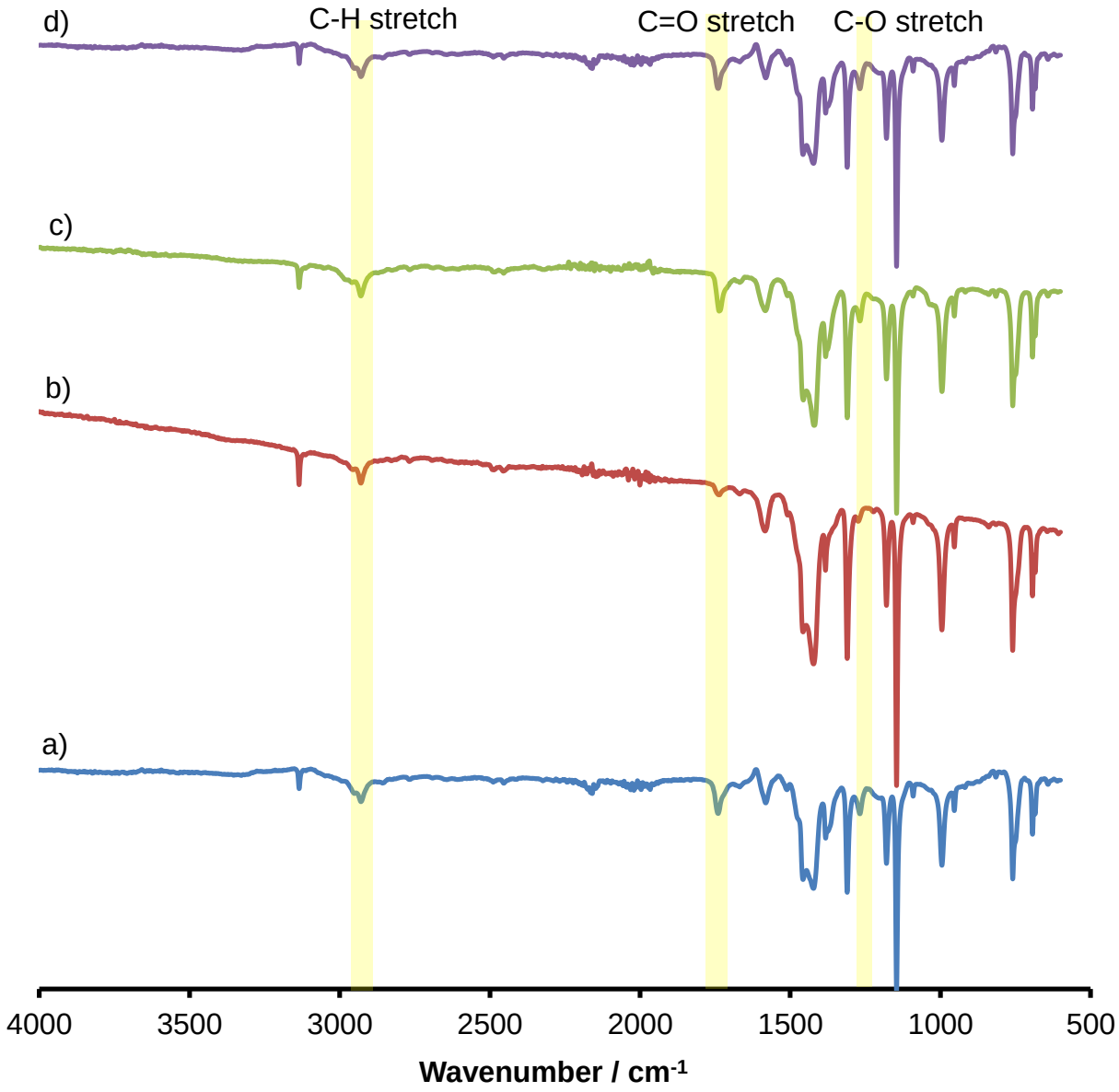

Figure 3.30 FTIR spectra of a) LeZIF8-$M2_{168h}$, b) LeZIF8-$E3_{168h}$, c) LeZIF8-$E4_{168h}$ and d) LeZIF8-$M5_{168h}$.

The PXRD pattern of each LeZIF8-ester obtained at 168 hours of exchange (**Figure 3.31, p 106**) are similar to the nZIF-8 starting material with peaks at 2θ: i) 7.5, ii) 10.5, iii) 12.9, iv) 14.8, v)

16.6 and vi) 18.2 °. The PXRD patterns of all the other LeZIF8-ester products can be found in **Appendix D.1** to **Appendix D.4**. In general, the structural integrity, SOD topology and crystallinity of the nZIF-8 starting material thus remained intact throughout the SALE process. The minimum particle size determined from the PXRD peaks ranges between 15 to 30 nm for all the samples, proof that the SALE process and different chain lengths of the ester ligand do not cause the particles to agglomerate or Ostwald ripening to occur.

The theoretical minimum particle sizes obtained by PXRD correlates well with the particle size measured from TEM images. The TEM images for each series of sample: LeZIF8-M2, b) LeZIF8-E3, c) LeZIF8-E4 and d) LeZIF8-M5 are shown in **Appendix C.2** to **Appendix C.5**. The images of the LeZIF8-esters exchanged for 168 hours are shown in **Figure 3.31 (p 106**). The particle sizes were measured by randomly choosing 100 particles to obtain an average. The particles maintained the spherical shape of the nZIF-8 starting material. The LeZIF8-ester particles all remain in the nano-range between 22 to 32 nm. The *S*-alkylation reactions during pre-synthetic modification of 2-mercaptoimidazole allow its functionalization with esters in high yield, resulting nanoparticles smaller than 50 nm After SALE. The ester chain length did not play a role in the exchange percentage or the particle size. Only 2-methylimidazolate linkers on the external surface area were exchanged as the benzimidazole-thioesters ligands are too bulky to diffuse into the nZIF-8 structure, thus reaching a maximum exchange of 13 %.

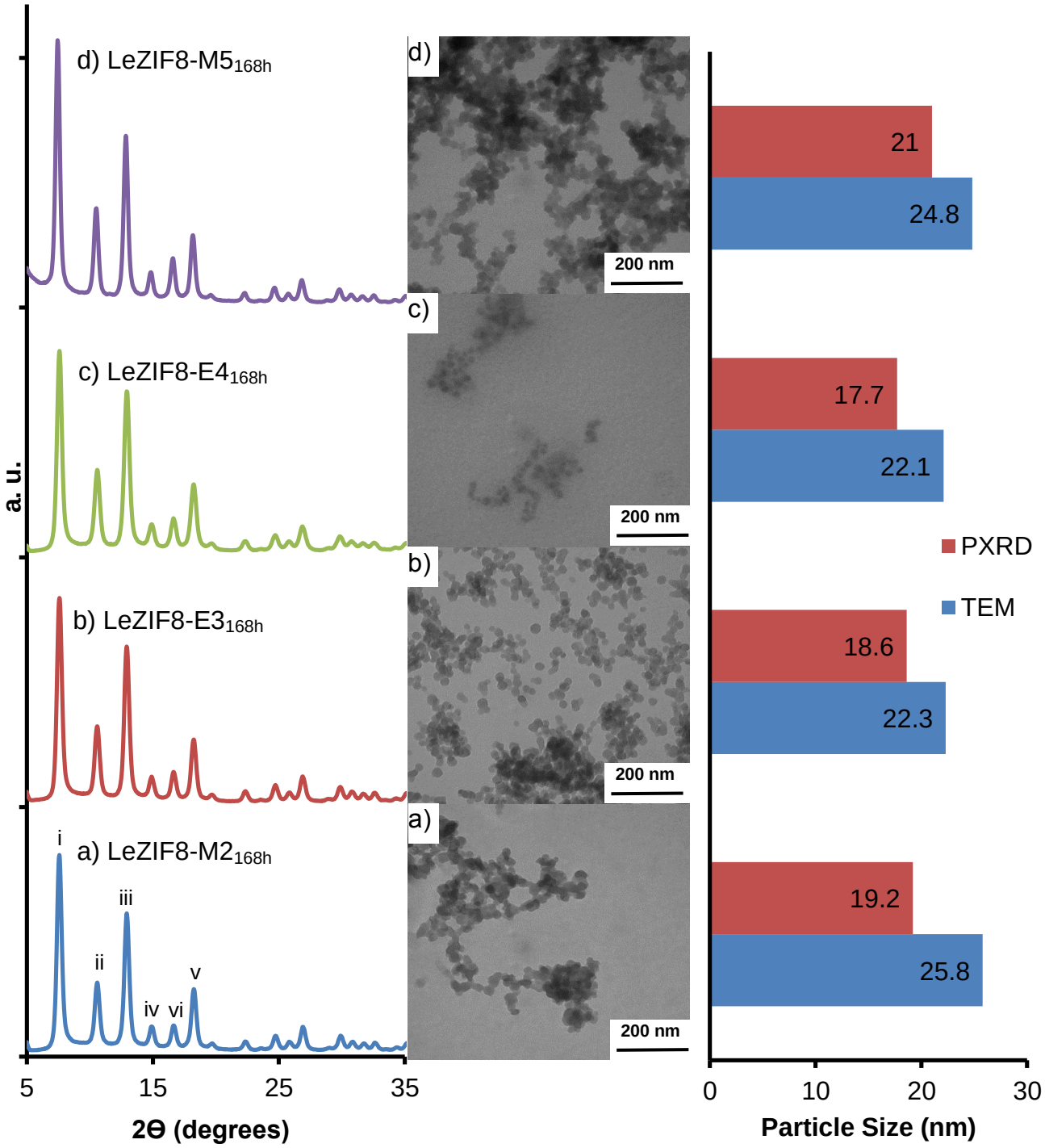

Figure 3.31 PXRD patterns (left) and TEM images (center) of a) LeZIF8-M2$_{168h}$, b) LeZIF8-E3$_{168h}$, c) LeZIF8-E4$_{168h}$ and d) LeZIF8-M5$_{168h}$. The relative particle size from PXRD and TEM are displayed on the right.

The LeZIF8-esters were activated at 150 ℃ for 16 hours prior to porosity analyses, giving typical Type-1 isotherms with nitrogen adsorption at 77 K: LeZIF8-M2 (**a**), LeZIF8-E3 (**b**), LeZIF8-E4 (**c**) and LeZIF8-M5 (**d**) are shown in (**Figure 3.32, p 107**) and the analysis summarized in **Table 3.8** (**p 108**). The nanoparticles remained microporous after SALE with benzimidazole-thioesters. The length of the alkyl chain in the benzimidazole-thioester linkers did

not affect the porosity of the materials. The amount of N_2 adsorbed did show a significant decrease as the exchange percentages increased, except for LeZIF8-E3 where the exchange percentages remained below 1.9 %.

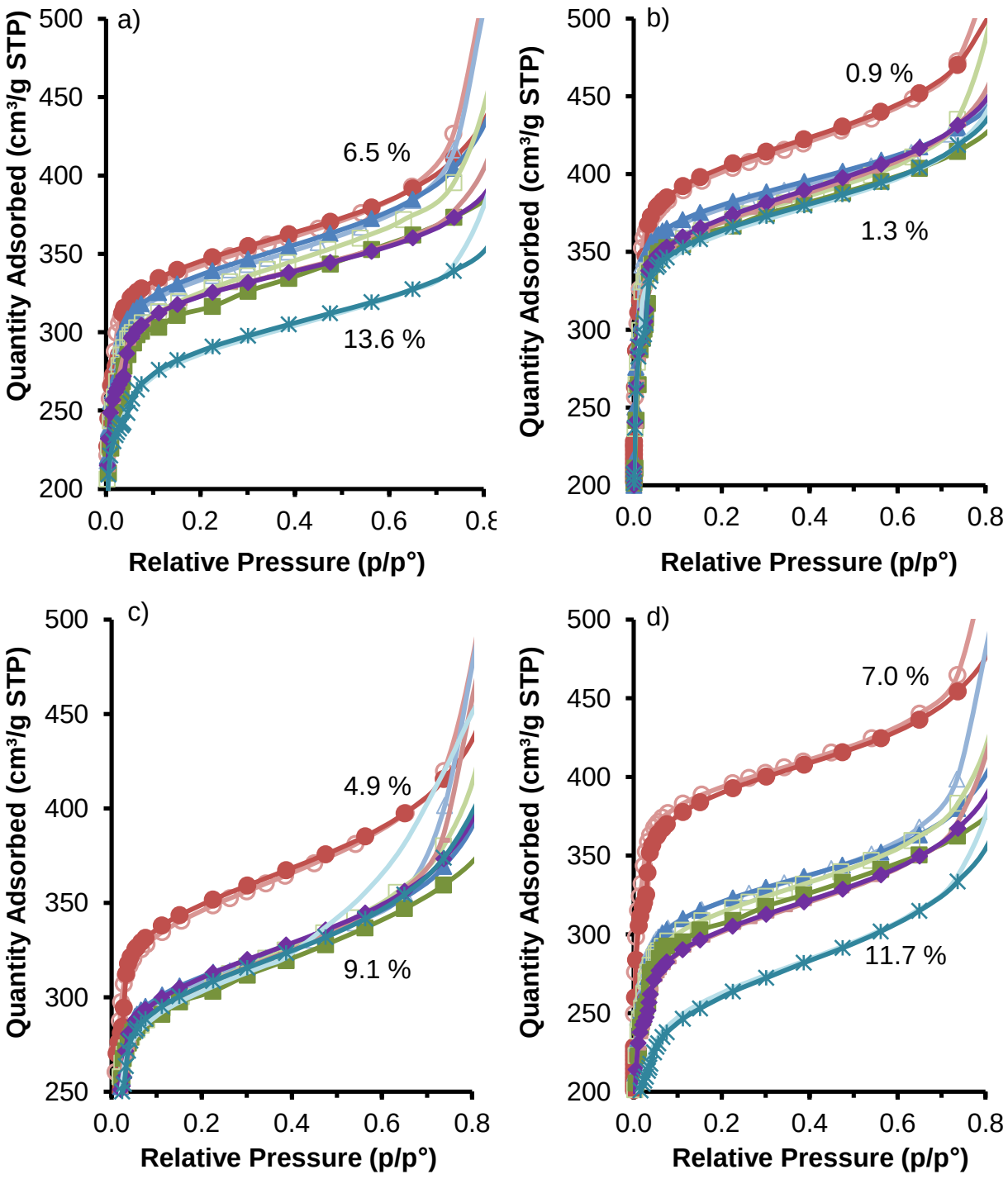

Figure 3.32 Nitrogen adsorption and desorption isotherms at 77 K of a) LeZIF8-M2, b) LeZIF8-E3, c) LeZIF8-E4 and d) LeZIF8-M5 obtained after different SALE times: 4 (red), 16 (blue), 24 (green), 72 (purple) and 168 (turquoise) hours. Adsorption marked as solid and desorption as hollow symbols. Exchange percentages are given in brackets.

The BET surface area of the nZIF-8 starting material (>1600 $m^2 g^{-1}$) decrease significantly after SALE with the benzimidazole-thioesters. After an exchange of > 10 % , the BET surface area shrunk by more than 500 $m^2 g^{-1}$ compared to the original nZIF-8. This is accompanied by a decrease in micropore volume from ~0.45 to ~0.3 $cm^3 g^{-1}$ (**Table 3.8, p 108**). The change in BET surface area however, did not alter the t-plot external surface area which stayed relatively constant around ~ 300 $m^2 g^{-1}$, due to the particle sizes remaining between 22 to 32 nm in diameter during the SALE process.

Table 3.8 N_2 porosity analyses at 77 K of LeZIF8-M2, LeZIF8-E3, LeZIF8-E4 and LeZIF8-M5 obtained after SALE of nZIF-8 with benzimidazole-thioesters using different exchange times. Exchange percentage are given in brackets. Quantities adsorbed were measured at 0.8 p/p°.

Exchange (%)	Quantity Adsorbed/ $cm^3 g^{-1}$	BET Surface Area/ $m^2 g^{-1}$	t-plot External Surface Area/ $m^2 g^{-1}$	Micropore volume/ $cm^3 g^{-1}$
LeZIF8-$M2_{168h}$ (13.6)	349	1042	297	0.315
LeZIF8-$M2_{72h}$ (9.5)	390	1187	263	0.383
LeZIF8-$M2_{24h}$ (8.4)	407	1232	292	0.370
LeZIF8-$M2_{16h}$ (7.3)	434	1307	282	0.396
LeZIF8-$M2_{4h}$ (6.5)	426	1350	289	0.407
LeZIF8-$E3_{168h}$ (1.3)	436	1434	321	0.424
LeZIF8-$E3_{72h}$ (1.3)	441	1476	304	0.441
LeZIF8-$E3_{24h}$ (1.9)	454	1492	295	0.446
LeZIF8-$E3_{16h}$ (1.4)	455	1528	274	0.469
LeZIF8-$E3_{4h}$ (0.9)	495	1598	315	0.487
LeZIF8-$E4_{168h}$ (9.1)	394	1174	269	0.355
LeZIF8-$E4_{72h}$ (9.1)	396	1188	282	0.356
LeZIF8-$E4_{24h}$ (8.9)	400	1222	285	0.352
LeZIF8-$E4_{16h}$ (7.6)	387	1226	293	0.354
LeZIF8-$E4_{4h}$ (4.9)	439	1385	276	0.418
LeZIF8-$M5_{168h}$ (11.7)	355	943	320	0.260
LeZIF8-$M5_{72h}$ (10.0)	394	1132	299	0.336
LeZIF8-$M5_{24h}$ (9.1)	409	1205	300	0.355
LeZIF8-$M5_{16h}$ (8.6)	395	1239	268	0.378
LeZIF8-$M5_{4h}$ (7.0)	465	1516	301	0.470

The TGA thermograms of LeZIF8-M2, LeZIF8-E3, LeZIF8-E4 and LeZIF8-M5 for 4 and 168 hours' exchange times are shown in **Figure 3.33** (**p 110**) while the thermograms for the other exchange times can be found in (**Appendix E.1** to **Appendix E.4**). In most cases, the exchanged ZIF-8 thermograms show a 3-step process: step 2 starts at ~400 ℃ with a mass loss of ~20 % associated with the decomposition of nZIF-8 backbone and the thermal collapse of the nZIF-8 structure, followed by a continued gradual loss of mass loss after 600 ℃ (step 3) for all samples. Step 1 for LeZIF8-M2 (**a** and **b**) at 330 ℃ with a mass loss increasing from 3 % (**a**) – 6 % (**b**) is associated with the decomposition of the newly exchanged M2 linker. The LeZIF8-E3 (**c** and **d**) does not have this first step, due to the low exchange percentage of the E3 linker. The LeZIF8-E4 (**e** and **f**) and LeZIF8-M5 (**g** and **h**) products, with higher exchange percentages, have a first step mass loss between 6 – 9.7 % and 7.4 – 11 % respectively. An increased exchange percentage, thus led to a higher mass loss. SALE introduced linkers with longer alkyl chains (E4 and M5) lowered the thermal stability from 330 ℃ (LeZIF8-M2) to ~180 ℃ (LeZIF8-E4 and LeZIF8-M5). Longer alkyl chains in the linker thus induced lower thermal stability than short ones. The newly exchanged benzimidazole-thioesters linkers lead to lower decomposition temperatures than that of the nZIF-8 backbone structure, which only decomposes at 450 ℃.

Since the exceptional stability of ZIF-8 in basic environments are well known (**Chapter 2.3.5**), a stability test was performed on the SALE product, LeZIF8-E4$_{24h}$, where nZIF-8 was exchanged with ethyl benzimidazole-2-ylthio butyrate. After LeZIF8-E4$_{24h}$ was refluxed in aqueous 2M NaOH solution for 24 hours, 62 % of the particles were recovered and analysed with PXRD (**Figure 3.34.a, p 110**). The pattern obtained show that LeZIF8-E4$_{24h}$ has the same SOD topology as before the test, with a particle size of 25 nm, ~10 nm larger, than at the start. Digestive ^{1}H NMR (**Figure 3.34.b, p 110**) revealed that the 2-methylimdiazole linkers remained, but that the benzimidazole-thioesters linkers, introduced through SALE, were etched from the external surface. The exchange percentages of the benzimidazole-thioesters decreased from 8.9 % to less than 1 %.

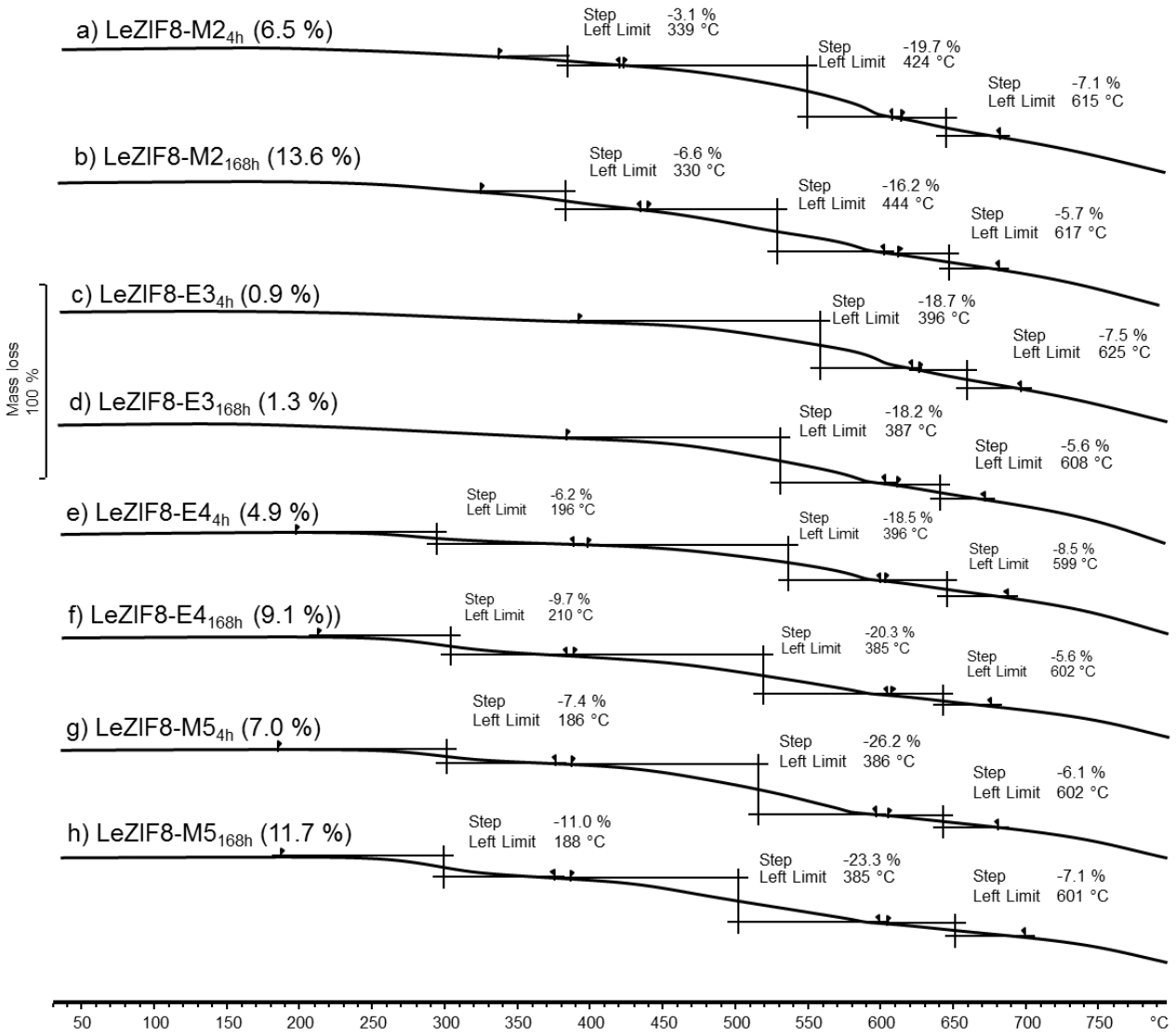

Figure 3.33 TGA thermogram in N_2 of LeZIF8-M2, LeZIF8-E3, LeZIF8-E4 and LeZIF8-M5 products from SALE of nZIF-8 with benzimidazole-thioesters for different exchange times: 4 and 168 hours. Exchange percentages in brackets.

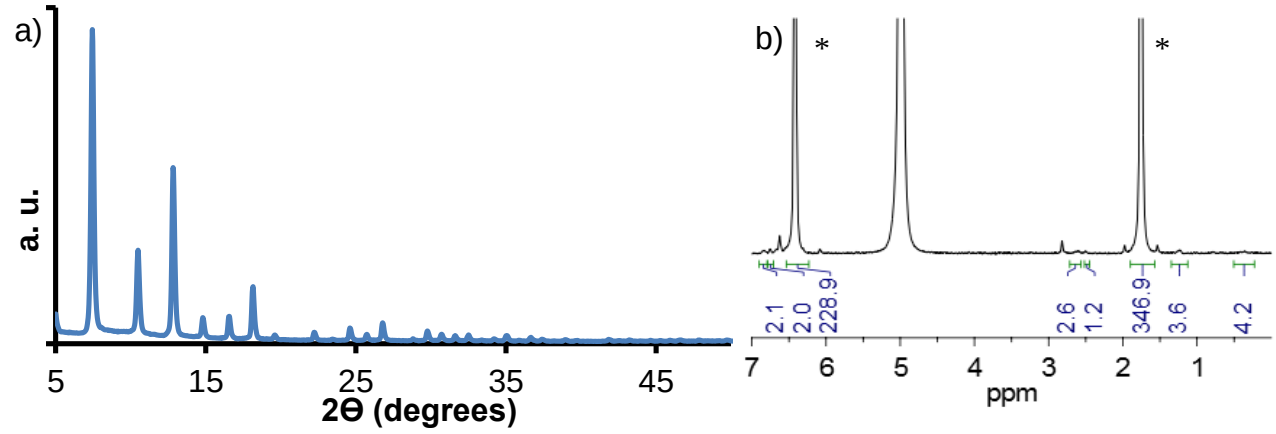

Figure 3.34 Analyses of LeZIF8-E4$_{24}$ after reflux in an aqueous 2M NaOH solution: PXRD (a) and (b) ^{1}H NMR. 2-Methylimidazole proton peaks marked by (*).

3.3.3 Time Resolved SALE of 2-Aminobenzimidazole

Amines are important functional groups, with a lone electron pair, to add functionality on the external surface area of nZIF-8 materials by post synthetic modification (PSM). Amine groups are known in typical reactions to form imines, amides and acylation with alkyl halides. In this section 2-aminobenzimidazole will be exchanged with the 2-methylimdiazolate linkers of nZIF-8 *via* the solvent assisted ligand exchange (SALE) process modified from (**Chapter 3.3.1, p 82**) (**Scheme 3.9, p 111**).

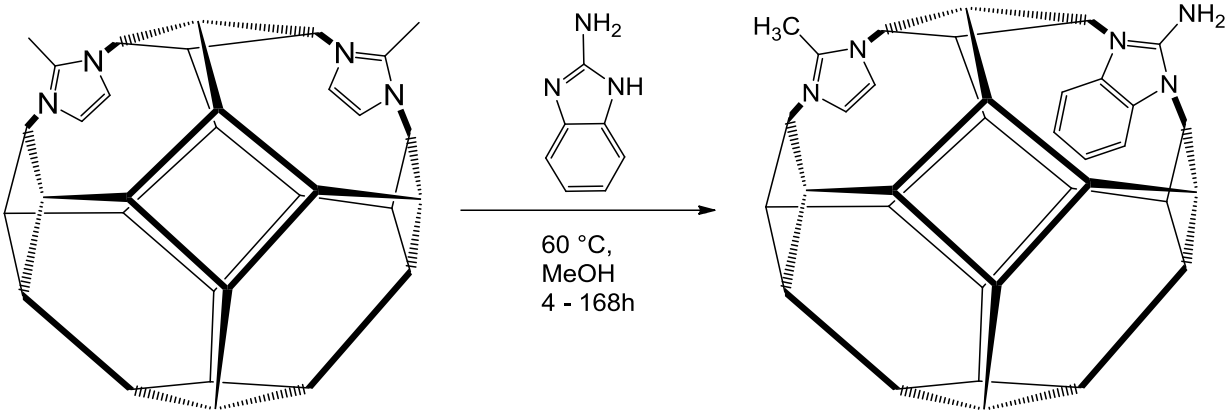

Scheme 3.9 Time resolved solvent assisted ligand exchange (SALE) of nZIF-8 with 2-aminobenzimidazole at 60 °C for 4, 16 and 168 hours.

In a typical reaction, 3 time excess 2-aminobenzimidazole in methanol was added to an nZIF-8 suspension in methanol, in a Teflon tube which was capped and heated under isothermal conditions (60 °C) at different time intervals of 4, 16 and 168 hours. The products, denoted as nZIF8-NH_2BzIm were obtained after work up as light brown powders with yields above 95 %. The basicity of amines did not breakdown the nZIF-8 structure as observed with the slightly acidic 2-mercaptobenzimidazole (**Chapter 3.3.2.1, p 94**). The exchange percentages was determined by digestive ^{1}H NMR, and can be seen in **Table 3.9** (**p 111**).

Table 3.9 LeZIF8-NH_2BzIm products from SALE of nZIF-8 (1.306 mmol) with 2-aminobenzimdazole (4.08 mmol) in methanol at various synthesis times. Exchange percentages were determined by ^{1}H NMR in D_2O/D_2SO_4.

Compound	Exchange time/ h	Yield/ %	Exchange/ %
LeZIF8-NH_2BzIm$_{168h}$	168	100	16
LeZIF8-NH_2BzIm$_{16h}$	16	98	10
LeZIF8-NH_2BzIm$_{4h}$	4	96	5

Digestive ^{1}H NMR spectra of LeZIF8-NH_2BzIm$_{4h}$ (**Appendix B.7**), LeZIF8-NH_2BzIm$_{16h}$ (**Figure 3.35.a, p 113**), LeZIF8-NH_2BzIm$_{168h}$ (**Appendix B.7**) were obtained on the 600 MHz resolutions. The 2-methylimidazolate resonates protons at 1.77 and 6.43 ppm for CH_3 and CH=CH respectively (*). The SALE introduced 2-aminobenzimidazolate protons resonate as multiplets at 6.40 and 6.47 ppm for the benzyl ring. The integration of the CH=CH protons of the 2-methylimidazolte linkers and these benzyl protons were used to calculate the exchange percentages summarised in **Table 3.9** (**p 111**). Similarly, to the previous SALE compounds, the LeZIF8-NH_2BzIm product reached an exchange of 5 % within 4 hours which steadily rose to 10 % after 16 hours, and reached a maximum of 16 % after 168 hours. This proves, as in the SALE with 2-mercaptobenzimidazole, that the benzyl ring adds enough bulkiness to the linker to prevent diffusion of the ligands into the pores. It is thus difficult to achieve a higher exchange than 16 %.

The LeZIF8-NH_2BzIm products remained crystalline and could be easily characterised with Solid-state ^{13}C NMR, as seen in **Figure 3.35.b** (**p 113**) for the exchange times of 4h (red), 16h (green) and 168h (blue). The 2-methylimidazolate peaks marked with (*), are at 16.87, 127.34 and 154.36 ppm for CH_3, CH=CH and N-C-N carbon atoms respectively. The 2-aminobenzimdazolate linkers gave peaks at 115.56, 123.66 and 145.36 ppm from the resonance of the carbon atoms of the aromatic ring and at 164.30 ppm for the resonance of the amino carbon atoms at the C2 position. In **Figure 3.35.b** (**p 113**) a systematic rise of the peaks for the aromatic carbon atoms was observed as ligand exchange times increased. As the ligand exchange time increased, from 4 to 168h the peak intensity increased up to three times corresponding well with the exchange percentages obtained by ^{1}H NMR of 5 and 16 % respectively.

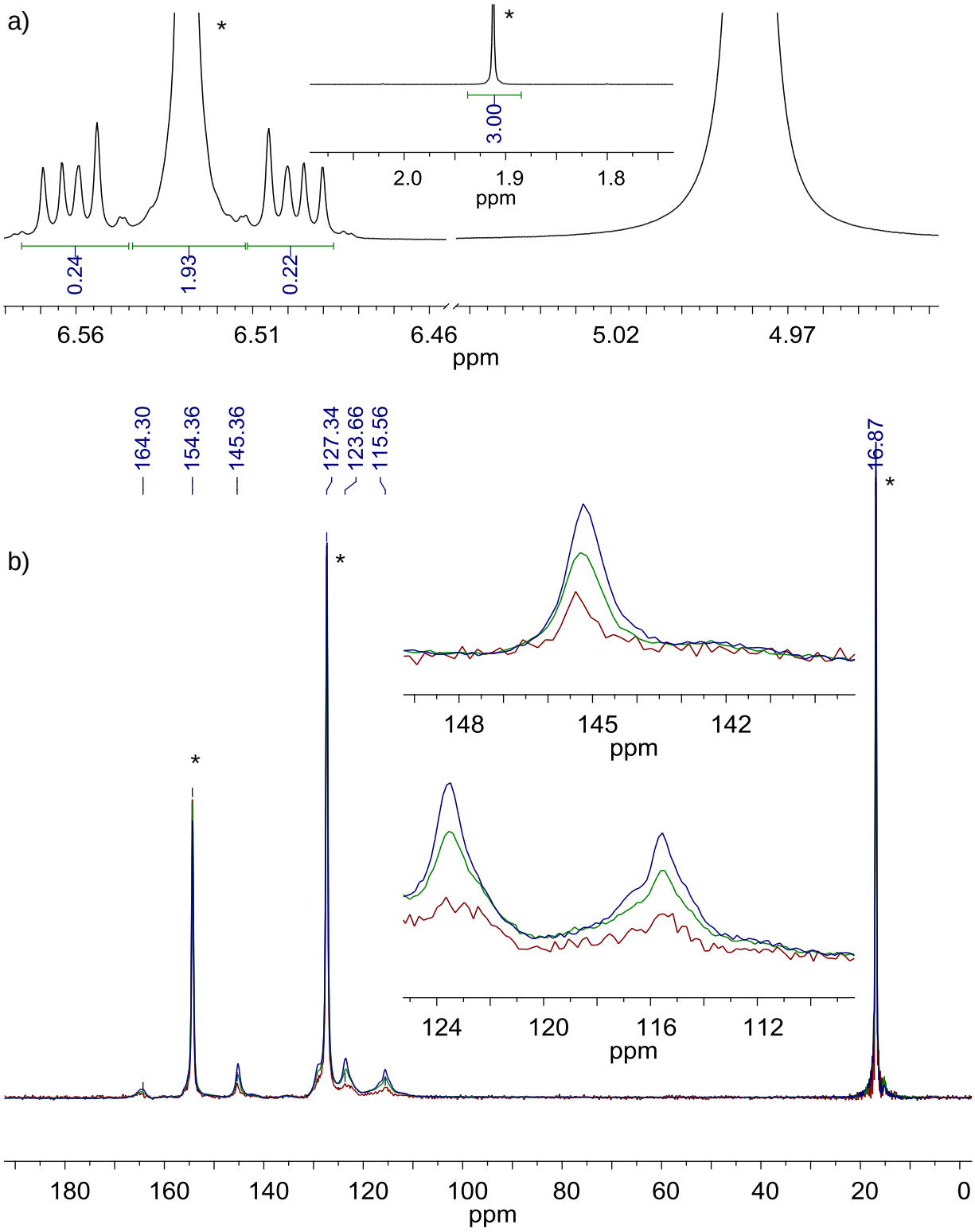

Figure 3.35 a) Digestive ^{1}H NMR spectra of LeZIF8-NH_2BzIm$_{16h}$ digested in D_2O/D_2SO_4 (9:1) and b) Solid-state ^{13}C NMR of LeZIF8-NH_2BzIm$_{4h}$ (red), LeZIF8-NH_2BzIm$_{16h}$ (green) and LeZIF8-NH_2BzIm$_{168h}$ (blue) obtained after SALE of nZIF-8 with 2-aminobenzimdazole in methanol after 16h. 2-Methylimidazole proton and carbon resonances marked with (*).

The FTIR spectra of LeZIF8-NH_2BzIm$_{168h}$ (**Figure 3.36, p 114**), as well as 4 and 16 h products (**Appendix A.6**) are similar to that of the nZIF-8 starting material (**Chapter 3.2.1, p 57**). The absence of a broad N-H stretching frequency indicates that both 2-methylimidazole and 2-aminobenzimidazole are bound to the zinc cations in the structure. In addition, vibration frequencies of the functional groups of 2-aminobenzimidazole are present: C=C aromatic stretching at 1480 cm^{-1} (i), the primary amine N-H stretching frequencies on the C2 position as two peaks at 3361 cm^{-1} (ii) and 3437 cm^{-1} (iii) and the N-H bend at 1626 cm^{-1} (iv).

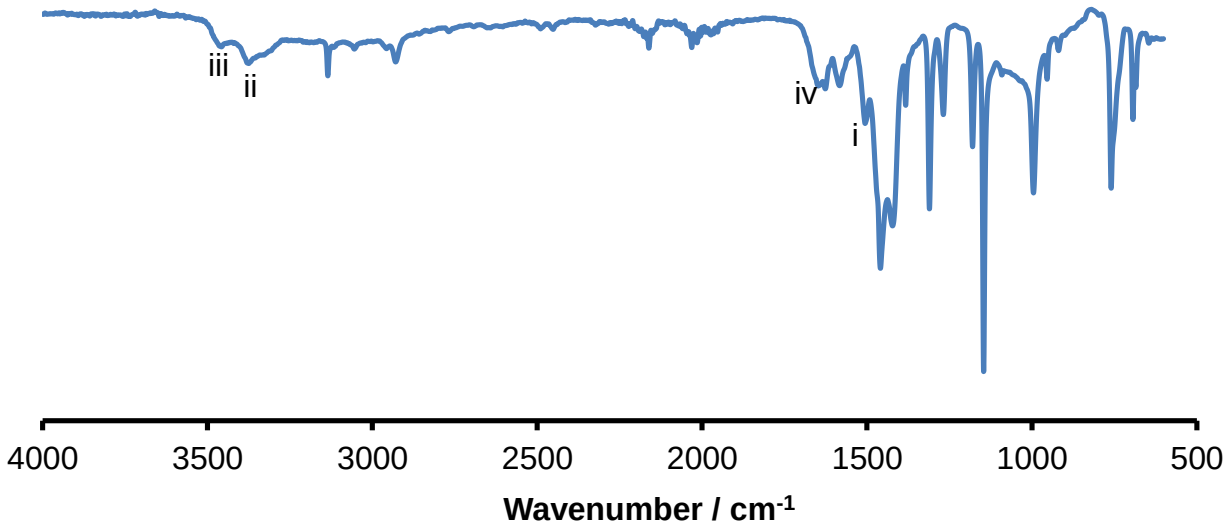

Figure 3.36 FTIR spectrum of LeZIF8-NH_2BzIm$_{168h}$.

From its PXRD pattern, it is seen that the topology of the LeZIF8-NH_2BzIm (**Figure 3.37, p 115**) remains intact and identical pattern (with the three mains peaks at: 7.43 (i), 10.42 (ii) and 12.8 (iii) °) to the SOD topology starting material, nZIF-8, after SALE with 2-aminobenzimidazole. The minimum particle sizes obtained from the PXRD patters (**Figure 3.37, p 115**) suggest that the nanoparticles had no significant increases in size. Only when the exchange time was increased to 168 hours, the minimum particle size was ~5 nm larger due to agglomeration or Ostwald ripening during the long SALE process. The actual particle sizes were determined from the TEM images of LeZIF8-NH_2BzIm after 4 hours (22.7 nm) and 168 hours (23.2 nm) of exchange (**Figure 3.38, p 115**) and after 16 hours (22.0 nm) in (**Appendix C.6**). The particle sizes remain consistent at ~22 nm throughout the exchange process. The values obtained by TEM correlate with those from PXRD.

For the 2-mercaptobenzimidazole exchange (**Section 3.3.2.1, p 94**), it was observed that the particle size increased to 174 nm. The thiol group on the C2, thus affected the particle size during the SALE process, while the amine group in the same position had no such effect with the particles remaining at ~22 nm.

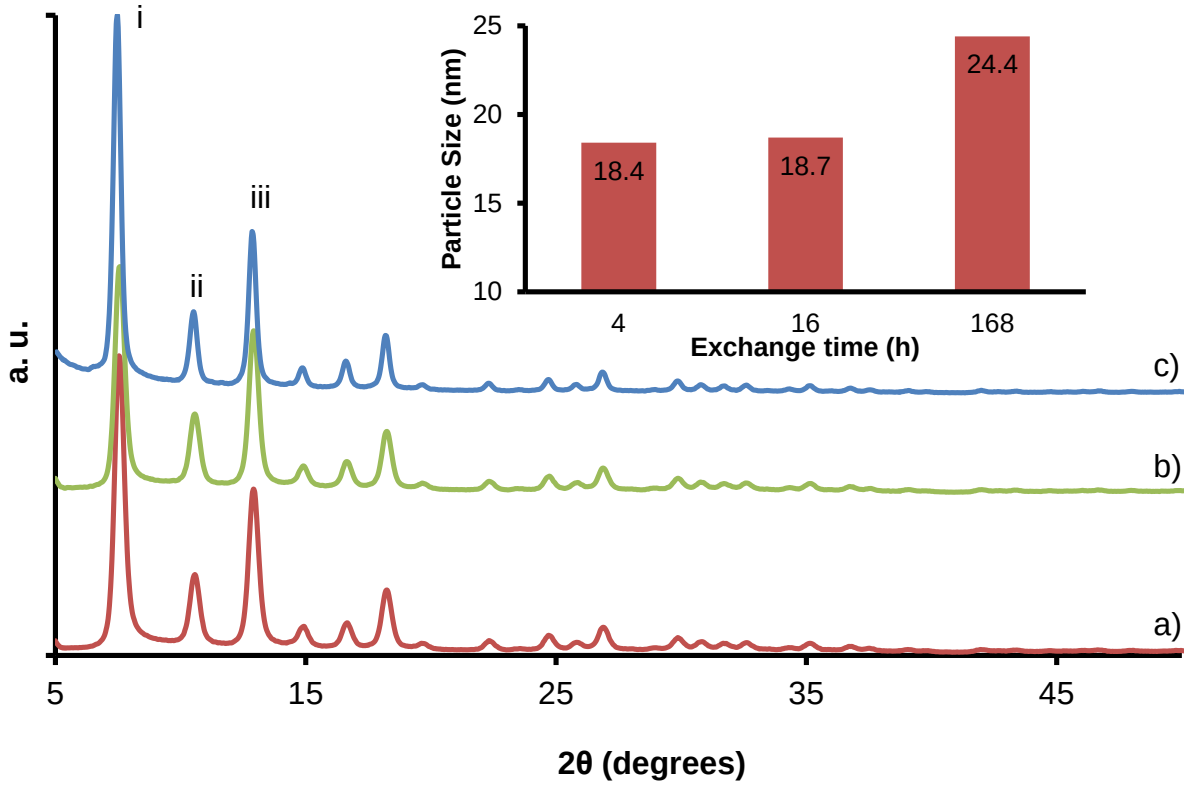

Figure 3.37 PXRD patterns of LeZIF8-NH_2BzIm products from SALE of nZIF-8 with 2-aminobenzimidazole in methanol at different exchange times: a) 4h, b) 16h and c) 168h. The insert show the relative particle size from PXRD.

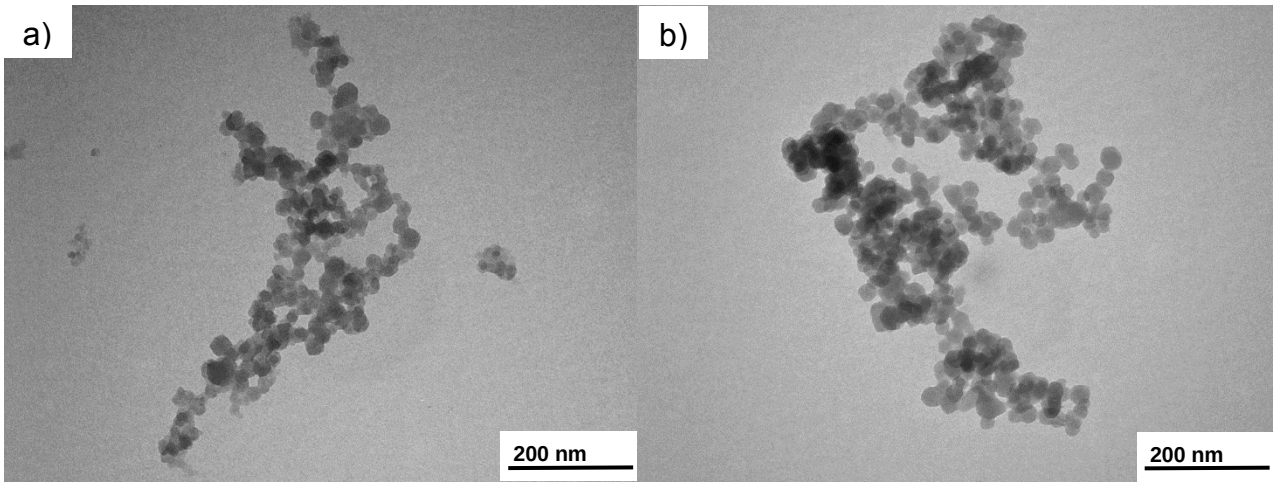

Figure 3.38 TEM images of LeZIF8-NH_2BzIm products from SALE of nZIF-8 with 2-aminobenzimidazole in methanol at different exchange times: a) 4h and b) 168h.

Type-1 isotherms were obtained after the porosity analyses of the activated LeZIF8-NH_2BzIm products from the SALE of nZIF-8 with 2-aminobenzimidazole for 4, 16 and 168 hours (**Figure 3.39, p 116**). The materials are thus microporous and maintain their porosity after SALE. The

quantity of nitrogen adsorbed remains high after 4 hours with a maximum adsorption of 469 cm^{-3} g^{-1} at 0.8 p/p° (**a**) after a conversion of 5 %, but decreased slightly at higher exchange percentages (**Table 3.10, p 117**).

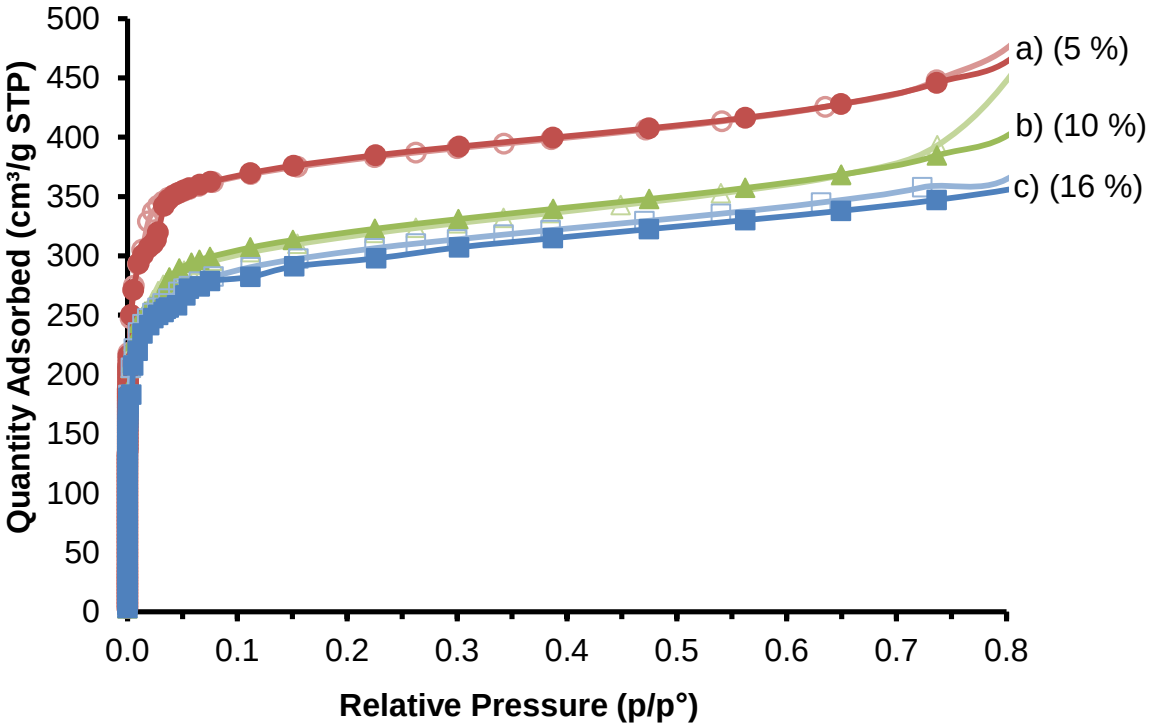

Figure 3.39 Nitrogen adsorption and desorption (at 77 K) isotherm of LeZIF8-NH_2BzIm products from the SALE of nZIF-8 with 2-aminobenzimidazole at different exchange times: a) 4 (red), b) 16 (blue) and c) 168 (green) hours. Adsorption marked as solids and desorption as hollow symbols. Exchange percentages are given in brackets.

The BET surface areas (**Table 3.10, p 117**) decreased from 1600 m^2 g^{-1} (nZIF-8) to 1108 m^2 g^{-1} as the exchange percentages increased to 16 %. Similarly, a decrease in the micropore volume from 0.47 cm^3 g^{-1} (nZIF-8) to 0.33 cm^3 g^{-1} was observed. This decrease in porosity can be attributed to the presence of the newly introduced benzimidazolate linker.[18] The t-plot external surface area was not affected during SALE and remained similar to that of the nZIF-8 starting material, at ~320 m^2 g^{-1} for all SALE times, corresponding to the constant particle size (~22 nm) obtained at different SALE times.

Table 3.10 N_2 porosity analyses at 77 K of LeZIF8-NH_2BzIm products obtained after SALE of nZIF-8 with 2-aminobenzimidazole at exchange times. Exchange percentages are written in brackets. Quantities adsorbed were measured at 0.8 p/p°.

Compound (Exchange %)	Quantity Adsorbed/ $cm^3\ g^{-1}$	BET Surface Area/ $m^2\ g^{-1}$	t-plot External Surface Area/ $m^2\ g^{-1}$	Micropore volume/ $cm^3\ g^{-1}$
LeZIF8-NH_2BzIm$_{4h}$ (5)	469	1523	325	0.441
LeZIF8-NH_2BzIm$_{16h}$ (10)	418	1216	318	0.350
LeZIF8-NH_2BzIm$_{168h}$ (16)	359	1108	320	0.330

The TGA thermogram of the LeZIF8-NH_2BzIm products (**Figure 3.40, p 117**) all show two mass loss steps. During the first step at ~250 °C, a mass loss of 7 %, 7.9 % and 8.8 % was observed for 4, 16, and 168h exchange times respectively. This step increased with the amount of exchange with the 2-aminobenzimidazole from 5 till 16 %, and can thus be attributed to the decomposition of this linker. The remaining nZIF-8 structure thermally collapse at 450 °C with a mass loss of 20 % shown by the second step.

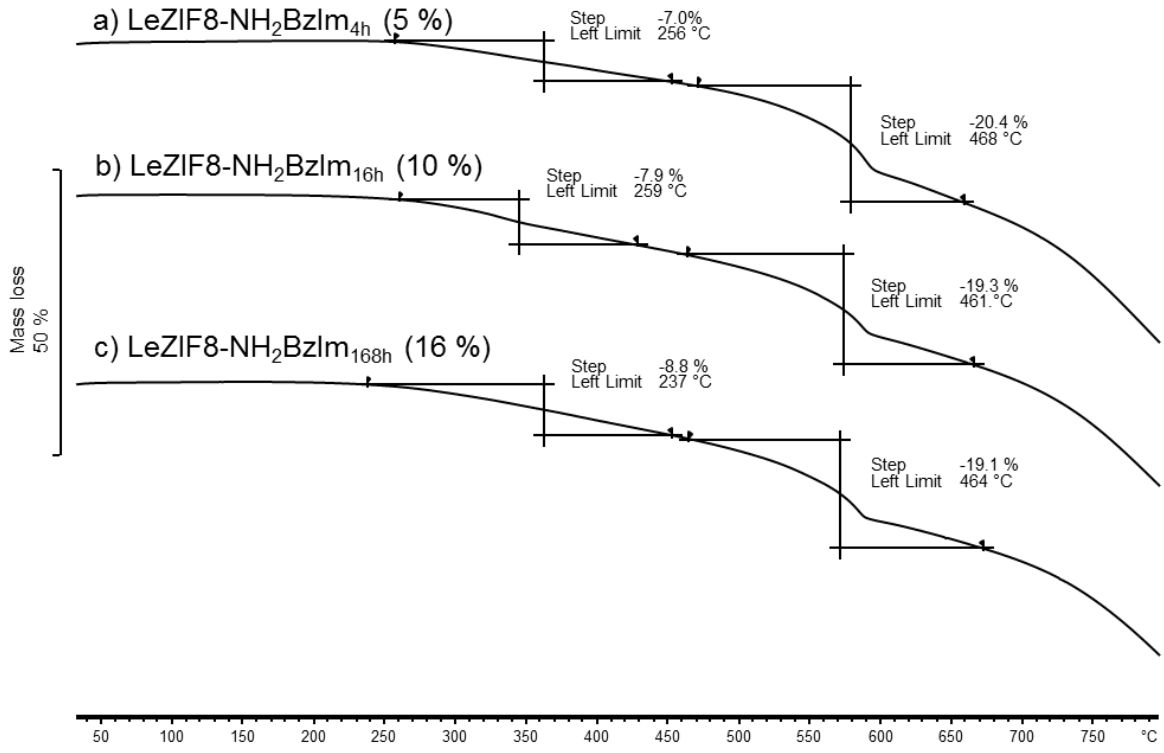

Figure 3.40 TGA thermograms (under N_2) of LeZIF8-NH_2BzIm products from SALE of nZIF-8 with 2-aminobenzimidazole in methanol at exchange times: a) 4h, b) 16h and c) 168h. Exchange percentages in brackets.

3.3.4 Other Imidazolate Ligands

The SALE behaviour of different functional groups at the C2 position of imidazole was investigated for gas storage applications. Imidazole with NO_2 and phenyl groups on the C2 position were employed in SALE with nZIF-8 (**Scheme 3.10, p 118**) *via* modified procedures from **Chapter 3.3.1 (p 82**).

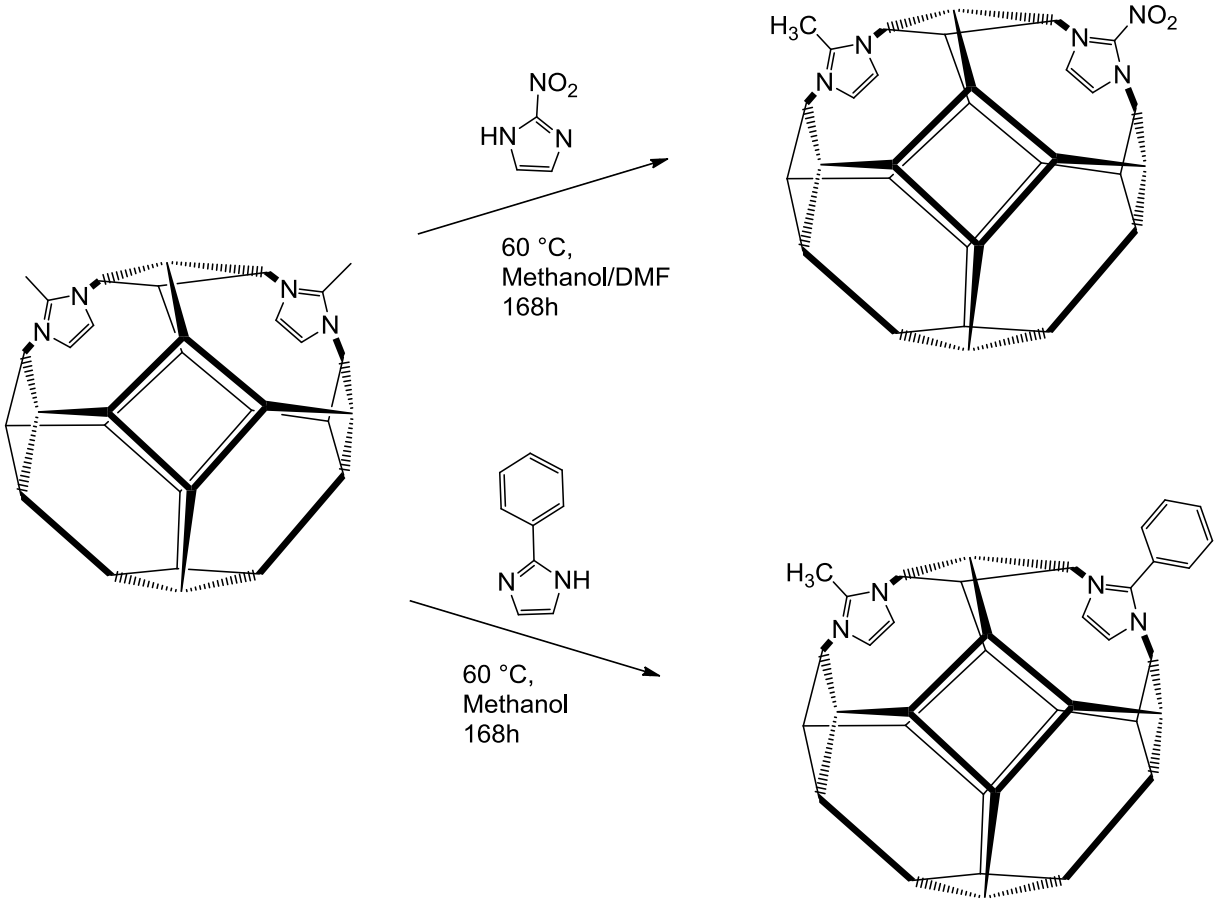

Scheme 3.10 Time resolved solvent assisted ligand exchange (SALE) of nZIF-8 with 2-nitroimidazole at 60 °C for 168 hours in a methanol and DMF mixture (top) and with 2-phenylimidazole at 60 °C for 168 hours in methanol (bottom).

The SALE process of 2-nitroimidazole was performed by suspending nZIF-8 in methanol. The suspension was transferred into a Teflon tube and the 3 times excess 2-nitroimidazole in a methanol/DMF solution (50 cm^3) solution was added. The 2-nitroimidazole was insoluble in methanol, therefore DMF was used in a 1:1 ratio. The solution was heated under isothermal conditions at 60 °C for 168 hours. The product, denoted as LeZIF8-NO_2Im were obtained after work up and activation as a light yellow powder with a yield of 57 %.

The same procedure (**Chapter 3.3.3, p 111)** was followed with 2-phenylimidazole, easily soluble in methanol. The mixture was heated to 60 °C for 168 hours to give LeZIF8-PhIm after

workup and activation as a white powder with a yield of 98 %. Both LeZIF8-NO_2Im_{168h} and LeZIF8-$PhIm_{168h}$ are stable in atmospheric conditions.

The digestive ^1H NMR spectra for LeZIF8-NO_2Im_{168h} (**Figure 3.41.a, p 119**), LeZIF8-$PhIm_{168h}$ (**Figure 3.41.b, p 119**) both display the distinct peaks of 2-methylimidazole at 1.67 and 6.33 ppm for the CH_3 and CH=CH protons respectively. The 2-nitroimidazole linker of the LeZIF8-NO_2Im_{168h} was partially soluble after digestion, enough to be detected by ^1H NMR, but the low solubility caused the signals for the two protons to be extremely weak at 6.75 ppm (**Figure 3.41.a, p 119**). The exchange percentage could not be calculated effectively. Solid-state ^{13}C NMR was then used to estimate the amount of exchange. For the LeZIF8-$PhIm_{168h}$ additional peaks for the phenyl protons were observed: a doublet at 6.8 ppm for the ortho position protons, a multiplet at 6.9 for meta position protons and a peak at 7.1 ppm for the para position protons. The CH=CH protons of 2-phenylimidazole, with the same chemical environment as the CH=CH protons of 2-methylimidazole, have a peak overlap at 6.3 ppm. The integration of the CH=CH protons and the ortho position protons was used to calculate the exchange percentage of 10.3 % after 168 hours of exchange.

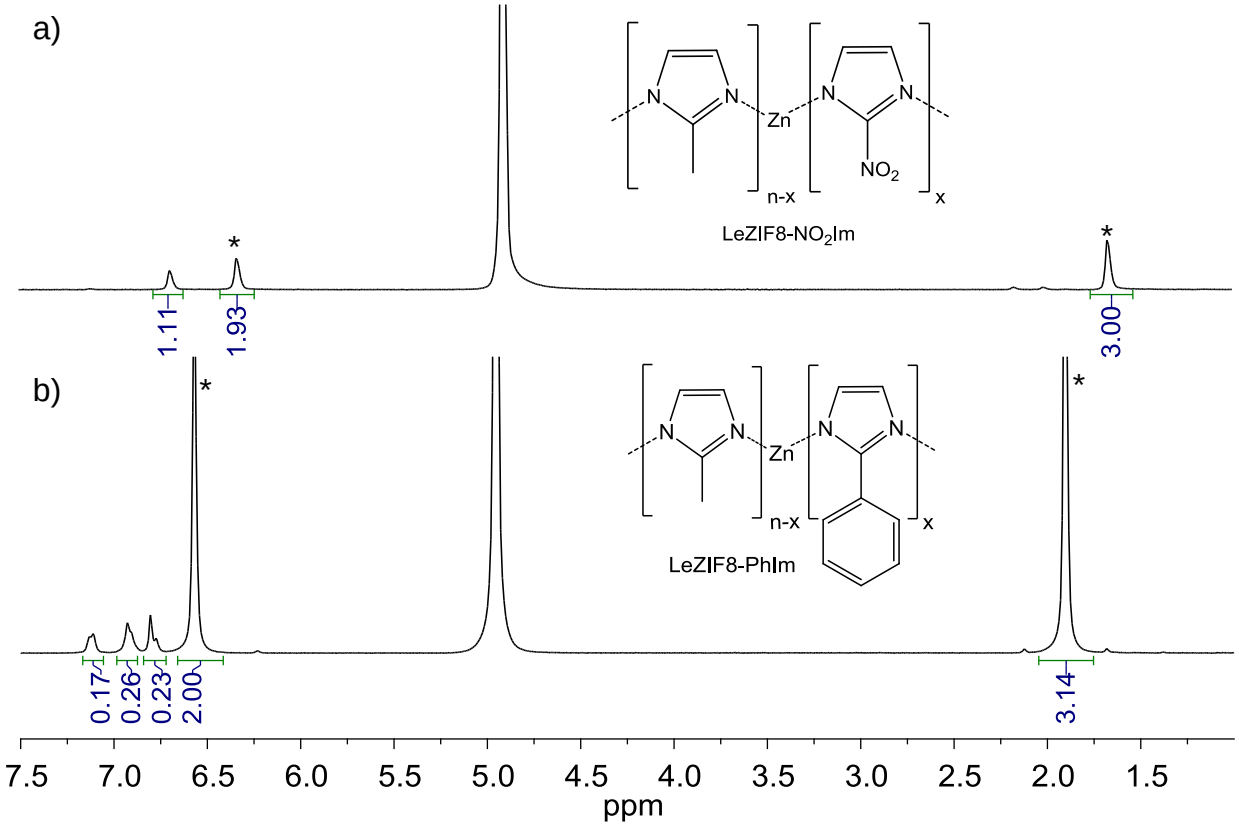

Figure 3.41 ^1H NMR spectrum of a) LeZIF8-NO_2Im_{168h} and b) LeZIF8-$PhIm_{168h}$. Digested in D_2O/D_2SO_4 (9:1). 2-methylimidazole marked with (*).

Solid-state ^{13}C NMR on LeZIF8-NO_2Im_{168h} (**Figure 3.42.a, p 120**) gave broad peaks, suggesting a loss of crystallinity with the formation of partially amorphous materials during SALE. The carbon integration ratio of these peaks was then used to estimate the exchange percentage. The integration of the CH=CH carbon atoms of both the 2-methylimidazole and 2-nitroimidizole were used to calculate the exchange percentage of 66.6 % for LeZIF8-NO_2Im_{168h}. Both products show the distinct peaks for the carbon atoms of 2-methylimidazole at 16.6, 126.7 and 154.1 ppm for CH_3, CH=CH and N-C-N respectively (marked with (*)). The carbon atoms of the 2-nitroimidazolate linker of LeZIF8-NO_2Im_{168h} are at 135.16 and 131.25 ppm for the CH=CH and C-NO_2 carbons respectively. The NO_2 is an electron-withdrawing group, deshielding the carbon atoms to resonate at a lower frequency. For LeZIF8-$PhIm_{168h}$ (**Figure 3.42.b, p 120**), the carbon resonances of the 2-phenylimdazolate linkers are seen at 131, 130, 129 ppm for the phenyl ring on the C2 position. A separate peak for the CH=CH protons was not observed in ^{1}H NMR which suggests similar chemical properties to 2-methylimidazole. The exchange percentage obtained from these linkers suggests that the bulkiness of the ligand plays an important role in the success of SALE. The ligands without a benzyl or phenyl group achieved a much higher exchange percentage of over 65 % compared to the ligands with aromatic rings, which are limited to a exchange of ~10 %.

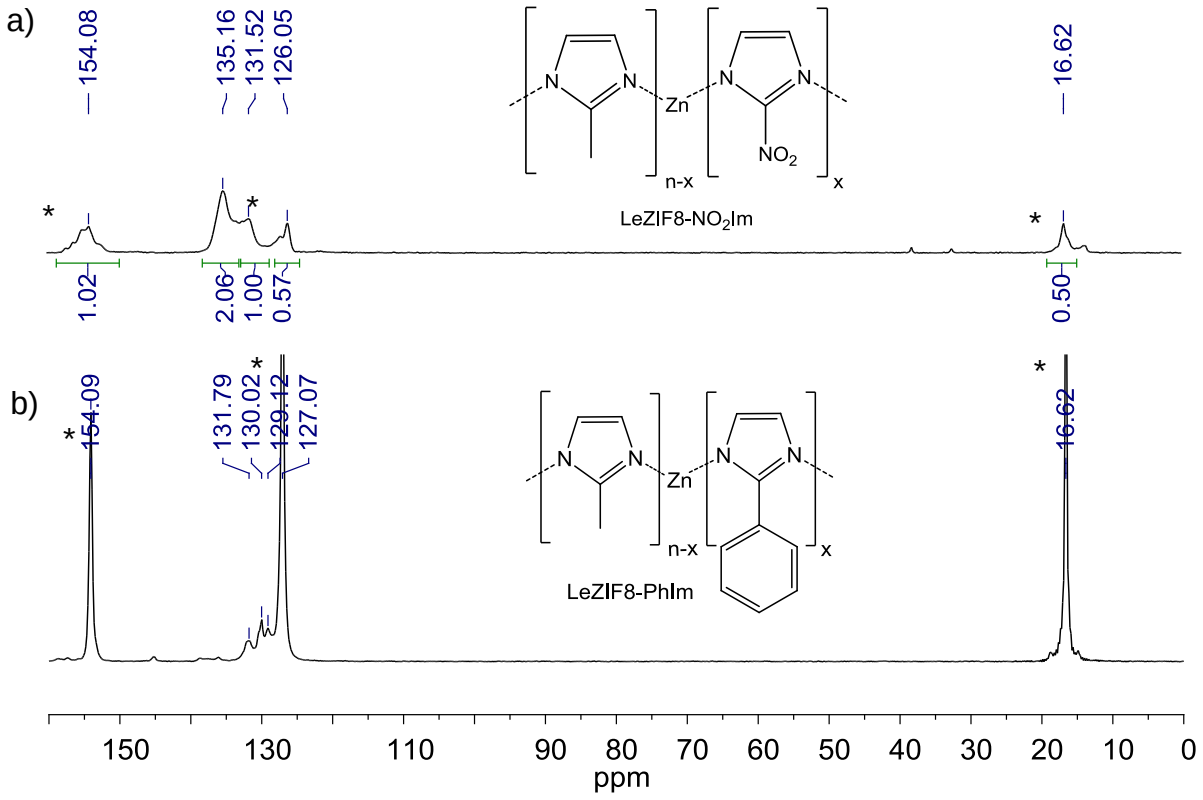

Figure 3.42 Solid-state ^{13}C NMR spectra of a) LeZIF8-NO_2Im_{168h} and b) LeZIF8-$PhIm_{168h.}$ 2-methylimidazolate carbons are marked with (*).

The FTIR spectrum of LeZIF8-PhIm$_{168h}$ (**Figure 3.43, p 121**) shows no significant difference to the spectrum of nZIF-8 (**c**) due to the low exchange percentage (< 10 %). For LeZIF8-NO$_2$Im$_{168h}$ (**b**), with an exchange percentage higher than 66 %, the two strong stretching frequencies of NO$_2$ at 1481 cm^{-1} (asymmetric) and 1356 cm^{-1} (symmetric) are observed. A broad peak for N-H stretching is absent for both samples, since all the organic ligands are bound to the zinc metal.

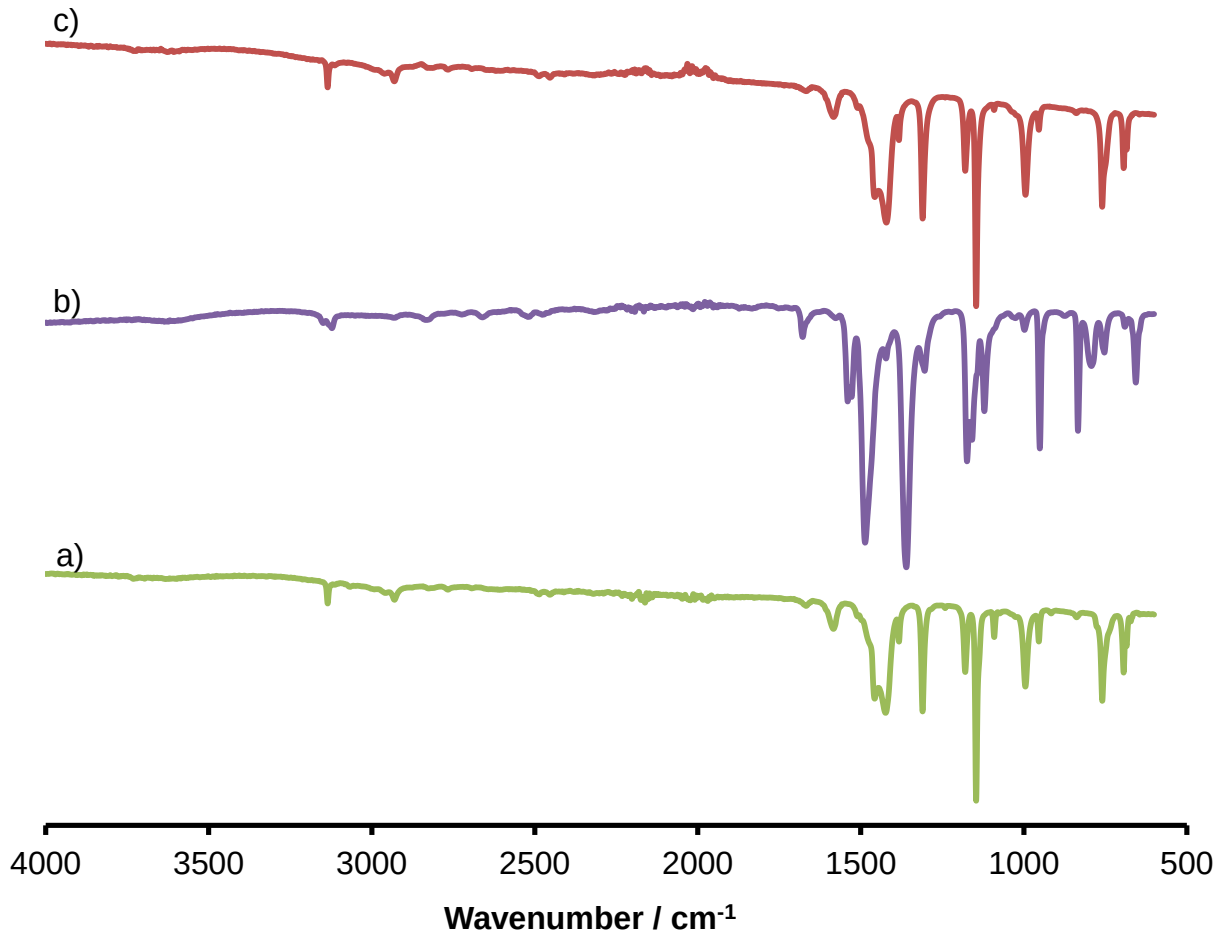

Figure 3.43 Infrared spectrum of a) LeZIF8-PhIm$_{168h}$, b) LeZIF8-NO$_2$Im$_{168h}$ and c) nZIF-8.

The PXRD pattern of LeZIF8-PhIm$_{168h}$ (**Figure 3.44, p 122**) shows sharp narrow peaks, suggesting that nanoparticles were not obtained and the Scherrer equation could thus not be used to determine the particle size. The LeZIF8-PhIm pattern maintained the SOD topology of the original nZIF-8starting material (simulated nZIF-8 PXRD pattern (**c**)). The PXRD pattern for LeZIF8-NO$_2$Im$_{168h}$ suggest, that the particles are not highly crystalline as was already confirmed by ^{13}C NMR spectrum with its broad peaks (**Figure 3.42, p 120**). Additional peaks representing a new topology were observed for LeZIF8-NO$_2$Im$_{168h}$. In the mixture of ligands, with 33.3 % 2-methylimidazole, the SOD topology remains as represented by broad or shoulder peaks at 2θ = 7.36, 10.59 and 12.74 °. The pattern showered similarity to the pattern of simulated ZIF-77 (Zn(NO$_2$Im)$_2$) (**Figure 3.44.a, p 122**) with a frl topology.[19,20] The relative intensity of the peaks

suggest that the frl topology is dominant over the SOD topology. From the broad peaks, the minimum size of the nanoparticles after SALE was determined as 35 nm.

Transmission electron microscopy (TEM) image of LeZIF8-PhIm$_{168h}$ (**a**) (**Figure 3.44**, **p 122**) shows that the particle size of LeZIF8-PhIm$_{168h}$ (after SALE of nZIF-8 with 2-phenylimidazole) has increased dramatically to an average of 244 nm while maintaining a hexagonal shape. This corresponds to the PXRD pattern suggesting that particles of LeZIF8-PhIm$_{168h}$ are exceeding the nano-meter range (> 100 nm). The image of LeZIF8-NO$_2$Im$_{168h}$ (**b**) shows that the original nZIF-8 structure has indeed changed, correlating to PXRD patterns where the topology change from dominant SOD to frl topology. The original spherical particles now have an irregular shape, with an average particle size of 58 nm.

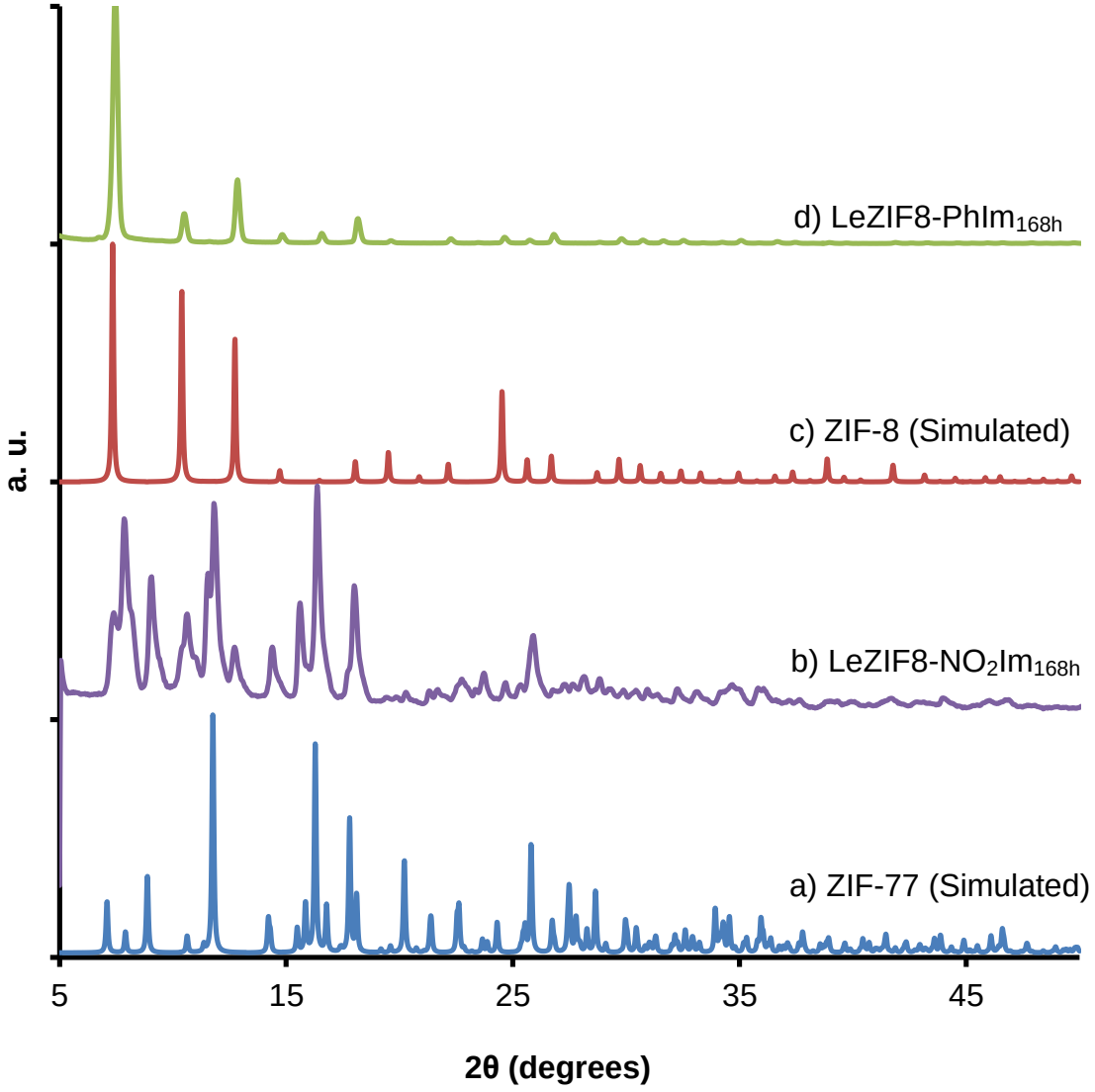

Figure 3.44 PXRD patterns of a) simulated pattern of ZIF-77 (CCDC code: GITWIQ), b) expanded LeZIF8-NO$_2$Im$_{168h}$, c) simulated pattern of ZIF-8 (CCDC code: FAWCEN) and d) LeZIF8-PhIm$_{168h}$.

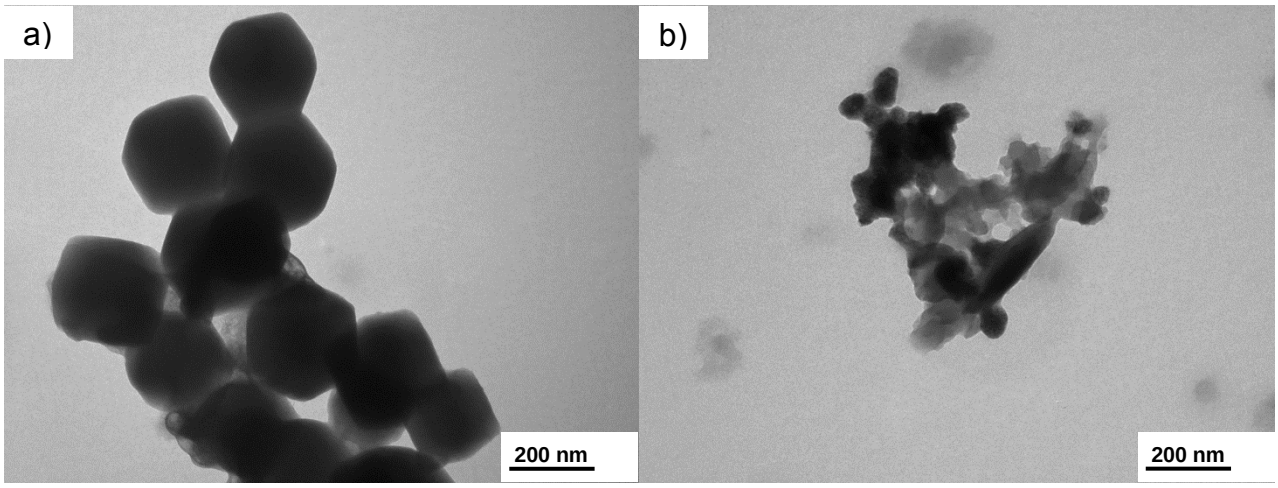

Figure 3.45 TEM images of a) LeZIF8-PhIm$_{168h}$ and b) LeZIF8-NO$_2$Im$_{168h}$.

After activation of LeZIF8-PhIm$_{168h}$ and LeZIF8-NO$_2$Im$_{168h}$ at 150 °C for 16 hours, typical Type-1 isotherms were obtained (**Figure 3.46, p 123**), showing that both materials are still microporous after SALE. The quantities of nitrogen adsorbed, determined at 0.9 p/p°, show that the porosity of LeZIF8-PhIm remained similar to that of the nZIF-8 starting material with 417 cm^3 g^{-1} adsorbed. LeZIF8-NO$_2$Im$_{168h}$, however, showed a sharp decrease in porosity, adsorbing only 168 cm^3 g^{-1} of nitrogen.

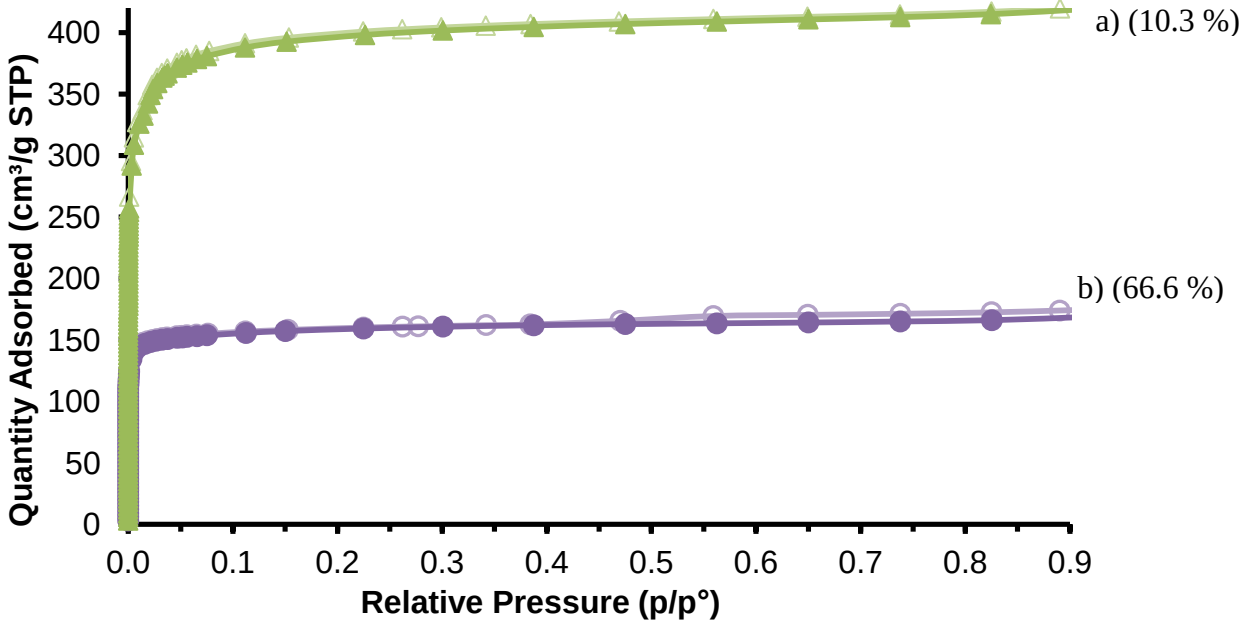

Figure 3.46 Adsorption and desorption N$_2$ isotherm at 77 K of a) LeZIF8-PhIm$_{168h}$ and b) LeZIF8-NO$_2$Im$_{168h}$ obtained after a 168 hours SALE of nZIF-8 with 2-phenylimidazole and 2-nitroimidazole respectively. Adsorption marked as solid and desorption as hollow symbols Exchange percentages are given in brackets.

The BET surface area (1579 m^2 g^{-1}) measured for LeZIF8-$PhIm_{168h}$ (10.3 % exchange) was similar to that of the nZIF-8 starting material, but the micropore volume of 0.549 cm^3 g^{-1} was an improvement of ~0.1 cm^3 g^{-1} compared to nZIF-8. The t-plot external surface area (144 m^2 g^{-1}) of LeZIF8-$PhIm_{168h}$ corresponds to the larger particles (~220 nm) obtained after 168 hours of SALE. LeZIF8-NO_2Im_{168h} (66.6 % exchange) with its large portion of frl topology saw a significant decrease in porosity during 168 hours of SALE, with both BET surface area (168 cm^3 g^{-1}) and micropore volume (0.213 cm^3 g^{-1}) dramatically reduced.

The TGA thermogram of LeZIF8-NO_2Im_{168h} (**Figure 3.47.a, p 124**), shows a sharp mass loss of 84 % after 287 ℃, indicating that the majority presence of the new frl topology is not as stable as the SOD topology of the nZIF-8 starting material. The 2-nitroimidazolate linker decomposed at a much lower temperature than other imidazolate linkers in this study. The TGA of LeZIF8-PhIm (**Figure 3.47.b, p 124**) shows an initial mass loss of 30 % after 400 ℃, followed by a gradual continuous mass loss as the nZIF-8 structure decomposes.

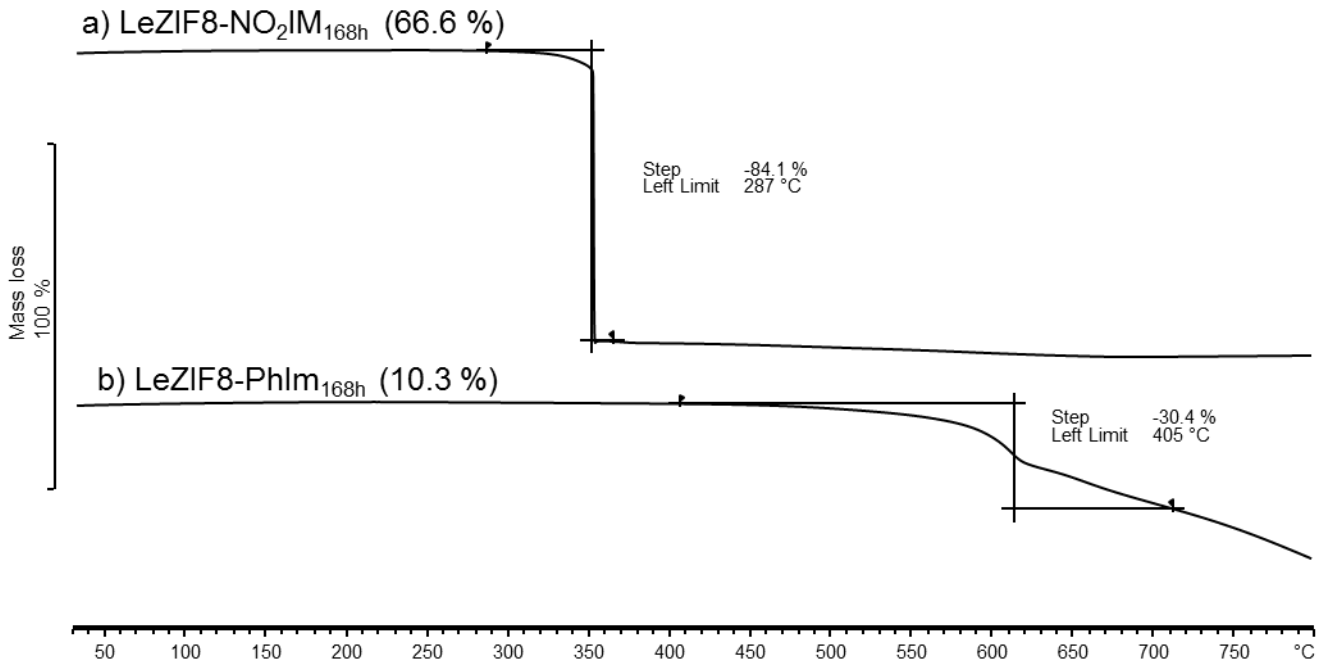

Figure 3.47 TGA thermogram (under N_2) of a) LeZIF8-NO_2Im_{168h}, and b) LeZIF8-$PhIm_{168h}$, obtained after a 168 h SALE of nZIF-8 with 2-phenylimidazole and 2-nitroimidazole respectively. Exchange percentages are given in brackets.

In conclusion, the ligands without a benzyl group on the C3 and C4 imidazolate positions all have exchange percentages above 66 % and with a benzyl group, it is limited to maximum of 15 % because of steric hindrance effects preventing the diffusion of ligands into the particles'

interior. The nanoparticles remained smaller than 100 nm after SALE, except during SALE with the phenyl and thiol functionalized imidazole derivatives. The particles kept their SOD topology, with the exception of SALEM-2, which transform into a ZIF-zni topology and LeZIF8-NO_2Im_{168h} into frl topology at higher exchange percentages.

In general, a decrease in BET surface area and micropore volume was observed for all the SALE products (**Figure 3.48, p 125**). The SALE product with the SH functionality, LeZIF8-$SHBzIm_{72h}$, has a 200 $m^2\ g^{-1}$ higher BET surface area than the SALE product with NH_2 substituents. The micropore volume stayed high at 0.47 $cm^3\ g^{-1}$ with these two products having approximately the same exchange percentage. However, the t-plot external surface area of LeZIF8-$SHBzIm_{72h}$ decrease by ~200 $m^2\ g^{-1}$ with the larger particles obtained. The phenyl substituents of LeZIF8-$PhIm_{168h}$ maintained the porosity of the original nZIF-8 with improved micropore volume, but a lower t-plot external surface area because of increase particle size. The NO_2 substituent of LeZIF8-NO_2Im_{168h}, with its partial frl topology, has a lower nitrogen adsorption and also the lowest BET surface area of the functionalized SALE products.

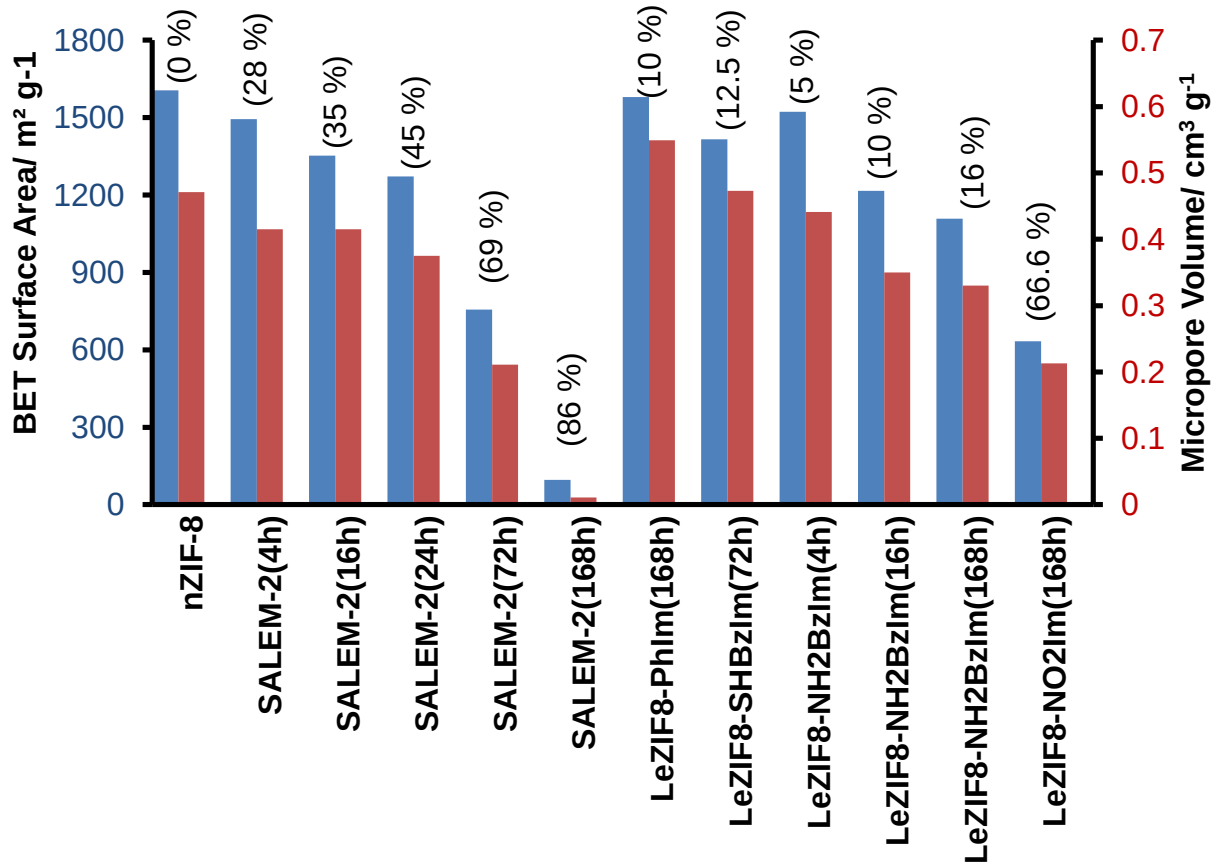

Figure 3.48 Graph representing the BET surface areas (blue) and micropore volume (red) of SALE-nZIF compounds. Exchange percentages are given in brackets.

3.4 Post Synthetic Modification on SALE-nZIFs

3.4.1 Ferrocenyl Derivatives

In this section, ferrocenyl derivatives, well known for their applications as industrial catalysts and biomedical applications (Chapter 2.5), and nZIF-8, an effective and low cytotoxic drug carrier (Chapter 2.6), are brought together via post synthetic modification (PSM). ZIF-8 nanoparticles, modified by SALE will be modified further with ferrocenyl derivatives on the external surface area, to act as possible drug carriers. The particle size must kept smaller than 200 nm, in order to function as a drug carrier. The synthetic methods employed during the PSM of ZIF nanoparticles are divided into two categories: PSM *via* Claisen condensation and ester amidation; PSM *via* imine condensation and carboxylic acid amidation (**Scheme 3.11, p 127**).

During a modified Claisen condensation method, described elsewhere[21,22] (**Scheme 3.11.a, p 127**), LeZIF8-$E4_{24h}$ nanoparticles as the substrate were reacted with acetyl ferrocene in dry THF under argon. The reaction is highly sensitive to moisture. After 16 hours the nanoparticles were washed, isolated and activated at 100 ℃ under vacuum to obtain LeZIF8-$E4_{24h}$-Fc-diketone as a light yellow powder (84 % yield).

In the second method, amidation of an ester functional group, modified from literature[23,24] (**Scheme 3.11.b, p 127),** ferrocenemethylamine was reacted with the substrate LeZIF8-$M2_{24h}$ in dry ethanol under argon flow. After 16 hours, the nanoparticles were washed with methanol, isolated and activated at 100 ℃ under vacuum to obtain LeZIF8-$M2_{24h}$-FcMNH as a light yellow powder (87 % yield).

In the second category (**c** and **d**) of PSM, LeZIF8-NH_2BzIm_{16h} (**Chapter 3.3.3, p 111**) was used as substrate for both procedures: imine condensation and amidation of carboxylic acids. In a typical reaction the amine functionalized substrate, LeZIF8-$NH2BzIm_{16h,}$ was reacted with ferrocenecarboxaldehyde solution in refluxing methanol for 22 hours. The nanoparticles were isolated, washed and activated at 100 ℃ under vacuum to obtain LeZIF8-NH_2BzIm-FcC=N as a light maroon powder (91 % yield). The first indication of imine formation was the colour change from a light brown powder to a light maroon powder.

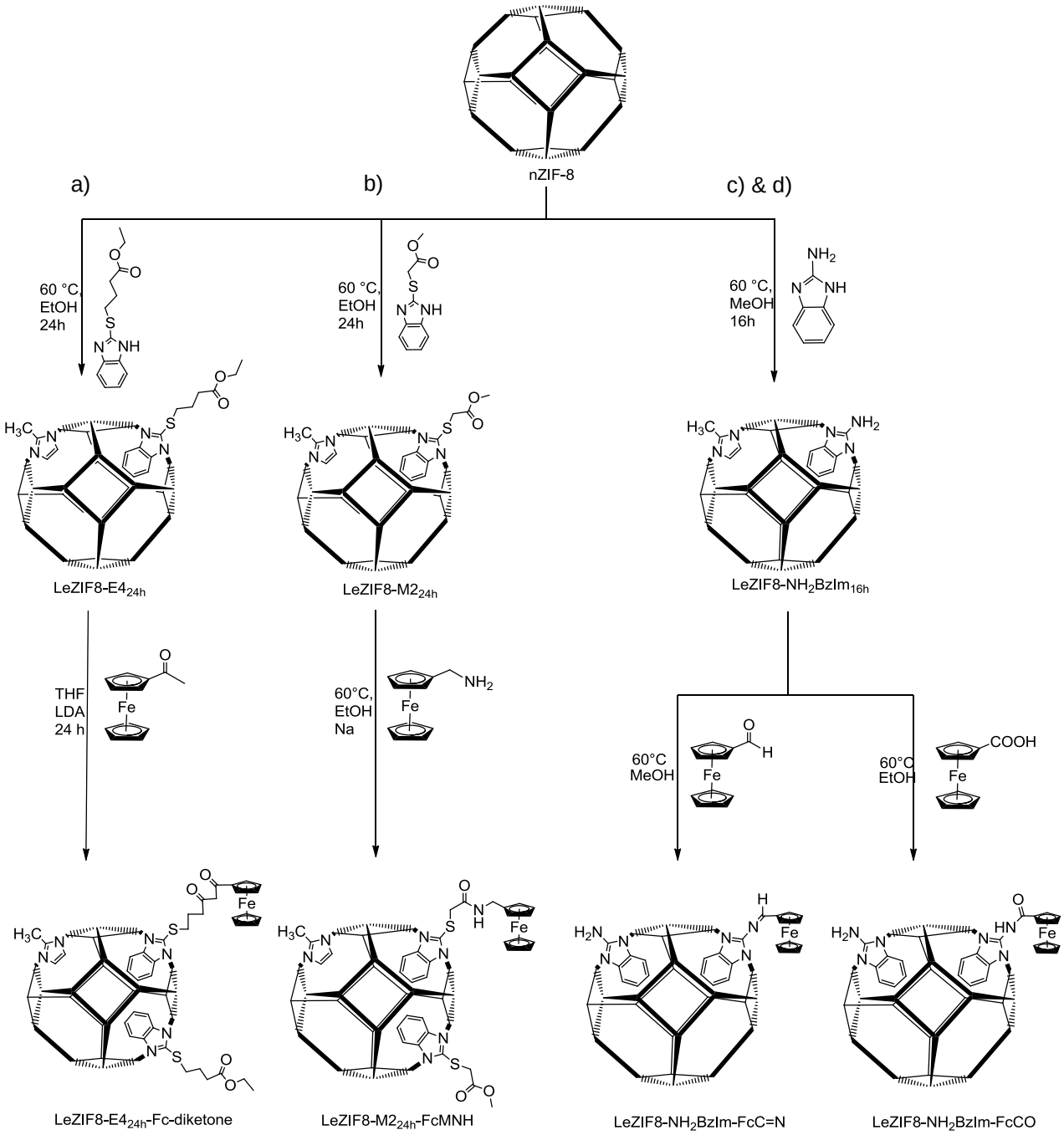

Scheme 3.11 Post Synthetic Modification on the external surface area of ligand exchanged nZIF-8 derivatives with ferrocenyl derivatives using four different methods: a) Claisen condensation, b) ester amidation, c) imine formation and d) carboxylic acid amidation.

The last method, peptide bond formation with ferrocene carboxylic acid (FcCOOH), was modified from literature.[25,26] The LeZIF8-NH_2BzIm$_{16h}$ substrate was reacted with FcCOOH in refluxing ethanol 48 hours. The nanoparticles was isolated, washed extensively with methanol and activated at 100 ℃ under vacuum to obtain LeZIF8-NH_2BzIm-FcCO as a yellow powder (99 % yield).

3.4.1.1 Infrared Spectroscopy

The FTIR spectra of three of the four SALE-PSM products (**Figure 3.49.a, b and d, p 129**) remained identical to the spectrum of the substrate (**Figure 3.30.e, p 104**). Infrared spectroscopy was thus not sensitive enough to detect most of the ferrocene compounds grafted on the external surface of the LeZIF8-derivatives in **Scheme 3.11 (p 127**).

Only for LeZIF8-NH_2BzIm-FcCO (**f**) a higher load of the ferrocenyl fragment was achieved as additional peaks appeared on the FTIR spectrum. The peaks remain difficult to classify due to the low amount of ferrocenyl fragments bound to the ZIF surface. The amide bond formation could be detected by peaks at 1534 cm^{-1} for the N-H bending (i). Between 3450 and 3250 cm^{-1} peaks for the unreacted primary (NH), secondary amines (NH_2) and secondary amides overlap. The secondary amide peak at 3422 cm^{-1} (ii) is stronger than amine peaks (**e**) with an overtone at 3100 cm^{-1} (iii). The carbonyl stretching frequency of the free acid (FcCOOH) at 1647 cm^{-1} (iv) shifted to 1576 cm^{-1} (v), ($C{=}O^{anti}$ stretching) after amide bond formation. The disappearance of the broad O-H stretching frequency between 2500 and 3000 cm^{-1} (vi) is another indication of bond formation. Three additional strong peaks at 1471 cm^{-1} (vii), 1391 cm^{-1} (viii) and 1361 cm^{-1} (ix) can be assigned to the $C{=}O^{sym}$ stretching frequency. The difference between the $C{=}O^{anti}$ and $C{=}O^{sym}$ frequencies can be used to determine the binding modes, *i.e.* ionic (150 – 200 cm^{-1}), unidentate (> 200 cm^{-1}), bidentate (< 120 cm^{-1}) or bridging (120 – 200 cm^{-1}).[27] The differences for the three peaks are 105 (vii), 182 (viii) and 215 (ix) cm^{-1}, suggesting that the carboxylic acid (FcCOOH) may also form carboxylates with various binding modes other than amides, on the surface of ZIF-8. Nuclear magnetic resonance will be used to confirm addition bond formation (**Section 3.4.1.2, p 130**).

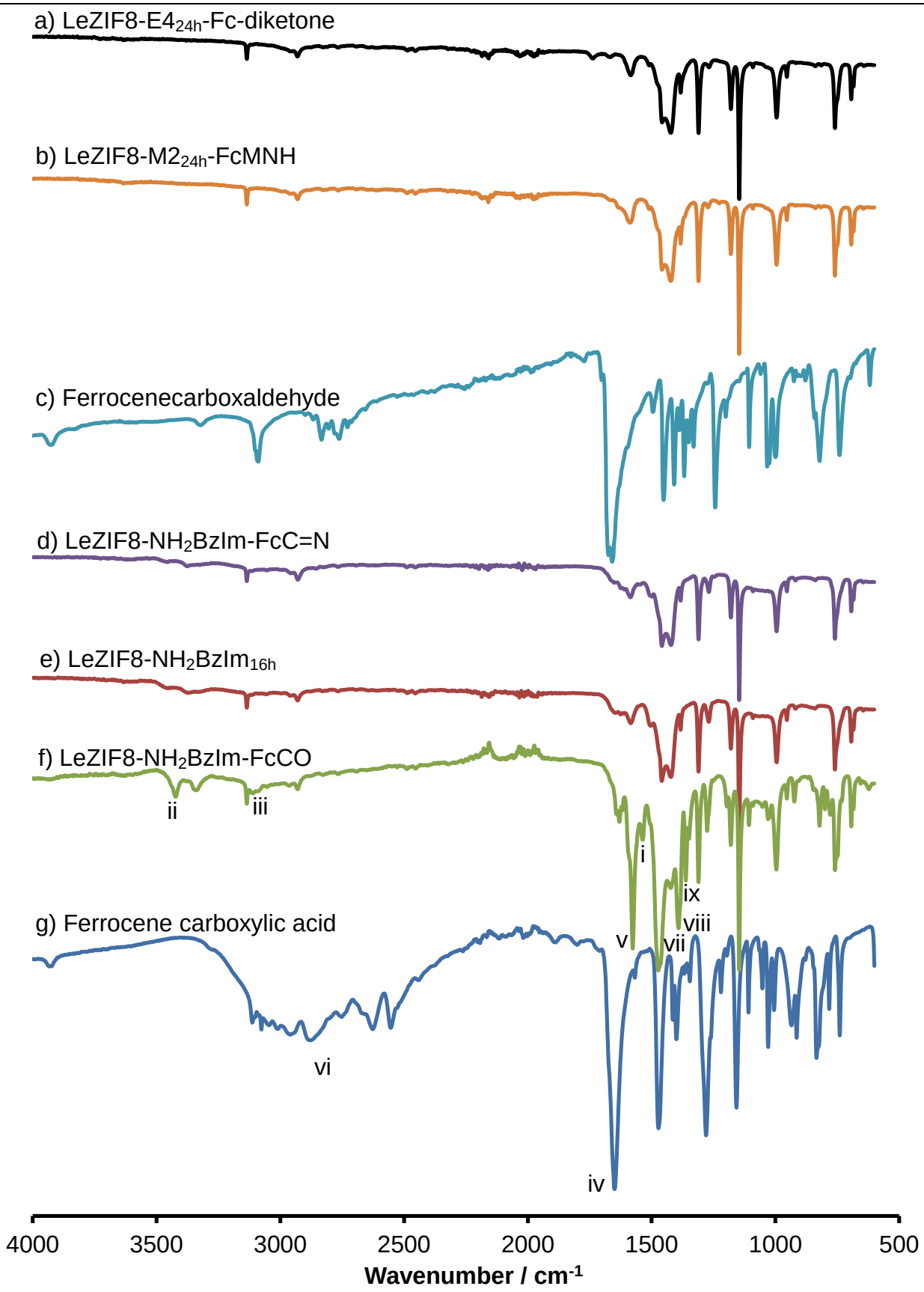

Figure 3.49 FTIR spectra of a) LeZIF8-E4$_{24h}$-Fc-diketone, b) LeZIF8-M2$_{24h}$-FcMNH, c) ferrocenecarboxaldehyde, d) LeZIF8-NH$_2$BzIm-FcC=N, e) LeZIF8-NH$_2$BzIm$_{16h}$, f) LeZIF8-NH$_2$BzIm-FcCO and g) ferrocene carboxylic acid.

3.4.1.2 Nuclear Magnetic Resonance

Most ferrocenyl compounds insoluble in water. During digestive ^{1}H NMR with D_2O/D_2SO_4 (9:1) solution these PSM modified compounds gave precipitates without detecting any of the ferrocenyl fragments. Solid-state NMR (SSNMR) was thus used to characterise the powder samples as is. Since the orientation of crystallite faces affect the chemical shielding and coupling through nuclear spin interaction, broad peaks are obtained. The Magic-angle spinning (MAS) of the rotor at a magic angle of 54.74° and a very high spin speed (14 kHz in this study) can cancel out anisotropic effects and is a line narrowing technique. Amorphous materials however still remain difficult to analyse with SSNMR due to the broad peaks obtained.[28]

In the SSNMR spectrum (**Figure 3.50, p 131)** of LeZIF8-$E4_{24h}$-Fc-diketone (**b**) the peaks corresponding to those of the substrate, LeZIF8-$E4_{24h}$ (**a**), are identified as previously determined (**Chapter 3.3.2.2, p 97**). In addition, the faint signal at 72.46 ppm originates from the resonance of the 10 cyclopentadienyl carbon atoms of the ferrocenyl fragments. For LeZIF8-$M2_{24h}$-FcMNH (**d**) the peaks corresponding to LeZIF8-$M2_{24h}$ (**c**) were identified and determined previously (**Chapter 3.3.2.2, p 97**). The 10 cyclopentadienyl carbon atoms resonating at 71.15 ppm indicate the presence of the ferrocenyl fragment. The disappearance of the peak for the -O-CH_3 carbon atom at 51.36 ppm (**c**) and the shift in the signal for the carbon atoms of the alkyl chain, from 39.12 ppm (**c**) to 44.37 ppm (**d**) indicates the cleaving of the ester to form an amide bond. The carbonyl carbon atom of LeZIF8-$M2_{24h}$ resonating at 169.07 ppm (**c**), shifted to a broader peak at 177.05 ppm (**d**) during amidation. With ^{13}C SSNMR the attachment of the ferrocenyl fragments on the ZIF surface remains barely observable, as very low amounts were linked during both Claisen condensation and ester amidation.

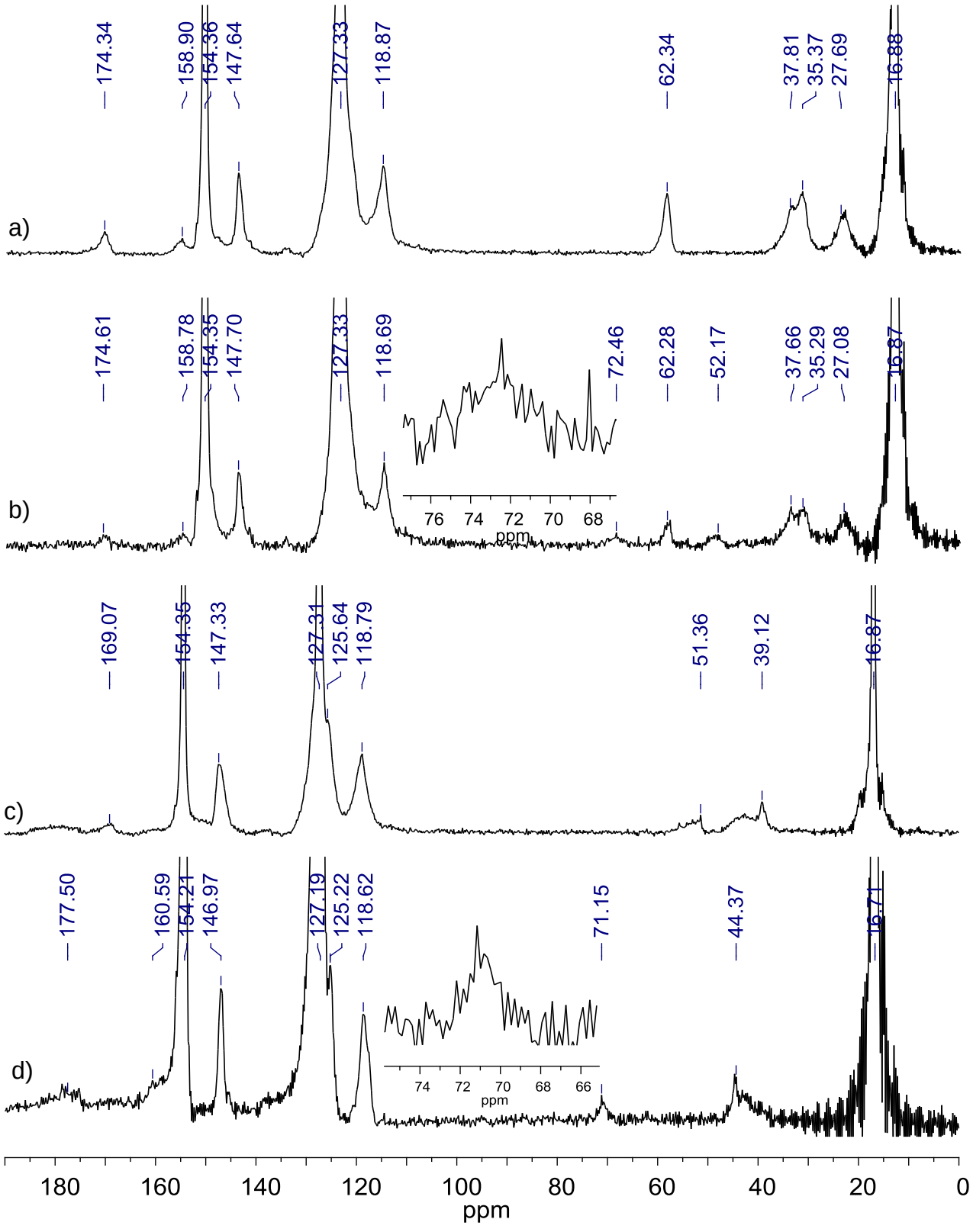

Figure 3.50 Solid-state ^{13}C NMR spectra of a) LeZIF8-E4$_{24h}$, b) LeZIF8-E4$_{24h}$-Fc-diketone, c) LeZIF8-M2$_{24h}$ and d) LeZIF8-M2$_{24h}$-FcMNH.

The SSNMR of the substrate, LeZIF8-NH_2BzIm$_{16h}$ (**c**) in (**Figure 3.51, p 133**) was discussed previously (**Chapter 3.3.3, p 111**). The imine bond formation between LeZIF8-NH_2BzIm$_{16h}$ and ferrocenecarboxaldehyde was confirmed by the presence of the 10 cyclopentadienyl carbon atoms of the ferrocenyl group resonating at 72.23 ppm, shifted from 73.78 ppm as for ferrocenecarboxaldehyde (**a**). The weakness of the peak means that the abundance of ferrocenyl groups remains low after the formation of the imine bonds which was shown to be effective for the PSM of ZIFs.[29] The low amount of bounding is due to the orientation and steric hindrance from the 2-aminobenzimidazole linker. For the amide formation between of LeZIF8-NH_2BzIm$_{16h}$ and ferrocene carboxylic acid a higher intensity was observed for the resonance of the ferrocenyl group's. The ferrocene carboxylic acid spectrum (**e**) has peaks at 75.03 and 76.88 ppm for the substituted and unsubstituted cyclopentadienyl rings respectively. After PSM the 10 carbon atom of the cyclopentadienyl ring resonated with multiple peaks close to 74 ppm (**d**). The shift in position of the most intense peak is an indication of amide bond formation between the COOH group of the ferrocene carboxylic acid and the NH_2 group of LeZIF8-NH_2BzIm$_{16h}$. The multiple peaks (**d**) in the region suggest different chemical bonding may be present.

The amino carbon atom on the C2 position of LeZIF8-NH_2BzIm$_{16h}$ resonating at 164.59 ppm (**c**), shifted to 165.37 ppm (**d**) after PSM with FcCOOH. The carbon atom of carbonyl peak of the unbonded FcCOOH resonates at 184.87 ppm (**e**) but after PSM, five distinct peaks were obtained in the region between 188 to 184 ppm (**d**). These multiple peaks support the probability of different chemical bonding seen with the additional peaks of the cyclopentadienyl carbon atoms.

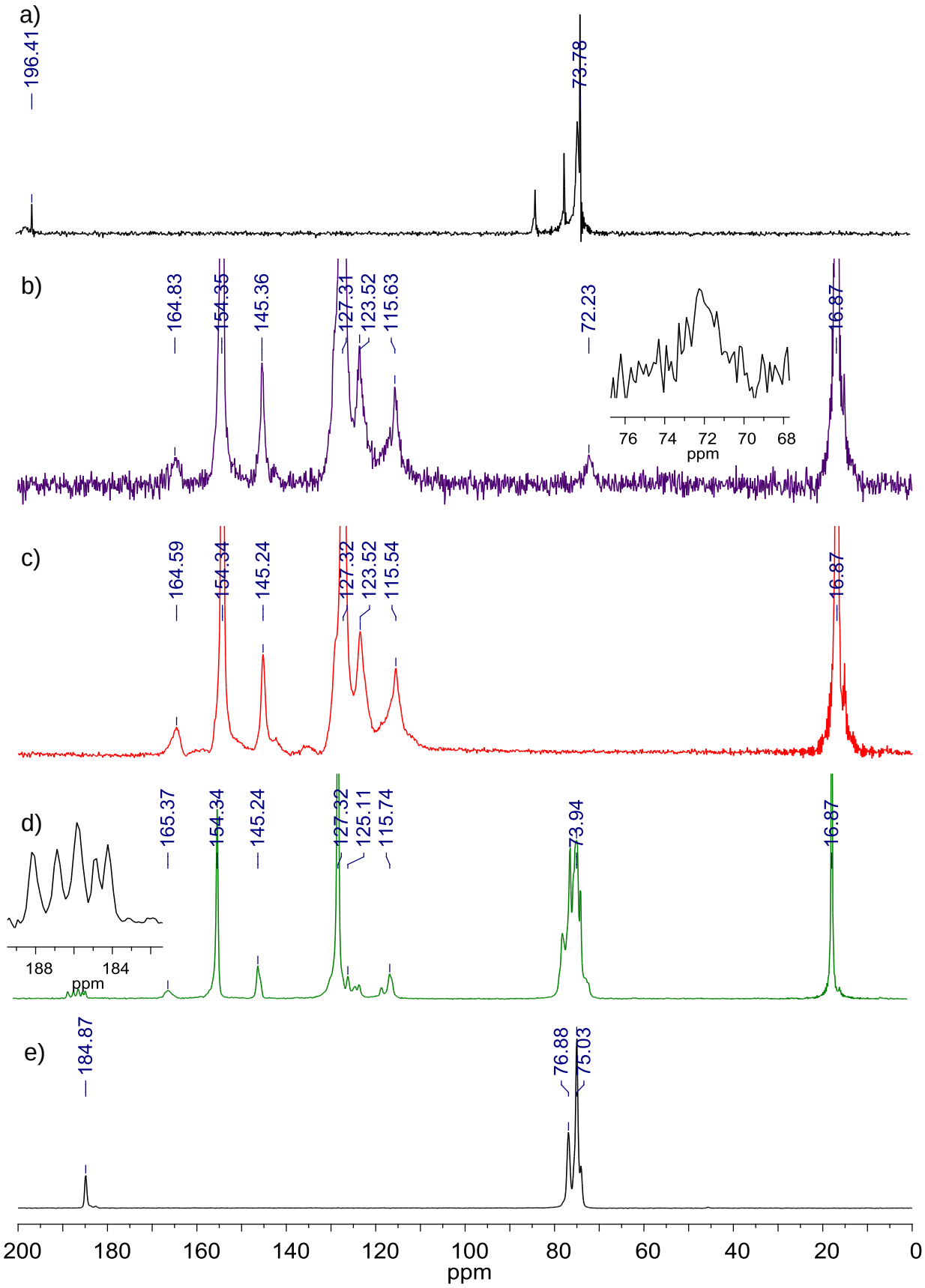

Figure 3.51 Solid-state ^{13}C NMR spectrum of a) ferrocenecarboxaldehyde, b) LeZIF8-NH_2BzIm-FcC=N, c) LeZIF8-NH_2BzIm_{16h}, d) LeZIF8-NH_2BzIm-FcCO and e) ferrocene carboxylic acid.

From DFT calculation and CO adsorption it is known that the external surface of ZIF-8 contain strong Lewis acid sites due to coordinative unsaturated Zn metal nodes,[13] useful for PSM of MOFs *via* grafting.[30,31,32] The multiple peaks between 188 to 184 ppm (**d**) can be assigned to the possible basic binding modes *i.e.* unidentate, chelating, bidentate and ionic of carboxylates with zinc metal nodes (**Figure 3.52, p 134**). Apart from the binding modes, different configurations exist within each mode *e.g. syn* unidentate, *anti* unidentate, symmetric chelating, asymmetric chelating, *syn-syn* bidentate etc.[27] These binding modes of zinc complexes can be identified from the separate peaks of a ^{13}C NMR spectrum.[33] The amount of chemical shift due to the different binding modes are in the following order: chelating > bidentate > unidentate.[34] The ^{13}C SSNMR spectrum (**Figure 3.51.d, p 133**) provides evidence of multiple carboxylate coordination, although specific peak allocation of the binding mode obtained with PSM and amide formation remains unclear.

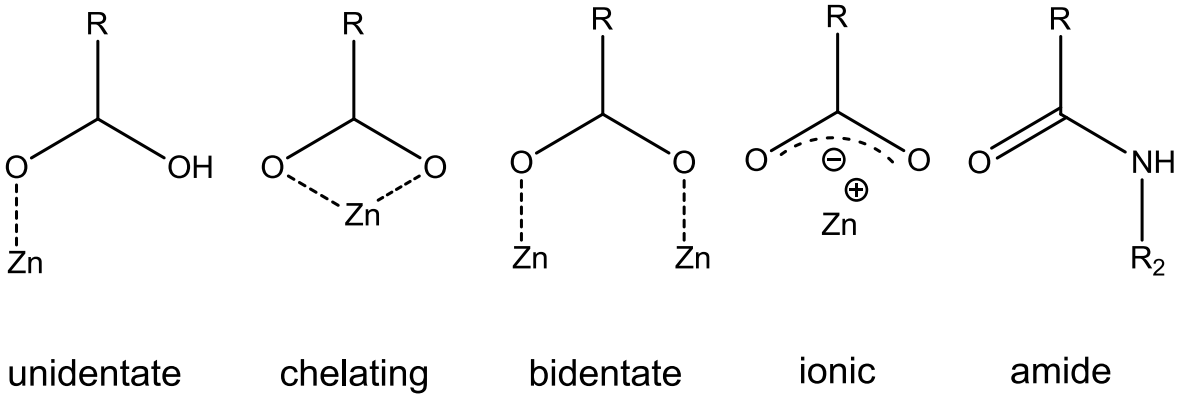

Figure 3.52 Possible carboxylate binding modes and amide formation between FcCOOH and LeZIF8-NH_2BzIm.R = Fc, R_2 = nZIF.[27]

In order to determine the amount of ferrocenyl fragments bound to the LeZIF8-NH_2BzIm nanoparticles, the presence and loading of iron will be determined by XPS, TEM-EDS and ICP-OES.

3.4.1.3 Transmission Electron Microscopy (TEM) and Powder X-ray Diffraction (PXRD)

Particle size, shape and topology of the products from PSM of LeZIF-8 derivatives with ferrocenyl groups were determined by a combination of transmission electron microscopy (TEM) images and powder X-ray diffraction (PXRD) patterns (**Figure 3.53, p 136**) and summarised in **Table 3.11 (p 135**). All the particles remained spherical and in the nanometer

range (<100 nm) which is important for biomedical applications and catalysis, while a SOD topology was maintained as seen from the PXRD patterns.

Table 3.11 Particle size of LeZIF-8 derivatives with ferrocenyl groups *via* PSM. Particle sizes were measured statically from TEM images and minimum particle sizes calculated from selected PXRD peaks.

Compound	Average Particle Size/ nm	
	TEM	PXRD
LeZIF8-E4$_{24h}$-Fc-diketone	21.9	20.3
LeZIF8-M2$_{24h}$-FcMNH	54.7	22.2
LeZIF8-NH$_2$BzIm-FcC=N	22.9	22.0
LeZIF8-NH$_2$BzIm-FcCO	27.0	21.3

For LeZIF8-M2$_{24h}$-FcMNH the particles agglomerate and remains difficult to disperse in solution, resulting in an average diameter of 54.67 nm (TEM), although the minimum particle size was 22.15 nm (PXRD). LeZIF8-M2$_{24h}$-FcMNH remains crystalline, with an irregular particle shape.

The PSM of amino functionalized ZIF-8 (LeZIF8-NH$_2$BzIm$_{16h}$ (**Chapter 3.3.3, p 111**)) with ferrocene gave a much higher loading, compared to LeZIF8-E4$_{24h}$-Fc-diketone and LeZIF8-M2-$_{24h}$-FcMNH, of iron as seen by the peak intensities at 6.4 keV for both EDS spectra for LeZIF8-NH$_2$BzIm-FcC=N (**c**) and LeZIF8-NH$_2$BzIm-FcCO (**d**). The LeZIF8-NH$_2$BzIm-FcCO shows various additional peaks throughout the enlarged (4 times) PXRD pattern, besides the SOD topology peaks of LeZIF8-NH$_2$BzIm at 2Θ = 7.53, 10.55, 12.90, 14.36 and 16.61 °. These additional peaks are due to the grafting of ferrocenyl groups on the external surface, reducing the crystallinity of the nanoparticles.

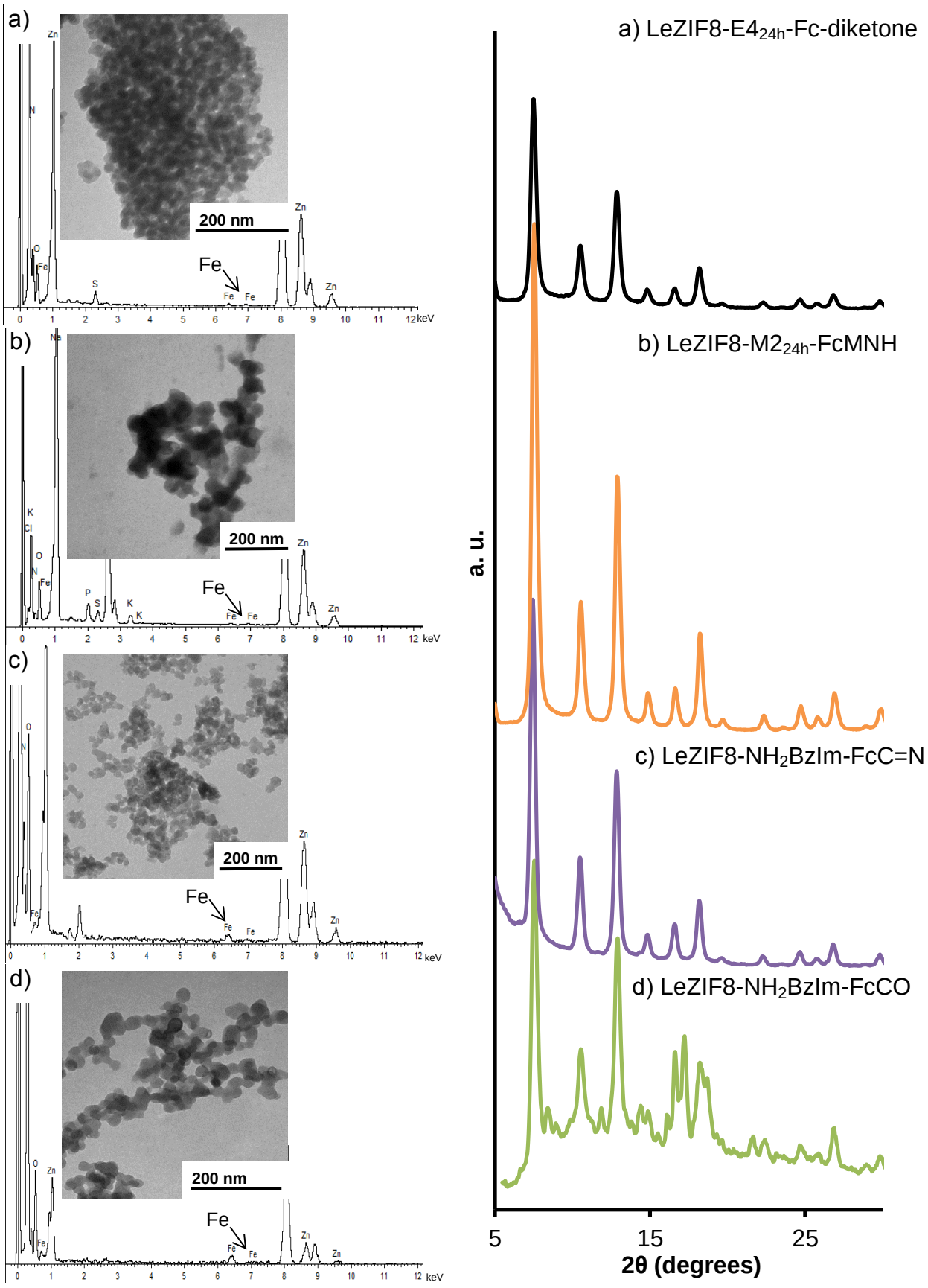

Figure 3.53 TEM images and EDS scans (left) and PXRD patterns (right) of a) LeZIF8-E4$_{24h}$-Fc-diketone, b) LeZIF8-M2$_{24h}$-FcMNH, c) LeZIF8-NH$_2$BzIm-FcC=N and d) LeZIF8-NH$_2$BzIm-FcCO.

Energy-dispersive X-ray spectroscopy (EDS) was used to identify the elements in a TEM sample (**Figure 3.53, p 136**). The intense peak at ~8 keV is due to the copper from the TEM grids. For LeZIF8-E4$_{24h}$-Fc-diketone (**a**) and LeZIF8-M2$_{24h}$-FcMNH (**b**) faint signals for iron was detected (**Figure 3.53, p 136**). The EDS spectra of LeZIF8-NH_2BzIm-FcC=N (**c**) and LeZIF8-NH_2BzIm-FcCO (**d**) show a much sharper peak for iron, indicating a higher iron content than for the first two samples. The iron content from EDS is reported in **Chapter 3.4.1.4 (p 137**).

3.4.1.4 X-ray photoelectron spectroscopy (XPS) and Inductively Coupled Plasma – Optical emission spectrometry ICP-OES

The ferrocene containing PSM nZIF-8 nanoparticles were probed by *ex situ* X-ray photoelectron spectroscopy (XPS) in an attempt to quantify the iron content of the nanoparticles. The X-ray penetration depth of XPS is ~1µm, and the nanoparticles' sizes ~20 nm, therefore the X-rays can penetrate to the bulk of the material.[35] XPS analysis of most samples will always contain adventitious carbon residue with the carbon within the sample and the carbon peak are shifted accordingly to 284.5 eV.[36] In at least one of the four PSM products XPS analyses gave a clear, quantitative, iron signal, proof that ferrocenyl fragments were grafted on the nanoparticles (**Figure 3.54, p 138**). The high resolution XPS scans of LeZIF8-NH_2BzIm-FcC=N (**a**) and LeZIF8-NH_2BzIm-FcCO (**b**) are shown for nitrogen and zinc and the iron spectra only for LeZIF8-NH_2BzIm-FcCO (**b**). The iron spectrum of LeZIF8-NH_2BzIm-FcC=N was omitted, since its iron content was below the detection limits of the XPS (< 1 %). This was also true for LeZIF8-E4$_{24h}$-Fc-diketone, LeZIF8-M2$_{24h}$-FcMNH. The XPS spectra of these two compounds are given in (**Appendix H.1**) and a summary of the relevant deconvoluted signals in **Table 3.12** (**p 138**), for all the compounds. For all the PSM nZIF-8 materials with attached ferrocenyl fragments, the Zn $2p_{1/2}$ (~1045 eV) and $2p_{3/2}$ (~1021 eV) signals are both deconvoluted into two distinct peaks which represents the four-coordinated Zn (highest abundance) and the lower-coordinated Zn (lower abundance) near the surface. Similarly, The N 1s signals was deconvoluted into two distinct peaks: the primary peak at ~399 eV represents the Zn-bound nitrogen atoms and the secondary peak at ~396 eV the nitrogen atoms of the amine and amide functionalities on the nanoparticles' surface.[37] The relative abundance percentages of these two N 1s peaks represent a 13.6 % average abundance of nitrogen atoms bound to the amine and amide functionalities. This amount closely corresponds to the exchange percentage determined by NMR spectroscopy (~10 %). The iron signal for LeZIF8-NH_2BzIm-FcCO was strong enough to detect two separate peaks for the $2p_{1/2}$ and $2p_{3/2}$ transitions at 720 and 707.4 eV respectively, typical for the monolayer Fe^{2+} transition state of ferrocene.[38]

Table 3.12 XPS data of LeZIF-8 derivatives with ferrocenyl groups *via* PSM. The respective deconvoluted peaks of each spin state for Nitrogen (1s) and Zinc ($2p_{1/2}$ and $2p_{3/2}$) are accompanied by their relative abundance percentages in brackets.

	Deconvoluted Binding Energy/ eV							
Compound	**N (1s)/ eV (Relative abundance %)***		**Zn ($2p_{1/2}$)/ eV (Relative abundance %)***		**Zn ($2p_{3/2}$)/ eV (Relative abundance %)***		**Fe ($2p_{1/2}$) / eV**	**Fe ($2p_{3/2}$) / eV**
LeZIF8-E4$_{24h}$-Fc-diketone	398.4 (86.0)	395.7 (14.0)	1044.5 (26.4)	1041.2 (7.0)	1021.8 (52.7)	1019.3 (14.0)	-	-
LeZIF8-M2$_{24h}$-FcMNH	398.9 (84.0)	396.7 (16.0)	1044.7 (28.3)	1042.0 (5.1)	1021.6 (56.56)	1019.3 (10.11)	-	-
LeZIF8-NH$_2$BzIm-FcC=N	398.6 (88.0)	395.8 (12.0)	1045.3 (28.2)	1042.9 (5.2)	1021.8 (56.4)	1019.3 (10.3)	-	-
LeZIF8-NH$_2$BzIm-FcCO	399.2 (87.5)	395.5 (12.5)	1045.1 (28.9)	1043.0 (4.5)	1022.0 (57.7)	1019.0 (8.9)	720	707.4

*Relative abundance percentages of each specific spin state.

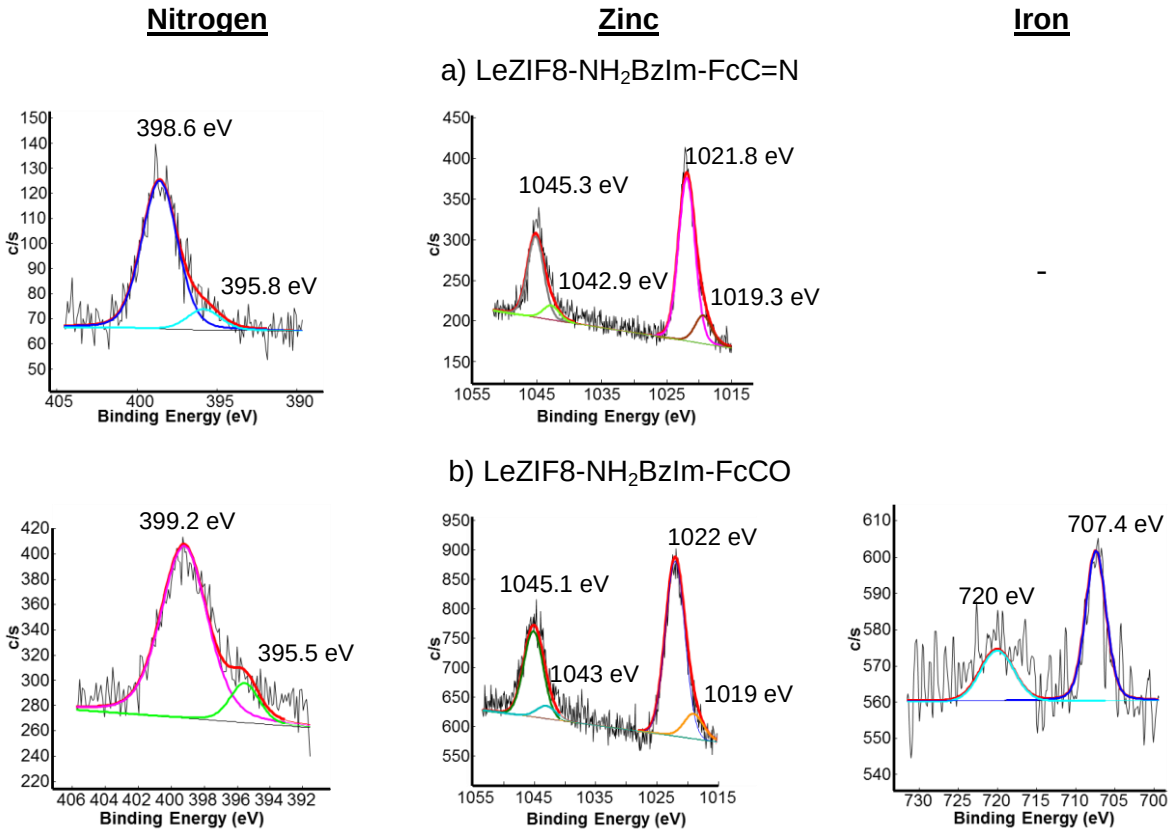

Figure 3.54 XPS spectra of N, Zn and Iron of a) LeZIF8-NH$_2$BzIm-FcC=N and b) LeZIF8-NH$_2$BzIm-FcCO. Red line: theoretical fit. Other lines: deconvoluted experimental fit.

Although XPS and EDS gave mostly qualitative proof of the presence of iron in the samples, the content and Fe:Zn ratio of LeZIF8-NH_2BzIm-FcCO could be determined as 0.253 (for XPS) and (0.320 (for EDS) . Quantification of the ion content of the other three compounds was unreliable for the XPS and EDS, due to low bonding percentages. To accurately determine the iron content, inductively couple plasma – optical emission spectrometry (ICP-OES) was performed in triplicate with a 95 % confidence interval. The Fe:Zn ratios from ICP-OES for LeZIF8-$E4_{24h}$-Fc-diketone, LeZIF8-$M2_{24h}$-FcMNH and LeZIF8-NH_2BzIm-FcC=N were also below the detection limits of the spectrometer. As for LeZIF8-NH_2BzIm-FcCO the Fe:Zn ratio from ICP-OES (0.446) corresponds with the approximate average of about 0.3, obtained by XPS and EDS. The lower ratios from XPS and EDS are due to the analyses being single spot, whereas ICP-OES measures the bulk of the sample. The ratio of Zn:MeIm:NH_2BzIm in the sample is 1:1.8:0.2 (NH_2BzIm = 10 % after SALE). A Fe:Zn ratio of 0.466:1, thus means that ferrocenyl fragments are not only bound to the NH_2-functionalized linker, but also on the extra binding sites of the unsaturated zinc nodes. It is thus possible to obtain ferrocenyl loadings higher than the expected amount, as the ferrocenyl fragments are bound in the form of amides or coordinated to the zinc.

Since only, LeZIF8-NH_2BzIm-FcC=N and LeZIF8-NH_2BzIm-FcCO, show significant binding of ferrocenyl fragments, they were selected for further analyses (porosity and TGA).

3.4.1.5 Porosity Analysis

The typical type-1 isotherms of LeZIF8-NH_2BzIm-FcC=N (**a**) and LeZIF8-NH_2BzIm-FcCO (**b**) (**Figure 3.55, p 140**) show that the compounds remain microporous. The nitrogen adsorption at 0.8 p/p° decreased from 418 (LeZIF8-NH_2BzIm_{16h} starting material) to 326 and 243 $cm^3\ g^{-1}$ for LeZIF8-NH_2BzIm-FcC=N and LeZIF8-NH_2BzIm-FcCO respectively.

When modified with ferrocencecarboxaldehyde the BET surface area of LeZIF8-NH_2BzIm-FcC=N (1206 $m^2\ g^{-1}$) remains similar to that of unmodified LeZIF8-NH_2BzIm_{16h} (1216 $m^2\ g^{-1}$) and it maintained a micropore volume of 0.359 $cm^3\ g^{-1}$ even though a decrease in N_2 adsorption was observed (**Table 3.13, p 140**). However, with an increased loading of FcCOOH the BET surface area decreased drastically to 243 $m^2\ g^{-1}$, and similarly the micropore volume was reduced to 0.194 $cm^3\ g^{-1}$, possibly due to the blocking of the pores by ferrocene fragments grafted to the external surface of the nanoparticles. The t-plot external surface areas of 323 and 275 $m^2\ g^{-1}$ for LeZIF8-NH_2BzIm-FcC=N and LeZIF8-NH_2BzIm-FcCO respectively, correlates to the nanoparticles' size of ~22 nm for both compounds.

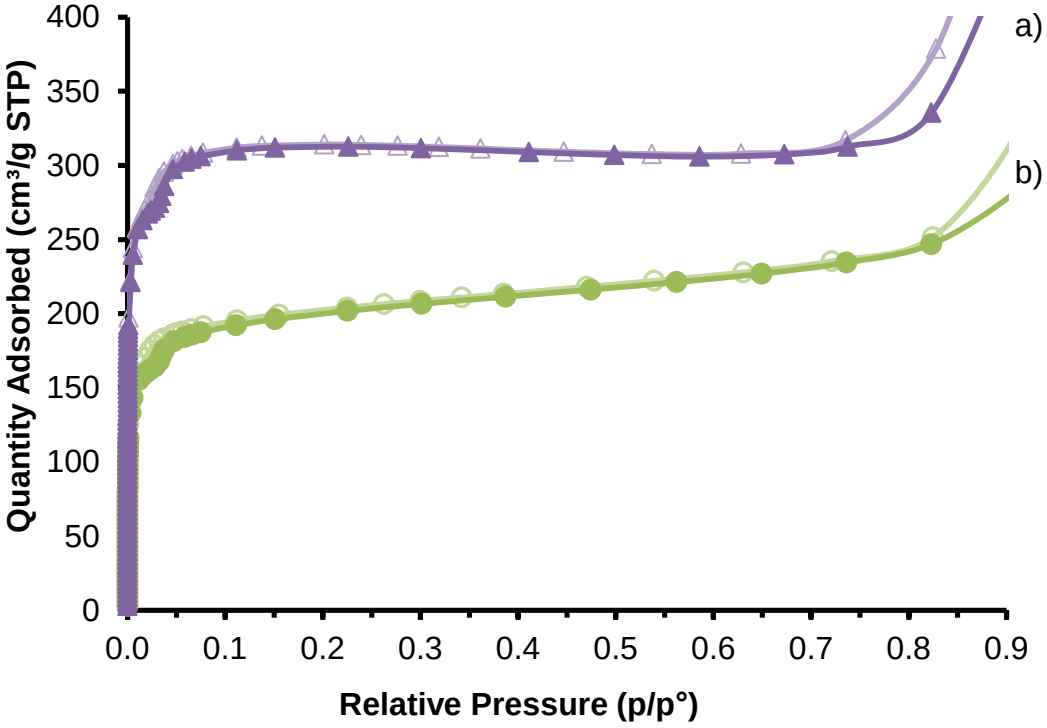

Figure 3.55 Nitrogen adsorption and desorption isotherms at 77 K of a) LeZIF8-NH_2BzIm-FcC=N and b) LeZIF8-NH_2BzIm-FcCO. Adsorption marked as solid and desorption as hollow symbols.

Table 3.13 N_2 porosity analyses at 77 K of LeZIF8NH_2BzIm post-synthetically modified with ferrocene derivatives. Quantities adsorbed were measured at 0.8 p/p°.

Compound	Quantity Adsorbed/ $cm^3\ g^{-1}$	BET Surface Area/ $m^2\ g^{-1}$	t-plot External Surface Area/ $m^2\ g^{-1}$	Micropore volume/ $cm^3\ g^{-1}$
LeZIF8-NH_2BzIm$_{16h}$	418	1216	318	0.350
LeZIF8-NH_2BzIm-FcC=N	326	1206	323	0.359
LeZIF8-NH_2BzIm-FcCO	243	760	275	0.194

3.4.1.6 Thermogravimetric Analysis (TGA)

The thermogram of LeZIF8-NH_2BzIm-FcC=N (**Figure 3.56.a, p 141**) shows three mass loss steps: The first step with a mass loss of 3.9 % is associated with the decomposition of the ferrocenyl fragments bound to the ZIF-8 structure. The second and third step corresponds to the thermal decomposition and collapse of the nZIF-8 structure. The thermogram of LeZIF8-NH_2BzIm-FcCO (**Figure 3.56.b, p 141**) shows a multiple mass loss steps: the initial step at 222 ℃ can be associated with the loss of weak bound ferrocene with a mass loss of 1.5 %; The second step at 312 ℃ with a mass loss of 23 %, is attributed to the decomposition of exchanged ligands as well as bound ferrocenyl fragments (seen in NMR); the last two steps after 473 ℃ is the decomposition and the collapse of the nZIF-8 backbone structure. This concludes that all the PSM nZIF-8 compounds with ferrocene remains stable up to 220 ℃.

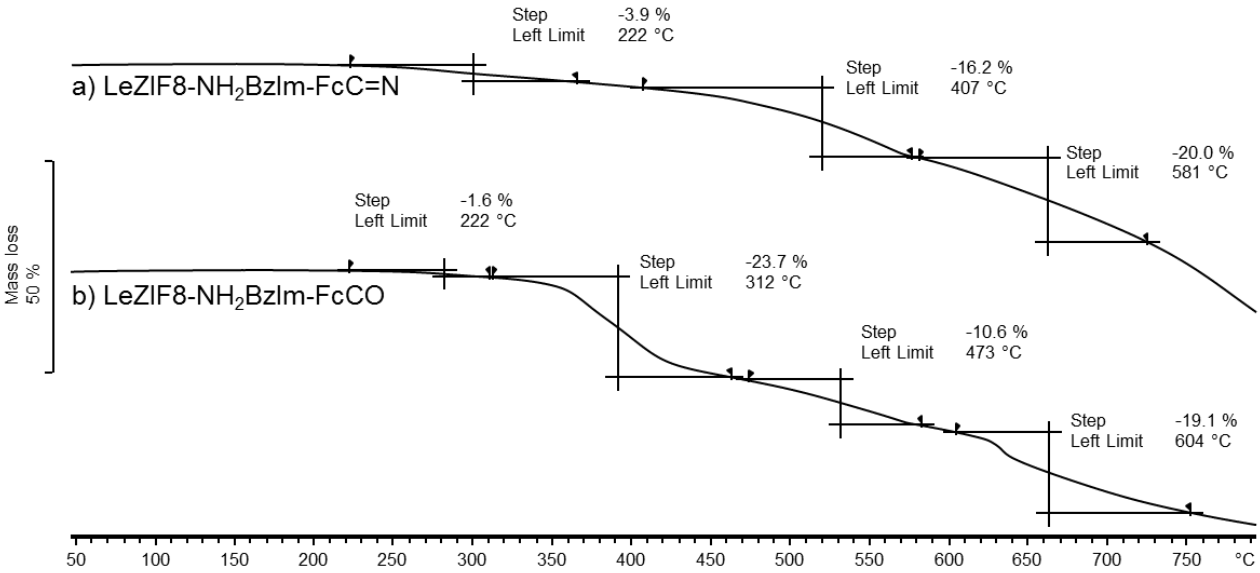

Figure 3.56 TGA thermograms under a nitrogen atmosphere of a) LeZIF8-NH_2BzIm-FcC=N and b) LeZIF8-NH_2BzIm-FcCO.

3.4.2 Modification of SALEM-with $(PPh_3)_2PdCl_2$

3.4.2.1 Synthesis

The effect on lithiation of SALEM-2, as a possible method to anchor $(PPh_3)_2PdCl_2$ *via* the formation of N-heterocyclic carbene sites, was investigated.[39] Another possible outcome of the process is the thermal decomposition of $(PPh_3)_2PdCl_2$ followed by incorporation of the resultant palladium compounds in the pores of SALEM-2 (**Scheme 3.12, p 142**).

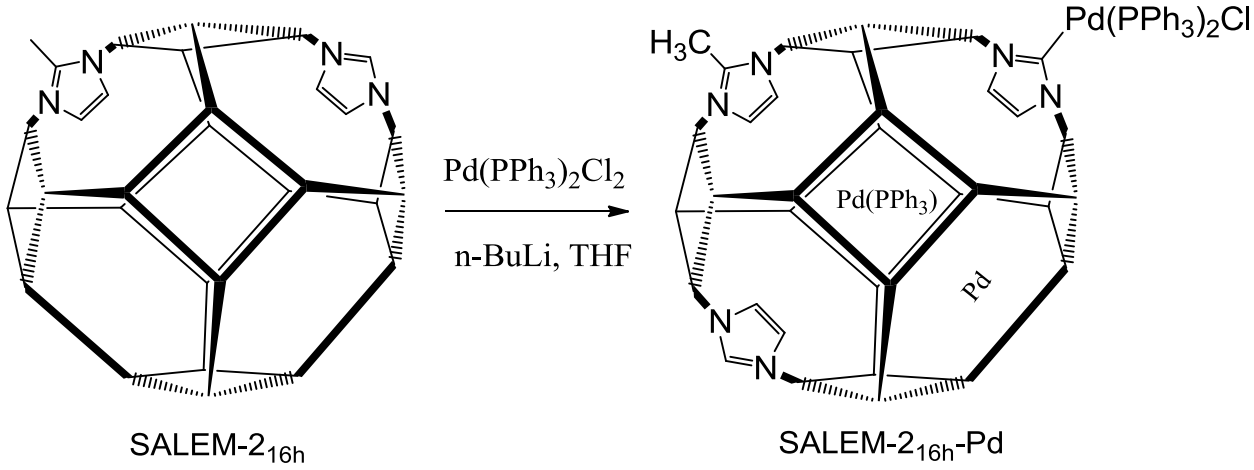

Scheme 3.12 Post Synthetic Modification of lithiated SALEM-2 with $(PPh_3)_2PdCl_2$.

In the synthesis, modified from literature,[39] a suspension of SALEM-2 nanoparticles in dry THF was treated with *n*-BuLi at -78 °C. After the suspension turned light yellow, $(PPh_3)_2PdCl_2$ was added and the mixture stirred for 24 hours at room temperature under argon. From the dark red suspension the nanoparticles were isolated, washed, dried and activated at 100 °C under vacuum. A grey powder was obtained and denoted as SALEM-2_{16h}-Pd with a yield of 60 % based on SALEM-2. The chlorine detected in the sample overlaps at the position of palladium.

3.4.2.2 Characterisation

FTIR (**Figure 3.57.a, p 143**), digestive ^{1}H NMR and ^{13}C Solid-state NMR (**Appendix B.9**) spectra of SALEM-2_{16h}-Pd were all identical to the corresponding spectra of the SALEM-2 starting material (**Figure 3.19, p 87**), without detecting any additional peaks. During digestion, a black precipitate was observed in the ^{1}H NMR solution. The SOD topology and crystallinity as well as the spherical shape of SALEM-2 was maintained during lithiation and PSM as seen from the identical PXRD pattern and TEM images (**Figure 3.57, p 143**) of SALEM-2-Pd. The

nanoparticles of SALEM-2-Pd have an average diameter of 31.8 nm (TEM) and a calculated minimum particle size of 21 nm (PXRD). EDS of the TEM image show the presence of palladium at ~2.6 eV. The chlorine detected in the sample overlaps at the position of palladium.

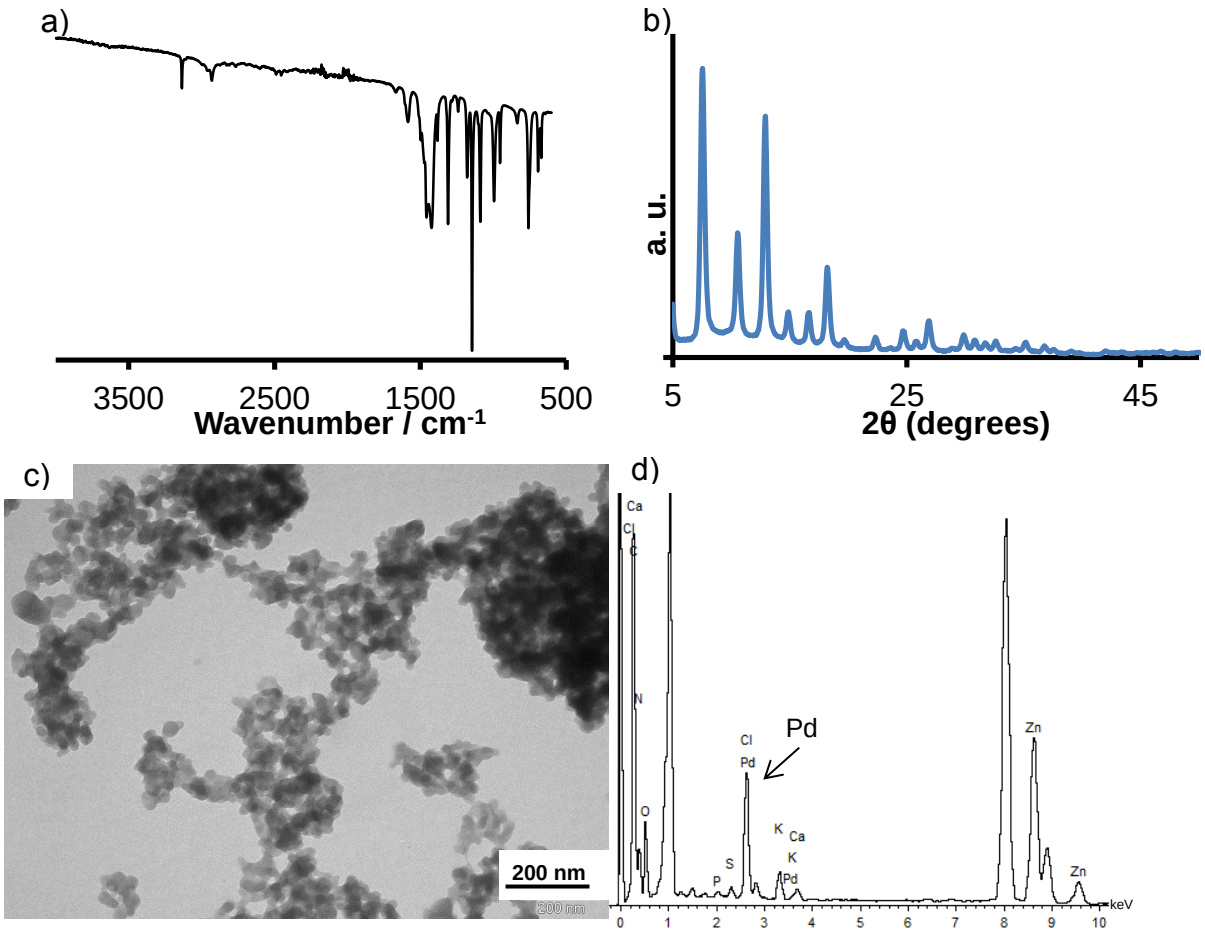

Figure 3.57: a) FTIR spectra, b) PXRD pattern, c) TEM image and d) EDS of TEM image of SALEM-2_{16h}-Pd.

The XPS spectrum of SALEM-2-Pd (**Figure 3.58, p 144**) shows that the N 1s orbital has a binding energy of 398.9 eV and that the Zn signals appear as two separate peaks and are deconvoluted for the $2p_{1/2}$ orbital: 1044.6 and 1042 eV and $2p_{3/2}$ orbital: 1021 and 1019.1 eV. The palladium signal appears as two separate peaks for the $3d_{3/2}$ and $3d_{5/2}$ orbitals with binding energies of 341.7 and 336.3 eV. This indicates that the palladium was reduced to Pd^0 metal and/or $Pd(PPh_3)_2$, both with a 0 oxidation state with a reported binding energy of 336.4 eV for the $3d_{5/2}$ orbitals.[40] Pd^{2+}, as in $(PPh_3)_2PdCl_2$, should have a binding energy of ~338 eV. The presence of Pd^0 thus suggests that the expected phosphineimidazolylidene palladium complex on SALEM-2 is unstable, and that the complex, $Pd(PPh_3)_2$ and/or palladium metal was mainly incorporated within in pores or on the external surface of SALEM-2-Pd. The XPS estimated the Pd:Zn ratio as 0.008 (0.85 wt %). Another, more accurate, quantitative test was performed, with

ICP-OES showing that the SALEM-2_{16h}-Pd compound has a Pd loading of 1.24 wt % with a 95 % confidence.

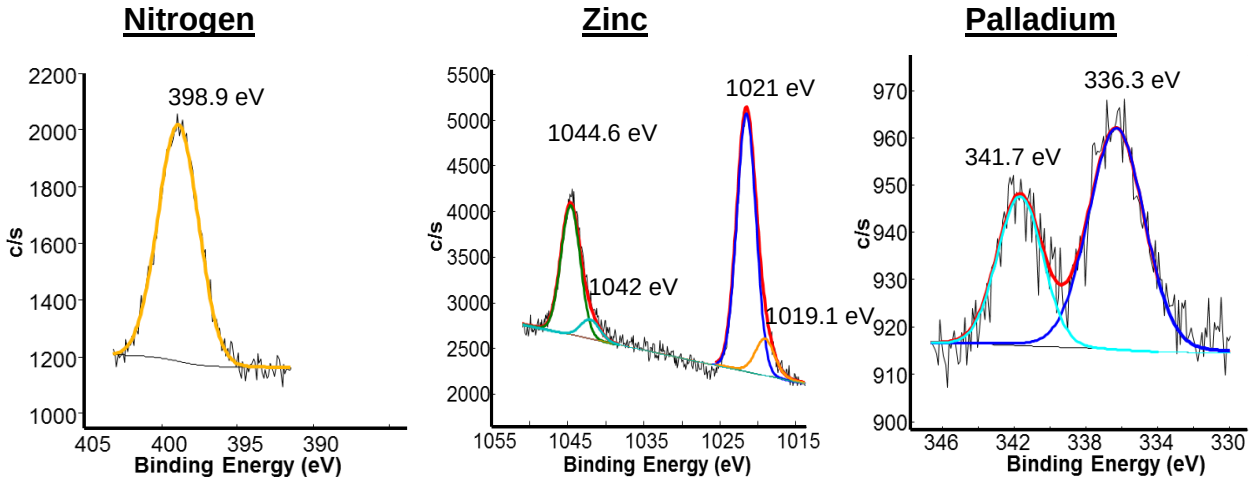

Figure 3.58 XPS peaks for the N, Zn and Pd in SALEM-2_{16h}-Pd. Red line: theoretical fit. Other lines: Peaks introduced to replicate the experimental fit.

A typical Type-1 isotherm was obtained after activation of SALEM-2_{16h}-Pd at 150 ℃ for 16 hours showing that the material is microporous. The material adsorbed 429 $cm^{-3}\,g^{-1}$ of nitrogen at 0.8 p/p° at 77 K, with a BET surface area of 1456 $m^2\,g^{-1}$, a micropore volume of 0.443 $cm^3\,g^{-1}$ and a t-plot external surface area of 284 $m^2\,g^{-1}$. These values correlate well with those of SALEM-2 starting material (**Table 3.4, p 72**). The loading of palladium within the pores assisted the porosity of SALEM-2. The BET surface area increased by ~10 $m^2\,g^{-1}$ and the micropore volume by ~0.03 $cm^3\,g^{-1}$ compared to unmodified SALEM-2 (**Chapter 3.3.1, p 82**).

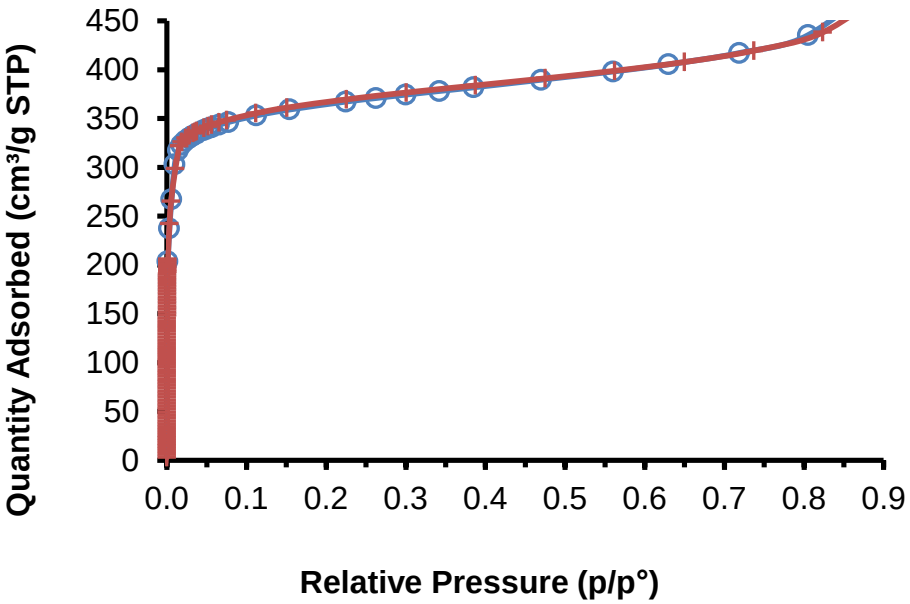

Figure 3.59 Nitrogen adsorption and desorption isotherm of SALEM-2_{16h}-Pd. Adsorption marked as solids and desorption as hollow symbols.

After PSM with $(PPh_3)_2PdCl_2$ the thermal stability limit of SALEM-2_{16h}-Pd was reduced from 400 ℃ (SALEM-2) to 344 ℃, with a first mass loss step of 25 % (**Figure 3.60, p 145**).

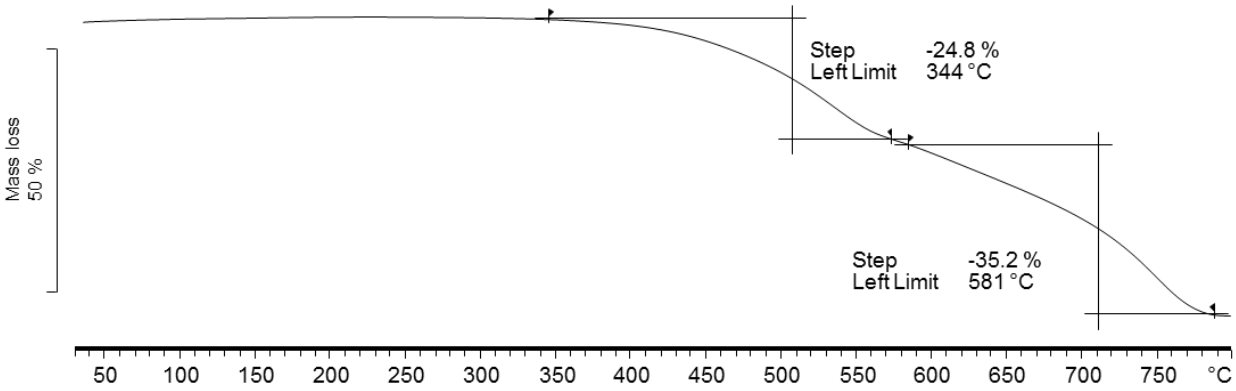

Figure 3.60 TGA thermogram, under nitrogen, of SALEM-2_{16h}-Pd.

3.4.3 Amidation of nZIF8-NH_2BzIm with Sebacoyl chloride and PAA-Cl

3.4.3.1 Synthesis

The nZIF8-NH_2BzIm nanoparticles with amine groups on the external surface area were post synthetically modified with sebacoyl chloride with a chain of 10 carbon atoms, as well as with polyacrylic acid (PAA) with a mw of ~2500 (**Scheme 3.13, p 146**). The effect of the attachment of short alkyl chains (Sebacoyl chloride) to the nanoparticle surface was compared to the effect of long alkyl chains (PAA). Sebacoyl chloride contains acyl chlorides on both ends and could be used for interlinking of the ZIF nanoparticles. Modifications with PAA may cause the nanoparticles to be "string" together on the long polymer chain.

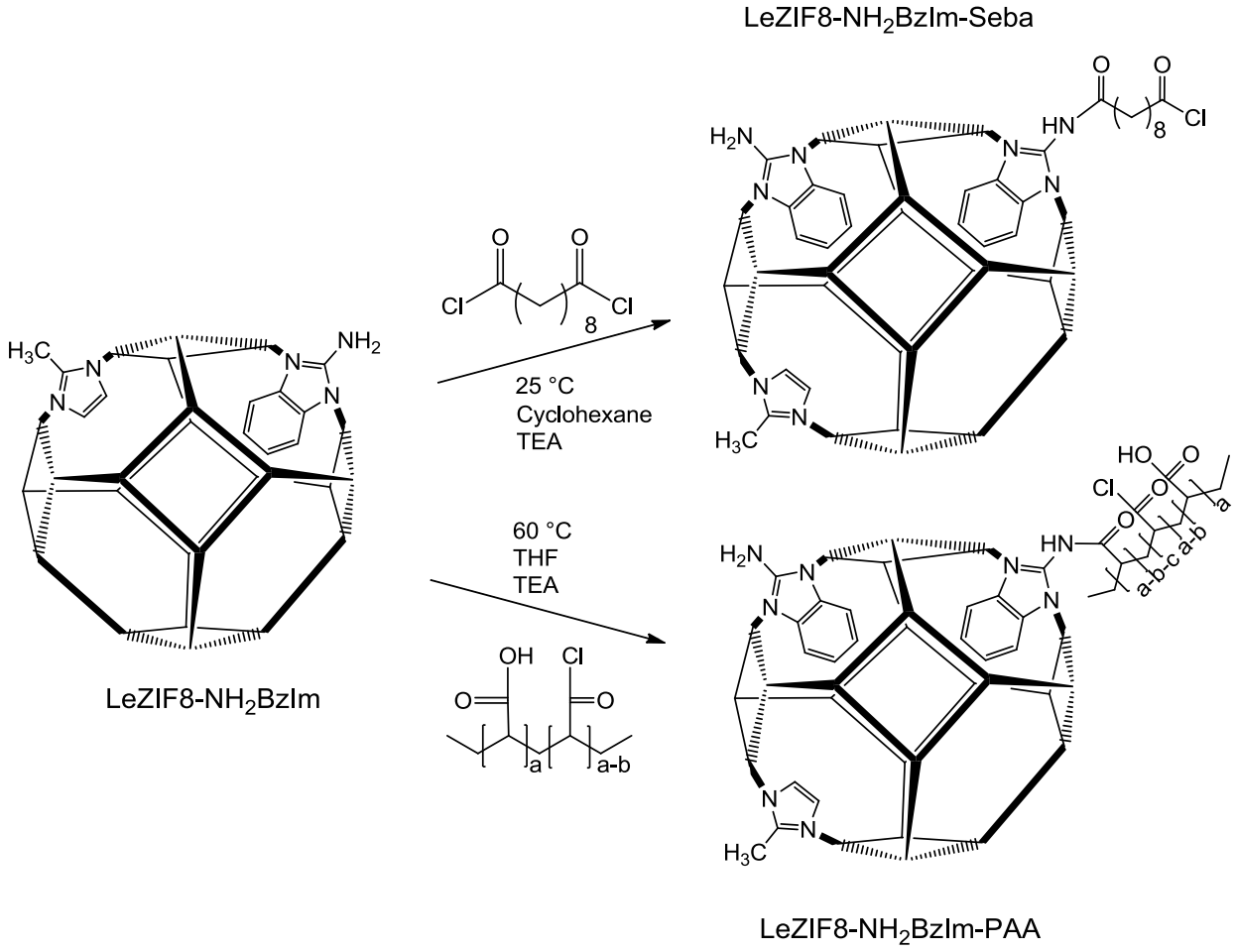

Scheme 3.13 Post Synthetic Modification of LeZIF8-NH_2BzIm with sebacoyl chloride (top) and Polyacrylic acid (bottom) to synthesise LeZIF8-NH_2BzIm-Seba and LeZIF8-NH_2BzIm-PAA.

A LeZIF8-NH_2BzIm$_{4h}$ (5 % exchanged) suspension in cyclohexane with TEA, as a base, was stirred with sebacoyl chloride for only 10 minutes to prevent gel formation as was observed with longer reaction times. The nanoparticles were isolated, washed and dried at 100 ℃ to obtain a light brown product denoted as LeZIF8-NH_2BzIm-Seba (100 % yield).

Prior to PSM of LeZIF8-NH_2BzIm$_{4h}$ with PAA, the polymer was treated with thionyl chloride in acetonitrile to chlorinate the carboxylic acid groups and give PAA-Cl, which was washed and dried for the next step. The PAA-Cl was dissolved in THF with TEA under argon, mixed with a suspension of LeZIF8-NH_2BzIm$_{4h}$ and stirred for 24 hours at 60 ℃. The product was isolated, washed and dried to give a white powder, denoted as LeZIF8-NH_2BzIm-PAA (83 % yield).

3.4.3.2 Characterisation

The structural integrity of the LeZIF8-NH_2BzIm$_{4h}$, through the PSM process, with sebacoyl chloride and polyacrylic acid was determined with PXRD (**Figure 3.61, p 148**). From the PXRD patterns LeZIF8-NH_2BzIm-Seba (**a**) and LeZIF8-NH_2BzIm-PAA (**b**) both maintained the SOD topology (compared to **Figure 3.37, p 115**) with a theoretical minimum particle size of 19.5 and 16.9 nm respectively.

The TEM image of LeZIF8-NH_2BzIm-Seba (**a**) (**Figure 3.61, p 148**) shows that it has an average a particle size of 30.3 nm. Some particles are interlinked with each other without much agglomeration (**a**). The reaction with PAA-Cl to form LeZIF8-NH_2BzIm-PAA (**Figure 3.61.b, p 148)** revealed a mixture of structures: nanoparticles of ~20 nm and larger spherical particles with an average of 165 nm in diameter. The latter could indeed be nanoparticles strung together on the PAA chains.

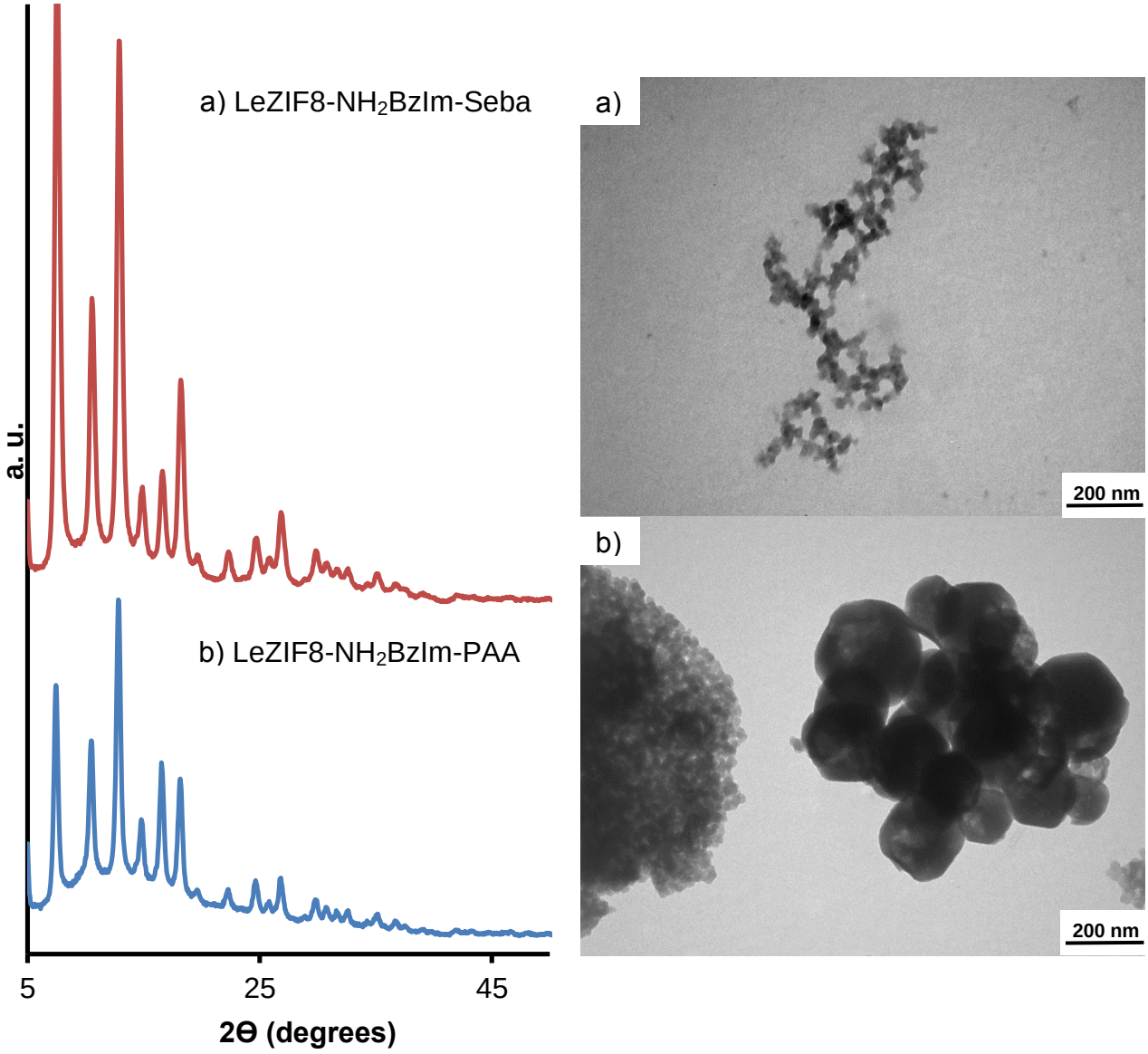

Figure 3.61 PXRD patterns (left) and TEM images (right) of a) LeZIF8-NH_2BzIm-Seba and b) LeZIF8-NH_2BzIm-PAA.

LeZIF8-NH_2BzIm-Seba and LeZIF8-NH_2BzIm-PAA was activated at 150 °C for 16 hours prior to porosity analyses (**Table 3.14, p 149**), resulting in Type-1 isotherms for both materials (**Figure 3.62, p 149**). LeZIF8-NH_2BzIm-Seba (**a**) adsorbed only 78 cm^3 of nitrogen at 0.8 p/p° compared to the 469 cm^3 g^{-1} of LeZIF8-NH_2BzIm_{4h} starting material. Similarly the BET surface area decreased significantly from 1523 m^2 g^{-1} (LeZIF8-NH_2BzIm_{4h}) to 203 m^2 g^{-1} for LeZIF8-NH_2BzIm-Seba, because of the nanoparticles reduced crystallinity. Its micropore volume of 0.042 cm^3 g^{-1} is much smaller than that of the LeZIF8-NH_2BzIm_{4h} (0.441 cm^3 g^{-1}) starting material. The t-plot external surface area of 107 m^2 g^{-1} for LeZIF8-NH_2BzIm-Seba is less than half that of the starting material (325 m^2 g^{-1}), due to the interlinked particles reducing the surface area.LeZIF8-NH_2BzIm-PAA adsorbed 343 cm^3 g^{-1} of nitrogen and maintained a BET surface

area of 1081 m^2 g^{-1} and a micropore volume of 0.324 cm^3 g^{-1}. The t-plot external surface area of 229 m^2 g^{-1} confirms that a mixture of small and large particles exists as seen in TEM.

Table 3.14 N_2 porosity analysis at 77 K of LeZIF8-NH_2BzIm-Saba and LeZIF8-NH_2BzIm-PAA. Quantities adsorbed were measured at 0.8 p/p°.

Compound	Quantity Adsorbed/ cm^3 g^{-1}	BET Surface Area/ m^2 g^{-1}	t-plot External Surface Area/ m^2 g^{-1}	Micropore volume/ cm^3 g^{-1}
LeZIF8-NH_2BzIm$_{4h}$ (5 %)	469	1523	325	0.441
LeZIF8-NH_2BzIm-Seba	78	203	107	0.042
LeZIF8-NH_2BzIm-PAA	343	1081	229	0.324

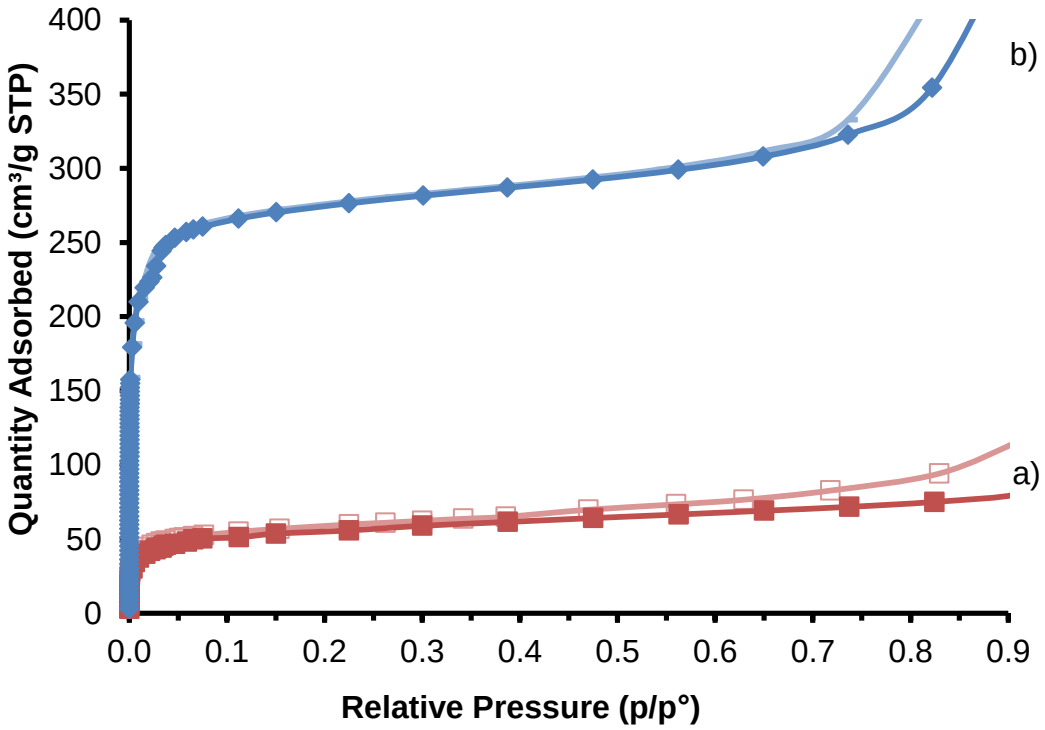

Figure 3.62 Nitrogen isotherms at 77K of a) LeZIF8-NH_2BzIm-Seba and b) LeZIF8-NH_2BzIm-PAA. Adsorption marked as solid and desorption as hollow symbols.

The FTIR spectra in **Figure 3.63** (**p 150**) show that the finger print region, below 1500 cm^3, of both of LeZIF8-NH_2BzIm-Seba (**a**) and LeZIF8-NH_2BzIm-PAA (**b**) correlate well with the fingerprint region of the starting material, to LeZIF8-NH_2BzIm (**c**). A peak at 1731 cm^{-1} (i)

represents the unbound C=O stretching frequency, while the C=O stretch peak at 1649 cm^{-1} (ii) is shifted to a lower wavenumber after formation of the amide bond. The broad peak between 3000 and 3500 cm^{-1} (iii) could be due to the OH-stretching, giving evidence that the unreacted ends of sebacoyl chloride are unstable, forming sebacic acid. Only one peak at ~3330 cm^{-1} (iv) remains for the secondary N-H stretching frequency. The presence of the 10-carbon alkyl chain is observed at 2921 cm^{-1} (v) for sp^2 C-H stretching and at 2850 cm^{-1} (vi) sp^3 for C-H Stretching frequency. When compared to the FTIR spectrum of LeZIF8-NH_2BzIm$_{4h}$ (**c**), LeZIF8-NH_2BzIm-PAA (**b**) show strong peaks at 1570 cm^{-1} (vii) and 1629 cm^{-1} (viii) cm^{-1}, evidence of the N-H bend and C=O stretching frequencies of the amide bond formed during PSM.

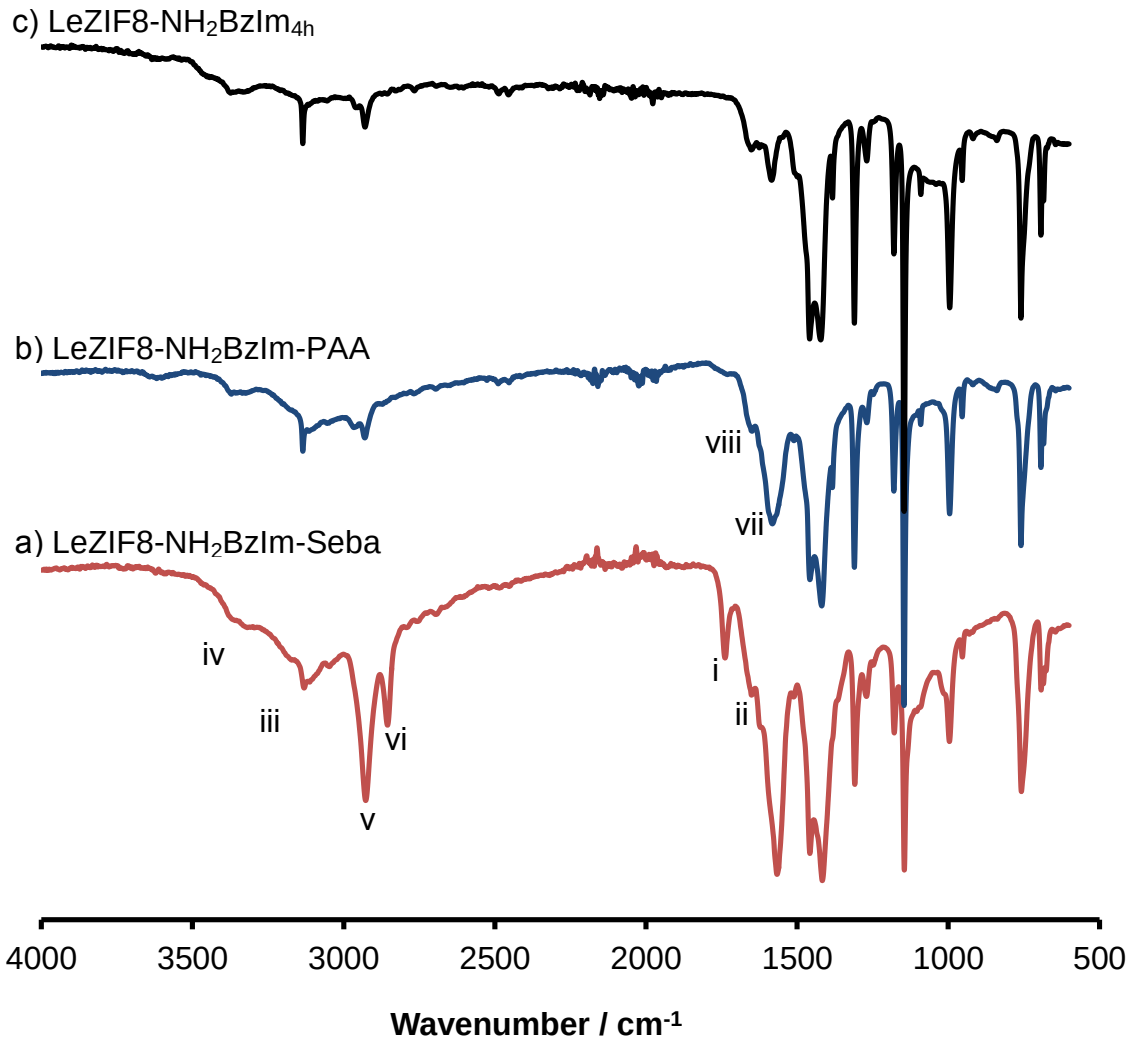

Figure 3.63 FTIR spectra of a) LeZIF8-NH_2BzIm-Seba, b) LeZIF8-NH_2BzIm-PAA and c) LeZIF8-NH_2BzIm$_{4h}$.

Solid-state ^{13}C NMR of LeZIF8-NH_2BzImSeba (**Figure 3.64.b, p 151**) show additional peaks when compared to the spectrum of LeZIF8-NH_2BzIm (**a**): The peaks between 20 to 45 ppm represent the 6 middle carbon atoms of the alkyl chain between the carbonyl ends of the attached

C_{10} sebacoly chloride fragments. The signal for the two carbon atoms of the C_{10} chain adjacent to the carbonyl ends is found at 52.5 ppm. The peaks between 113 to 124 ppm represent the benzene carbon atoms on the linkers.

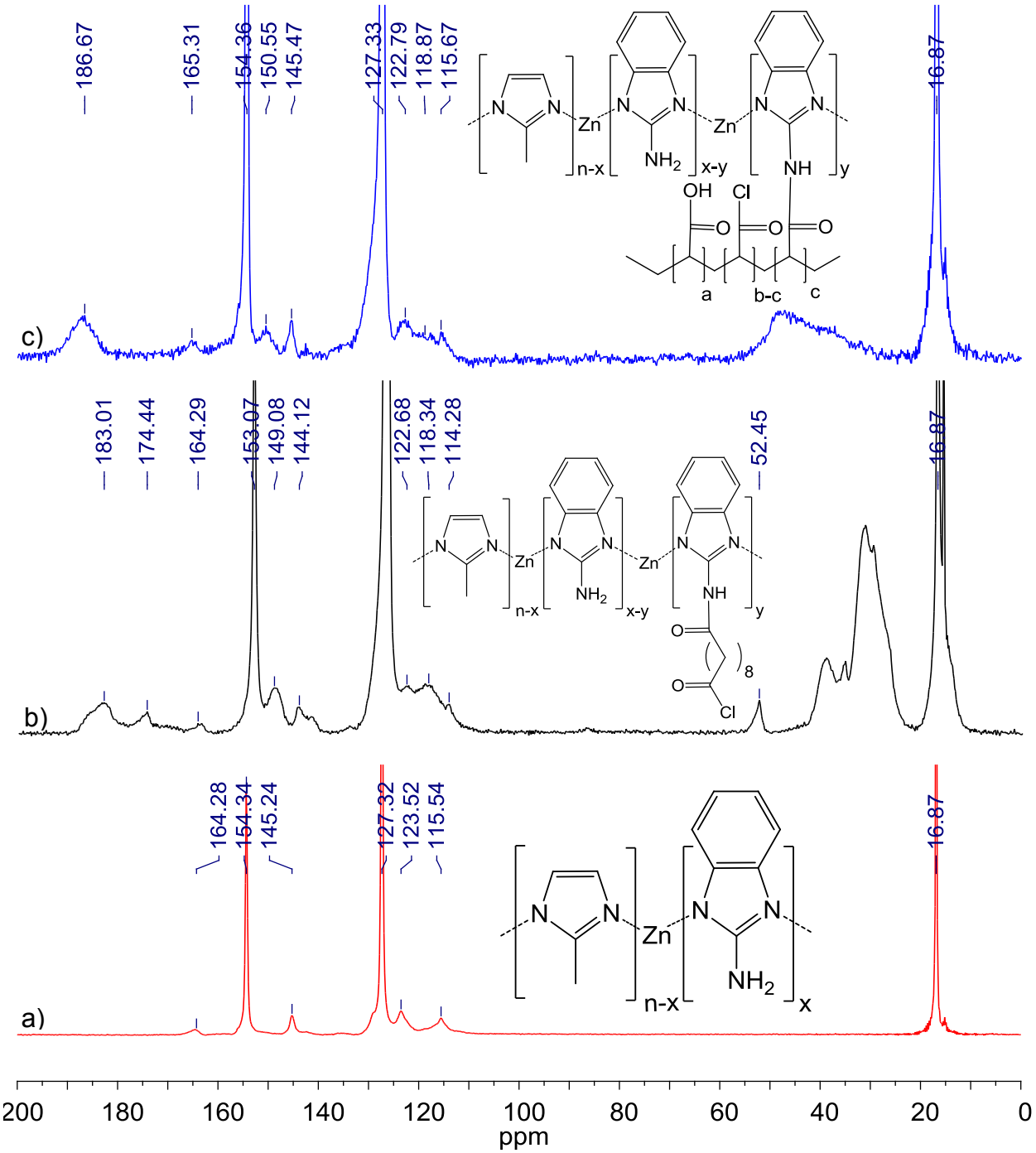

Figure 3.64 Solid-state ^{13}C NMR spectra of a) LeZIF8-NH_2BzIm$_{4h}$, b) LeZIF8-NH_2BzIm-Seba and c) LeZIF8-NH_2BzIm-PAA.

The broad peak at ~118 ppm represents the shifted resonance of the benzene carbon atoms after amide bond formation. This can also be seen for LeZIF8-NH_2BzIm-PAA. In addition, the carbon atom of the amide bond resonates at 149 ppm, confirming bond formation. The carbon atoms of

the unreacted C-NH_2 resonate at 164.29 ppm, while two additional peaks resonate at 174.44 and 183 ppm for the unreacted acyl chloride and carboxylic acid carbon atoms (at the loose end of the C_{10} chain) respectively. The LeZIF8-NH_2BzIm-PAA (**b**) spectrum shows a similar pattern to sebacoyl chloride, with the alkyl carbon chain of the PAA polymer giving a broad peak between 30 to 50 ppm. The amide carbon atom resonating at 150 ppm is present as well as the signal for the carbon atoms of the unreacted carboxylic acid, at 186 ppm.

The TGA thermogram of LeZIF8-NH_2BzIm-Seba (**Figure 3.65.a, p 152**) shows a first mass loss step after ~145 ℃, attributed to the decomposition of both the attached sebacoyl chloride fragments and the 2-aminobenzimidazolate linker. The presence of the long alkyl chain of the sebacoyl fragment lowers the thermal stability of LeZIF8-NH_2BzIm starting material, which is thermally stable up to 250 ℃. TGA analysis of LeZIF8-NH_2BzIm-PAA (**Figure 3.65.b, p 152**), show multiple steps with the first step at 53 ℃ which can be associated with PAA trapped water leaving the material. The compound remain stable up to 180 ℃ with a second mass loss of 8.8 % for the decomposition of the attached PAA. After 385 ℃ thermal degradation of the nZIF-8 structure follows.

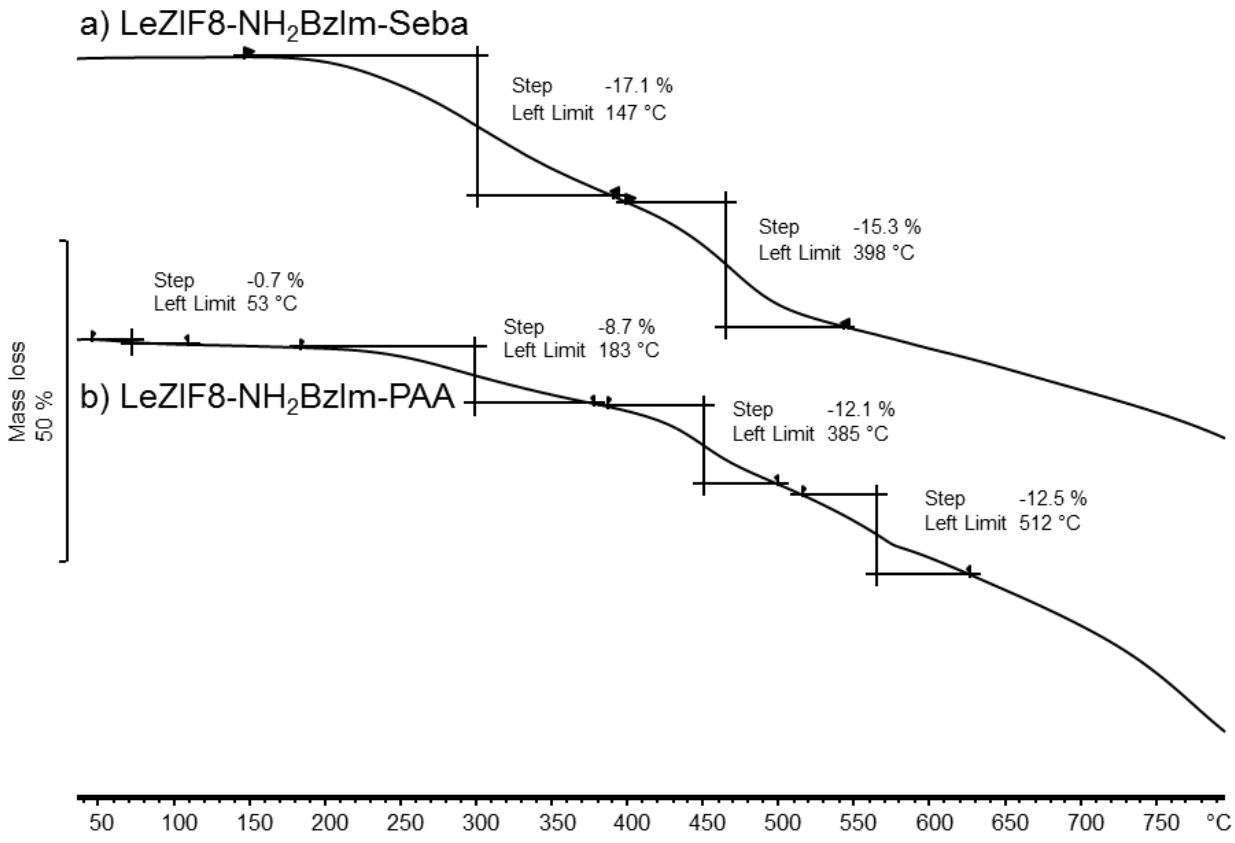

Figure 3.65 TGA thermograms under a nitrogen atmosphere of a) LeZIF8-NH_2BzIm-Seba and b) LeZIF8-NH_2BzIm-PAA.

3.5 Catalytic Testing via Knoevenagel condensation

The catalytic activity of nZIF-8 and solvent assisted ligand exchanged nZIF-8 nanoparticles were investigated utilizing the Knoevenagel condensation reaction between ferrocenecarboxaldehyde (FcCHO) and malononitrile in THF (**Scheme 3.14, p 153**), optimized for this reaction at 50 °C. Selected catalysts: nanoparticles of nZIF-8, LeZIF8-NH_2BzIm (exchanged for 4, 16 and 168 hours) and SALEM-2 (exchanged for 4 and 168 hours). The catalytic activities of these heterogeneous catalysts will be compared to the activities of 2-methylimidazole and 2-aminobenzimidazole, employed as homogeneous catalysts as well as a reaction without any catalyst.

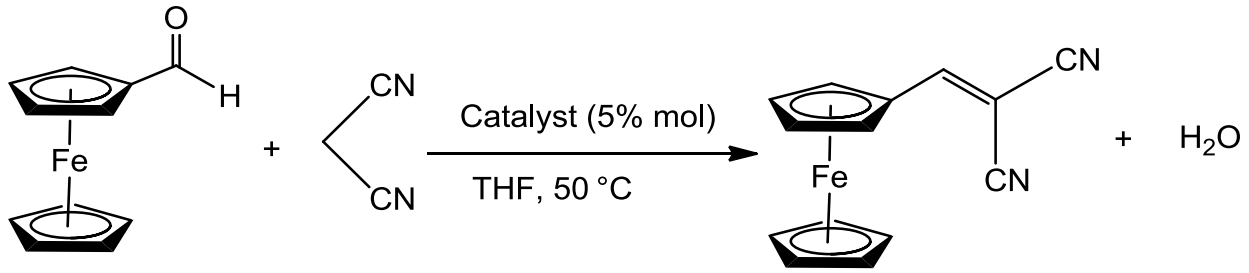

Scheme 3.14 Knoevenagel condensation reaction scheme of ferrocenecarboxaldehyde and malononitrile with ZIF catalyst to synthesis 1,1-dicyanovinyl-2-ferrocene in THF at 50 °C.

The catalytic reaction (**Scheme 3.14, p 153**) was monitored by UV/vis spectroscopy, using the slight colour change from the ferrocenecarboxaldehyde reagent to the 1,1-dicyanovinyl-2-ferrocene product. Because of the high absorbance intensity of the product, the reactions were performed at low concentrations, with the limitations of the instrument. A higher reaction rate was achieved by an increased concentration of the colourless malononitrile reagent. Increasing the rate will reduce experimental error and solvent evaporation over prolonged periods. Various FcCHO:malonotrile ratios, ranging from 1:1, 3:1 and 5:1, were employed with 5% mole of catalyst. The aliquots extracted at regular time intervals were diluted 1000 times in cold THF to quench the reaction. The dilution ensures that the absorbance remains within instrumental limits. The UV/vis absorbance spectrum between 370 to 730 nm (**Figure 3.66, p 154**) shows that FcCHO has a maximum absorbance at 450 nm and the product, 1,1-dicyanovinyl-2-ferrocene, at 522 nm. Due to interference from the FcCHO peaks up to at 560 nm, 570 nm was used to monitor the evolution of product.

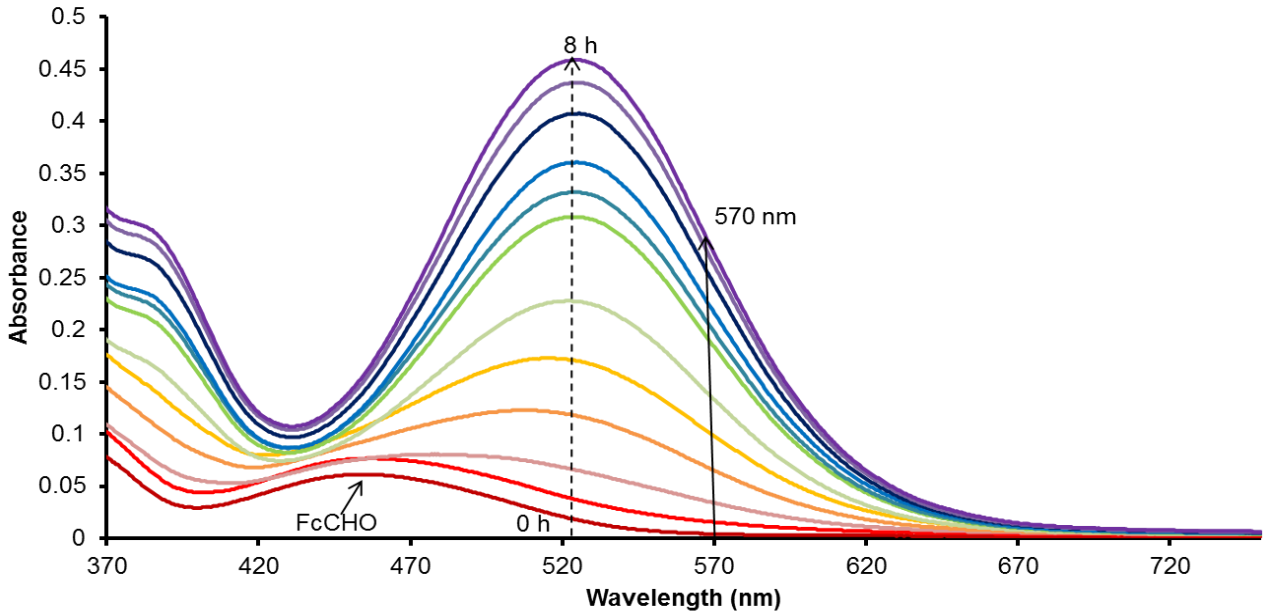

Figure 3.66 UV/vis absorbance spectra *vs.* wavelength, time resolved for the Knoevenagel condensation of ferrocenecarboxaldehyde and malononitrile (1:5 ratio) with nZIF-8 as catalyst between 0 and 8 hours' reaction time.

The absorbance *vs.* time graph (see **Figure 3.67, p 154**), obtained for each ratio, shows that by increasing the malononitrile concentration the reaction reached completion within 8 hours with a 1:5 ratio. The turnover frequency calculated (TOF) for the first 4 hours are tabulated in (**Table 3.15, p 155**). The TOF of 0.46, 1.18 and 2.61 h^{-1} was determined for 1:1, 1:3 and 1:5 reagent ratio. The reaction rate increased by 5.7 fold when the malononitrile ratio is increased from to 5.

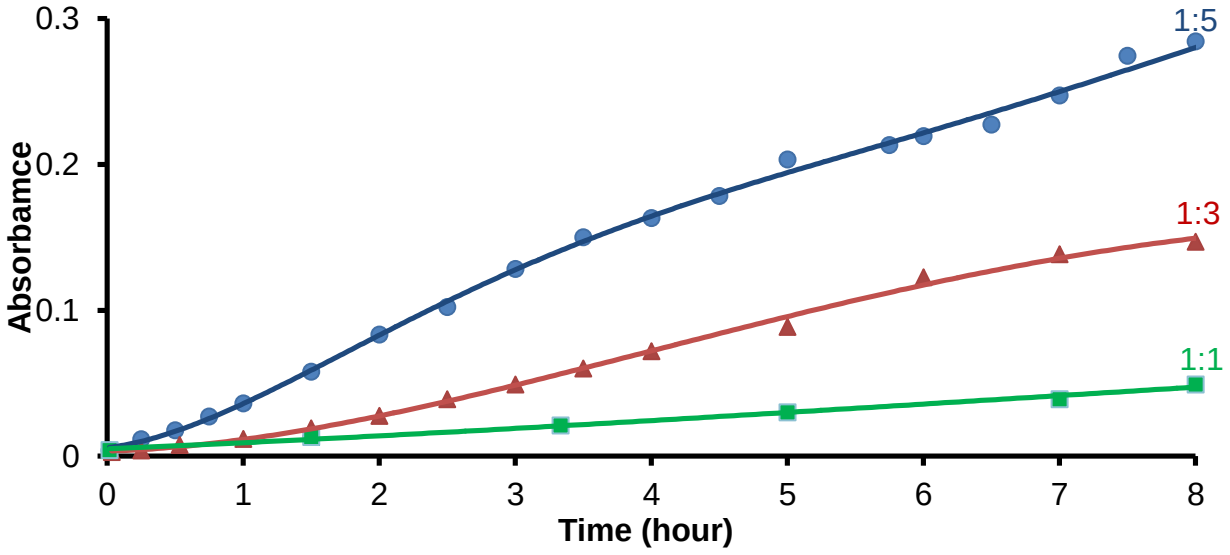

Figure 3.67 Absorbance (at 570 nm) *vs.* time groups of Knoevenagel condensation between ferrocenecarboxaldehyde and malononitrile with ratios of 1:1 (green), 1:3 (red) and 1:5 (blue), and nZIF-8 as catalyst.

Table 3.15 nZIF-8 derivatives used as catalysts with the respective ratios of ferrocenecarboxaldehyde and malononitrile during Knoevenagel condensation. Turnover frequencies (TOF) were determined at 4-hour intervals. For reference purposes, 2-methylimidazole and 2-aminobenzimidazole were employed as homogeneous catalysts. TOF and t-plot external surface areas are compared.

Catalyst	Ratio (FcO:malononitrile)	TOF/ h^{-1}	t-plot external surface area/ m^2 g^{-1}
nZIF-8	1:1	0.46	321
nZIF-8	1:3	1.18	321
nZIF-8	1:5	2.61	321
No catalyst	1:5	0.18	-
LeZIF8-NH_2BzIm$_{4h}$ (5 %)	1:5	1.76	326
LeZIF8-NH_2BzIm$_{16h}$ (10 %)	1:5	1.92	318
LeZIF8-NH_2BzIm$_{168h}$ (16 %)	1:5	2.37	320
SALEM-2$_{4h}$ (28 %)	1:5	2.29	268
SALEM-2$_{168h}$ (86 %)	1:5	0.48	74
2-methylimidazole*	1:5	4.36	-
2-aminibenzimdazole*	1:5	4.15	-
$Zn(NO_3)_2.4H_2O$*	1:5	1.87	-

*Homogeneous catalyst

In addition to nZIF-8, LeZIF8-NH_2BzIm (4, 16 and 168 hours) and SALEM-2 (4 and 168 hours) was selected as heterogeneous catalysts and employed under identical conditions with FcCHO:Malononitrile of 1:5. The absorbance (at 570 nm) *vs.* time graph of each catalyst are represented in **Figure 3.69 (p 157**) and the TOF values given in **Table 3.15 (p 155**). After SALE of nZIF-8 with imidazolate linkers, the TOF decreased to 2.29 and 0.48 h^{-1} for SALEM-2$_{4h}$ (28 % exchange) and SALEM-2$_{168h}$ (86 % exchange) respectively. This represents a 13 % and 81 % decrease in reactivity after SALE with imidazole for 4h and 168h respectively, when compared to nZIF-8. After SALE with 2-aminobenzimidazole for 4h (5 % exchange), 16h (10 % exchange) and 168h (16 % exchange), the nanoparticles gave a TOF values of 1.76, 1.92 and 2.37 h^{-1} respectively. Reactivity of the amino-exchanged products was thus decreased with respect to nZIF-8. However, with an increase of amino groups, from 5 till 16 %, the reactivity was improved 25 %. Without the addition of catalyst, no product formation was detected within the first 8 hours.

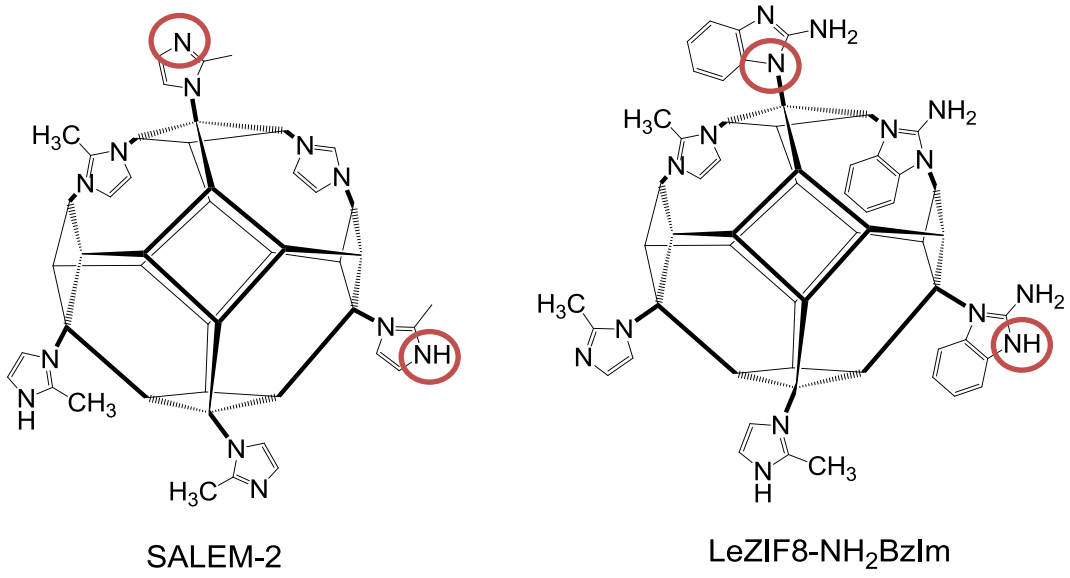

Figure 3.68 Different orientation of imidazolate linkers binding on the zinc terminal nodes of SALEM-2 and LeZIF8-NH_2BzIm.

The SALE process clearly has an effect on the catalytic activity. Ferrocenecarboxaldehyde molecules has kinetic diameter of 6.4 Å and ZIF-8 has an opening of 3.4 Å, thus the catalytic activity mainly occurs on the external surface of the nanoparticle.[41] It can be postulated that during the SALE, under basic conditions, the 2-methylimidazolate linkers with free NH groups protruding from the terminal zinc nodes (see **Figure 3.68, p 156**) on the external surface, are exchanged with the new linkers, without NH groups on the imidazolate ring. This phenomenon was also observed with SALEM-2 showing decreased catalytic activity (**Figure 3.69, p 157**). As surface area plays on important role in catalytic activity, the decrease in t-plot external surface area earlier observed for the SALEM-2 compounds can thus be the cause of the decreased activity of SALEM-2. Reduced catalytic activity of LeZIF8-NH_2BzIm after only 4 hours of SALE, while retaining its original t-plot external surface area, confirms the removal of free NH groups on the external surface. By increasing the amino concentration to 10 and 16 %, the catalytic activity increased as described previously.

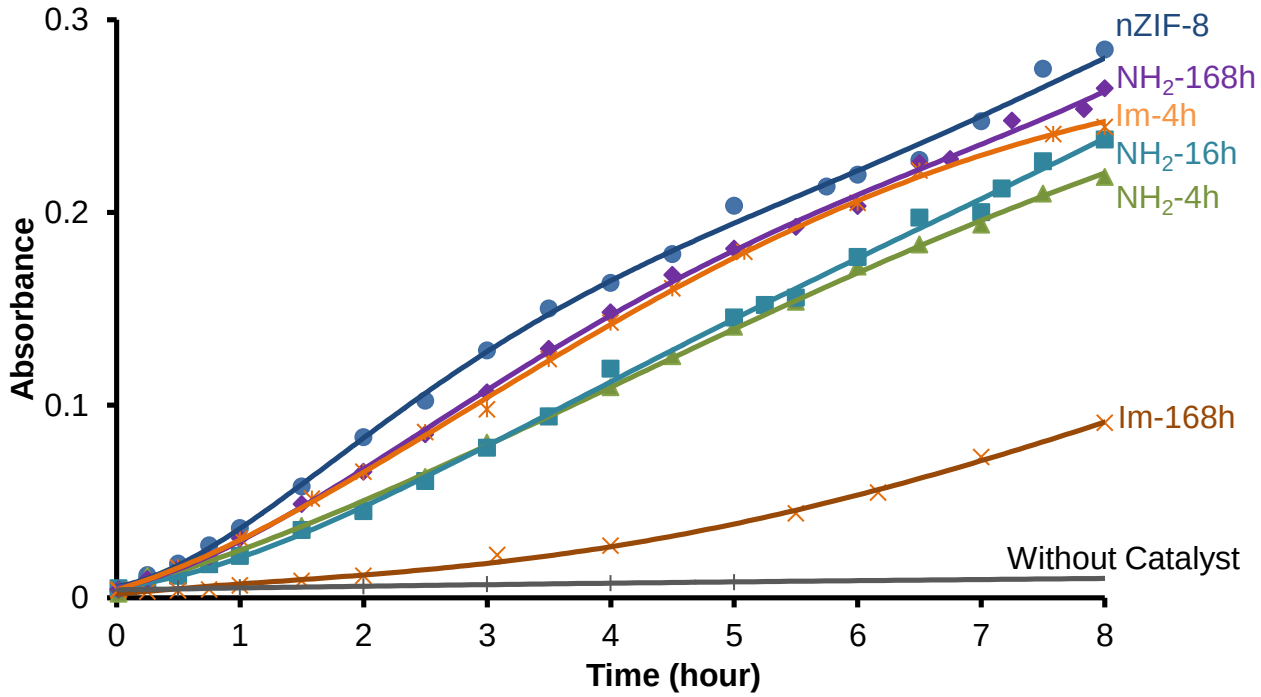

Figure 3.69 Plot of Absorbance (at 570 nm) *vs.* time for the Knoevenagel condensation between ferrocenecarboxaldehyde and malononitrile with various SALE-ZIF8 catalysts (5 % mol): NH_2 (ZIF8-NH_2BzIm) and Im (SALEM-2) derivatives.

The additional primary amine in the C2 position of ZIF8-NH_2BzIm was investigated for catalytic activity and compared to 2-methylimdazole of pure nZIF-8. Both organic linkers were also employed as homogeneous catalysts. The catalytic activity was measured at 570 nm and curve represented in **Figure 3.70** (**p 158**). With the use of the homogeneous catalysts, the reaction reached completion at ~5 hours, much faster than nZIF-8 (8h). Relatively identical TOFs, 4.364 and 4.15 h^{-1} were calculated for 2-methylimidazole and 2-aminoimidazole respectively. These similar values show that the additional primary amine (in 2-aminobenzimidazole) does not enhance the catalytic activity. Surprisingly, $Zn(NO_3)_2$ with a TOF of 1.89 h^{-1}, catalysed the reaction, which is normally catalysed by a base. Studies have shown that zinc chloride can also act as an efficient catalyst for the Knoevenagel condensation.[42] With the two homogeneous catalysts, both of the exposed NH groups can contribute to the catalytic activity. However, after SALE of ZIF-8 with 2-aminobenzimidazole, the NH groups are bound to the zinc metal, leaving the primary amine to catalyse the reaction.

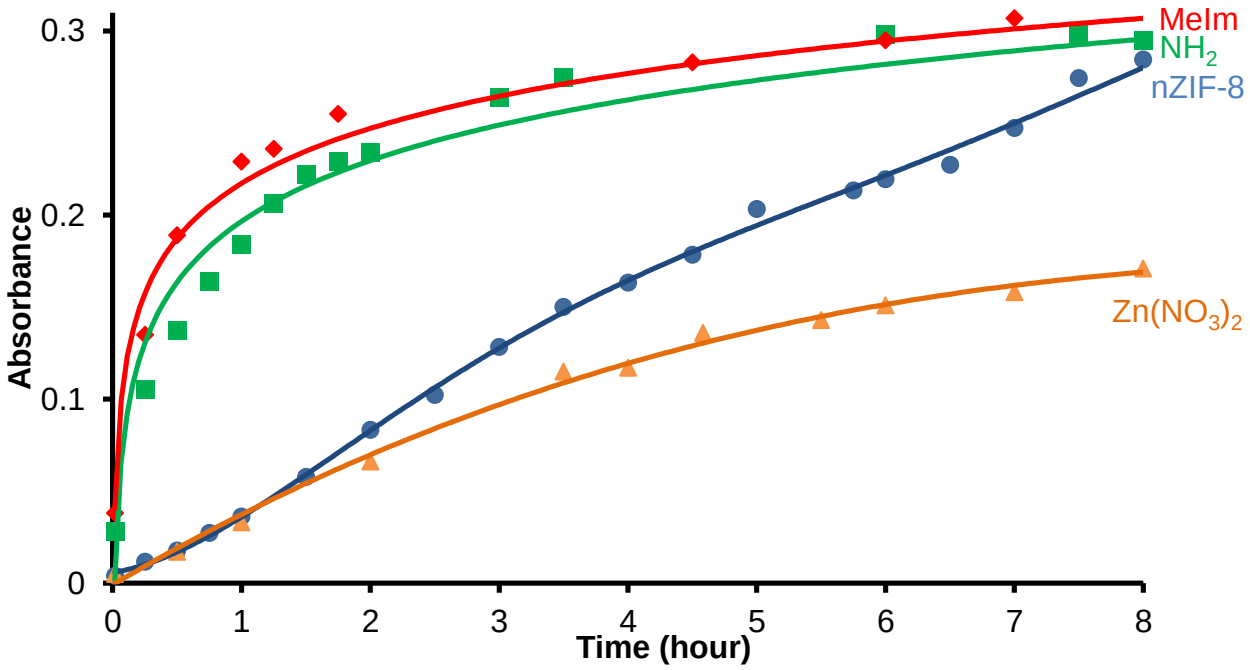

Figure 3.70 Absorbance (at 570 nm) *vs.* time graphs of Knoevenagel condensation between ferrocenecarboxaldehyde and malononitrile with various catalysts (5 % mol): MeIm (2-methylimidazole), NH_2 (2-aminobenzimidazole), nZIF-8 and $Zn(NO_3)_2$.

The increasing catalytic activity of LeZIF8-NH_2BzIm when the density of amino groups on the surface of the nanoparticles provides evidence that the reaction is indeed catalysed by the amino functional groups. It is thus proposed that the Knoevenagel condensation reaction is catalysed *via* by amino functional groups the imine route, while the traditional base catalysed route was followed with nZIF-8 as catalyst.[43] With a t-plot external surface area of ~320 $m^2 g^{-1}$ and an exchange of 16 %, it can be assumed the entire external surface area is covered with 2-aminobenzimidazole linkers. The mechanism (**Scheme 3.15, p 159**) of the imine route is much more complex than the base catalysed route. The steric hindrance by large ferrocene molecules, reduces the rate of imine bond formation as previously determined (**Chapter 3.4.1, p 126**), and therefore lowers the catalytic activity of the amino-functionalized nanoparticles in general.

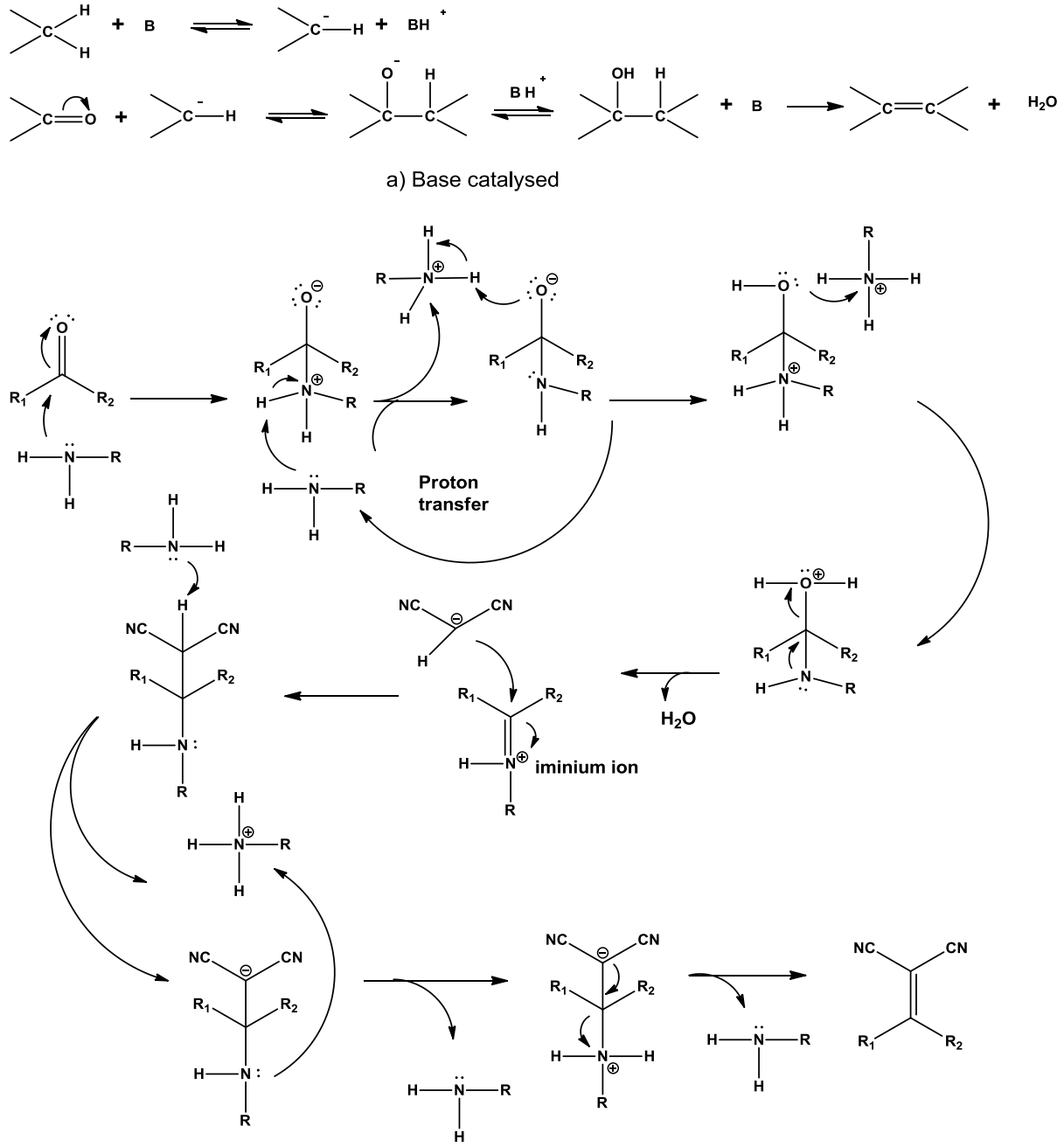

Scheme 3.15 Proposed mechanisms for the Knoevenagel condensation of an aldehyde or ketone with a methylene group *via* a) the base catalysed and b) the imine routes.[44,43,45]

3.6 Gas storage

3.6.1 Carbon Dioxide Adsorption

The low pressure CO_2 adsorption isotherms of selected compounds (**Appendix G.2 to Appendix G.15**) were obtained at absolute pressure up to 900 mmHg at 273 K. The selected multivariate ZIF particles with the quantity of CO_2 adsorbed are tabulated in **Table 3.16** (**p 161**). nZIF-8_{1500}, used as a benchmark adsorbs 38.50 $cm^3\ g^{-1}$ of CO_2. By performing a series of solvent assisted ligand exchanges with linkers having different functional groups, nanoparticles with linkers carrying SH and NO_2 functionalities showed a tremendous ~2 fold improvement in CO_2 adsorption to 77 and 76 $cm^3\ g^{-1}$ respectively. Phenyl groups in LeZIF8-$PhIm_{168h}$ caused a slight increase of ~10 $cm^3\ g^{-1}$ in the uptake of CO_2. LeZIF8-NH_2BzIm_{4h} with a 5 % exchange increased the CO_2 adsorption from 38.50 to 42.71 $cm^3\ g^{-1}$. Increasing the abundance of the amino groups to 10 and 16 % further increased the CO_2 adsorption to 44.29 and 48.17 $cm^3\ g^{-1}$ respectively. The SALE products with alkyl thioesters, LeZIF8-$M5_{168h}$ and LeZIF8-$E3_{168h}$, did not show any significant deviation in CO_2 adsorption compared to the nZIF-8 benchmark. SALE with imidazole (SALEM-2_{16h} 28 % exchange) resulted in a minute increase in CO_2 adsorption to 44.97 $cm^3\ g^{-1}$, but a higher exchange percentage as in SALEM-2_{168h} (86 % exchange), the CO_2 adsorption decreased significantly to 25.23 $cm^3\ g^{-1}$, since the compound now mainly has a ZNI topology and is almost completely non-porous.

Post synthetic modification of LeZIF8-NH_2BzIm_{16h} with PAA did now show any significant improvement and PSM with sebacoyl chloride and FcCOOH led to a decrease in CO_2 adsorption 41.48, 32.4 and 24.63 $cm^3\ g^{-1}$ respectively.

Table 3.16 CO_2 adsorption values of selected SALE and PSM ZIFs at 900 mmHg and 273 K: quantities adsorbed, BET surface areas and micropore volumes.

Compound (% exchange)	CO_2 Quantity Adsorbed ($cm^3\ g^{-1}$)	BET Surface Area ($m^2\ g^{-1}$)	Micropore Volume ($cm^3\ g^{-1}$)
nZIF-8_{1500}	38.50	1605	0.471
nZIF8-SHBzIm$_{72h}$ (12.5)	77.21	1416	0.473
LeZIF8-NO_2Im$_{168h}$ (66.6)	76.02	633	0.213
LeZIF8-PhIm$_{168h}$ (10)	49.89	1579	0.549
LeZIF8-NH_2BzIm$_{4h}$ (5)	42.71	1523	0.441
LeZIF8-NH_2BzIm$_{16h}$ (10)	44.29	1216	0.350
LeZIF8-NH_2BzIm$_{168h}$ (16)	48.17	1108	0.330
LeZIF8-M5_{168h} (11.7)	36.12	943	0.260
LeZIF8-E3_{168h} (1.3)	41.3	1434	0.424
SALEM-2_{16h} (28)	44.97	1353	0.415
SALEM-2_{168h} (86)	25.23	96	0.011
LeZIF8-NH_2BzIm-PAA	41.48	1081	0.324
LeZIF8-NH_2BzIm-FcCO	24.63	760	0.200
LeZIF8-NH_2BzIm(4h)-Seba(10min)	32.44	405	0.078

nZIF-8 derived compounds with NO_2, SH, Phenyl and NH_2 containing substituents all have above average CO_2 adsorption compared to their available surface area (**Figure 3.71, p 162**), in the following order: NO_2 > SH > NH_2 > Phenyl. Electron withdrawing groups (NO_2 and SH in this study) improves the efficiency of CO_2 adsorption by pulling electron density away from the hydrogen atoms on the linkers (in the case of NO_2) or the hydrogen bound to sulphur (in the case of SH).[46] The frl topology (as for LeZIF8-NO_2Im$_{168h}$) has a better uptake in adsorbing CO_2 (0.12 cm^3 CO_2 m^{-2}) without the need for high surface area, as compared to nZIF8-SHBzIm$_{72h}$ with SOD topology (0.054 cm^3 CO_2 m^{-2}). The nZIF-8 derivatives modified with amine groups by SALE show all an improvement in CO_2 adsorption. By increasing the amine containing linker percentage from 5 % to 16 %, an increase in CO_2 adsorption was observed from 42.71 to 48.17 cm^3 g^{-1}. Although SALE reduced the BET surface area of all LeZIF8-NH_2BzIm derivatives, their CO_2 adsorption increased. Amine modified compounds are known to enhance CO_2 adsorption.[47] In general, all the compounds (see **Figure 3.71, p 162**) obtained *via* PSM, without electron-withdrawing groups, showed that an increase in BET surface area correlates to

a steady rise for CO_2 adsorbed. In this study, SALE thus provided an easy and efficient way to improve CO_2 adsorption on nZFI-8 nanoparticles.

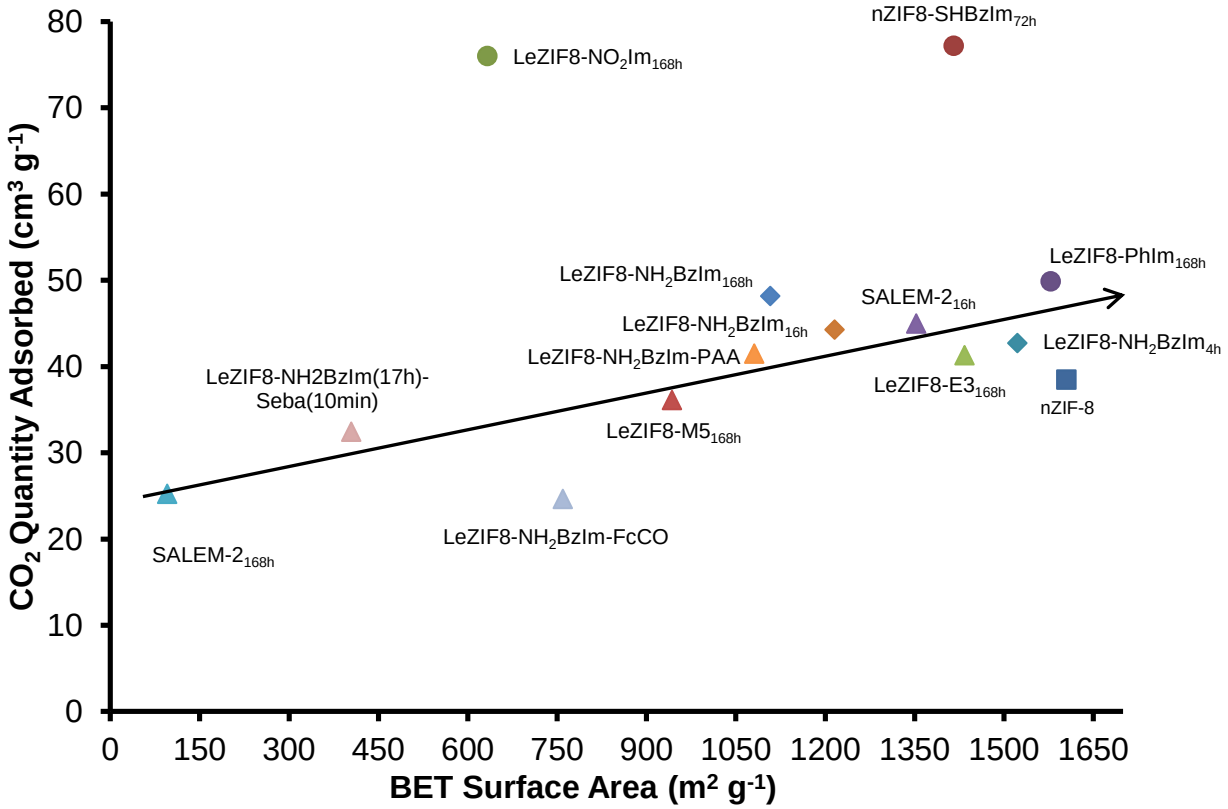

Figure 3.71 Maximum CO_2 quantity adsorbed at 900 mmHg ($cm^3\ g^{-1}$) vs BET surface area ($m^2\ g^{-1}$) for selected SALE and PSM ZIF structures. Compounds are grouped according to: nZIF-8 (■), NH_2 substituents (♦), electron-withdrawing substituents (●) and non-electron withdrawing substituents (▲).

3.6.2 Hydrogen Adsorption

The high-pressure H_2 isotherm of nZIF8-NH_2BzIm$_{17h}$ and SALEM-2$_{16h}$-Pd nanoparticles (**Figure 3.72, p 163**) are Type-1 isotherms, typical for the microporous materials with a maximum excess uptakes of 2.55 wt % (21 bar) and 3.07 wt % (47 bar) respectively. The desorption isotherms follow the same pattern and are identical to the associated adsorption isotherms, showing that hydrogen adsorption and desorption is reversible and that the high pressure does not damage the pores.

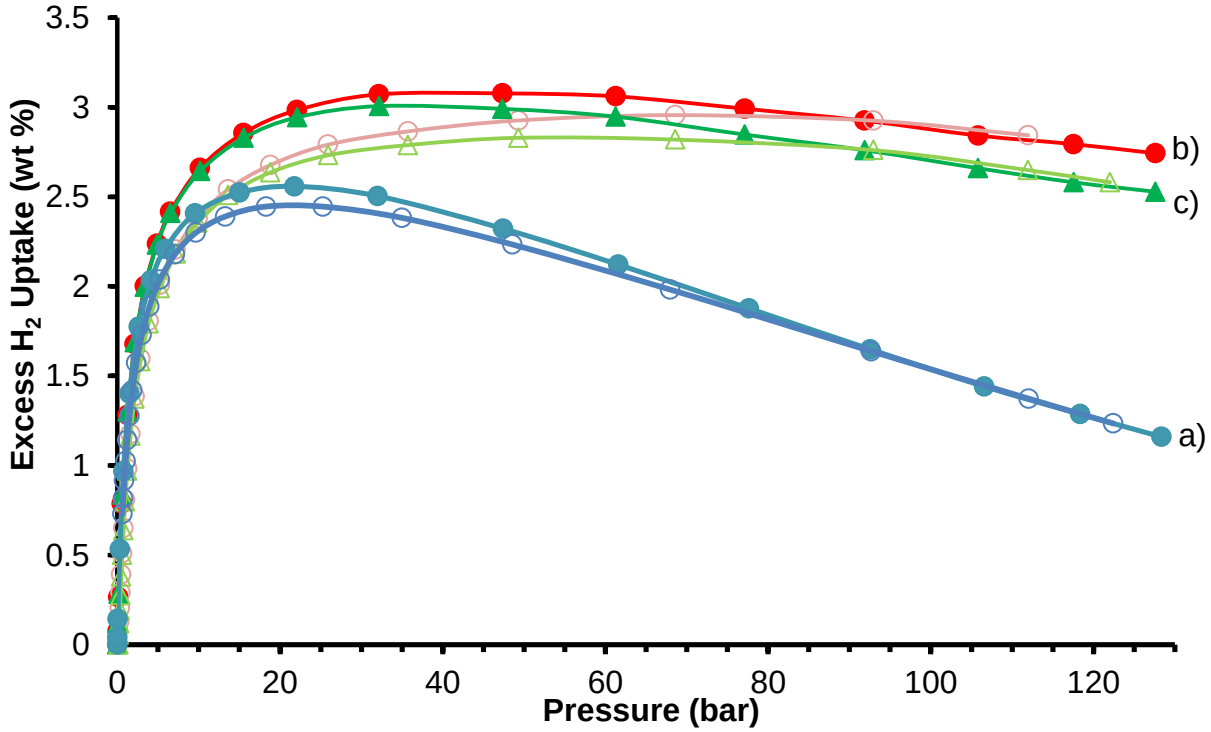

Figure 3.72 Excess hydrogen adsorption and desorption isotherms of LeZIF8-NH_2BzIm$_{17h}$ (blue), SALEM-2$_{16h}$-Pd cycle 1 (red) and cycle 2 (green) at 77 K. Adsorption marked as solid and desorption as hollow symbols.

Both nZIF8-NH_2BzIm$_{17h}$ and SALEM-2$_{16h}$-Pd nanoparticles reaches the maximum uptake at relative low pressures (21 and 40 bar respectively), since these materials have small pore volumes which fills up faster than materials with larger pores. The hydrogen uptake of the SALEM-2$_{16h}$-Pd nanoparticles was reproducible after a second cycle (**Figure 3.72.c, p 163**).

For both materials the micropore region, between 0 and 20 bar, shows a smooth curve with no hysteresis, an indication of little flexibility or change in the pore structure at high hydrogen pressure.

The H_2 isotherm of LeZIF8-NH2BzIm$_{17h}$ shows a sharper drop than the isotherm of SALEM-2$_{16h}$-Pd, after reaching maximum uptake (**Figure 3.72, p 163**), due to its lower micropore volume (0.355 $cm^3\ g^{-1}$) (**Table 3.17, p 164**). A material with a smaller micropore volume reaches the maximum density of hydrogen to the bulk much quicker than a material with larger micropore volume. The isotherm of SALEM-2$_{16h}$-Pd with a micropore volume of 0.443 $cm^3\ g^{-1}$, gave a more flattened isotherm (**Figure 3.72, p 163**). The smaller micropore volume also caused the maximum uptake of hydrogen for LeZIF8-NH2BzIm$_{17h}$ to be reached already at 20 bar and only at 47 bar for SALEM-2$_{16h}$-Pd with its larger micropore volume. A linear relationship was observed between micropore volume and excess H_2 uptake (wt %), for the selected ZIF-8 derivatives (**Figure 3.73, p 165**). Interestingly, the additional Pd complexes in SALEM-2$_{16h}$-Pd did not boost the excess H_2 uptake (wt %).

The maximum excess H_2 uptake for both LeZIF8-NH2BzIm$_{17h}$ and SALEM-2$_{16h}$-Pd was lower than that of ZIF-8, which has a 3.46 wt % excess hydrogen uptake. In the case of LeZIF8-NH2BzIm$_{17h}$ this lower H_2 uptake could be due to the presence of the benzene ring on the exchanged linkers. This was also observed for ZIF-7 and ZIF-11, both with benzene rings on the linker, where the excess H_2 uptake was 1.43 and 2.53 wt % respectively.

Table 3.17 ZIF derivatives with their BET surface areas, Micropore Volumes and excess H_2 uptake (wt %).

Compound	BET Surface Area ($m^2\ g^{-1}$)[#]	Micropore Volume ($cm^3\ g^{-1}$)[#]	Excess H_2 Uptake (wt %)
LeZIF8-NH2BzIm$_{17h}$	1216	0.355	2.55
SALEM-2$_{16h}$-Pd	1455	0.443	3.07
ZIF-8	1752	0.536	3.46*
ZIF-7 (SOD BzIm)	-	-	1.43*
ZIF-11 (RHO BzIm)	1676	0.582	2.53*

*Values obtain from literature.[48]

[#] Values obtained by N_2 adsorption at 77 K.

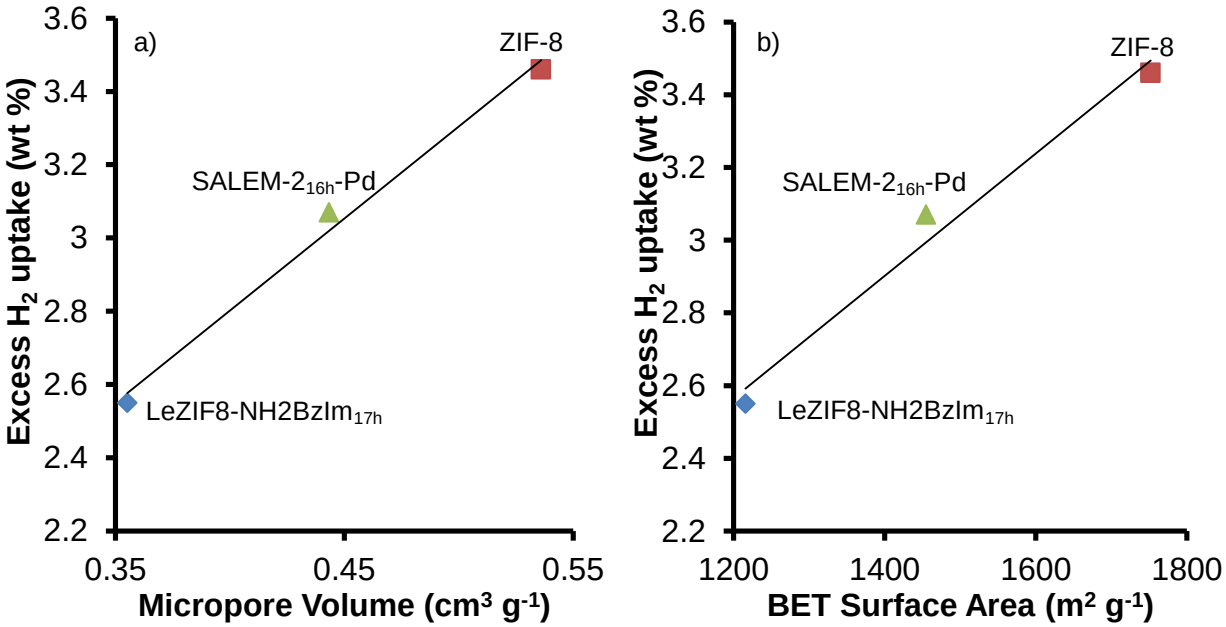

Figure 3.73 a) Maximum excess H_2 uptake (wt %) *vs.* micropore volume (cm^3 g^{-1}) and b) Maximum excess H_2 uptake (wt %) *vs.* BET surface area (m^2 g^{-1}) for LeZIF8-NH2BzIm$_{17h}$, SALEM-2$_{16h}$-Pd and ZIF-8.

A linear relationship was also observed between surface area and excess hydrogen uptake (**Figure 3.73, p 165**), The larger the surface area of the ZIF materials, the more excess H_2 the material can adsorb, correlating well to the Chahine rule[48] which states that the excess hydrogen uptake of a porous material is 2 wt % per 1000 m^2 g^{-1}. LeZIF8-NH2BzIm$_{17h}$ has a 2.09 wt % uptake per 1000 m^2 g^{-1} and SALEM-2$_{16h}$-Pd a 2.1 wt % uptake per 1000 m^2 g^{-1}. The topology of ZIF play an important role in hydrogen uptake as seem from the examples in literature where ZIF-7 and ZIF-11 have identical ligands, but different topologies, RHO and SOD respectively. ZIF-11 has a higher uptake than ZIF-7 with its SOD topology. Therefore it was observed that the LeZIF8-NH2BzIm$_{17h}$ which maintains its SOD topology through ligand exchange have a lower excess hydrogen uptake.

3.7 Reference

1 K. S. Park, Z. Ni, A. P. Côté, J. Y. Choi, R. Huang, F. J. Uribe-Romo, H. K. Chae, M. O'Keeffe and O. M. Yaghi, *Proc. Natl. Acad. Sci. U. S. A.*, 2006, **103**, 10186–10191.

2 I. B. Vasconcelos, T. G. Da Silva, G. C. G. Militão, T. a. Soares, N. M. Rodrigues, M. O. Rodrigues, N. B. Da Costa, R. O. Freire and S. a. Junior, *RSC Adv.*, 2012, **2**, 9437.

3 A. F. Gross, E. Sherman and J. J. Vajo, *Dalt. Trans.*, 2012, **41**, 5458.

4 J. Cravillon, R. Nayuk, S. Springer, A. Feldhoff, K. Huber and M. Wiebcke, *Chem. Mater.*, 2011, **23**, 2130–2141.

5 H. Y. Cho, J. Kim, S. N. Kim and W. S. Ahn, *Microporous Mesoporous Mater.*, 2013, **169**, 180–184.

6 K. Kida, M. Okita, K. Fujita, S. Tanaka and Y. Miyake, *CrystEngComm*, 2013, **15**, 1794.

7 R. Dhani, *Int. J. Pharm. Chem. Biol. Sci.*, 2012, **2**, 718–721.

8 S. Ram, D. S. Wise and L. B. Townsend, *J. Heterocycl. Chem.*, 1985, **22**, 1269–1274.

9 O. Karagiaridi, M. B. Lalonde, W. Bury, A. a. Sarjeant, O. K. Farha and J. T. Hupp, *J. Am. Chem. Soc.*, 2012, **134**, 18790–18796.

10 R. Lehnert and F. Seel, *Zeitschrift für Anorg. und Allg. Chemie*, 1980, **464**, 187–194.

11 J. P. Zhang, Y. B. Zhang, J. Bin Lin and X. M. Chen, *Chem. Rev.*, 2012, **112**, 1001–1033.

12 P. J. Beldon, L. Fábián, R. S. Stein, a. Thirumurugan, A. K. Cheetham and T. Friščić, *Angew. Chemie - Int. Ed.*, 2010, **49**, 9640–9643.

13 C. Chizallet, S. Lazare, D. Bazer-Bachi, F. Bonnier, V. Lecocq, E. Soyer, A. A. Quoineaud and N. Bats, *J. Am. Chem. Soc.*, 2010, **132**, 12365–12377.

14 M. Kondo, S. Furukawa, K. Hirai and S. Kitagawa, *Angew. Chemie - Int. Ed.*, 2010, **49**, 5327–5330.

15 Mahfouz, A. A. Aziz and F. M. Elhabashy, *Arch. Pharm. Res.*, 1990, **13**, 9–13.

16 M. I. Ali, M. A. Abou-State and A. F. Ibrahim, *J. f. Prakt. Chemie*, 1974, **316**, 147–153.

17 R. Besse, P. J. Garratt, C. J. Hobbs, H. M. Rogers, A. Mannan Sueleiman, C. S.J. Walpole and R. Wrigglesworth, *Tetrahedron*, 1990, **46**, 7803–7812.

18 J. A. Thompson, N. A. Brunelli, R. P. Lively, J. R. Johnson, C. W. Jones and S. Nair, *J. Phys. Chem. C*, 2013, **117**, 8198–8207.

19 A. Phan, C. J. Doonan, F. J. Uribe-Romo, C. B. Knobler, M. O'Keeffe and O. M. Yaghi, *Acc. Chem. Res.*, 2010, **43**, 58–67.

20 R. Banerjee, A. Phan, B. Wang, C. Knobler, H. Furukawa, M. O'Keeffe and O. M. Yaghi, *Science*, 2008, **319**, 939–943.

21 W. C. (Ina) du Plessis, T. G. Vosloo and J. C. Swarts, *J. Chem. Soc. Dalt. Trans.*, 1998, 2507–2514.

22 X. Zhang, M. Cui, R. Zhou, C. Chen and G. Zhang, *Macromol. Rapid Commun.*, 2014, **35**, 566–573.

23 T. Ohshima, Y. Hayashi, K. Agura, Y. Fujii, A. Yoshiyama and K. Mashima, *Chem. Commun.*, 2012, **48**, 5434.

24 C. M. Bertha, R. S. Hosmane, H. Zhang and N. S. Hosmane, *J. Org. Chem.*, 1992, **57**, 5868–5873.

25 T. Ahnfeldt, D. Gunzelmann, T. Loiseau, D. Hirsemann, J. Senker, G. Férey and N. Stock, *Inorg. Chem.*, 2009, **48**, 3057–3064.

26 J. E. Halls, A. Hernán-Gómez, A. D. Burrows and F. Marken, *Dalton Trans.*, 2012, **41**, 1475–80.

27 G. Deacon, *Coord. Chem. Rev.*, 1980, **33**, 227–250.

28 M. J. Duer, *Introduction to Solid-State NMR Spectroscopy*, Wiley, 2005.

29 W. Morris, C. J. Doonan, H. Furukawa, R. Banerjee and O. M. Yaghi, *J. Am. Chem. Soc.*, 2008, **130**, 12626–12627.

30 Y. K. Hwang, D. Y. Hong, J. S. Chang, S. H. Jhung, Y. K. Seo, J. Kim, A. Vimont, M. Daturi, C. Serre and G. Férey, *Angew. Chemie - Int. Ed.*, 2008, **47**, 4144–4148.

31 A. Demessence, D. M. D'Alessandro, M. L. Foo and J. R. Long, *J. Am. Chem. Soc.*, 2009, **131**, 8784–8786.

32 T. Gadzikwa, G. Lu, C. L. Stern, S. R. Wilson, J. T. Hupp and S. T. Nguyen, *Chem. Commun. (Camb).*, 2008, **47**, 5493–5495.

33 A. Patra, T. K. Sen, R. Bhattacharyya, S. K. Mandal and M. Bera, *RSC Adv.*, 2012, **2**, 1774.

34 B. H. Ye, X. Y. Li, I. D. Williams and X. M. Chen, *Inorg. Chem.*, 2002, **41**, 6426–6431.

35 S. Prakash and J. Yeom, *Nanofluidics and Microfluidics - Systems and Applications - Knovel*, Elsevier Science, 2014.

36 B. Xi, Y. C. Tan and H. C. Zeng, *Chem. Mater.*, 2016, **28**, 326–336.

37 M. C. McCarthy, V. Varela-Guerrero, G. V. Barnett and H. K. Jeong, *Langmuir*, 2010, **26**, 14636–14641.

38 C. M. Woodbridge, D. L. Pugmire, R. C. Johnson, N. M. Boag and M. A. Langell, *J. Phys. Chem. B*, 2000, **104**, 3085–3093.

39 O. Karagiaridi, M. B. Lalonde, W. Bury, A. a. Sarjeant, O. K. Farha and J. T. Hupp, *J. Am. Chem. Soc.*, 2012, **134**, 18790–18796.

40 S. Men, K. R. J. Lovelock and P. Licence, *RSC Adv.*, 2015, **5**, 35958–35965.

41 G. Riveros, S. Meneses, S. Escobar, C. Garín and B. Chornik, 2010, **1**, 61–66.

42 P. Shanthan Rao and R. V. Venkataratnam, *Tetrahedron Lett.*, 1991, **32**, 5821–5822.

43 J. Gascon, U. Aktay, M. D. Hernandez-Alonso, G. P. M. van Klink and F. Kapteijn, *J. Catal.*, 2009, **261**, 75–87.

44 E. Knoevenagel, *Berichte der Dtsch. Chem. Gesellschaft*, 1898, **31**, 2596–2619.

45 M. Hartmann and M. Fischer, *Microporous Mesoporous Mater.*, 2012, **164**, 38–43.

46 X. J. Hou and H. Li, *J. Phys. Chem. C*, 2010, **114**, 13501–13508.

47 D. Liu, Y. Wu, Q. Xia, Z. Li and H. Xi, *Adsorption*, 2013, **19**, 25–37.

48 A. Noguera-Díaz, N. Bimbo, L. T. Holyfield, I. Y. Ahmet, V. P. Ting and T. J. Mays, *Colloids Surfaces A Physicochem. Eng. Asp.*, 2016, **496**, 77–85.

4 Experimental

4.1 Introduction

In this chapter, all chemicals, equipment, methods and procedures for synthesis characterisation and analyses are described.

4.2 Chemicals

All synthesis reagents were purchased from Sigma-Aldrich and all solvents from Merck. These were used without further purification unless stated otherwise. When needed, solvents were dried and distilled for further use accordingly.[2] Double distilled water was used where necessary.

4.3 Equipment

Melting points were determined with an Olympus BX51 polarised microscope, fitted with a LINKAM THMS 600 heating/cooling stage. Transmission electron microscopy (TEM) was performed with a Philips (FEI) CM100 equipped with a Megaview III digital camera and coupled to an Oxford X-Max (80 mm^2), energy-dispersive X-ray spectroscope (EDS). TEM pictures were analysed utilising Soft Imaging System (analySIS) software.

^1H Nuclear magnetic resonance (^1H NMR) spectra were measured on a 300 MHz Bruker FOURIER NMR spectrometer with a 5 mm 13C/1H high-resolution NMR probe equipped with Z gradient coil or a Bruker Advance II 600 NMR spectrometer operating at 25 °C. The ^1H chemical shifts were reported relative to $SiMe_4$ at 0.0 ppm as external standard and utilising the solvent peak as internal standard were applicable. All insoluble ZIF-8 (15-20 mg) derivatives were digested in D_2O:D_2SO_4 (9:1) until a homogeneous solution was obtained for NMR measurements, taken after locking directly to D_2O. Soluble compounds were dissolved in $CDCl_3$ unless stated otherwise. ^{13}C Solid-state nuclear magnetic resonance (^{13}C SSNMR) spectra were measured on a 400 MHz AVANCE III NMR spectrometer with a 4 mm VTN multinuclear double resonance magic angle spinning probe operating at 25 °C having a ^{13}C frequency of

100.61 MHz. All infrared spectra were measured on a Thermo Scientific Nicolet iS50 ATR Infrared Spectrometer with OMNIC v9.2.86 software.

All porosity and surface area measurements were performed on a Micromeritics ASAP 2020 Surface Area and Porosity Analyser and the data analysed with ASAP 2020 V2.0 for physisorption with nitrogen and carbon dioxide. Nitrogen was measured with relative pressure at 77 K and carbon dioxide with absolute pressure at 273 K. The nZIF-8 derivatives were activated at 150 °C for 16 hours for porosity analysis and a typical amount of ~40 mg was used for each analysis with the warm and cold free space determined separately with helium. Porosity results were refined by MicroActive V1.01 Software. High-pressure hydrogen adsorption was performed on a volumetric Hiden HTP-1 sorption analyser using a liquid nitrogen immersion dewar at 77 K.

Powder X-ray diffraction patterns (PXRD) were collected on a Bruker D2 Phaser powder X-ray diffractometer at room temperature, employing a flat plate sample holder and Cu radiation (λ = 1.54 Å). Diffraction patterns were collected in the range 5° to 50° for 2θ, with a step size of 0.1° and a counting time of two seconds per step.

X-ray Photoelectron Spectroscopy (XPS) data were recorded on a PHI 5000 Versaprobe system with a monochromatic AlK X-ray source. Spectra were obtained using the aluminium anode (Al Kα = 1486.6 eV) operating at 50 μm, 12.5 W and 15 kV energy (97 X-ray beam). The survey scans were recorded at constant pass energy of 187.85 eV and region scans at constant pass energy of 29.35 eV with the analyser resolution ≤ 0.5 eV. The background pressure was 2 x 10^{-8} mbar. The XPS data sets were analysed utilizing Multipak version 8.2c computer software with Gaussian–Lorentz fits (the Gaussian/Lorentz ratios were always > 95 %).

A Shimadzu ICPS-7510 Inductively Coupled Plasma–Optical emission spectrometry (ICP-OES) with a radial-sequential plasma spectrometer was used for the wet chemical analysis of all the samples during the current study. The vertically oriented ICP-OES with the 'radial viewing' plasma was found to be suitable due to its better detection limits. The emission intensity measurements were made using the default conditions as indicated in (see **Table 4. 1**, p **171**).

Table 4. 1 ICP-OES operating conditions.

Parameter	Condition
RF power	1.2 kW
Coolant gas flow rate	14.0 L/min
Plasma gas flow rate	45 L/min
Auxiliary gas flow rate	0.5 L/min
Carrier gas flow rate	0.7 L/min
Sample uptake method	Peristaltic pump
Type of spray chamber	Glass cyclonic
Type of nebuliser	Concentric
Injector tube diameter	3.0 mm

Thermo-gravimetric analyses (TGA) were performed on a Mettler-Toledo TGA/SDTA851 under an argon atmosphere. The temperature program for TGA analysis: 30 ℃ for 30 minutes to stabilise the TGA; heating to 800 ℃ at 10 ℃ min^{-1}; 800 ℃ for 1 min and cooled to 30 ℃. TGA data were analysed utilising Mettler Star^{e} Evaluation software to determine % mass loss at specific temperatures

UV/vis spectra were measured on a Shimadzu UV-1650 PC UV-Visible spectrophotometer fitted with a 6 cell attachment and a Shimadzu CPS-240A Temperature controller. Spectra obtained were analysed with the UVProbe Version 2.20 software.

4.4 Synthesis of nano-sized 2-Methylimidazole Zinc salt or nano-ZIF-8 (nZIF-8)

4.4.1 Synthesis of nZIF-8 at various methanol ratios[3]

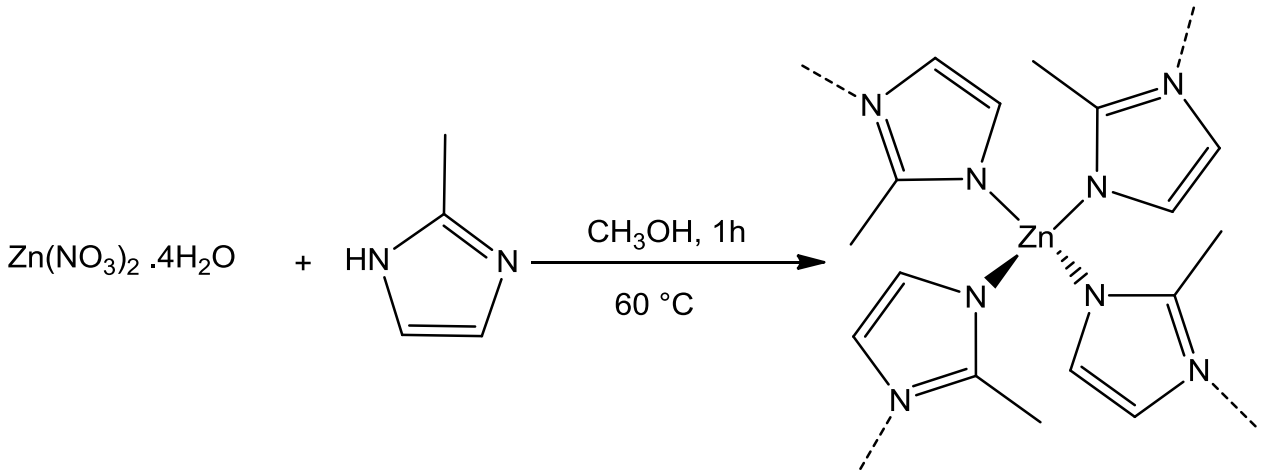

A solution of $Zn(NO_3)_2.4H_2O$ (1.298 g, 5 mmol) in methanol (100; 150; 200[#] cm^3)* at 60 ℃ was added rapidly to a solution of 2-methylimidazole (3.28 g, 40 mmol) in methanol (100; 150; 200[#] cm^3)* at 60 ℃. The mixture was stirred for 1 hour at 60 ℃. The precipitate was isolated by centrifugation (7000 rpm, 30 min, 15 ℃). The solid product was washed with methanol (3 x 150 cm^3), isolated by centrifugation and dried in air overnight. [#]The solid product was purified by dialysis and freeze dried. The dried product was activated at 150 ℃ under vacuum to obtain a white powder (0.518 g, 45 %). ν_{max}/cm^{-1} (**Spectrum 3.1**): ν(C=N) = 1584, ν(C-H) = 3135; 2929. PXRD (**Figure 3.3)**.

Table 4.2 Synthesis of nZIF-8 at various methanol ratios.

[*]**Total methanol solvent/ cm^3**	**Yield avg/ g (%)**
200	0.540 (47 %)
300	0.518 (45 %)
400	0.193 (35 %)

[#]The product in the synthesis described here was obtained from a total solvent volume of 400 cm^3. The characterisation (FTIR and PXRD) of the two products from the same procedure, were similar to this product.

4.4.2 Bulk Synthesis of nZIF-8 for SALE

A solution of $Zn(NO_3)_2.4H_2O$ (1.297 g, 5 mmol) was dissolved in methanol (150 cm^3) at 60 ℃ and was added rapidly to a solution of 2-methylimidazole (3.306 g, 40 mmol) dissolved in methanol (150 cm^3). The mixture was stirred for 1 hour at 60 ℃. The nano crystals were isolated by centrifugation (8500 rpm, 30 min, 15 ℃), washed with methanol (3 x 150 cm^3) and isolated by centrifugation. The precipitate was dried in air overnight and activated by heating at 150 ℃ under vacuum to obtain a white powder (0.5480 g, 48 %).

4.4.3 Synthesis of nZIF-8 with Triethylamine

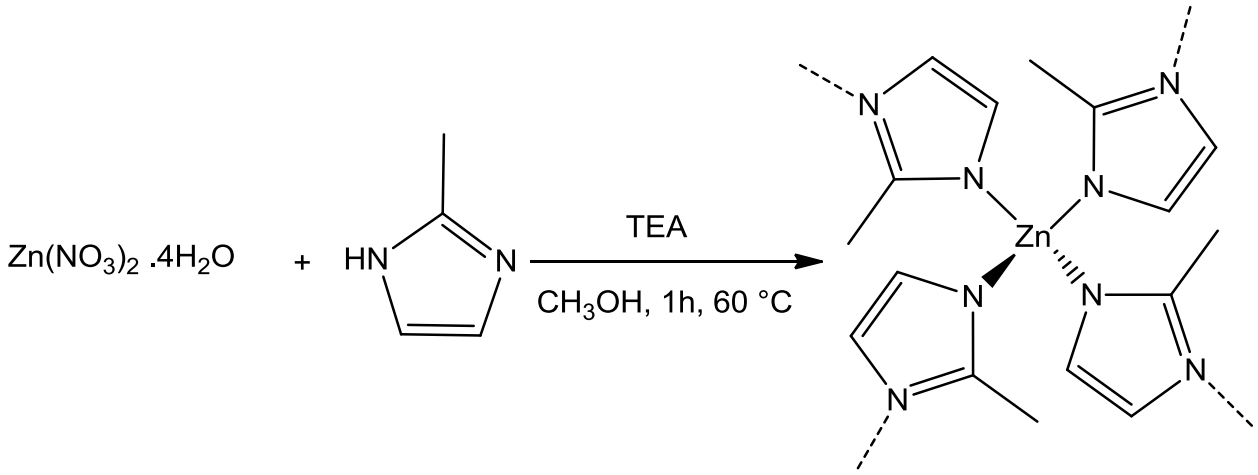

A solution of $Zn(NO_3)_2.4H_2O$ (1.297 g, 5 mmol) was dissolved in methanol (150 cm^3) at 60 ℃ and was added rapidly to a solution of 2-methylimidazole (3.306 g, 40 mmol) and triethylamine [(0.6 cm^3, 5 mmol); (1.3 cm^3, 10 mmol); (1.8 cm^3, 15 mmol); (2.5 cm^3, 20 mmol); (5.5 cm^3, 40 mmol)] (see **Table 4.3**) was dissolved in methanol (150 cm^3) at 60 ℃. The mixture was stirred for 1 hour at 60 ℃. The nano crystals were isolated by centrifugation (7000 rpm, 30 min, 15 ℃), washed with methanol (3 x 100 cm^3) and isolated by centrifugation. The precipitate was dried in air overnight and activated by heating at 250 ℃ under nitrogen flow for 90 minutes to obtain a white powder[#] (0.982 g, 85 %). ν_{max}/cm^{-1} (**Spectrum A.1**:): ν(C=N) = 1584, ν(C-H) = 3135; 2929. PXRD (**Spectrum 3.9)**.

Table 4.3 Synthesis of nZIF-8 with TEA at various ratios.

Triethylamine cm^3 (mmol)	Yield avg/ g (%)
0.6 (5)	0.458 (40 %)
1.3 (10)	0.475 (41 %)
1.8 (15)	0.982 (85 %)[#]
2.5 (20)	0.955 (83 %)
5.5 (40)	0.965 (84 %)

[#]The characterisation (FTIR and PXRD) of all the products from the same procedure, were similar to this product.

4.5 Synthesis of *S*-Alkylated imidazole derivatives

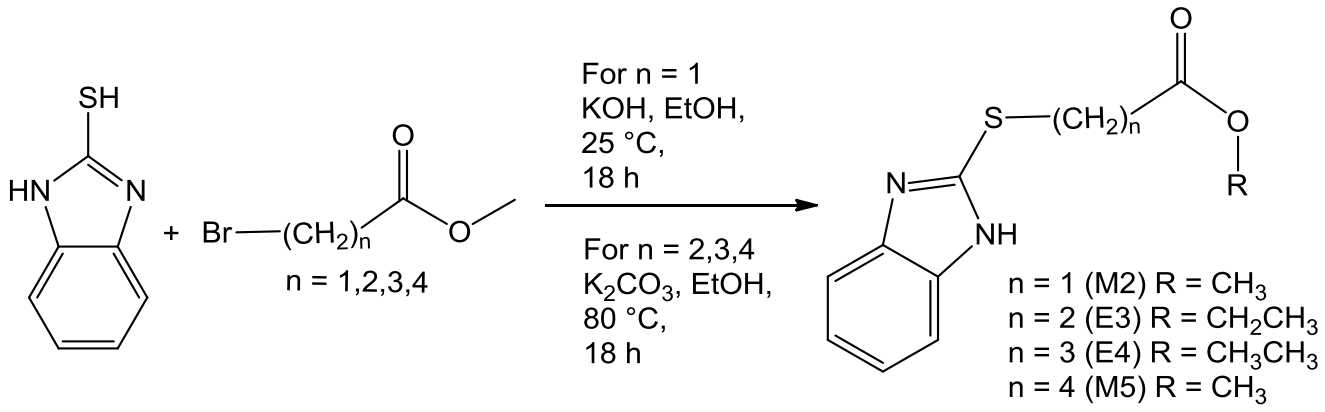

4.5.1 Methyl benzimidazole-2-ylthio acetate (M2)

After 2-mercaptobenzimidazole (1.500 g, 10 mmol) and KOH (0.600 g) was dissolved in ethanol (20 cm^3). Methylbromoacetate was added while stirring. The reaction mixture was continuously stirred for 18 hours at 25 ℃. Ice (30 g) was added and stirred for 30 minutes. The precipitate was filtered and washed with water. The crude product was purified by recrystallisation (dichloromethane and *n*-hexane) and dried under vacuum to obtain a fine white powder (1.605 g, 72 %). Melting point 118 °C. ν_{max}/cm^{-1} (**Spectrum 3.12**): 3046 (C-H), 2949 (N-H), 1740 (C=O), 1588 ν(C=N), 741 ν (C-S-C). ^{1}H NMR: δ_H (300 MHz, $CDCl_3$)/ppm (**Spectrum 3.13**): 10.3 (s, 1H, N-H), 7.4 (s, 2H, C_6H_4), 7.1 (m, 2H, C_6H_4), 3.9 (s, 2H, CH_2), 3.7 (s, 3H, CH_3).

4.5.2 Ethyl benzimidazole-2-ylthio propionate (E3)

2-Mercaptobenzimidazole (1.500 g, 10 mmol) was added slowly to an ethanol (40 cm^3) solution of K_2CO_3 (0.7 g, 5 mmol) and ethyl-3-bromopropionate (1.28 cm^3, 10 mmol). The solution was refluxed at 80 ℃ for 18 hours, during which it turned light brown. The solvent was removed under vacuum, the crude product washed with H_2O (30 cm^3) and extracted with chloroform (2 x 50 cm^3). The extract was washed with H_2O (3 x 50 cm^3) and dried with magnesium sulphate, filtered and the chloroform evaporated under vacuum to obtain a white solid. The solid was purified by recrystallisation (dichloromethane and *n*-hexane) to obtain a fine white powder (1.819 g, 73 %). Melting point: 114 °C. ν_{max}/cm^{-1} (**Spectrum 3.12**): 3051 (C-H), 2956 (N-H), 1716 (C=O), 1617 (C=N), 742 (C-S-C). ^{1}H NMR: δH (300 MHz, $CDCl_3$)/ppm (**Spectrum 3.13**): 9.5 (s, 1H, N-H), 7.4 (s, 2H, C_6H_4), 7.1 (m, 2H, C_6H_4), 4.1 (m, 2H, CH_2), 3.4 (t, 2H, CH_2), 2.8 (t, 2H, CH_2), 1.2 (t, 3H, CH_3).

4.5.3 Ethyl benzimidazole-2-ylthio butyrate (E4)

2-Mercaptobenzimidazole (1.500 g, 10 mmol) was added slowly to an ethanol (40 cm^3) solution of K_2CO_3 (0.7 g, 5 mmol) and ethyl-4-bromobutyrate (1.43 cm^3, 10 mmol). The solution was refluxed at 80 ℃ for 18 hours, during which it turned light brown with the solvent removed under vacuum, the crude product washed with H_2O (30 cm^3) and extracted with chloroform (2 x 50 cm^3). The extract was washed with H_2O (3 x 50 cm^3) and dried with magnesium sulphate, filtered and the chloroform evaporated under vacuum to obtain a white solid. The solid was purified by recrystallisation (dichloromethane and *n*-hexane) to obtain a fine white powder (2.224 g, 84 %). Melting point: 85 °C. ν_{max}/cm-1 (**Spectrum 3.12**): 3047 (C-H), 2972 (N-H), 1719 (C=O), 1619 (C=N), 743 (C-S-C). ^{1}H NMR: δH (300 MHz, $CDCl_3$)/ppm (**Spectrum 3.13**): 10 (s, 1H, N-H), 7.4 (s, 2H, C_6H_4), 7.1 (m, 2H, C_6H_4), 4.1 (m, 2H, CH_2), 3.2 (t, 2H, CH_2), 2.5 (t, 2H, CH_2), 2.1 (m, 3H, CH_2), 1.2 (t, 3H, CH_3).

4.5.4 Methyl benzimidazole-2-ylthio valerate (M5)

2-Mercaptobenzimidazole (1.500 g, 10 mmol) was added slowly to an ethanol (40 cm^3) solution of K_2CO_3 (0.7 g, 5 mmol) and methyl-5-bromovalerate (1.43 cm^3, 10 mmol) at 35 ℃. The solution was refluxed at 80 ℃ for 18 hours, during which it turned light brown. The solvent removed under vacuum, the crude product was washed with H_2O (30 cm^3) and extracted with chloroform (2 x 50 cm^3). The extract was washed with H_2O (3 x 50 cm^3) and dried with magnesium sulphate, filtered and the chloroform evaporated under vacuum to obtain a white

solid. The solid was purified by recrystallisation (dichloromethane and *n*-hexane) to obtain a fine white powder (2.419 g, 92 %). Melting point 88 °C. ν_{max}/cm-1 (**Spectrum 3.12**): 3038 (C-H), 2948 (N-H), 1732 (C=O), 1617 (C=N), 736 (C-S-C). ^{1}H NMR: δH (300 MHz, $CDCl_3$)/ppm (**Spectrum 3.13**): 9.3 (s, 1H, N-H), 7.4 (s, 2H, C_6H_4), 7.1 (m, 2H, C_6H_4), 3.6 (t, 3H, CH_3), 3.2 (s, 2H, CH_2), 2.3 (s, 2H, CH_2), 1.7 (t, 4H, C_2H_2).

4.6 Synthesis of Ferrocene Derivative

4.6.1 Ferrocenecarboxaldehyde

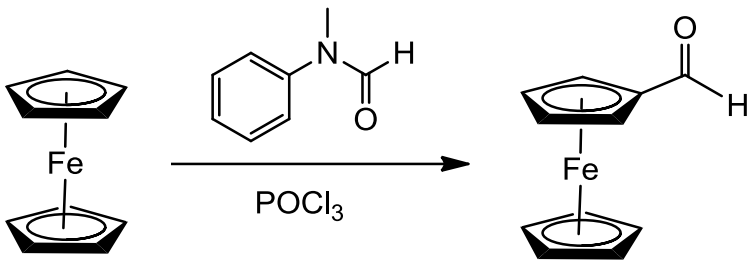

N-Methylformanilide (18 cm^3, 146 mmol) and phosphorus oxychloride (8.5 cm^3, 91 mmol) was stirred carefully under an argon atmosphere for 10 minutes. Ferrocene (10.08 g, 54 mmol) was slowly added over 30 minutes to the N-methylformanilide solution. The reaction mixture turned rapidly into a dark purple viscous liquid which was stirred at 25 ℃ for 1 hour and at 65 ℃ for 2 hours. The mixture was cooled to 0 ℃ before sodium acetate (30.06 g) in water (250 cm^3) was added. The product was extracted with diethyl ether (6 x 75 cm^3). The dark red extract was washed with hydrochloric acid (1 M, 100 cm^3), water (100 cm^3), saturated sodium bicarbonate (2 x 200 cm^3) in water and saturated sodium chloride (100 cm^3) in water. The extract was dried with anhydrous magnesium sulphate, filtered and the diethyl ether evaporated under vacuum to obtain a viscous red liquid. The crude product was purified with column chromatography (hexane:ether 2:1 on silica) and dried under vacuum to obtain red crystals (6.382 g, 55 %); Melting point 105 ℃, R_f = 0.3 (hexane:ether = 2:1). ν_{max}/cm^{-1} (**Spectrum 3.14**): 1664 (C=O). ^{1}H NMR: δ_H (300 MHz, $CDCl_3$)/ppm (**Spectrum 3.15**): 9.9 (s, 1H, C-H), 4.8 (t, 2H, C_5H_2), 4.6 (t, 2H, C_5H_2), 4.3 (s, 5H, C_5H_5).

4.6.2 Ferrocenemethylamine

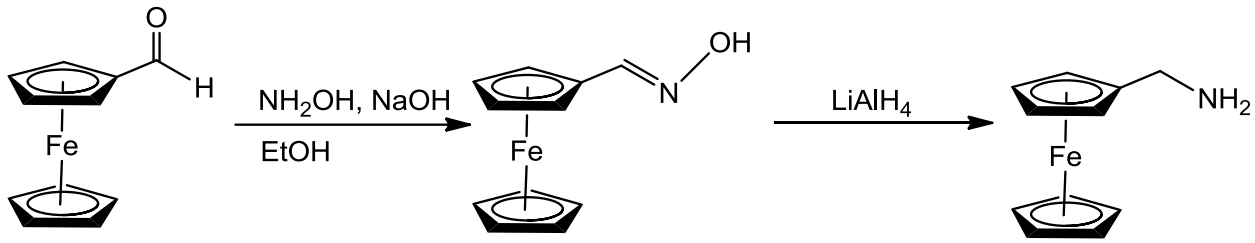

Ferrocenecarboxaldehyde (2.0 g. 9.36 mmol), NaOH (2.2 g, 55 mmol) and hydroxylamine chlorohydrate (1.3 g, 18.6 mmol) was dissolved in ethanol (100 cm^3) and refluxed for 3 hours while stirring. The mixture was cooled to room temperature and H_2O (100 cm^3) was added and extracted with dichloromethane (3 x 100 cm^3). The organic extract was washed with brine (200 cm^3) and dried with anhydrous magnesium sulphate, filtered and evaporated under vacuum to obtain a crude orange solid. The solid was dissolved in dry tetrahydrofuran (THF) (20 cm^3) under argon. The solution was added dropwise to a mixture of $LiAlH_4$ (1.5 g, 38 mmol) and THF (20 cm^3), and refluxed for 16 hours. The yellow mixture was cooled before H_2O (30 cm^3) was added and filtered over celite. The filtrate was extract with diethyl ether (3 x 100 cm^3). The organic phase was washed with brine and dried with anhydrous magnesium sulphate, filtered and the diethyl ether evaporated under vacuum to obtain a viscous orange oil (1.1284 g, 50 %). ν_{max}/cm^{-1} (**Spectrum 3.14**): 3360 and 3289 (N-H_2), 1581 (N-H) and 2842 (C-H aliphatic). ^1H NMR: δ_H (300 MHz, $CDCl_3$)/ppm (**Spectrum 3.15**): 4.18 (t, 2H, C_5H_2), 4.16 (s, 5H, C_5H_2), 4.12 (t, 5H, C_5H_5) 3.55 (s, 2H, CH_2) and 1.41 (s, 2H, NH_2).

4.6.3 1,1-Dicyanovinyl-2-ferrocene with nZIF-8 as catalyst

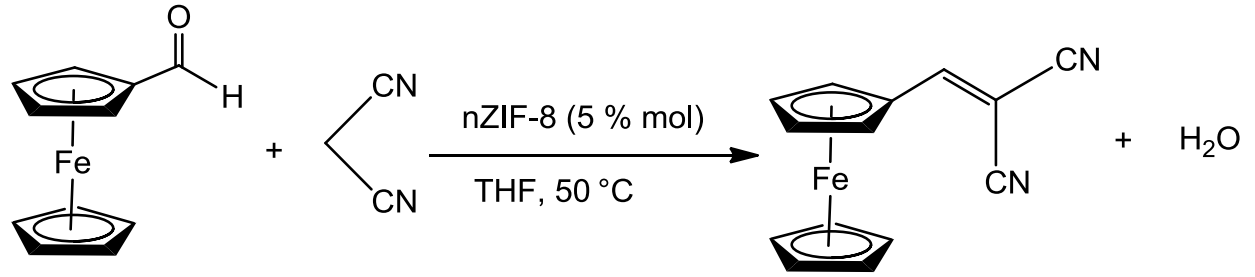

Ferrocenecarboxaldehyde (0.407 g, 1.9 mmol) was dissolved and nZIF-8 (0.02 g, 0.087 mmol) suspended in THF (10 cm^3). Malononitrile (0.396 g, 6 mmol) was added to the solutions at 50 ºC. The reaction was stirred for 3 days and turned to dark purple. The crude product was purified with column chromatography (hexane:ether 1:1 on silica) and dried in air at room temperature to obtain fine purple crystals (0.2709 g, 46 %); Melting point 95 ºC, R_f = 0.35 (hexane:ether = 1:1)

ν_{max}/cm^{-1} (**Spectrum A.7**): 2217 (C≡N), 1103/986 (C-C, Cp-ring). ^{1}H NMR: δ_H (300 MHz, $CDCl_3$)/ppm (**Spectrum B.10**): 7.73 (s, 1H, CH), 5.01 (s, 2H, C_5H_4), 4.88 (s, 2H, C_5H_4), 4.36 (s, 2H, C_5H_5).

4.7 Solvent Assisted Ligand Exchange (SALE) of nZIF-8

4.7.1 Time-resolved ligand Exchange of nZIF-8 with imidazole to synthesize SALEM-2.[4]

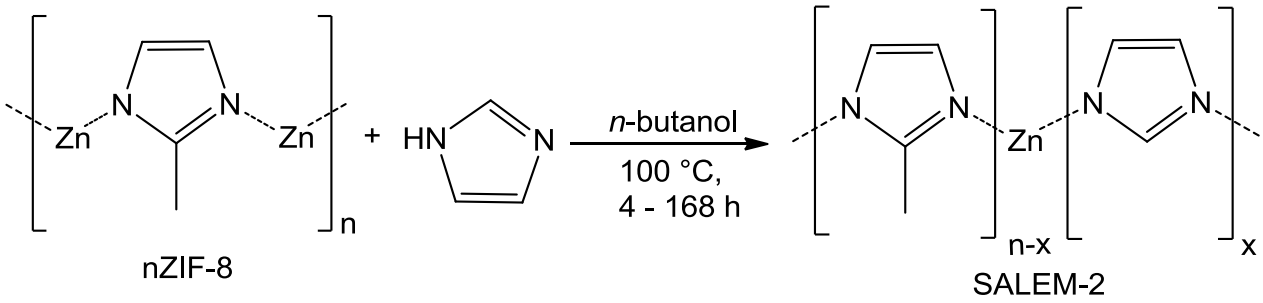

nZIF-8 (0.300 g, 1.306 mmol) was suspended in *n*-butanol (25 cm^3) with an ultra-sonic probe for 60 seconds and transferred into a Teflon tube. Imidazole (0.603 g, 8.858 mmol), dissolved in *n*-butanol (25 cm^3) was mixed with the nZIF-8 suspension. The tube was capped and heated at 100 ℃ for periods between 4 and 168 hours (see **Table 4.4**). After cooling the nano crystals were isolated by centrifugation (8500 rpm, 30 min, 15 ℃), washed with methanol (3 x 100 cm^3) and centrifuged. The product was dried in air overnight and obtained as a white powder, SALEM-2_{168h} (0.203 g, 68 % based on nZIF-8). ^{1}H NMR: δ_H (300 MHz, D_2O)/ppm (**Spectrum 3.16**): 7.82 (s, 1H, CH), 6.61 (s, 2H, CH=CH), 6.41 (s, 2H, CH=CH), 1.75 (s, 3H, CH_3). ^{13}C SSNMR: δ_H (400 MHz)/ppm (**Spectrum 3.18**): 151 (s, 1C, N-C-N), 142 (s, 1C, N-C-N), 128 (s, 2C, CH=CH), 125 (s, 1C, CH=CH), 13 (s, C, CH_3). PXRD: (**Spectrum 3.20**).

Table 4.4 Ligand exchange of nZIF-8 (1.3 mmol) with imidazole (8.9 mmol) in *n*-butanol using different reaction times.

Product	*Time/ h	Yield/ g (%)	Exchange (%)
SALEM-2_{168h}	168	0.203 (68)	86
SALEM-2_{72h}	72	0.246 (82)	69
SALEM-2_{24h}	24	0.213 (71)	45
SALEM-2_{16h}	16	0.206 (69)	35
SALEM-2_{4h}	4	0.260 (87)	28

4.7.2 Ligand Exchange of nZIF-8 with 2-mercaptobenzimidazole (SHBzIm)

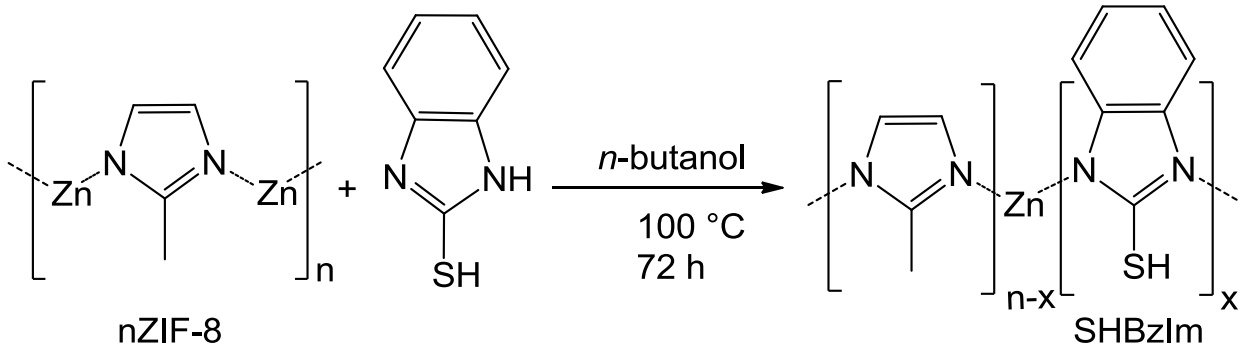

nZIF-8 (0.300 g, 1.306 mmol) was suspended in *n*-butanol (30 cm^3) with an ultra-sonic probe for 3 minutes and transferred into a Teflon reactor. 2-Mercaptobenzimidazole (1.33 g, 8.858 mmol), dissolved in *n*-butanol (20 cm^3) was mixed with the nZIF-8 suspension. The reactor was sealed and heated at 100 ℃ for 72 hours. After cooling the nano crystals were isolated by centrifugation (8500 rpm, 30 min, 15 ℃), washed with methanol (3 x 100 cm^3), centrifuged, dried in air overnight and obtained as a light yellow powder nZIF8-$SHBzIm_{72h}$ (0.068 g, 23 % based on nZIF-8). 12 % exchange. ^1H NMR: δ_H (300 MHz, D_2O)/ppm (**Spectrum 3.25.a**): 6.82 (s, 2H, C_6H_4), 6.72 (s, 2H, C_6H_4), 6.15 (s, 2H, CH=CH), 1.84 (s, 3H, CH_3). ^{13}C SSNMR: δ_H (400 MHz)/ppm (**Spectrum 3.25.b**): 154 (s, 1C, N-C-N), 145 (s, 2C, C_6H_4), 137 (s, 1C, N-C-N), 127 (s, 1C, CH=CH), 119 (s, 1C, C_6H_4), 17 (s, C, CH_3). PXRD: (**Spectrum 3.25.c**)

4.7.3 Time-resolved ligand Exchange of nZIF-8 with M2

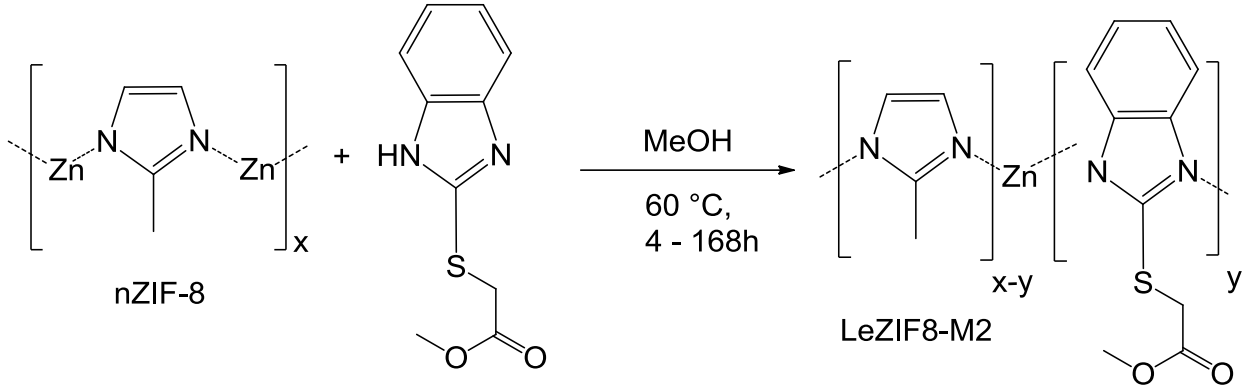

nZIF-8 (0.300 g, 1.306 mmol) was suspended in methanol (25 cm^3) with an ultra-sonic probe for 60 seconds and transferred into a Teflon tube. M2 (0.905 g, 4.08 mmol), dissolved in methanol (25 cm^3) was mixed with the nZIF-8 suspension. The tube was capped and heated at 60 °C for 168* hours. After cooling the nano crystals were isolated by centrifugation (8500 rpm, 30 min, 15 °C), washed with methanol (3 x 100 cm^3), centrifuged, dried in air overnight and obtained as a white powder LeZIF8-$M2_{168h}$ (0.286 g, 95 % based on nZIF-8)*. ^{1}H NMR: δ_H (300 MHz, D_2O)/ppm (**Spectrum B.3**): 6.72 (s, 2H, C_6H_4), 6.59 (s, 2H, C_6H_4), 6.35 (s, 2H, CH=CH), 3.4 (s, 3H,CH_3), 2.89 (s, 2H, CH_2), 1.67 (s, 3H, CH_3). ^{13}C SSNMR: δ_H (400 MHz)/ppm (**Spectrum 3.29**): 169 (s, 1C, C=O), 160 (s, 1C, N-C-N), 154 (s, 1C, N-C-N), 147 (s, 2C, C_6H_4), 127 (s, 1C, CH=CH), 125 (s, 1C, C=C), 118 (s, 1C, C_6H_4), 51 (s,1C,CH_3), 39 (s, 1C, CH_2), 17 (s, C, CH_3). PXRD: (**Spectrum D.1**).

Table 4.5 Ligand exchange of nZIF-8 (1.3 mmol) with M2 (4.08 mmol) in methanol, using different reaction times.

Product	*Time/ h	Yield/ g (%)	Exchange (%)
LeZIF8-$M2_{168h}$	168	0.286 (95)	13.6
LeZIF8-$M2_{72h}$	72	0.298 (99)	9.5
LeZIF8-$M2_{24h}$	24	0.288 (96)	8.4
LeZIF8-$M2_{16h}$	16	0.299 (99)	7.3
LeZIF8-$M2_{4h}$	4	0.293 (98)	6.5

*The product for the different exchange times are identical to this one for 168 h.

4.7.4 Time-resolved ligand Exchange of nZIF-8 with E3

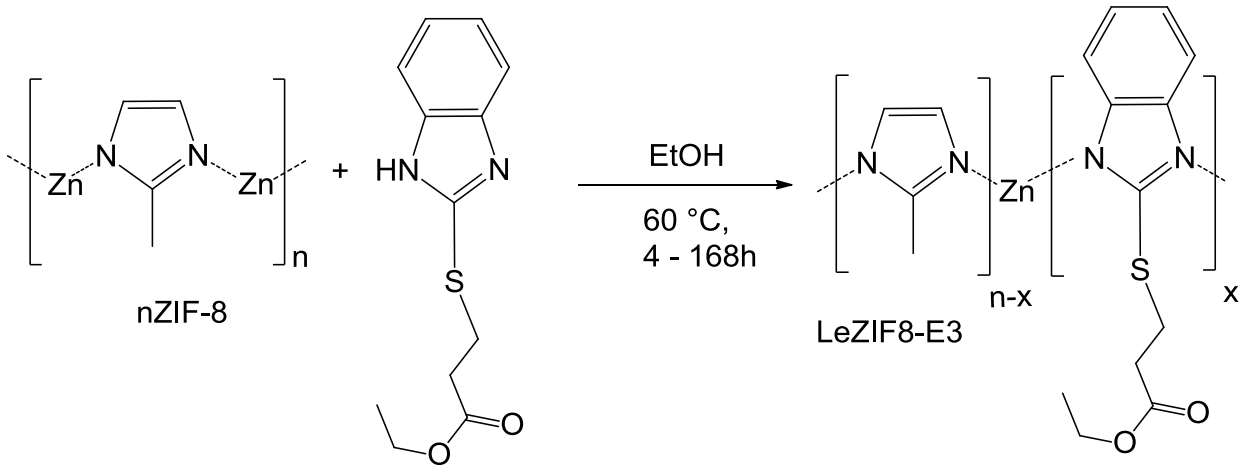

nZIF-8 (0.300 g, 1.306 mmol) was suspended in ethanol (25 cm^3) with an ultra-sonic probe for 60 seconds and transferred into a Teflon tube. E3 (1.02 g, 4.08 mmol), dissolved in ethanol (25 cm^3) was mixed with the nZIF-8 suspension. The tube was capped and heated at 60 ℃ for 168* hours. After cooling the nano crystals were isolated by centrifugation (8500 rpm, 30 min, 15 ℃), washed with methanol (3 x 100 cm^3), centrifuged, dried in air overnight and obtained as a white powder LeZIF8-$E3_{168h}$ (0.196 g, 65 % based on nZIF-8)*. ^{1}H NMR: δ_H (300 MHz, D_2O)/ppm (**Spectrum B.4**): 6.95 (s, 2H, C_6H_4), 6.81 (s, 2H, C_6H_4), 6.55 (s, 2H, CH=CH), 3.3 (s, 2H,CH_2), 2.91 (s, 2H, CH_2), 2.21 (s, 2H, CH_2), 1.87 (s, 3H, CH_3), 0.45 (s, 3H, CH_3). ^{13}C SSNMR: δ_H (400 MHz)/ppm (**Spectrum 3.29**): 172 (s, 1C, C=O), 165 (s, 1C, N-C-N), 154 (s, 1C, N-C-N), 147 (s, 2C, C_6H_4), 127 (s, 1C, CH=CH), 124 (s, 1C, C=C), 118 (s, 1C, C_6H_4), 63 (s,1C,CH_2), 45 (s, 1C, CH_2), 63 (s, 1C, CH_2), 33 (s, 1C, CH_3), 17 (s, C, CH_3). PXRD: (**Spectrum D.2**).

Table 4.6 Ligand exchange of nZIF-8 (1.3 mmol) with E3 (4.08 mmol) in ethanol, using different reaction times.

Product	*Time/ h	Yield/ g (%)	Exchange (%)
LeZIF8-$E3_{168h}$	168	0.196(65)	1.3
LeZIF8-$E3_{72h}$	72	0.234 (78)	1.3
LeZIF8-$E3_{24h}$	24	0.255 (85)	1.9
LeZIF8-$E3_{16h}$	16	0.213 (77)	1.4
LeZIF8-$E3_{4h}$	4	0.259 (86)	0.9

*The product for the different exchange times are identical to this one for 168 h.

4.7.5 Time-resolved ligand Exchange of nZIF-8 with E4

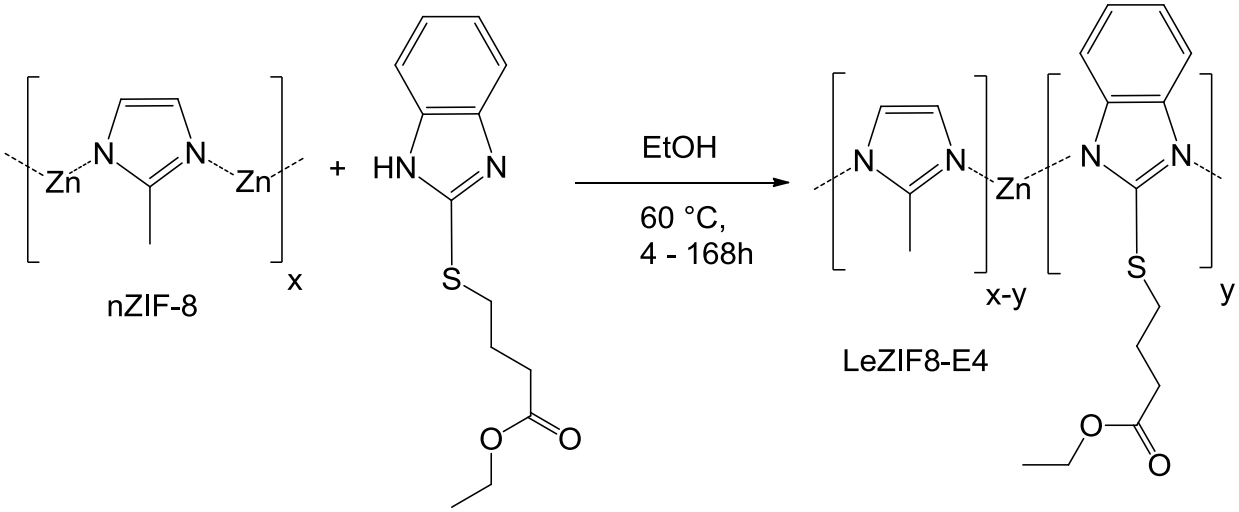

nZIF-8 (0.300 g, 1.306 mmol) was suspended in ethanol (25 cm^3) with an ultra-sonic probe for 60 seconds and transferred into a Teflon tube. E4 (1.077 g, 4.08 mmol), dissolved in ethanol (25 cm^3) was mixed with the nZIF-8 suspension. The tube was capped and heated at 60 °C for 168* hours. After cooling the nano crystals were isolated by centrifugation (8500 rpm, 30 min, 15 °C), washed with methanol (3 x 100 cm^3), centrifuged, dried in air overnight and obtained as a white powder LeZIF8-$E4_{168h}$ (0.295 g, 98 % based on nZIF-8)*. ^{1}H NMR: δ_H (300 MHz, D_2O)/ppm (**Spectrum B.5**): 6.89 (s, 2H, C_6H_4), 6.73 (s, 2H, C_6H_4), 6.57 (s, 2H, CH=CH), 3.3 (s, 2H,CH_2), 2.91 (s, 2H, CH_2), 2.67 (s, 2H, CH_2), 1.35 (s, 2H, CH_2), 1.85 (s, 3H, CH_3), 0.4 (t, 3H, CH_3). ^{13}C SSNMR: δ_H (400 MHz)/ppm (**Spectrum 3.29**): 174 (s, 1C, C=O), 159 (s, 1C, N-C-N), 154 (s, 1C, N-C-N), 147 (s, 2C, C_6H_4), 127 (s, 1C, CH=CH), 123 (s, 1C, C=C), 119 (s, 1C, C_6H_4), 62 (s,1C,CH_2), 36 (s, 1C, CH_2), 35 (s, 1C, CH_2), 29 (s, 1C, CH_2), 27 (s, 1C, CH_3), 17 (s, C, CH_3). PXRD: (**Spectrum D.3**).

Table 4.7 Ligand exchange of nZIF-8 (1.3 mmol) with E4 (4.08 mmol) in ethanol, using different reaction times.

Product	*Time/ h	Yield/ g (%)	Exchange (%)
LeZIF8-$E4_{168h}$	168	0.295 (98)	9.1
LeZIF8-$E4_{72h}$	72	0.290 (97)	9.1
LeZIF8-$E4_{24h}$	24	0.288 (96)	8.9
LeZIF8-$E4_{16h}$	16	0.297 (99)	7.6
LeZIF8-$E4_{4h}$	4	0.280 (93)	4.9

*The product for the different exchange times are identical to this one for 168 h.

4.7.6 Time-resolved ligand Exchange of nZIF-8 with M5

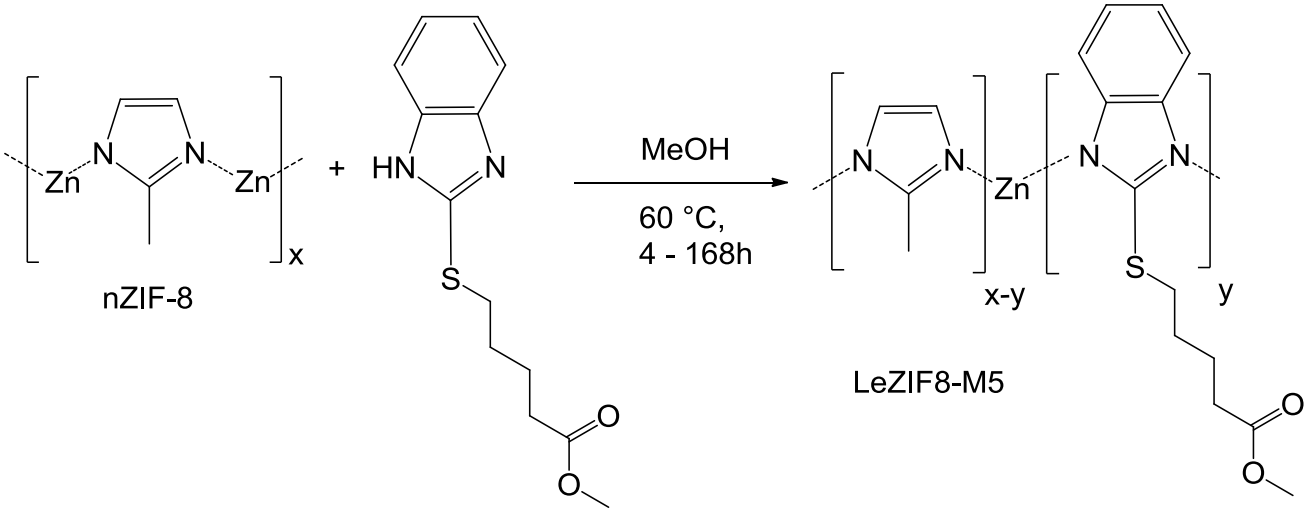

nZIF-8 (0.300 g, 1.306 mmol) was suspended in ethanol (25 cm^3) with an ultra-sonic probe for 60 seconds and transferred into a Teflon tube. M5 (1.077g, 4.08 mmol), dissolved in ethanol (25 cm^3) was mixed with the nZIF-8 suspension. The tube was capped and heated at 60 ℃ for 168* hours. After cooling the nano crystals were isolated by centrifugation (8500 rpm, 30 min, 15 ℃), washed with methanol (3 x 100 cm^3) centrifuged, dried in air overnight and obtained as a white powder LeZIF8-$M5_{168h}$ (0.300 g, 100 % based on nZIF-8)*. ^{1}H NMR: δ_H (300 MHz, D_2O)/ppm (**Spectrum B.6**): 6.89 (s, 2H, C_6H_4), 6.73 (s, 2H, C_6H_4), 6.51 (s, 2H, CH=CH), 2.85 (s, 3H,CH_3), 2.66 (s, 2H,CH_2),1.84 (s, 3H,CH_3), 1.66 (s, 2H, CH_2), 1.01 (s, 4H, CH_2CH_2). ^{13}C SSNMR: δ_H (400 MHz)/ppm (**Spectrum 3.29**): 174 (s, 1C, C=O), 159 (s, 1C, N-C-N), 154 (s, 1C, N-C-N), 147 (s, 2C, C_6H_4), 127 (s, 1C, CH=CH), 125 (s, 1C, C=C), 119 (s, 1C, C_6H_4), 52 (s,1C, CH_3), 37 (s, 1C, CH_2), 35 (s, 1C, CH_2), 31 (s, 1C, CH_2), 26 (s, 1C, CH_3), 17 (s, C, CH_3). PXRD: (**Spectrum D.4**).

Table 4.8 Ligand exchange of nZIF-8 (1.3 mmol) with M5 (4.08 mmol) in methanol, using different reaction times.

Product	***Time/ h**	**Yield/ g (%)**	**Conversion (%)**
LeZIF8-$M5_{168h}$	168	0.300 (100)	11.7
LeZIF8-$M5_{72h}$	72	0.293 (98)	10.0
LeZIF8-$M5_{24h}$	24	0.270 (90)	9.1
LeZIF8-$M5_{16h}$	16	0.295 (98)	8.6
LeZIF8-$M5_{4h}$	4	0.286 (95)	7.0

*The product for the different exchange times are identical to this one for 168 h.

4.7.7 Time-resolved ligand Exchange of nZIF-8 with 2-Aminobenzimidazole (NH_2BzIm)

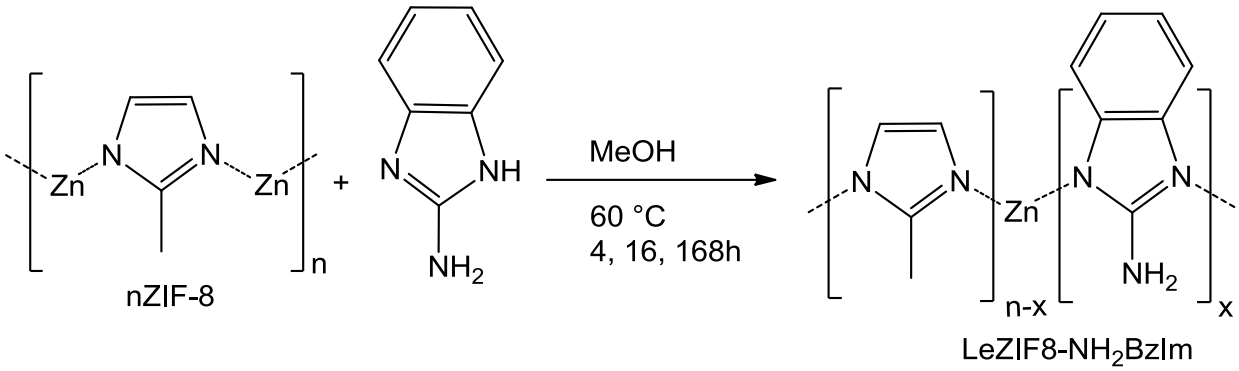

nZIF-8 (0.300 g, 1.306 mmol) was suspended in methanol (25 cm^3) with an ultra-sonic probe for 60 seconds and transferred into a Teflon tube. 2-Aminobenzimidazole (0.540 g, 4.08 mmol), dissolved in methanol (25 cm^3) was mixed with the nZIF-8 suspension. The tube was capped and heated at 60 °C for 16* hours. After cooling the nano crystals were isolated by centrifugation (8500 rpm, 30 min, 15 °C), washed with methanol (3 x 100 cm^3), centrifuged, dried in air overnight and obtained as a light brown powder LeZIF8-NH_2BzIm_{16h} (0.2945 g, 90 % based on nZIF-8)*. ^1H NMR: δ_H (300 MHz, D_2O)/ppm (**Spectrum B.7**): 6.47 (s, 2H, CH=CH), 6.43 (s, 2H, CH=CH), 6.40 (s, 2H, CH=CH), 1.77 (s, 3H, CH_3). ^{13}C SSNMR: δ_H (400 MHz)/ppm (**Spectrum 3.35**): 164.3 (s, 1C, C-NH_2), 154.36 (s, 1C, N-C-N), 145.3 (s, 2C, C_6H_4), 127.3 (s, 2C, CH=CH), 123.66 (s, C, C_6H_4), 115.56 (s, C, C_6H_4), 16.87 (s, C, CH_3). PXRD: (**Spectrum 3.37**).

Table 4.9 Ligand exchange of nZIF-8 (1.3 mmol) with 2-aminobenzimidazle (4.08 mmol) in methanol, using different reaction times.

Product	*Time/ h	Yield/ g (%)	Exchange (%)
LeZIF8-NH_2BzIm_{4h}	4	0.289 (96)	5
LeZIF8-NH_2BzIm_{16h}	16	0.296 (98)	10
LeZIF8-NH_2BzIm_{168h}	168	0.300 (100)	16

*The product for the different exchange times are identical to this one for 16 h.

4.7.8 Ligand Exchange of nZIF-8 with 2-Phenylimidazole (PhIm)

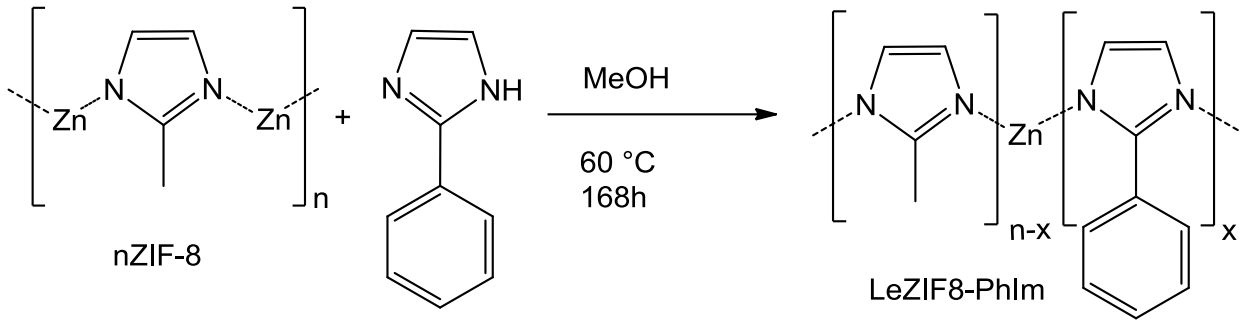

nZIF-8 (0.300 g, 1.306 mmol) was suspended in n-butanol (30 cm^3) with an ultra-sonic probe for 3 minutes and transferred into a Teflon reactor. 2-phenylimidazole (1.28 g, 8.858 mmol), dissolved in n-butanol (30 cm^3) was mixed with the nZIF-8 suspension. The reactor was sealed and heated at 100 ℃ for 168 hours. After cooling the nano crystals were isolated by centrifugation (8500 rpm, 30 min, 15 ℃), washed with methanol (3 x 100 cm^3), centrifuged, dried in air overnight and obtained as a light yellow powder LeZIF8-$PhIm_{168h}$ (0.294 g, 98 % based on nZIF-8). ^{1}H NMR: δ_H (300 MHz, D_2O)/ppm (**Spectrum B.8**): 7.1 (d, 1H, C_6H_5), 6.9 (m, 2H, C_6H_5), 6.8 (d, 2H, C_6H_5), 6.5 (s, 2H, CH=CH), 6.5 (s, 2H, CH=CH), 1.8 (s, 3H, CH_3). ^{13}C SSNMR: δ_H (400 MHz)/ppm (**Spectrum 3.42**): 154 (s, 1C, N-C-N), 131.8 (s, 1C, C_6H_5), 130 (s, 2C, C_6H_5), 129 (s, 2C, C_6H_5), 127 (s, C, CH=CH) 127 (s, C, CH=CH), 16.62 (s, C, CH_3). PXRD: (**Spectrum 3.44**)

4.7.9 Ligand Exchange of nZIF-8 with 2-Nitroimidazole (NO_2Im)

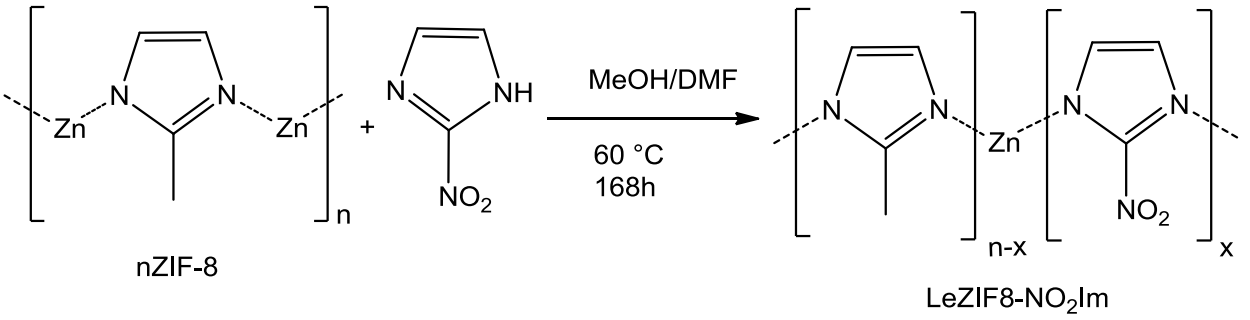

nZIF-8 (0.300 g, 1.306 mmol) was suspended in methanol (25 cm^3) with an ultra-sonic probe for 3 minutes and transferred into a Teflon reactor. 2-Nitroimidazole (0.461 g, 4.08 mmol), dissolved in dimethylformamide (25 cm^3) was mixed with the nZIF-8 suspension. The tube was sealed and heated at 60 ℃ for 168* hours. After cooling the nano crystals were isolated by centrifugation (8500 rpm, 30 min, 15 ℃), washed with DMF (2 x 100 cm^3) and methanol (3 x 100 cm^3), centrifuged, dried in air overnight and obtained as a light yellow powder LeZIF8-NO_2Im_{168h} (0.1715 g, 57 % based on nZIF-8). 66.6 % exchange. ^{1}H NMR: δ_H (300 MHz,

D_2O)/ppm (**Spectrum 3.41**): 6.6 (s, 2H, C_6H_4), 6.33 (s, 2H, C_6H_4), 1.67 (s, 3H, CH_3). ^{13}C SSNMR: δ_H (400 MHz)/ppm (**Spectrum 3.42**): 154 (s, 1C, N-C-N), 135 (s, 2C, CH=CH), 131.5 (s, 1C, C-NO_2), 126 (s, 2C, CH=CH), 16.6 (s, C, CH_3). PXRD: (**Spectrum 3.44**).

4.8 Post Synthetic modification

4.8.1 Claisen condensation of Ethylester functionalised nZIF8-E4 with acetylferrocene

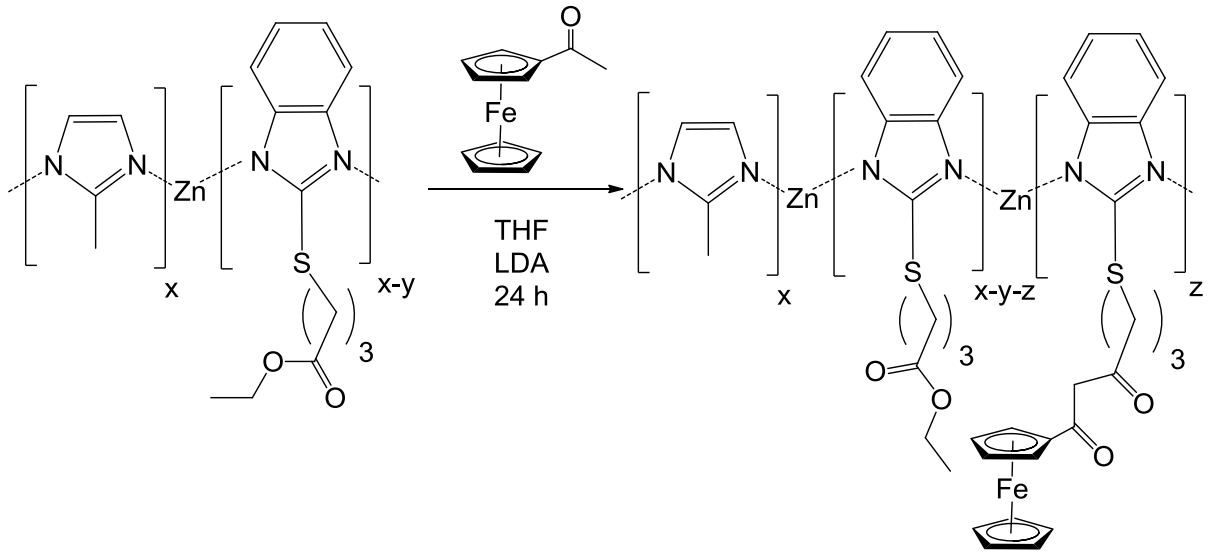

After acetylferrocene (0.020 g, 0.09 mmol) was dissolved in dry THF (20 cm^3) under argon gas, it was cooled to 0 ℃. 2M LDA (0.5 cm^3, 1 mmol) was added dropwise and the red solution stirred for 45 minutes. LeZIF8-$E4_{24h}$ (0.200 g, 0.68 mmol) was added and the solution was left to stir overnight at room temperature. Diethyl ether (50 cm^3) was added and centrifuged. The precipitate was washed and centrifuged with diethyl ether (2 x 50 cm^3), H_2O (50 cm^3) and methanol (2 x 50 cm^3). The product was dried in air and activated at 100 ℃ under vacuum to give a light yellow powder (0.167 g, 84 % based on LeZIF8-$E4_{24h}$). ^{13}C SSNMR: δ_H (400 MHz)/ppm (**Spectrum 3.50**): 174 (s, 1C, C=O), 159 (s, 1C, N-C-N), 154 (s, 1C, N-C-N), 147 (s, 2C, C_6H_4), 127 (s, 1C, CH=CH), 123 (s, 1C, C=C), 119 (s, 1C, C_6H_4), 72 (m, 10C, $C_{10}H_9$), 62 (s,1C,CH_2), 36 (s, 1C, CH_2), 35 (s, 1C, CH_2), 29 (s, 1C, CH_2), 27 (s, 1C, CH_3), 17 (s, C, CH_3). ICP-OES: 0.063 % Fe.

4.8.2 Amidation of LeZIF8-M2 with ferrocenemethyl amine

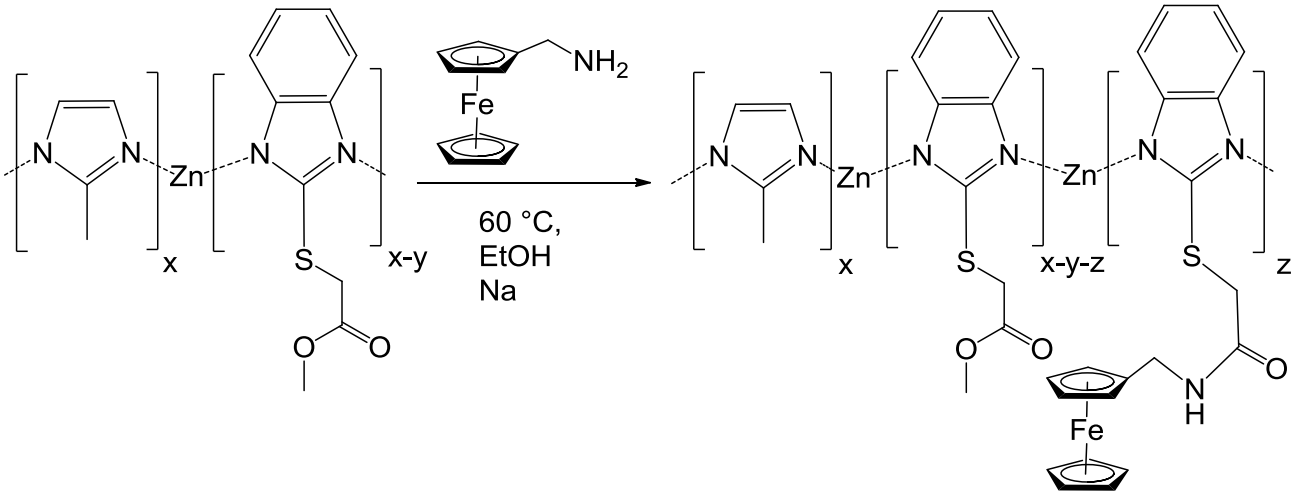

After ferrocenemethylamine (0.30 g, 1.23 mmol) was dissolved in dry ethanol (10 cm^3) under argon, LeZIF8-$M2_{24h}$ (0.200 g, 0.075 mmol) was added and stirred for 15 minutes. Sodium (0.040 g) was added and the reaction mixture stirred at 50 °C for 24 hours. The orange solution was then centrifuged and washed with methanol (50 cm^3) repeatedly until the decant was clear. The product was dried in air and activated at 100 °C under vacuum to give a light yellow powder (0.1748 g, 87.4 % based on LeZIF8-M2). ^{13}C SSNMR: δ_H (400 MHz)/ppm (**Spectrum 3.50**): 177.5 (s, 1C, C=O), 160 (s, 1C, N-C-N), 154 (s, 1C, N-C-N), 147 (s, 2C, C_6H_4), 127 (s, 1C, CH=CH), 125 (s, 1C, C=C), 118 (s, 1C, C_6H_4), 71 (m, 10C, $C_{10}H_9$), 44 (s, 1C, CH_2), 17 (s, C, CH_3). ICP-OES: 0.029 % Fe.

4.8.3 Binding of ferrocene aldehyde to LeZIF8-NH_2BzIm

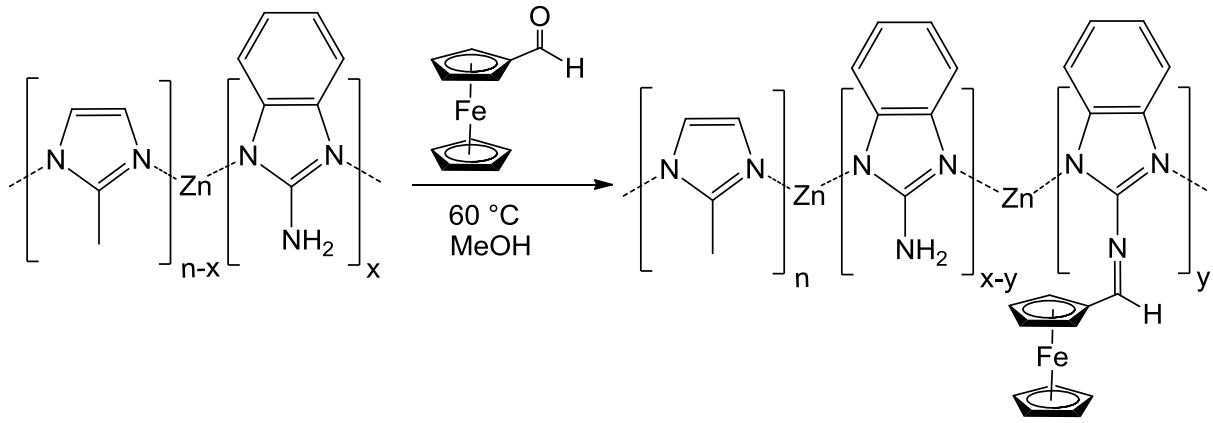

LeZIF8-NH_2BzIm_{16h} (0.250 g, 0.187 mmol) was suspended in methanol (10 cm^3) with an ultra-sonic bath for 2x5 minutes. Ferrocene aldehyde (0.050 g, 0.23 mmol) dissolved in methanol (10 cm^3) was added while stirring and the mixture refluxed for 22 hours. The solution was then

centrifuged at 8500 rpm for 30 minutes and washed with methanol (50 cm^3) repeatedly until the decant was clear. The product was dried in air and activated at 100 ℃ under vacuum to give a light maroon powder (0.228 g, 91 % based on LeZIF8-NH_2BzIm). ^{13}C SSNMR: δ_H (400 MHz)/ppm (**Spectrum 3.51**): 164.83 (s, 1C, C-NH_2), 154.36 (s, 1C, N-C-N), 145.3 (s, 2C, C_6H_4), 127.3 (s, 2C, CH=CH), 123.52 (s, C, C_6H_4), 115.56 (s, C, C_6H_4), 72.23 (m, 10C, $C_{10}H_9$), 16.87 (s, C, CH_3). ICP-OES: 0.5 % Fe.

4.8.4 Ligand Exchange of nZIF-8 with 2-Aminobenzimidazole with ferrocene carboxylic acid

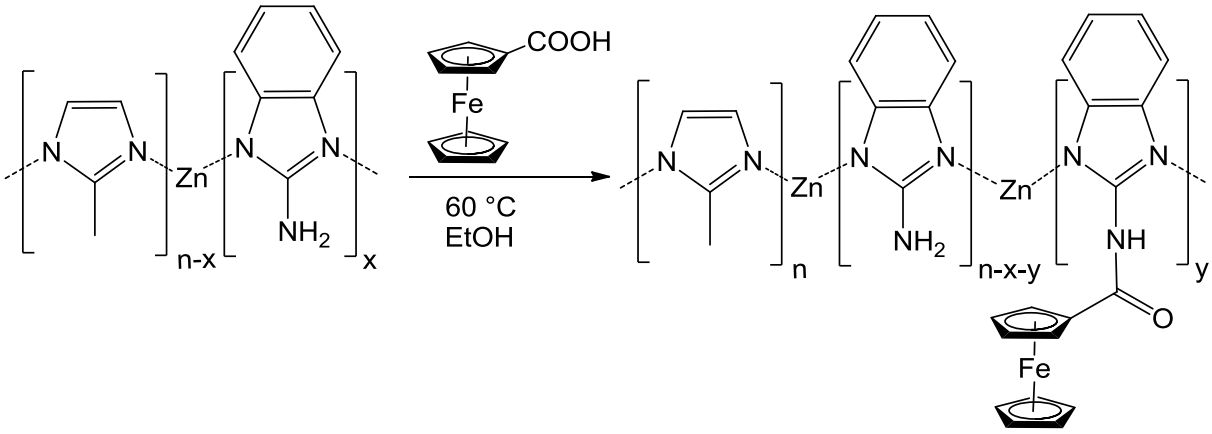

LeZIF8-NH_2BzIm$_{16h}$ (0.250 g, 0.187 mmol) was suspended in ethanol (20 cm^3) with an ultra-sonic bath for 5 minutes. Ferrocenecarboxylic acid (0.156 g, 0.68 mmol) was added while stirring and the mixture refluxed for 48 hours. The solution was then centrifuged at 9500 rpm for 30 minutes and washed with methanol (50 cm^3) repeatedly until the decant was clear. The product was dried in air and activated at 100 ℃ under vacuum to give a yellow powder (0.2491 g, 99 % based on LeZIF8-NH_2BzIm). ^{13}C SSNMR: δ_H (400 MHz)/ppm (**Spectrum 3.51**): 184-188 (s, 1C, C=O), 165.37 (s, 1C, C-NH_2), 154.3 (s, 1C, N-C-N), 145.2 (s, 2C, C_6H_4), 127.3 (s, 2C, CH=CH), 125.1 (s, C, C_6H_4), 115.5 (s, C, C_6H_4), 73.94 (m, 10C, $C_{10}H_9$), 16.87 (s, C, CH_3). ICP-OES: 8.3 % Fe.

4.8.5 Modification of lithiated SALEM-2 with $(PPh_3)_2PdCl_2$

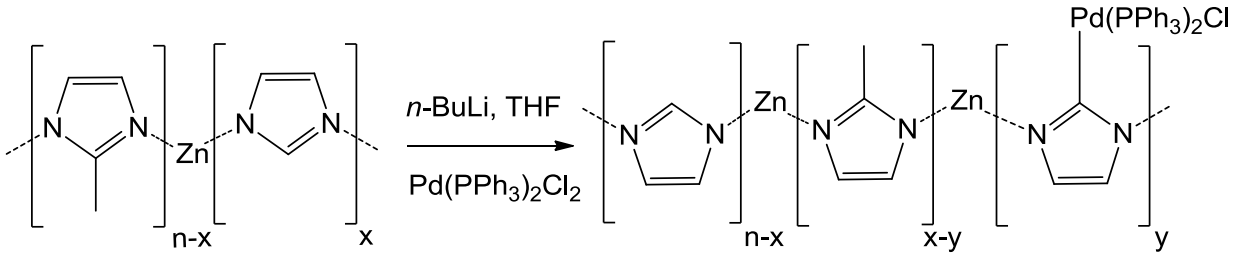

SALEM-2_{16h} (0.200 g, 0.1 mmol imidazole) was activated at 100 °C for 16 hours and was suspended in THF (20 cm^3) for 10 minutes under nitrogen. While stirring under argon, the solution was cooled to -78 °C and *n*-butylithium in hexane (0.8 cm^3) was added dropwise. The solution was stirred for 30 minutes. After $(PPh_3)_2PdCl_2$ (0.100 g, 0.14 mmol) was added and the reaction was stirred overnight at room temperature to afford a dark red suspension. The suspended particles were isolated by centrifugation (8500 rpm, 30 min, 15 °C), washed with THF (50 cm^3), methanol (2 x 50 cm^3) and centrifugated. The product was dried in air overnight and give a grey powder SALEM-2_{16h}-Pd (0.120 g, 60 % based on nZIF-8). ICP-OES: 1.2 % Pd.

4.8.6 Binding of Sebacoyl chloride with LeZIF8-NH_2BzIm

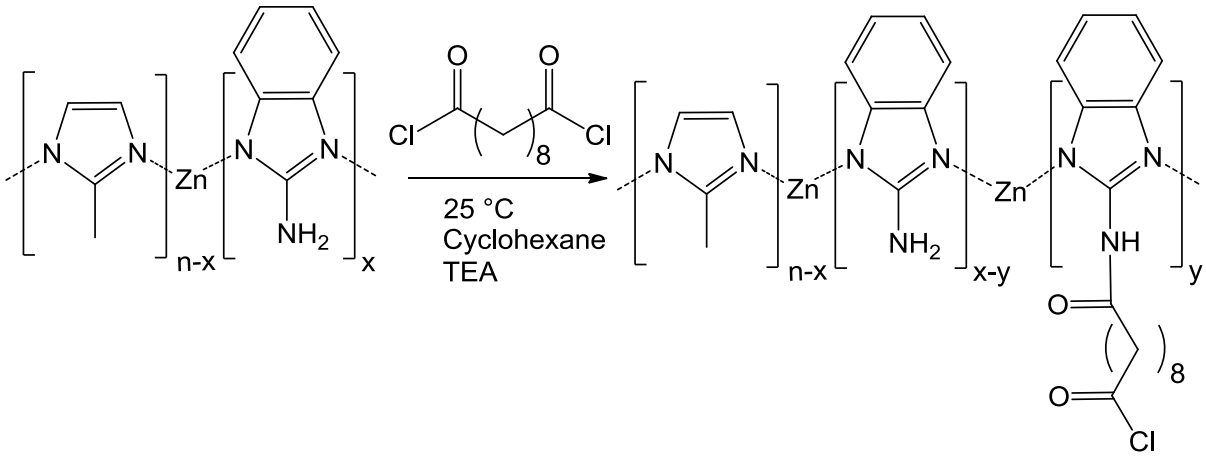

LeZIF8-NH_2BzIm4_h (0.200 g, 0.094mmol) was suspended in cyclohexane (20 cm^3) with an ultra-sonic probe for 2 x 30 seconds. After TEA (1 cm^3) was added while stirring, sebacoyl chloride (0.1 cm^3, 0.5 mmol) was added dropwise and stirred for 10 minutes at 25 °C. The crude brown product was filtered, washed with H_2O (80 cm^3) and methanol (100 cm^3). The product was dried in an oven at 100 °C for 5 hours and give a light brown powder nZIF8-NH2BzIm-Seba (0.200 g, 100 % based on ZIF8-NH_2BzIm$_{4h}$). ^{13}C SSNMR: δ_H (400 MHz)/ppm (**Spectrum 3.64**): 183.59 (s, C, COOH), 174 (s, C, COCl), 164 (s, 1C, C-NH_2), 153 (s, 1C, N-C-N), 149.43 (s, C, CON), 144 (s, 2C, C_6H_4), 127 (s, 2C, CH=CH), 123 (s, 2C, C_6H_4), 118 (s, 2C, C_6H_4), 114.36 (s, 2C, C_6H_4), 52 (s, 2C, C_8H_{16}), 20-45 (m, 6C, C_8H_{16}), 16.87 (s, C, CH_3).

4.8.7 Amidation of nZIF8-NH_2BzIm with PAA-Cl

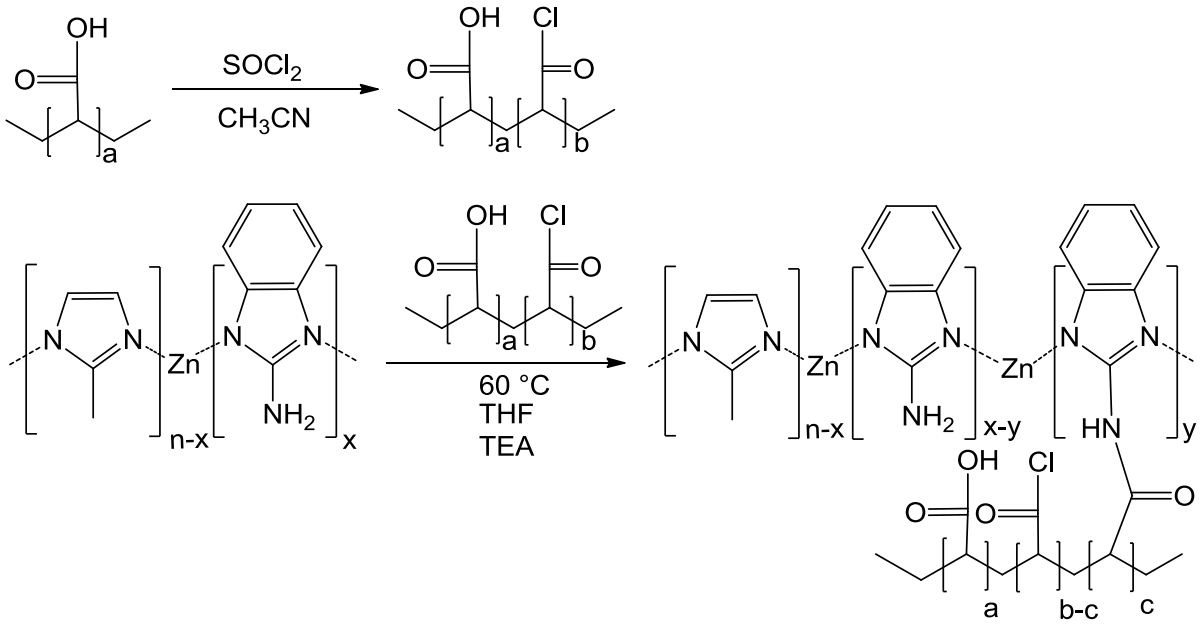

Polyacrylic acid (2.5 g, Mw = 2500) was dissolved in acetonitrile. Thionyl chloride (2.9 cm^3) was added dropwise and stirred for 30 minutes at room temperature. The crude product was filtered, washed with acetonitrile (3x50 cm^3) and dried at room temperature to obtain fine white crystals (2.015 g).

PAA-Cl (0.200 g, 50 wt %) and triethylamine (5 cm^3) were suspended in THF and stirred under argon. LeZIF8-NH_2BzIm$_{4h}$ (0.200g, 0.04684 mmol) was added slowly and stirred for 24 hours. The precipitate was isolated by centrifugation (8500 rpm, 30 min, 15 ℃). The solid product was washed with methanol (3 x 150 cm^3), isolated by centrifugation and dried in air overnight to give a white powder (0.166 g, 83 % based on nZIF-8). ^{13}C SSNMR: δ_H (400 MHz)/ppm (**Spectrum 3.64**): 186.67 (s, C, COOH), 165.3 (s, 1C, C-NH_2), 154.36 (s, 1C, N-C-N), 150.55 (s, C, CON), 145.47 (s, 2C, C_6H_4), 127 (s, 2C, CH=CH), 123 (s, 2C, C_6H_4), 118 (s, 2C, C_6H_4), 115.67 (s, 2C, C_6H_4), 30-50 (s, 2C, C_2H_3), 16.87 (s, C, CH_3).

4.8.8 Stability of LeZIF8-E4$_{24}$ in aqueous basic solution

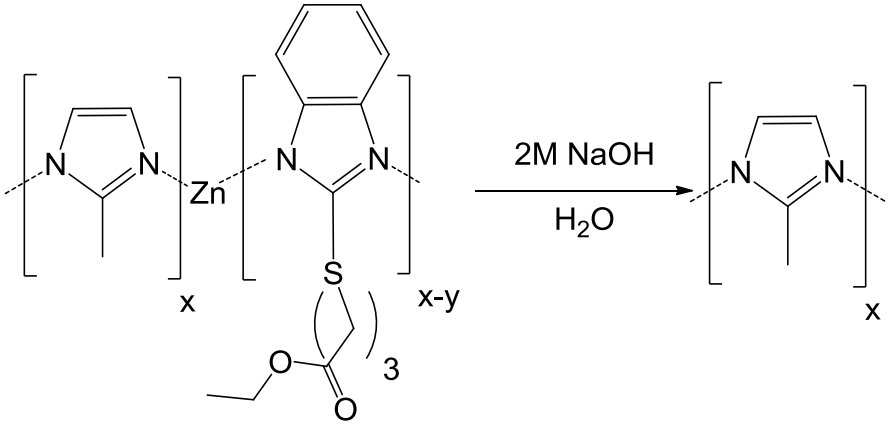

LeZIF8-E4$_{24}$ (0.150g) was suspended in an aqueous 2M NaOH solution (20 cm^3) with a ultrasonic bath for 5 min. The solution was refluxed for 24 hours. The yellow solution was isolated by centrifugation (8500 rpm, 30 min, 15 ℃) with the addition of methanol (20 cm^3) The solid product was washed with methanol (3 x 150 cm^3), isolated by centrifugation and dried in air overnight to obtain white powder (0.0926 g, 62 % based on LeZIF8-E4$_{24}$). ^{1}H NMR: δ_H (300 MHz, D_2O)/ppm (**Spectrum 3.34**): 6.4 (s, 2H, CH=CH), 1.78 (s, 3H, CH_3)

4.9 Catalytic Testing: Knoevenagel Condensation of Ferrocenecarboxaldehyde and malononitrile using nZIF-8 derivatives as catalysts

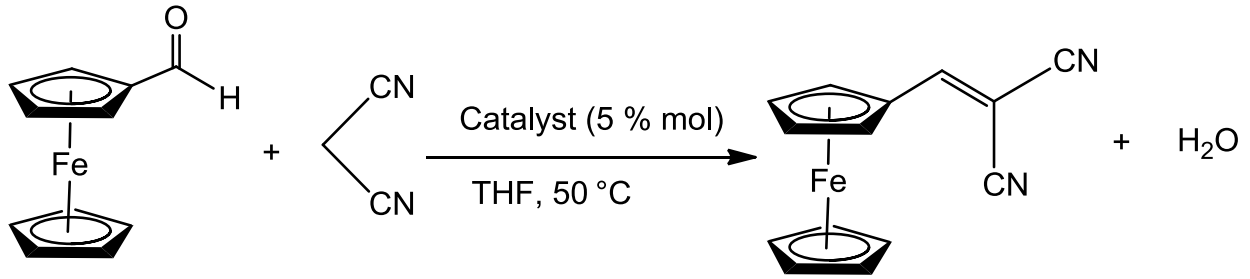

The kinetics of the Knoevenagel condensation reaction between ferrocenecarboxaldehyde and malononitrile was monitored *ex situ* by UV/vis spectrophotometry (by measuring the change of absorbance at 570 nm) at 10 ℃. THF was used as reaction solvent. The reactant was diluted 1000 times with cold THF after extraction and immediately measured on the UV/vis spectrophotometer. All kinetic measurements were done in a 1:5 molar ratio (ferrocenecarboxaldehyde:malononitrile), unless stated otherwise.

In a typical catalytic test reaction, ferrocenecarboxaldehyde (FcCHO) (0.407 g, 2 mmol) and 5 mol % base on FcCHO of nZIF-8 catalyst[§] (0.020 g, 0.087 mmol) was dispersed in THF (10

cm^3) using an ultrasonic bath before malononitrile (0.660 g, 10 mmol) was added. The solutions were heated to 50 ℃ before adding the malononitrile to the ferrocenecarboxaldehyde solution while stirring at 50 ℃. A small aliquot (0.1 cm^3) was extracted at each measuring interval, cooled to 10 ℃, diluted with cold THF (100 cm^3) and transferred to a glass cuvette for UV/vis measurement. The procedure was repeated with selected ligand exchanged ZIFs and starting materials as well as without any catalyst (see **Table 4.10**).

Table 4.10 List of catalyst for the Knoevenagel condensation between ferrocenecarboxaldehyde and malononitrile.

[§]Catalyst	**Ratio(FcCHO:malononitrile)**	**5 mol % catalyst/ mg**
nZIF-8	1:1	20
nZIF-8	1:3	20
nZIF-8	1:5	20
No catalyst	1:5	-
ZIF8-NH_2BzIm_{4h}	1:5	20
ZIF8-NH_2BzIm_{16h}	1:5	20
ZIF8-NH_2BzIm_{168h}	1:5	20
SALEM-2_{4h}	1:5	20
SALEM-2_{168h}	1:5	20
2-methylimidazole	1:5	0.008
2-aminibenzimdazole	1:5	0.013
$Zn(NO_3)_2.4H_2O$	1:5	0.026

4.10 Reference

1 A. I. Vogel, *A Text-book of Practical Organic Chemistry Including Qualitative Organic Analysis*, Longmans Green and Co, Third edit., 1961.

2 D. B. G.Williams and M. Lawton, *J. Org. Chem.*, 2010, **75**, 8351–8354.

3 J. Cravillon, S. Münzer, S. J. Lohmeier, A. Feldhoff, K. Huber and M. Wiebcke, *Chem. Mater.*, 2009, **21**, 1410–1412.

4 O. Karagiaridi, M. B. Lalonde, W. Bury, A. A. Sarjeant, O. K. Farha and J. T. Hupp, *J. Am. Chem. Soc.*, 2012, **134**, 18790–18796.

5 Conclusion and Future Perspectives

5.1 Conclusion

In this study, nano-sized ZIF-8 of with an average diameter of 22 nm was successfully synthesised with an optimum reagent to methanol ratio of 1:8:1500 (Zn:MeIm:MeOH) in a simple benchtop reaction at 60 ℃. The particle size of nZIF-8_{1500} (the optimised product) was statistically measured from TEM images and correlated with the minimum particle size (21.6 nm) calculated with the Scherrer equation from the peak broadening in PXRD patterns. PXRD and FTIR confirmed the SOD topology and chemical structure of the synthesised nZIF-8 particles. With lower methanol ratios larger particles were obtained, and higher methanol ratios led to smaller particles of ~15 nm, due to the lower concentration of reagents, inhibiting crystal growth. These smaller particles could not be isolated and purified successfully. Porosity analyses showed that nZIF-8_{1500} adsorbed more than 450 $cm^3 g^{-1} N_2$ at 77 K (STP) and has a BET surface area of ~1600 $m^2 g^{-1}$. The nanoparticles have an external surface area of ~320 $m^2 g^{-1}$, calculated from t-plot analysis with Harkins and Jura thickness curve. TGA of nZIF-8_{1500} showed a high thermal stability up to 450 ℃ before structural collapse.

The yield of nZIF-8 was improved from 40 % (nZIF-8_{1500}) to a maximum of 85 % by adding trimethylamine (TEA) at different ratios from 1 to 8 (TEA:Zn) under the same optimal conditions as described above. The yield increased two fold for TEA ratios of > 3 at a pH > 9.0. Digestive ^{1}H NMR, FTIR spectra and PXRD patterns of the products confirmed that these particles are identical to nZIF-8_{1500}. The particles maintained a size of ~22 nm (TEM), but with TEA ratios of 4 and higher, the particles size decreased to ~16 nm. An increased TEA molar ratio improved the yield, but unfortunately caused the formation of smaller particles, which are more difficult to isolate from suspension. TEA acts as a base to deprotonate the 2-methylimidazole, but in excess it also acts as a modulating ligand to inhibit crystal growth. Although the BET surface area of nZIF-8 synthesised with TEA addition is slightly smaller (~1400 $m^2 g^{-1}$) that that of nZIF-8_{1500} (~1600 $m^2 g^{-1}$), the smaller nanoparticles (~16 nm) gave a high t-plot external surface area (383 $m^2 g^{-1}$).

A series of benzimidazolethio esters with alkyl chains of n = 1, 2, 3 and 4 namely: methyl benzimidazole-2-ylthio acetate, ethyl benzimidazole-2-ylthio propionate, ethyl benzimidazole-2-ylthio butyrate and methyl benzimidazole-2-ylthio valerate, was successfully synthesized *via*

S-alkylation and characterized with FT-IR and ^{1}H NMR. As the chain length of the benzimidazole-thioesters (BzImS-COOR) increased the melting point decreased from 114 to 88 ℃, due to the growth in the linear alkane character of the products.

Ferrocenecarboxaldehyde was synthesized *via* the Vilsmeier formylation reaction (55 % yield). It was further converted to an oxime, which was reduced to ferrocenemethylamine (50 % yield). All the products were characterised by FT-IR and ^{1}H NMR.

The benzimidazole-thioesters (BzImS-COOR) together with a variety of imidazole derivatives with unique functional groups namely: imidazole, 2-mercaptobenzimidazole (BzIm-SH), 2-aminobenzimidazole (BzIm-NH_2), 2-nitroimidazole (Im-NO_2) and 2-phenylimidazole (Im-C_6H_5) were successfully employed in Solvent Assisted Ligand Exchange (SALE) processes to replace the 2-methylimidazolate linkers of nZIF-8 to various degrees with these new functionalised linkers. The degree of exchange was controlled by synthesis time, as determined during time resolved studies on the benzimidazolethio esters, imidazole and 2-aminobenzimidazole. Imidazolate linkers containing an aromatic ring on the 4 and 5 positions of the imidazole ring had a maximum exchange of 14 % after 168 hours as determined by digestive ^{1}H NMR, and confirmed with ^{13}C solid state NMR. Functionalised imidazolate linkers without a benzene ring can reach up to 86 % exchange, due to the absence of steric hindrance and restrictions to diffusion into the nanoparticles. The SALE processes gave good yields (above 80 %), of the nanoparticles except for 2-mercaptobenzimidazole with a low yield of 23 %. The SOD topology of the nZIF-8 starting material was not affected by the newly introduced linkers except during the SALE with imidazole and 2-nitroimidazole linkers. Imidazole linkers resulted in a change towards the zni topology after 24 hours (45 % exchange). Porosity analysis showed that the zni topology led to a non-porous material in this case. With the SALE of the 2-nitroimidazole linker, a change to the frl topology was observed after 168 hours. The porosity of the exchanged ZIF remained high, with a BET surface area above 1000 $m^2\ g^{-1}$. As the exchange percentage for the SALE compounds with aromatic ring-containing linkers increased, their porosity decreased. The porosity of the nanoparticles without benzene rings, on the exchanged linkers, remained similar to that of the original nZIF-8. After ligand exchange, the particle sizes remained less than 100 nm, except in the case of exchange with 2-phenylimidazole and 2-mercaptobenzimidazole, which both resulted in particles between 150 – 250 nm. The particles remained thermally stable up to 250 ℃, after which the decomposition of the newly exchanged ligands started (TGA).

Post synthetic modification (PSM) of LeZIF8-NH_2BzIm with ferrocenecarboxaldehyde (imine formation) and ferrocenecarboxylic acid (amidation) gave an Fe content of 0.5 and 8.3 wt % respectively (ICP-OES). The ^{13}C SSNMR of LeZIF8-NH_2BzIm-FcCO revealed additional

binding modes for ferrocenecarboxylic acid on the nanoparticles surface, explaining its high iron content. The ferrocenyl-grafted nanoparticles remained smaller than 50 nm, within the size limits for cellular uptake in biomedical applications. During PSM the SOD topology of the nanoparticles was maintained, but the BET surface area of the FcCOOH-grafted nZIF-8 decreased from 1216 to 760 $m^2 g^{-1}$, due to pore blocking by the ferrocenyl fragments. Another set of modifications on LeZIF8-NH_2BzIm were the binding of sebacoyl chloride and polyacrylic acid (PAA) onto the surface of the nanoparticles *via* amide bonds. Reactions with sebacoyl chloride resulted in the interlinking of the nanoparticles, as seen from TEM images. However, after reacting LeZIF8-NH_2BzIm with PAA, large spherical particles (165 nm), mixed with unreacted ZIF nanoparticles, were obtained. Throughout the PSM procedures with sebacoyl chloride and PAA the SOD topology remained intact, but the thermal stability of the particles decreased below 200 °C, due to the decomposition of the attached sebacoyl chloride and PAA.

After SALEM-2 was lithiated and modified with $(PPh_3)_2PdCl_2$, XPS showed peaks for Pd^0, proof that the $(PPh_3)_2PdCl_2$ complex was reduced during the PSM, possibly to a phosphineimidazolylidene palladium complex residing within the pores. ICP-OES measured a Pd loading of 1.24 wt % in the modified SALEM-2. The encapsulated palladium complexes improved the BET surface area of the material by 100 $m^2 g^{-1}$.

Selected ligand exchanged nZIF-8 derivatives showed heterogeneous catalytic activity towards the Knoevenagel condensation reaction. The catalysis occurred on the external surface of the nanoparticles since the reagents and products were too large to enter the pores. Amino-decoration of nZIF-8 particles resulted in lower TOFs even though the external surface areas remain similar. nZIF-8 with the highest percentage amino-groups (16 %) gave a TOF of 2.37 h^{-1}, on par to original nZIF-8 with a TOF of 2.61 h^{-1}. It is thus proposed that the surface bound amino groups follow a slower catalytic mechanism *via* the imine route, while the base catalysed route of pristine nZIF-8 have a faster catalytic activity.

Low pressure (up to 900 mmHg) CO_2 adsorption of nZIF-8 (39 $cm^3 g^{-1}$) at 0 °C was doubled to ~77 $cm^3 g^{-1}$ after SALE with SH and NO_2 functionalised imidazoles. The adsorption of CO_2 improved in the following order NO_2 > SH > NH_2 > phenyl, arranged according to CO_2 uptake. Electron withdrawing groups (NO_2, SH and NH_2) thus improved the efficiency of CO_2 adsorption. LeZIF8-NO_2Im$_{168h}$, with an frl topology, adsorbed 76 $cm^3 g^{-1}$ CO_2, even though its BET surface area (633 $m^2 g^{-1}$) is half that of nZIF8-SHBzIm$_{72h}$, which adsorbed 77 $cm^3 g^{-1}$. For the LeZIF8-NH_2BzIm derivatives, the NH_2 groups on the surface of the nanoparticles helped to increase their CO_2 uptake from 38.5 $cm^3 g^{-1}$ for nZIF-8 to 43 $cm^3 g^{-1}$ (5 % exchange) to 48 $cm^3 g^{-1}$ (16 % exchange). The CO_2 uptake of nZIF-8 derivatives without electron withdrawing groups

rose steadily with increasing BET surface area. High pressure H_2 adsorption of LeZIF8-NH_2BzIm_{17h} (2.55 wt %) and SALEM-2_{16h}-$(PPh_3)_2PdCl$ (3.07 wt %) did not show any significant improvement on H_2 uptake compared to pristine nZIF-8 (3.46 wt %). Their uptake did follow the Chahine rule: H_2 uptake is proportional to BET surface area.

5.2 Future Perspectives

In this study important ways to modify and improve multivariate ZIF nanoparticles for applications in the fields like catalysis and gas storage was demonstrated. Further investigation should include the following:

I. Solvent assisted ligand exchange on nZIF-8 with imidazoles containing SH, NH_2, phenyl and benzimidazole-thioesters, without a benzene ring on the 4 and 5 carbon position of the imidazole. This should minimize steric hindrance and prevent a decrease in porosity and exchange percentage.

II. Cytotoxicity testing and evaluation of antitumor activity of the ferrocenyl-grafted nZIF-8 particles for biomedical applications.

III. Catalytic activity testing of SALE-nZIF-8 derivatives with the same external surface area to directly compare their catalytic activity. In this way a link between functional groups on the nanoparticle surface and catalytic activity may be established.

IV. Improvement of the SALE of 2-mercaptobenzimidazole and 2-nitroimidazole to obtain higher exchange percentages and better yields to maximise their CO_2 adsorption.

V. Computer simulations to determine the mechanism of the SALE process. This will explain the limitation of the exchange process and predict how more ligands can be exchanged without altering the SOD topology or porosity of nZIF-8

VI. Computer simulations to determine the CO_2 and H_2 adsorption sites of the solvent assisted ligand exchanged nZIF-8 derivatives, and also calculate the theoretical adsorption amounts of gases in functionalised nZIF-8 particles with different exchange percentages.

VII. Development of XPS protocols to determine the ratio of different Zn oxidation states on the interior and external surface area of nZIF-8 derivatives. This information would be crucial towards the understanding of surface-based catalysis or coordination of functionalised moieties (*e.g.* COOR) on the surface of nZIF-8 where unsaturated Zn cations may be present.

Appendix

A. ATR-FTIR Spectrum

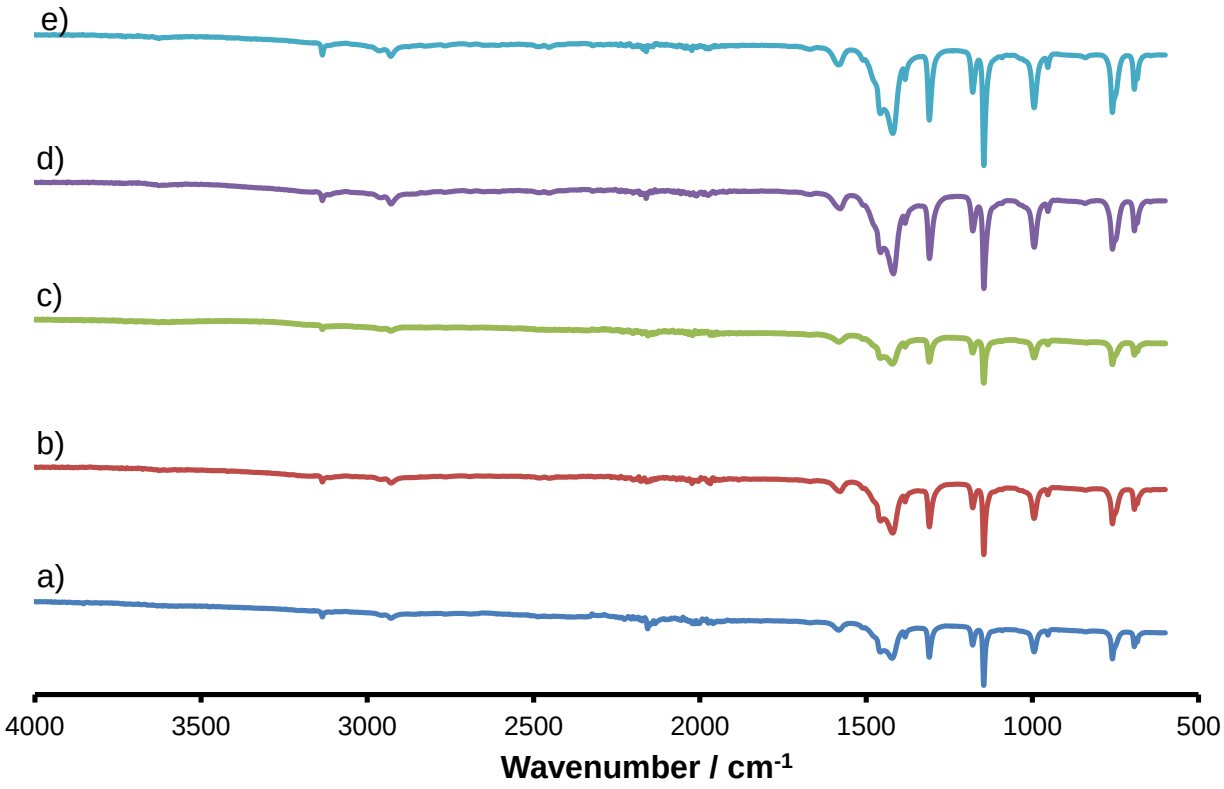

Figure A.1 Infrared spectra of nZIF-8 synthesised with TEA at different molar ratios: a) 1, b) 2, c) 3, d) 4 and e) 8.

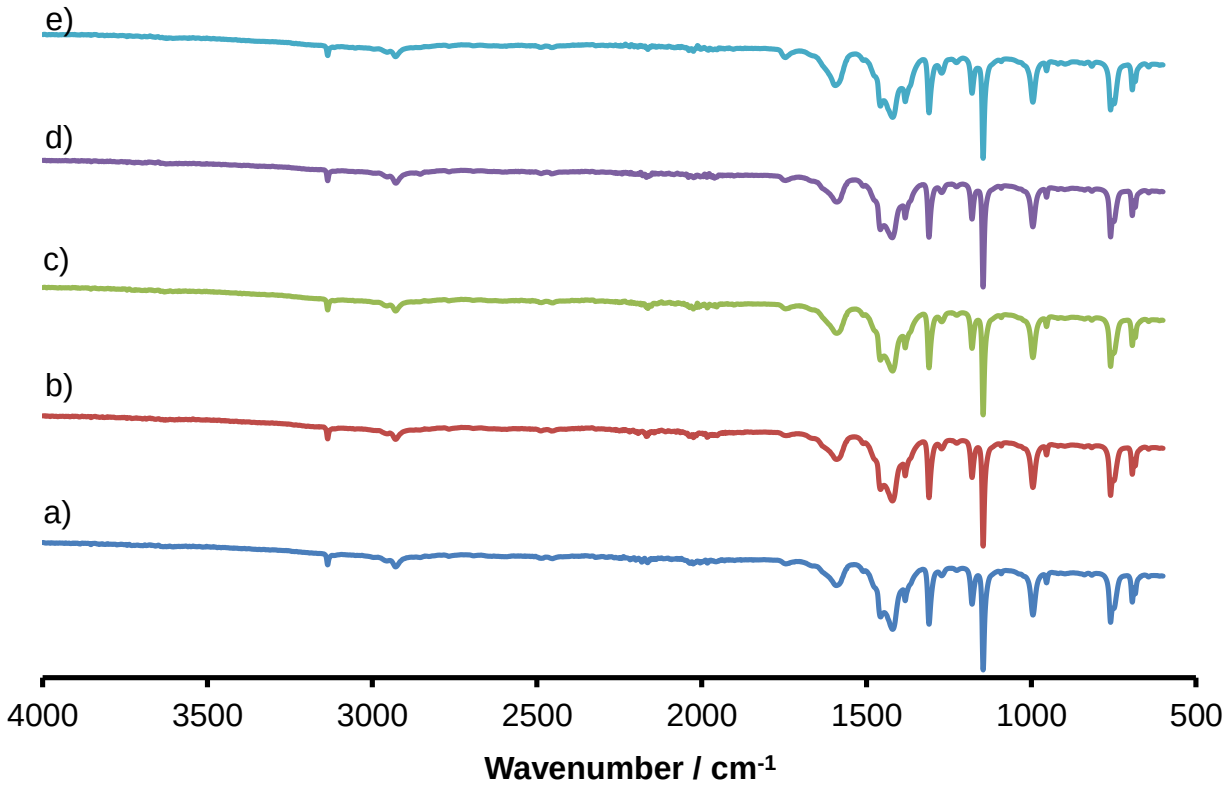

Figure A.2 Infrared spectrum of LeZIF8-M2 between nZIF-8 and methyl benzimidazole-2-ylthio acetate in methanol at different synthesis times: a) 4h, b) 16h, c) 24h, d) 72h and e) 168h

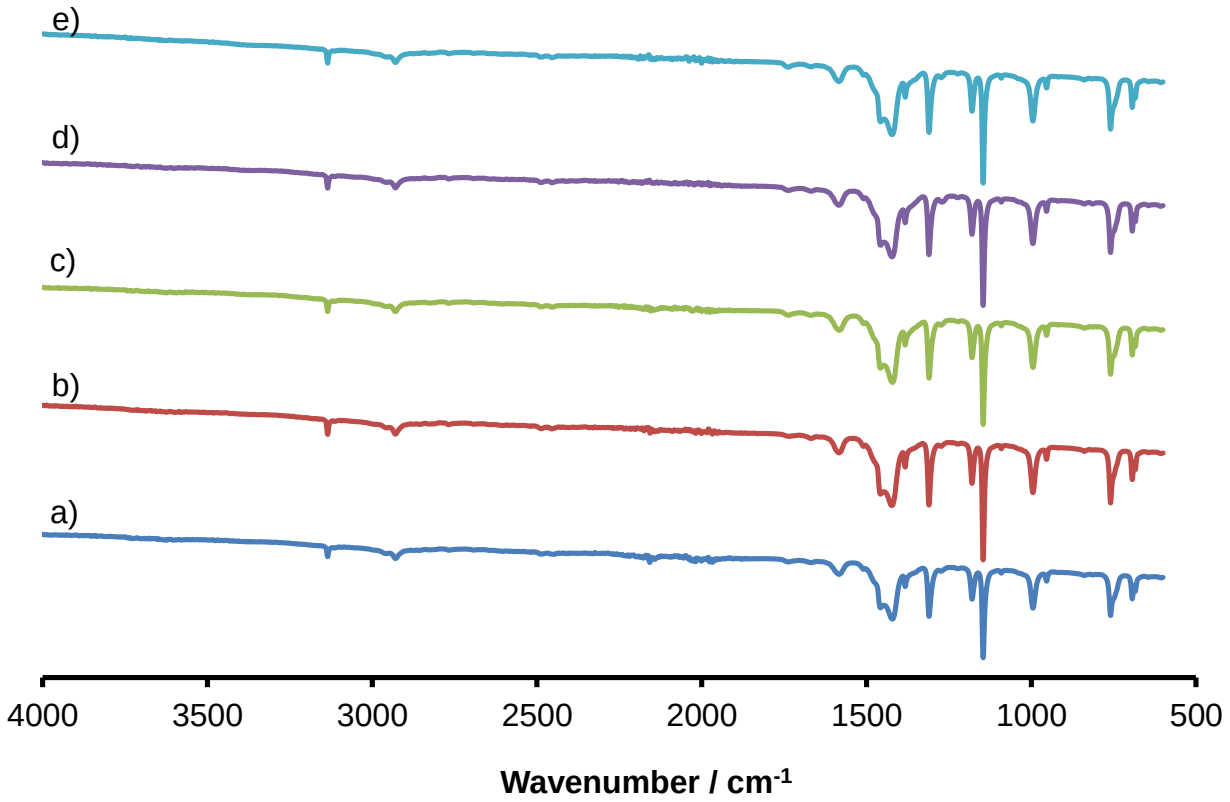

Figure A.3 Infrared spectrum of LeZIF8-E3 between nZIF-8 and ethyl benzimidazole-2-ylthio propionate in methanol at different synthesis times: a) 4h, b) 16h, c) 24h, d) 72h and e) 168h.

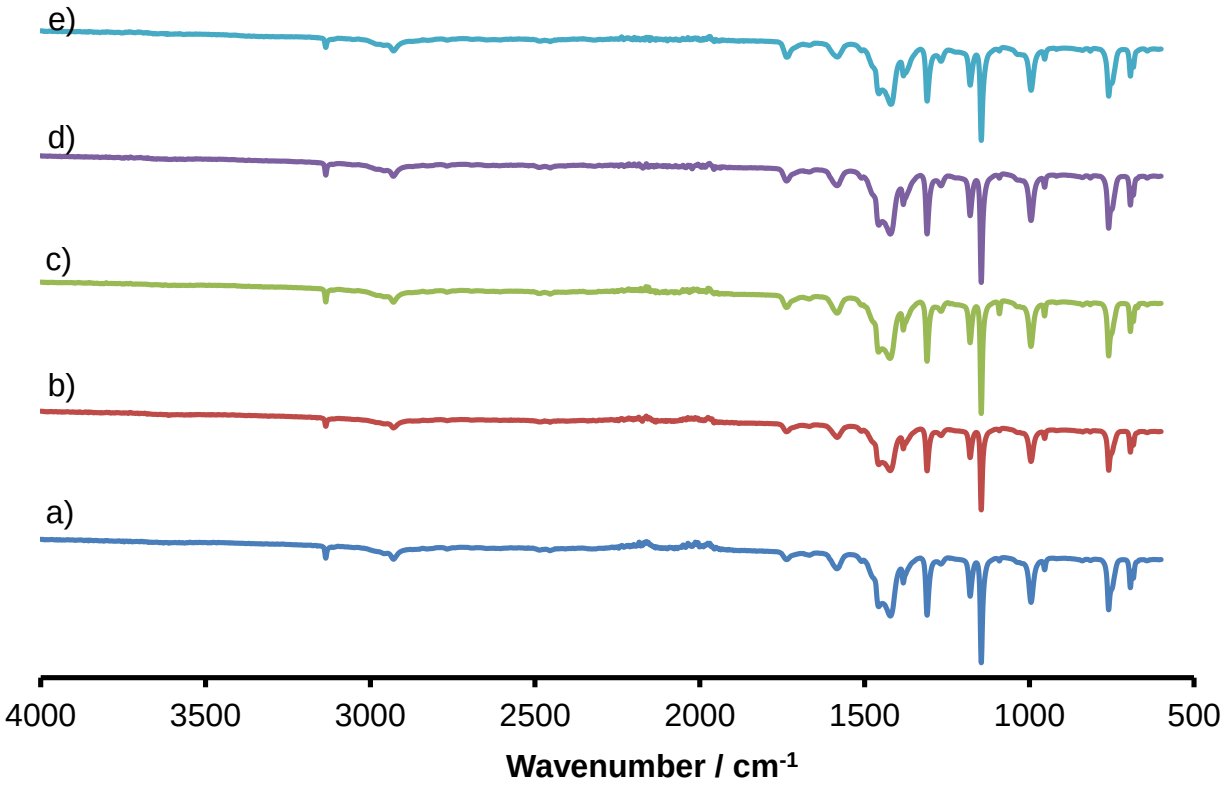

Figure A.4 Infrared spectrum of LeZIF8-E4 between nZIF-8 and ethyl benzimidazole-2-ylthio butyrate in methanol at different synthesis times: a) 4h, b) 16h, c) 24h, d) 72h and e) 168h.

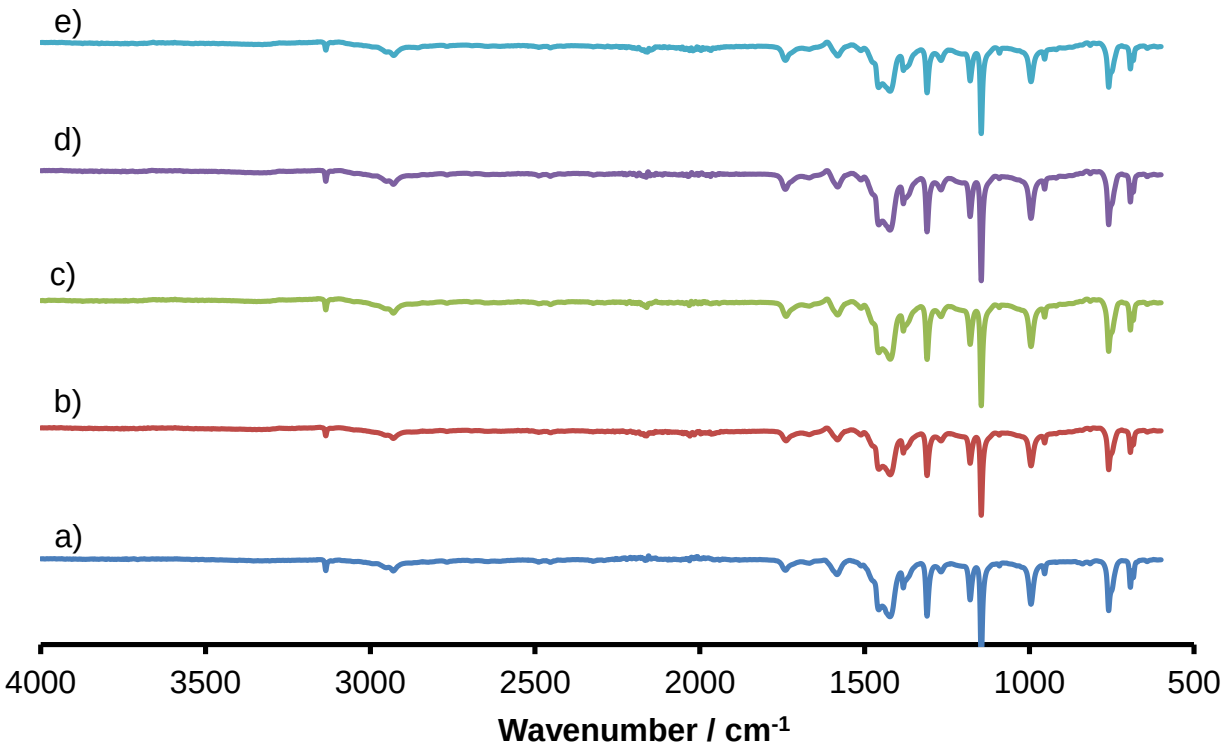

Figure A.5 Infrared spectrum of LeZIF8-M5 between nZIF-8 and methyl benzimidazole-2-ylthio valerate in methanol at different synthesis times: a) 4h, b) 16h, c) 24h, d) 72h and e) 168h

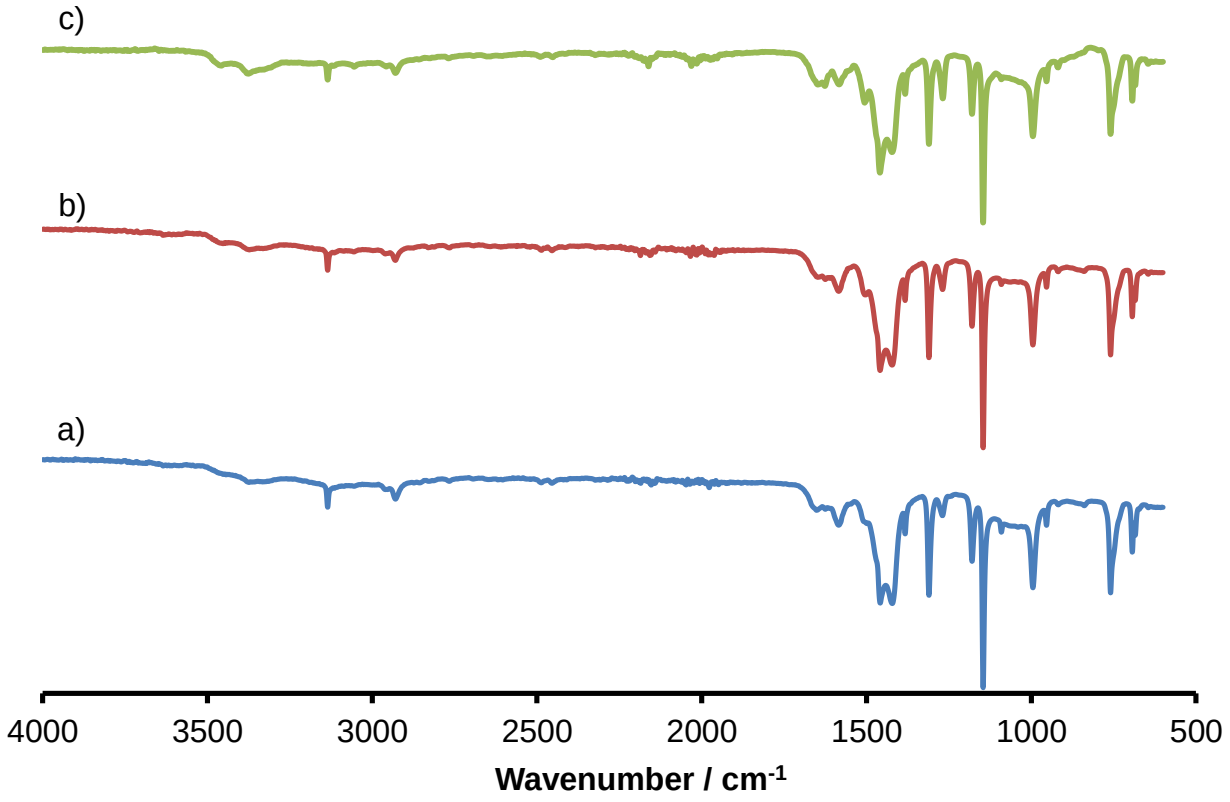

Figure A.6 Infrared spectrum of LeZIF8-NH_2BzIm between nZIF-8 and 2-aminobenzimidazole in methanol at different synthesis times: a) 4h, b) 16h and e) 168h.

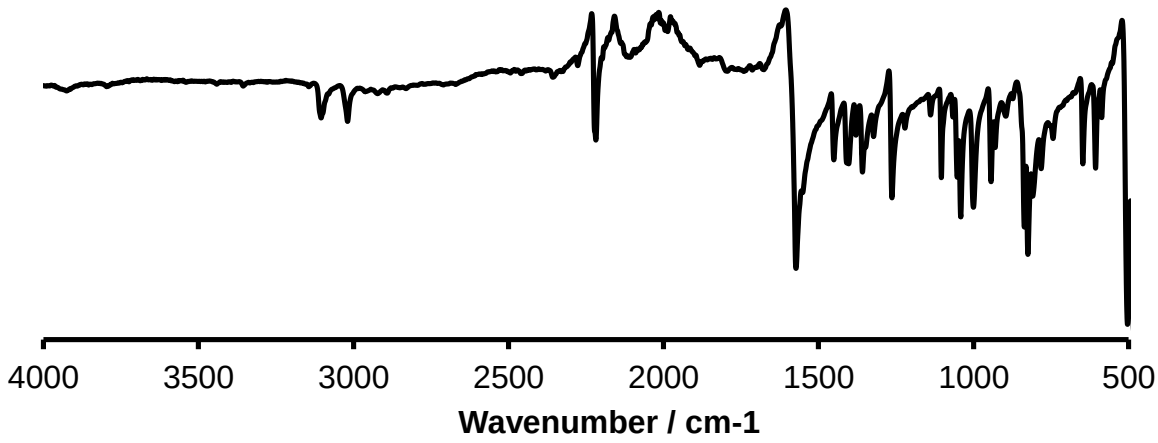

Figure A.7 FTIR spectrum of 1,1-dicyanovinylferrocene.

B. NMR Spectrum

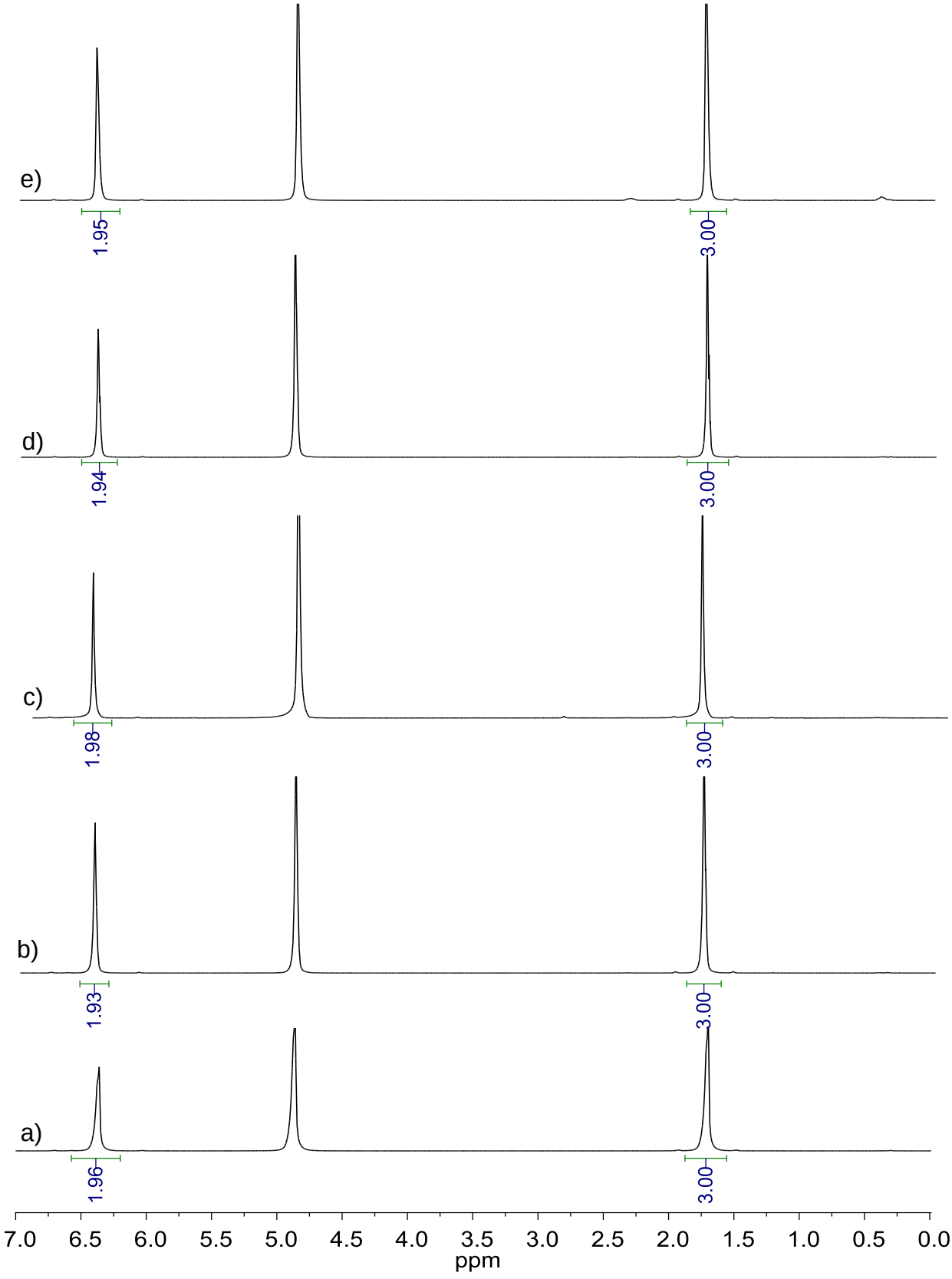

Figure B.1 ^{1}H NMR spectrum of nZIF-8 synthesised with TEA at different molar ratios: a) 1, b) 2, c) 3, d) 4 and e) 8. Digested in D_2O/D_2SO_4 (9:1).

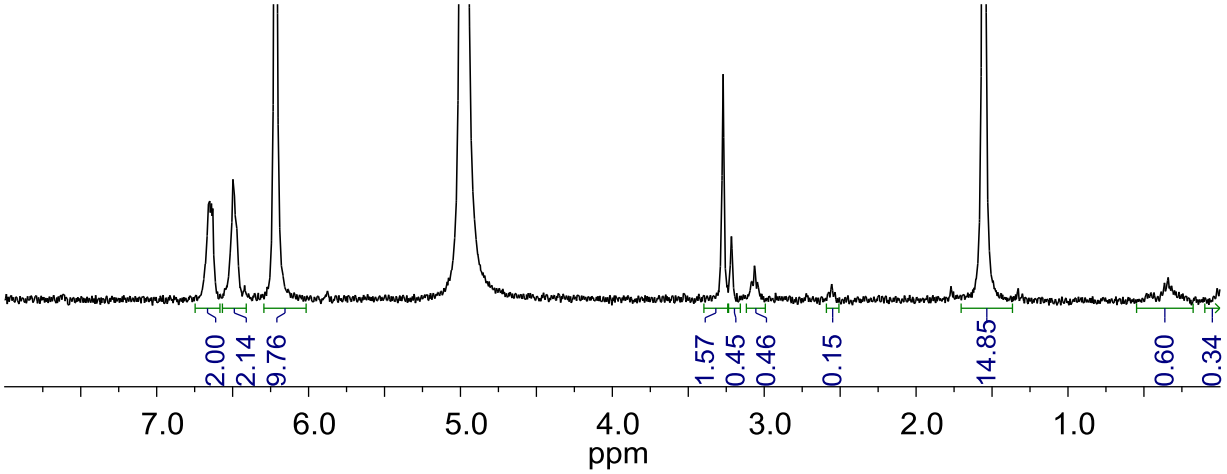

Figure B.2 ^{1}H NMR spectrum of LeZIF8-M2$_{72h}$ between nZIF-8 and methyl benzimidazole-2-ylthio acetate in *n*-butanol at 72h. Digested in D_2O/D_2SO_4 (9:1).

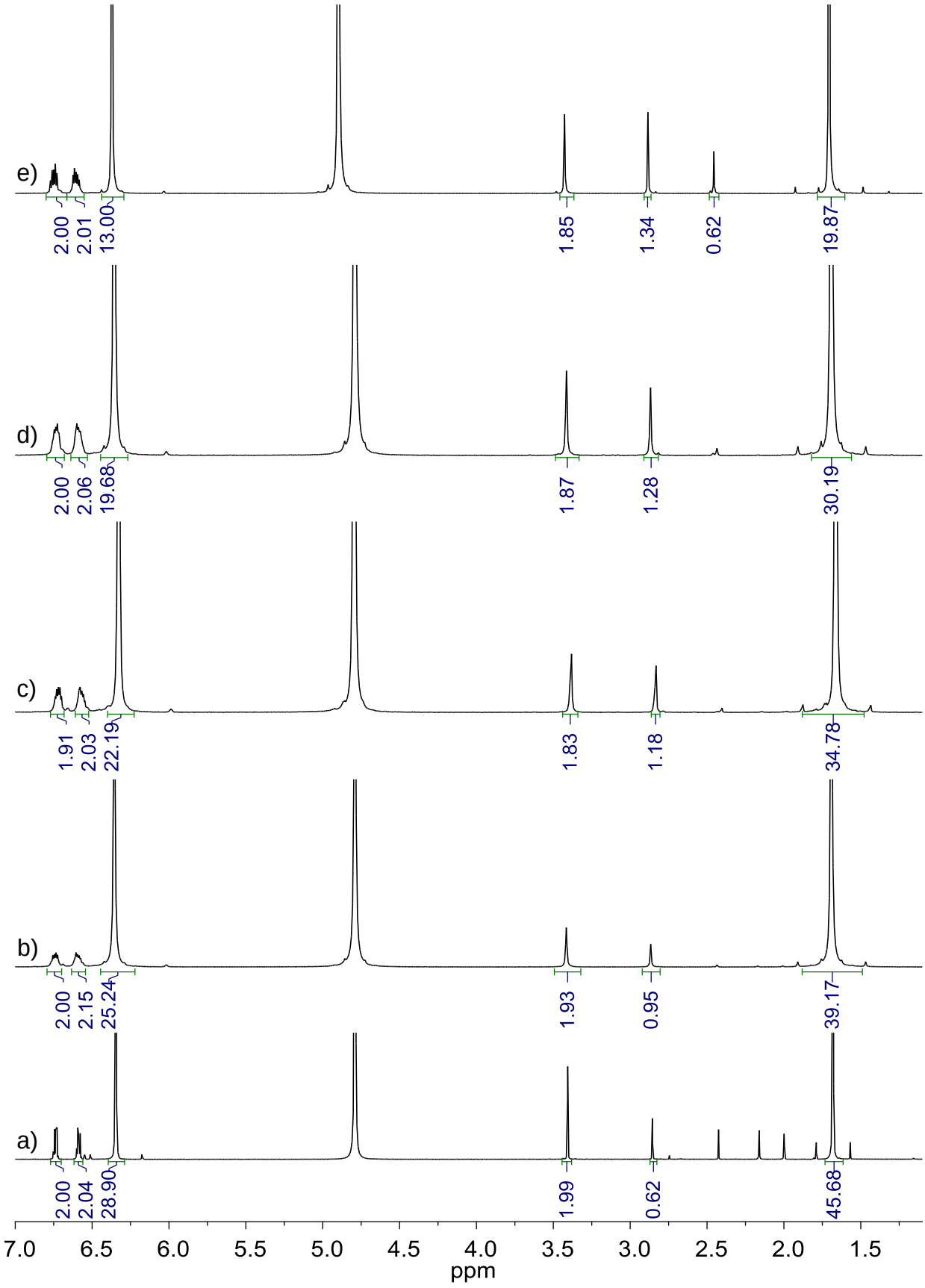

Figure B.3 ^{1}H NMR spectrum of LeZIF8-M2 between nZIF-8 and methyl benzimidazole-2-ylthio acetate in methanol at different synthesis times: a) 4h, b) 16h, c) 24h, d) 72h and e) 168h. Digested in D_2O/D_2SO_4 (9:1).

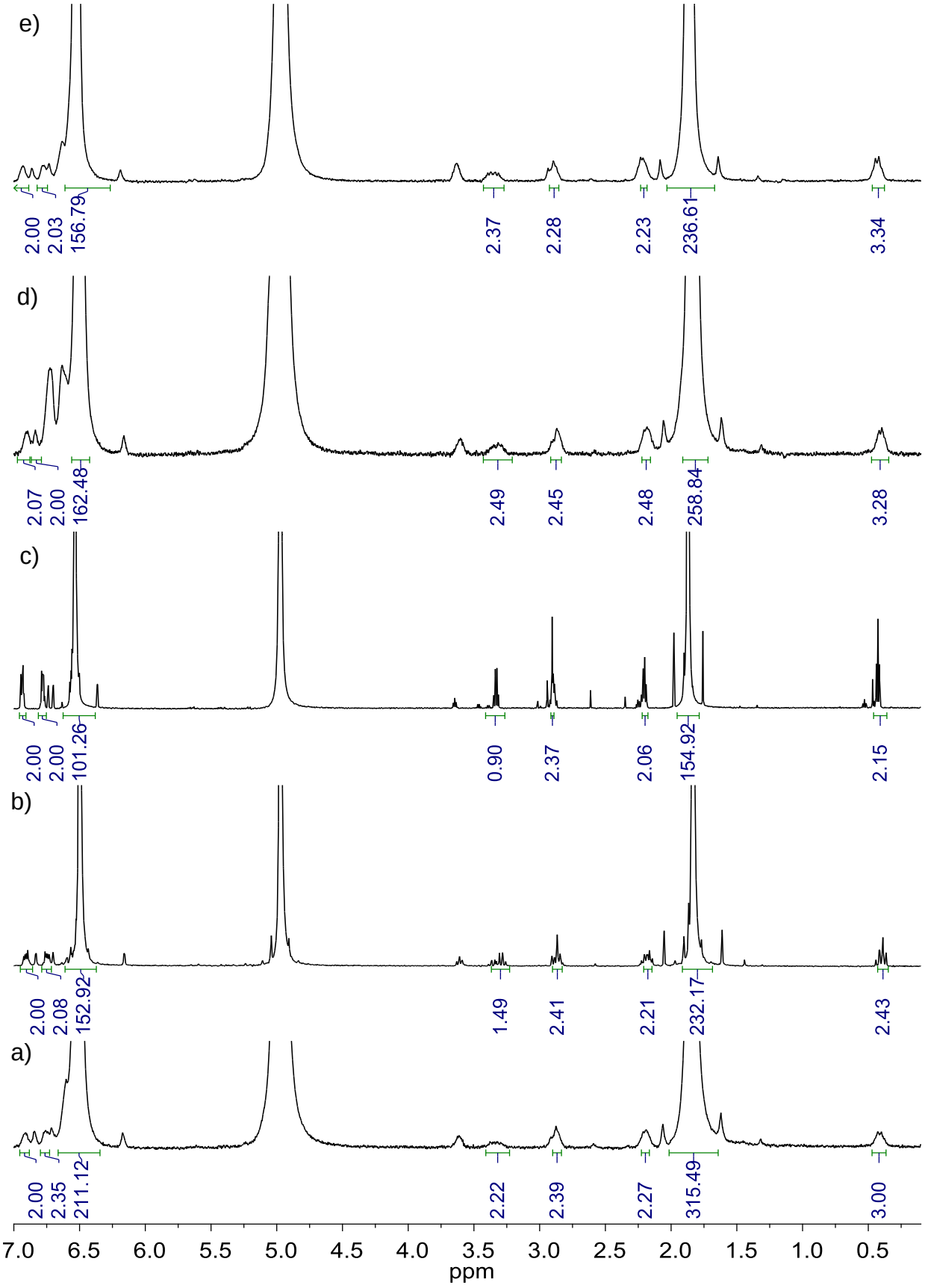

Figure B.4 ^{1}H NMR spectrum of LeZIF8-E3 between nZIF-8 and ethyl benzimidazole-2-ylthio propionate in methanol at different synthesis times: a) 4h, b) 16h, c) 24h, d) 72h and e) 168h. Digested in D_2O/D_2SO_4 (9:1).

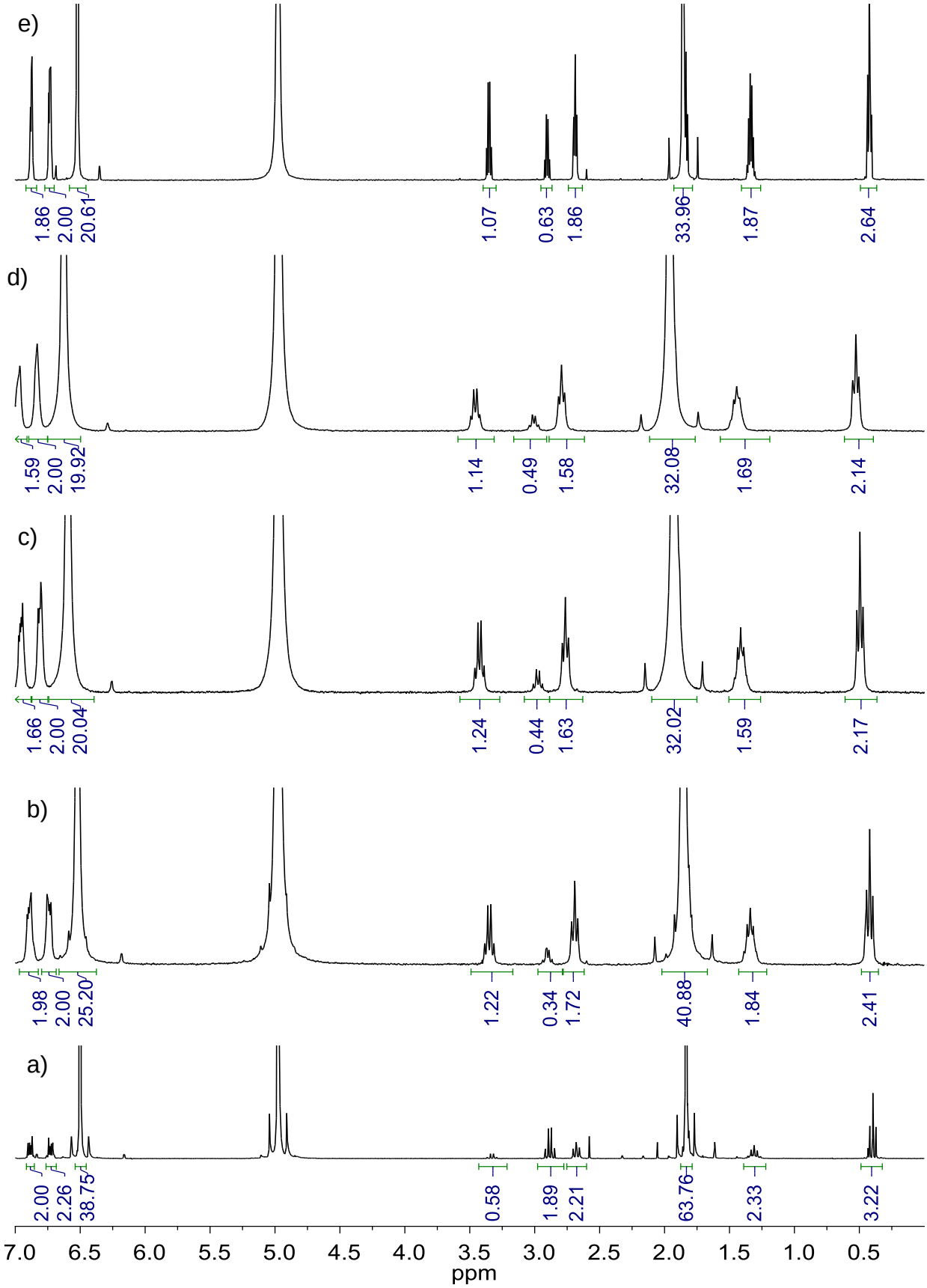

Figure B.5 ^{1}H NMR spectrum of LeZIF8-E4 between nZIF-8 and ethyl benzimidazole-2-ylthio butyrate in methanol at different synthesis times: a) 4h, b) 16h, c) 24h, d) 72h and e) 168h. Digested in D_2O/D_2SO_4 (9:1).

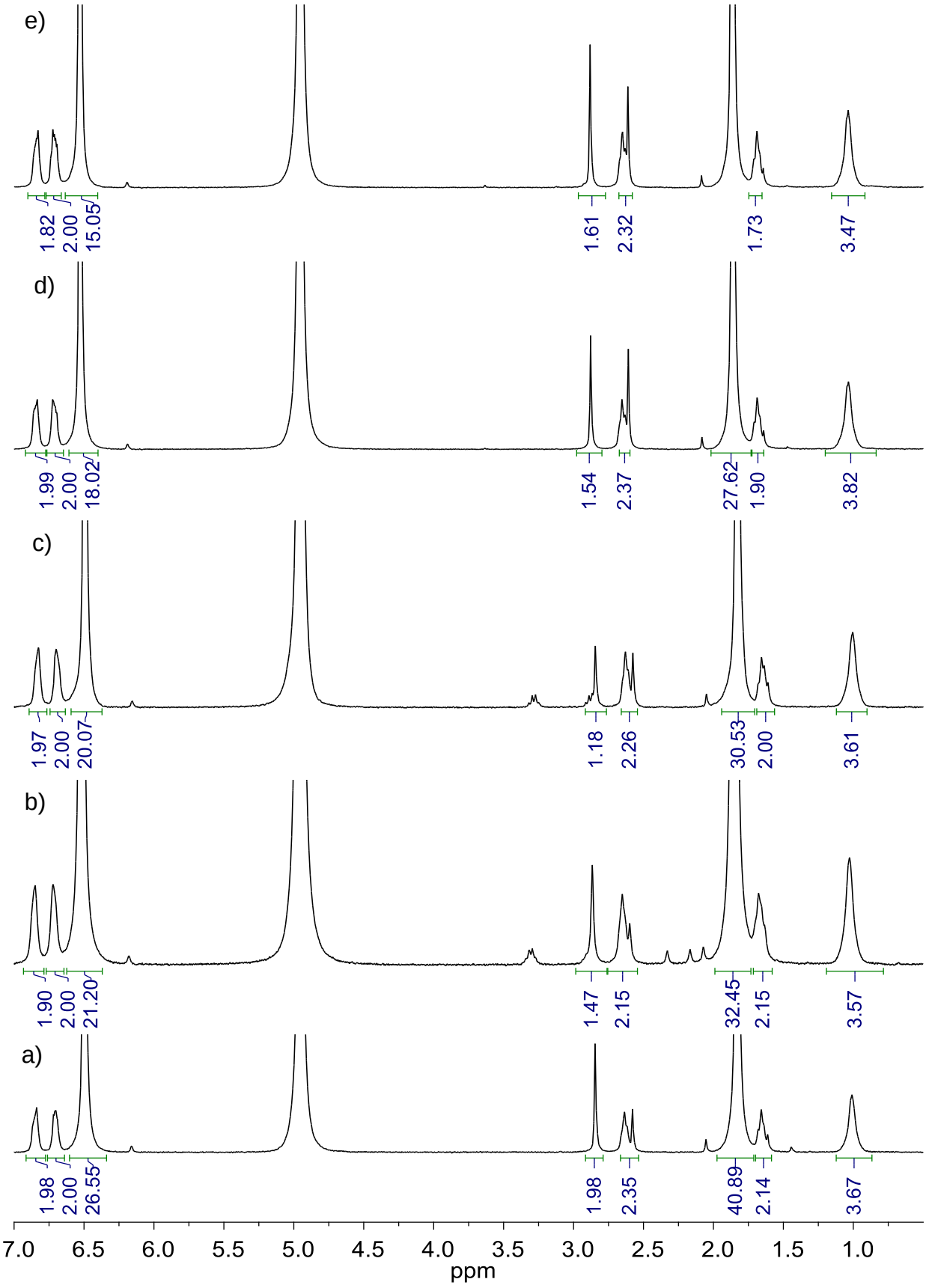

Figure B.6 ^{1}H NMR spectrum of LeZIF8-M5 between nZIF-8 and methyl benzimidazole-2-ylthio valerate in methanol at different synthesis times: a) 4h, b) 16h, c) 24h, d) 72h and e) 168h. Digested in D_2O/D_2SO_4 (9:1).

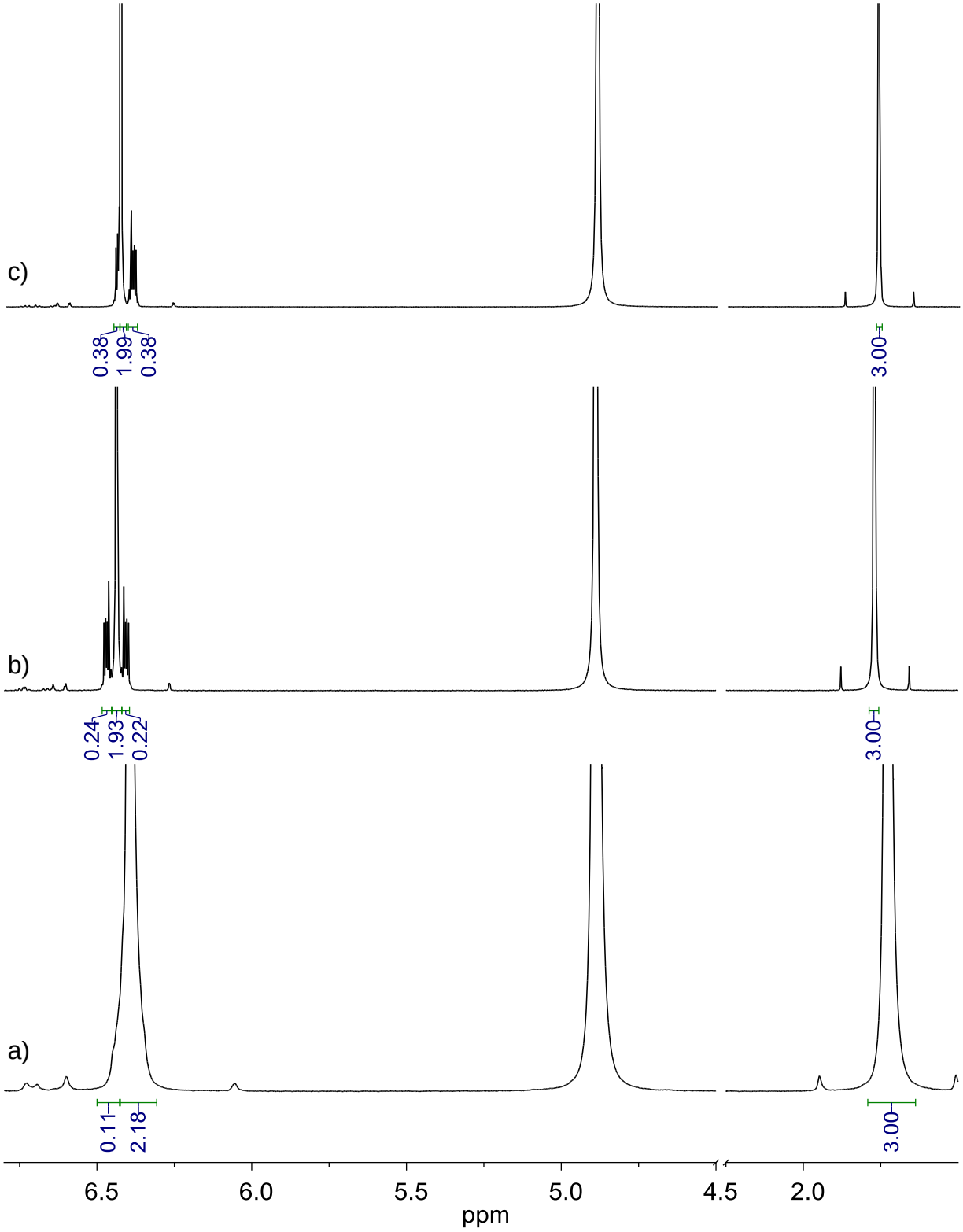

Figure B.7 ^{1}H NMR spectrum of LeZIF8-NH_2BzIm between nZIF-8 and 2-aminobenzimdazole in methanol at different synthesis times: a) 4h, b) 16h and e) 168h. Digested in D_2O/D_2SO_4 (9:1).

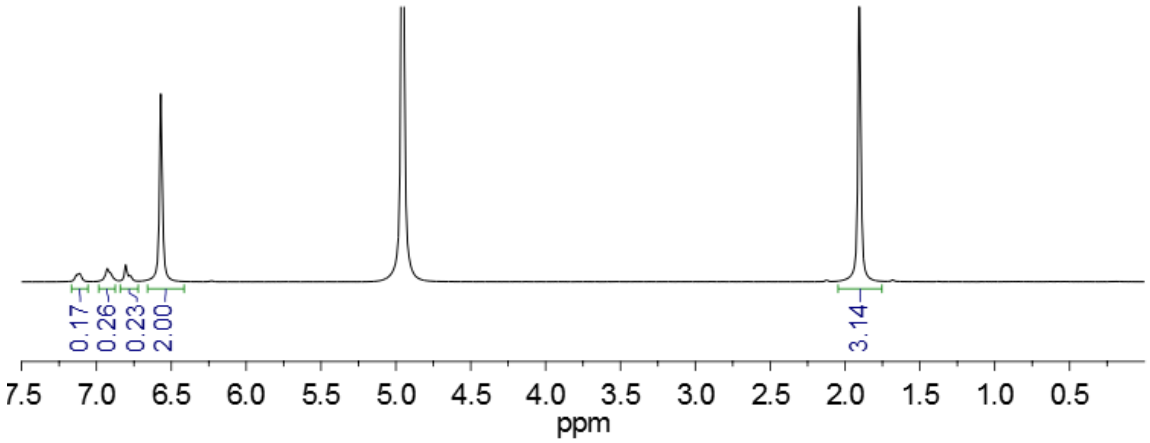

Figure B.8 ^{1}H NMR spectrum of LeZIF8-PhIm$_{168h}$ between nZIF-8 and 2-phenylimidazole in methanol at 168 hours. Digested in D_2O/D_2SO_4 (9:1).

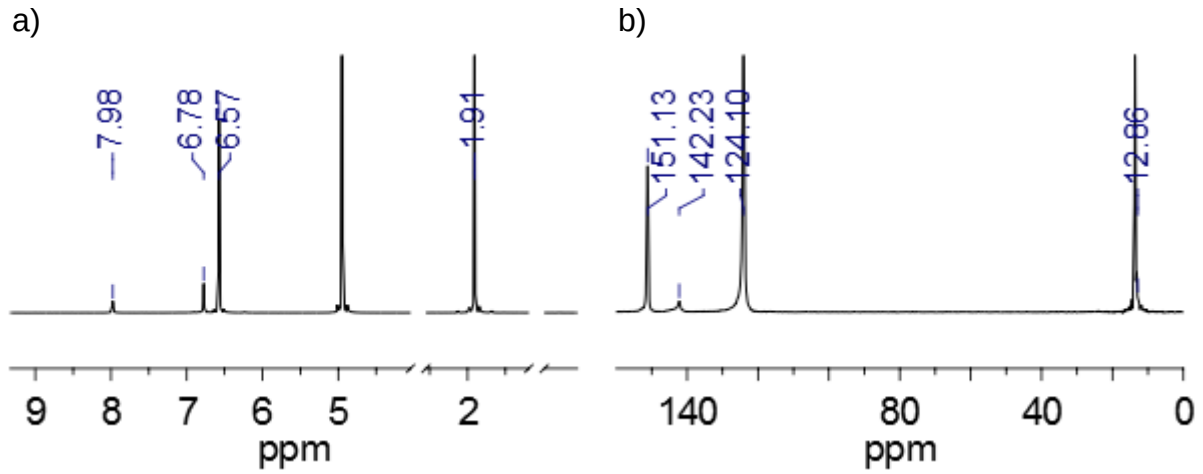

Figure B.9 NMR spectrums of SALEM-2$_{16h}$-Pd: a) digestive ^{1}H NMR (D_2O/D_2SO_4 (9:1)) and b) ^{13}C solid state NMR.

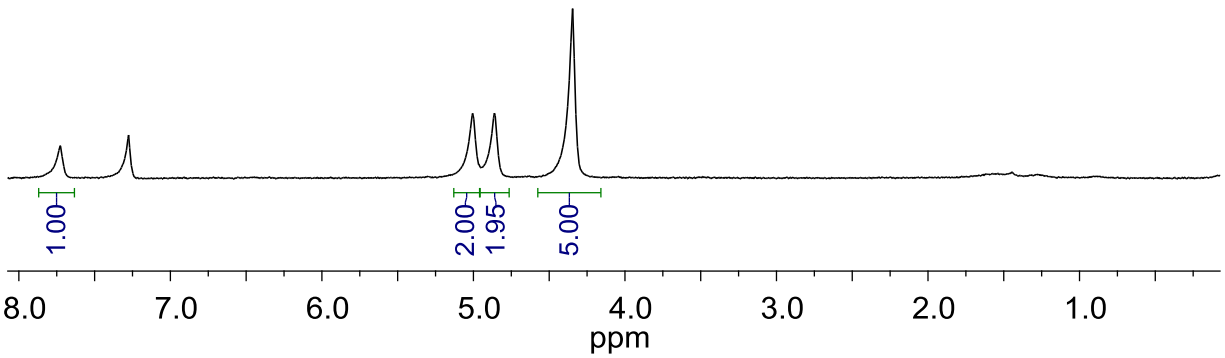

Figure B.10 ^{1}H NMR spectrum of 1,1-dicyanovinylferrocene in $CDCl_3$.

C. TEM Images

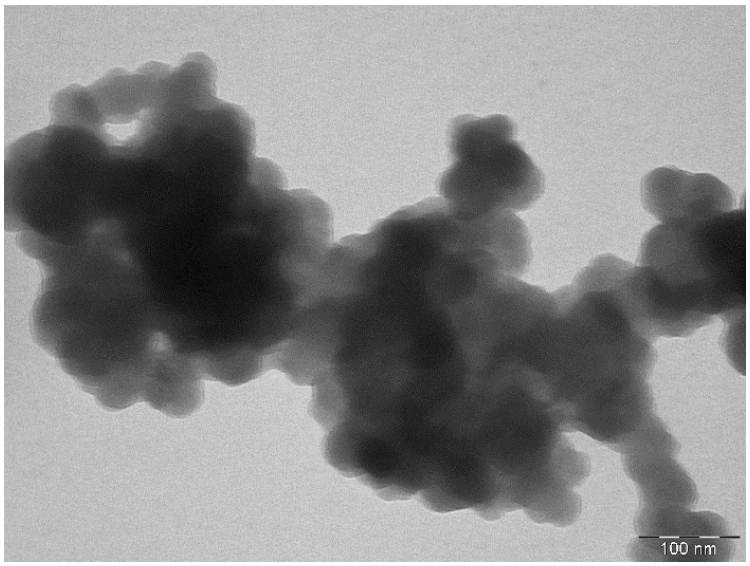

Figure C.1 TEM images of nZIF-8 synthesised with methanol ratio nZIF-8_{2000} after 3 days of dialysis.

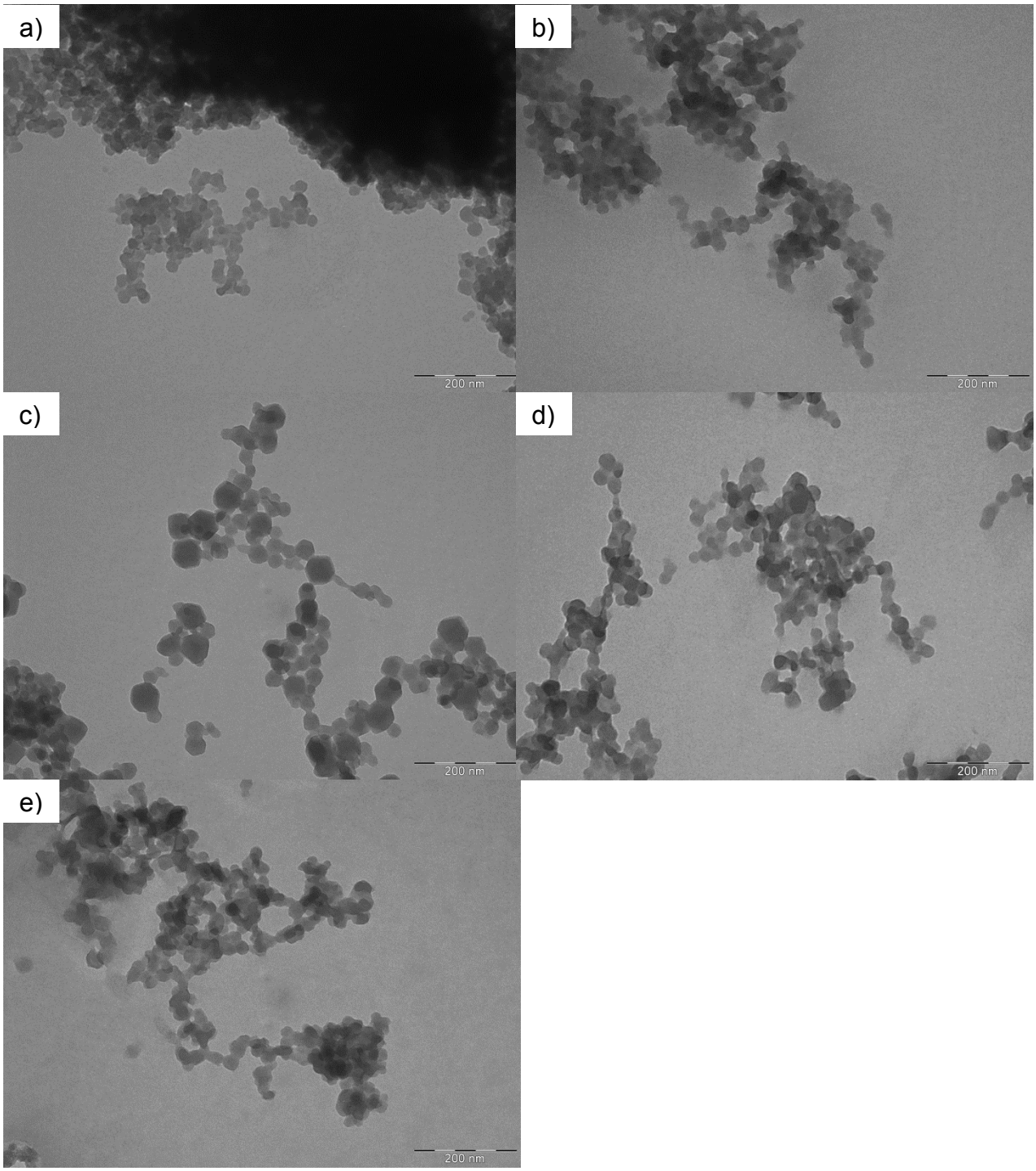

Figure C.2 TEM images of LeZIF8-M2 between nZIF-8 and methyl benzimidazole-2-ylthio acetate in methanol at different synthesis times: a) 4h, b) 16h, c) 24h, d) 72h and e) 168h.

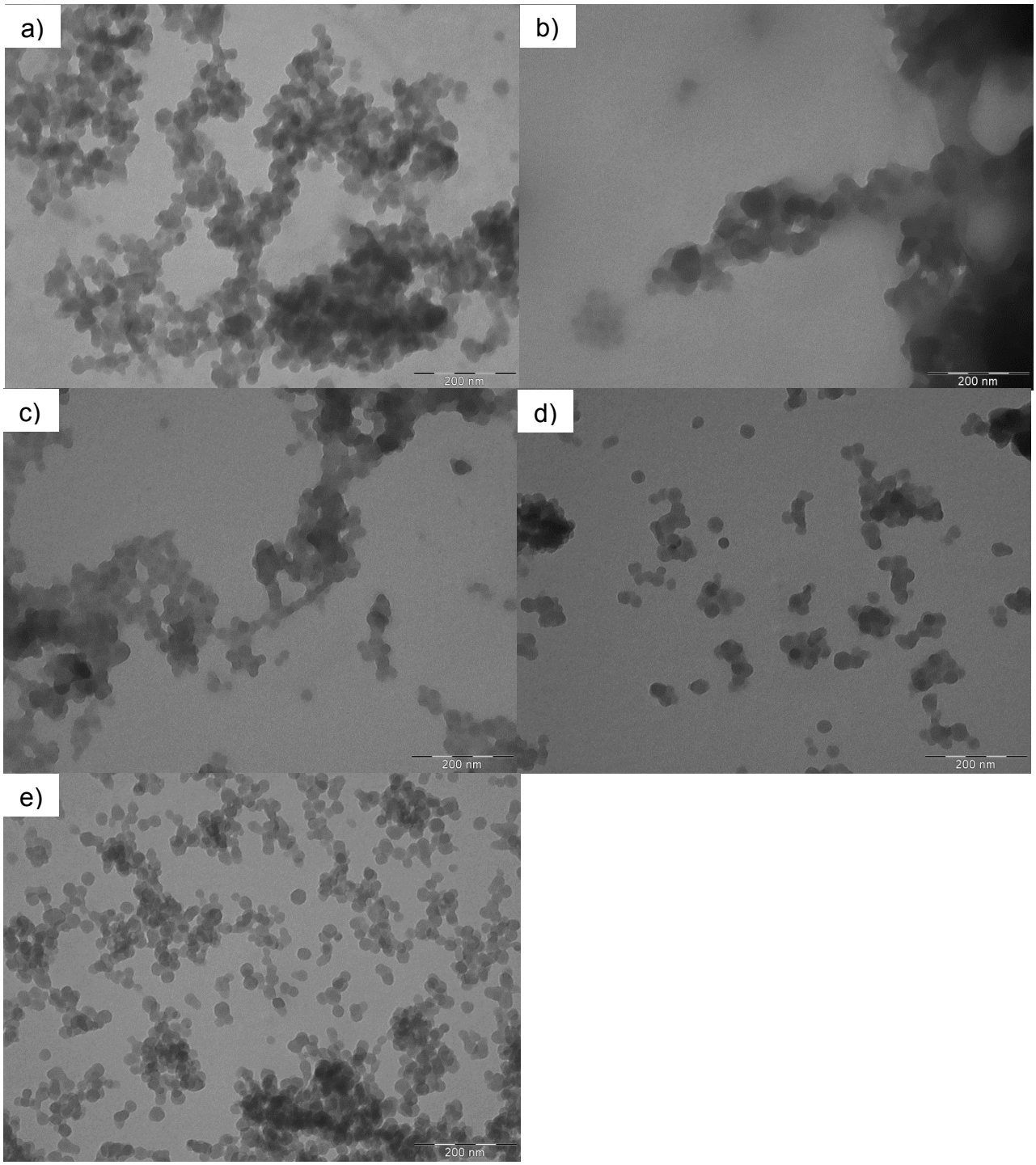

Figure C.3 TEM images of LeZIF8-E3 between nZIF-8 and ethyl benzimidazole-2-ylthio propionate in methanol at different synthesis times: a) 4h, b) 16h, c) 24h, d) 72h and e) 168h.

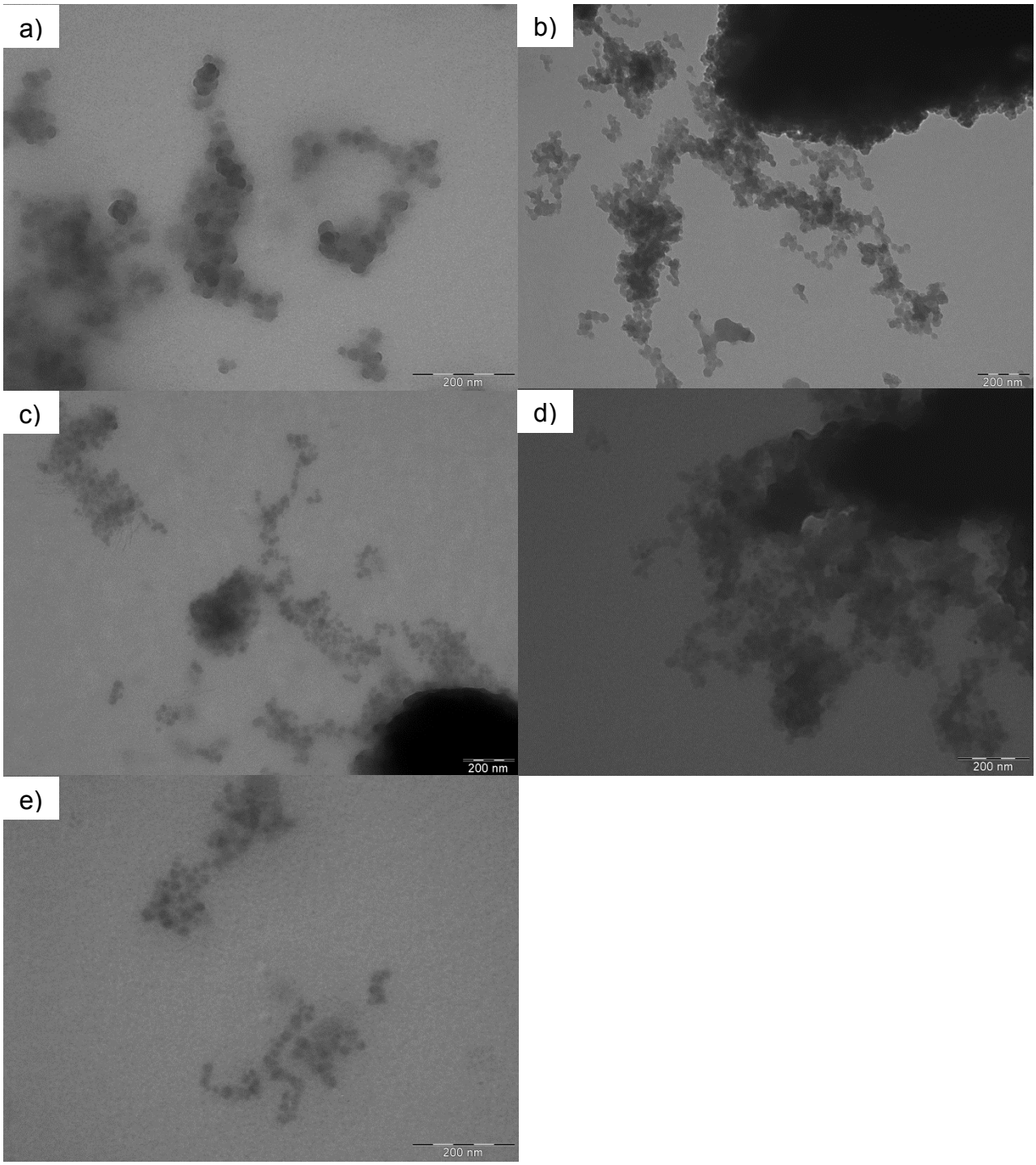

Figure C.4 TEM images of LeZIF8-E4 between nZIF-8 and ethyl benzimidazole-2-ylthio butyrate in methanol at different synthesis times: a) 4h, b) 16h, c) 24h, d) 72h and e) 168h.

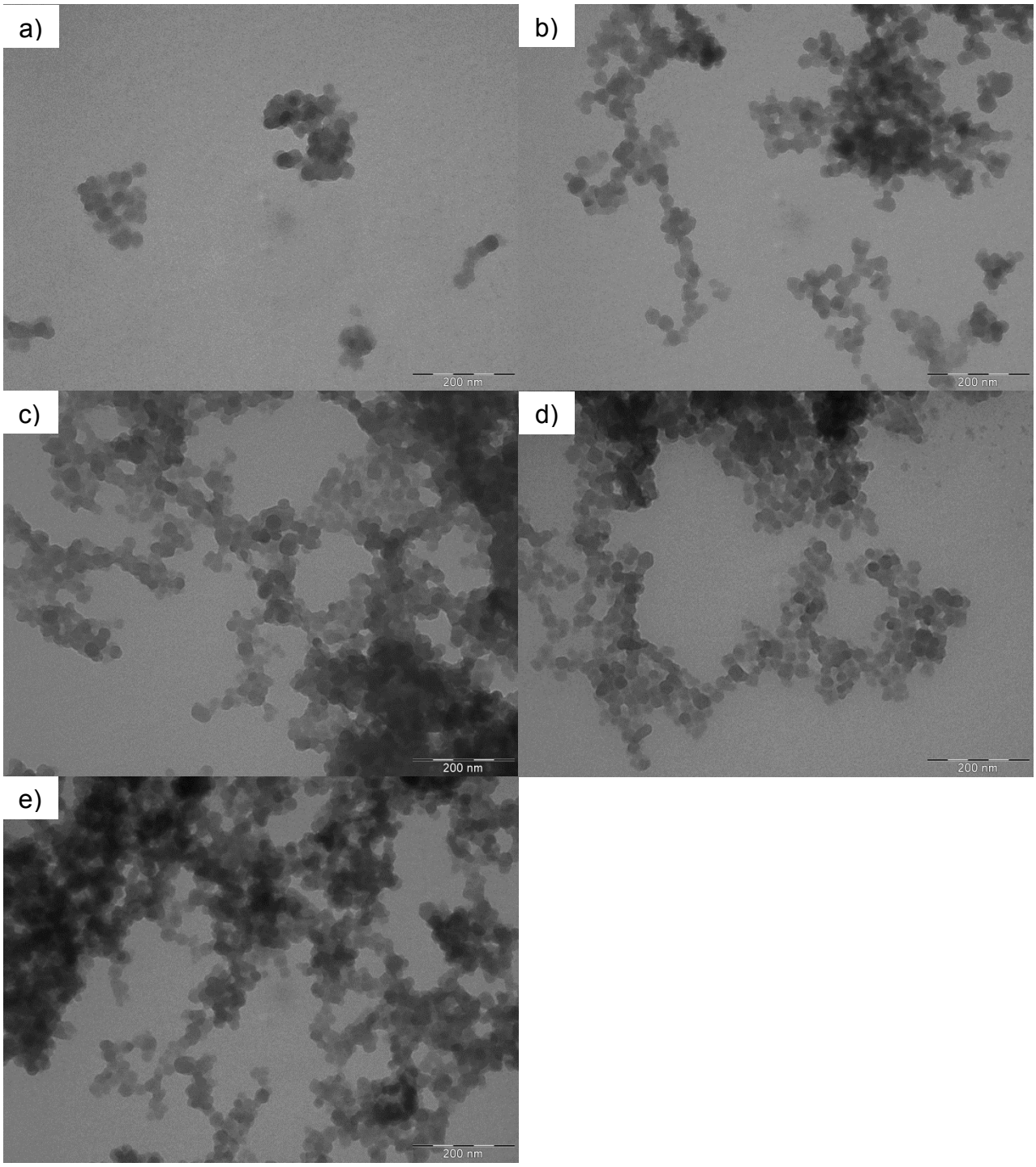

Figure C.5 TEM images of LeZIF8-M5 between nZIF-8 and methyl benzimidazole-2-ylthio valerate in methanol at different synthesis times: a) 4h, b) 16h, c) 24h, d) 72h and e) 168h.

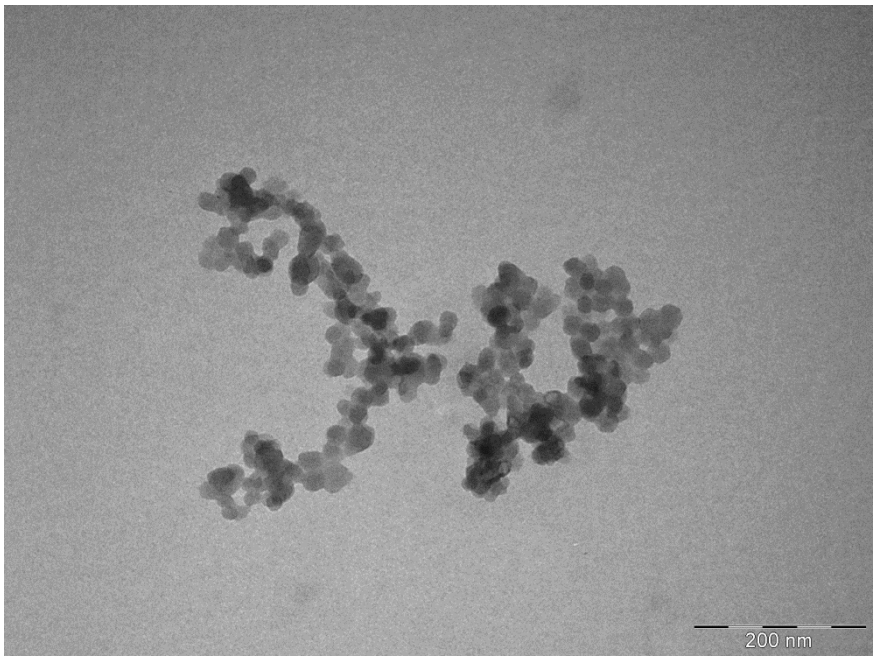

Figure C.6 TEM images of LeZIF8-NH_2BzIm between nZIF-8 and 2-aminobenzimidazole in methanol at 16 hours.

D. PXRD patterns

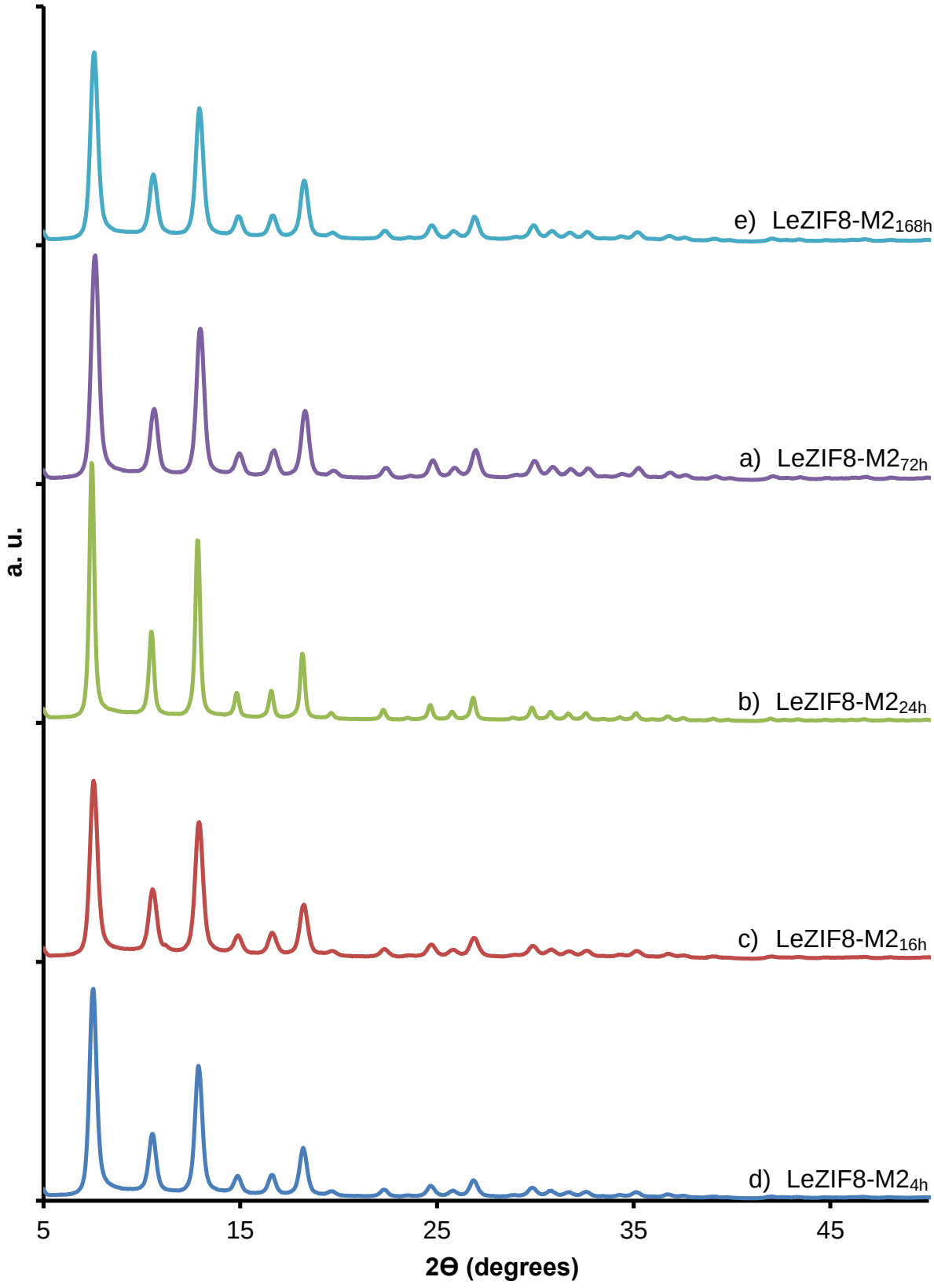

Figure D.1 PXRD pattern of LeZIF8-M2 between nZIF-8 and methyl benzimidazole-2-ylthio acetate in methanol at different synthesis times: a) 4h, b) 16h, c) 24h, d) 72h and e) 168h.

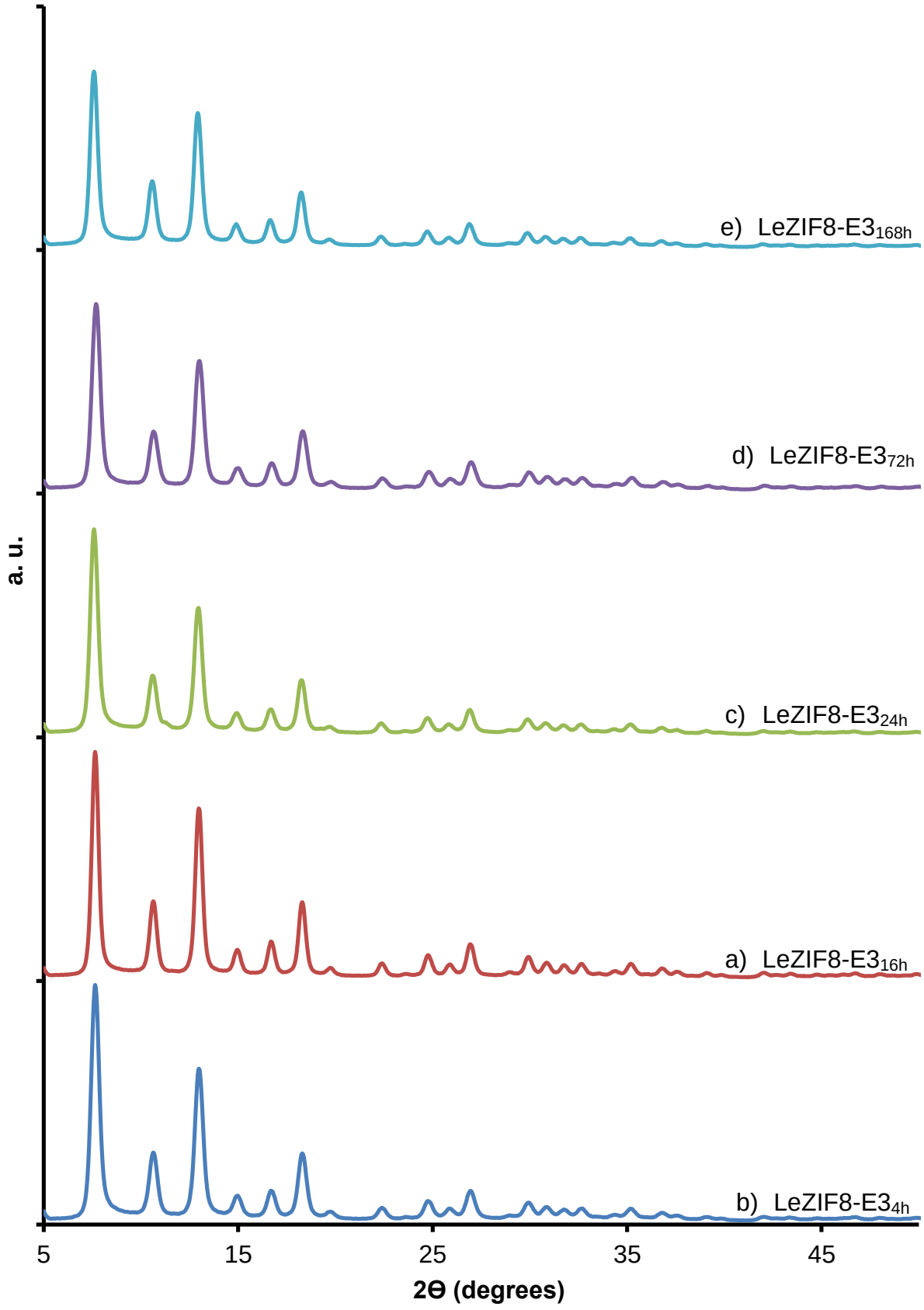

Figure D.2 PXRD pattern of LeZIF8-E3 between nZIF-8 and ethyl benzimidazole-2-ylthio propionate in methanol at different synthesis times: a) 4h, b) 16h, c) 24h, d) 72h and e) 168h.

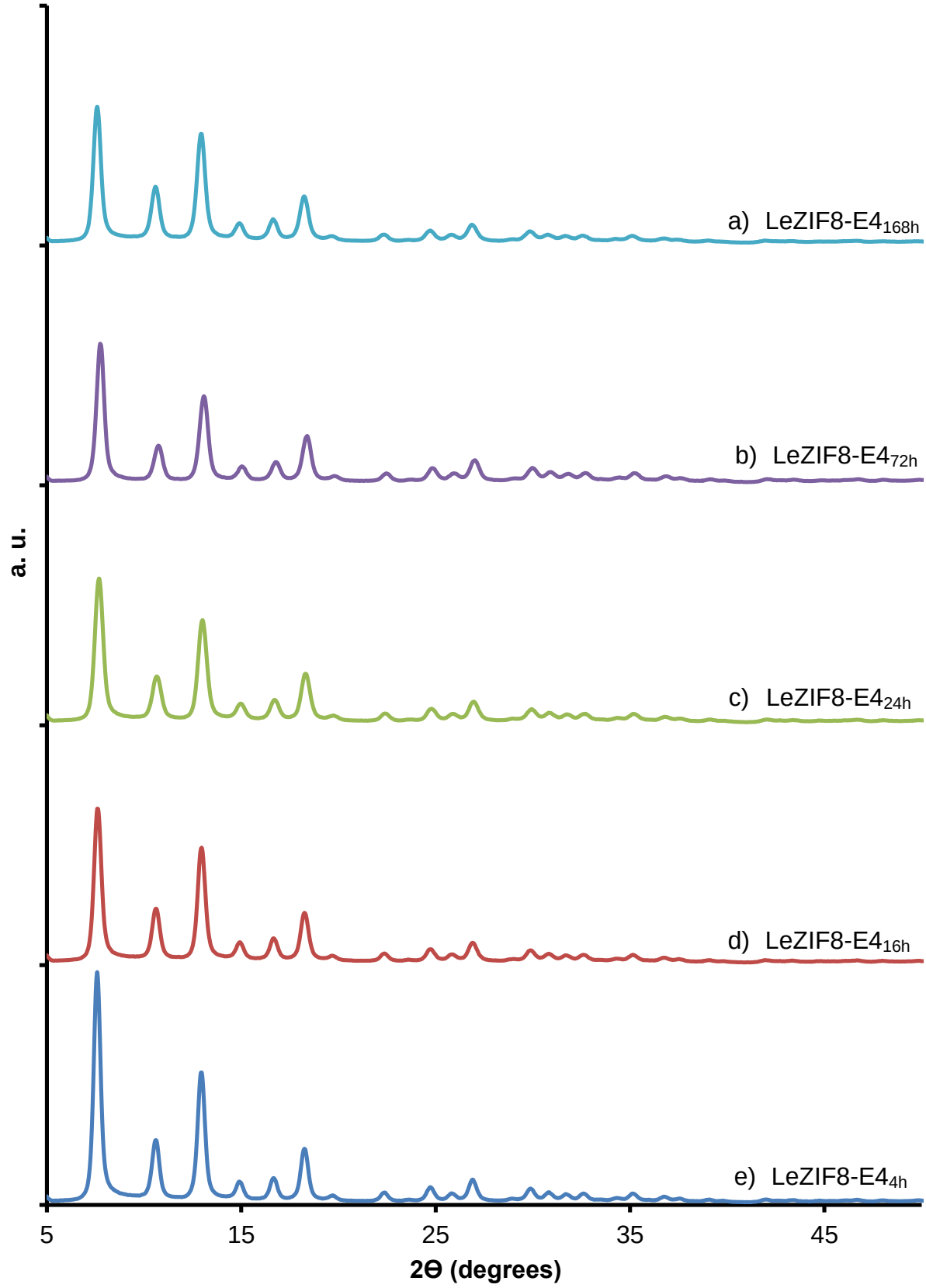

Figure D.3 PXRD pattern of LeZIF8-E4 between nZIF-8 and ethyl benzimidazole-2-ylthio butyrate in methanol at different synthesis times: a) 4h, b) 16h, c) 24h, d) 72h and e) 168h.

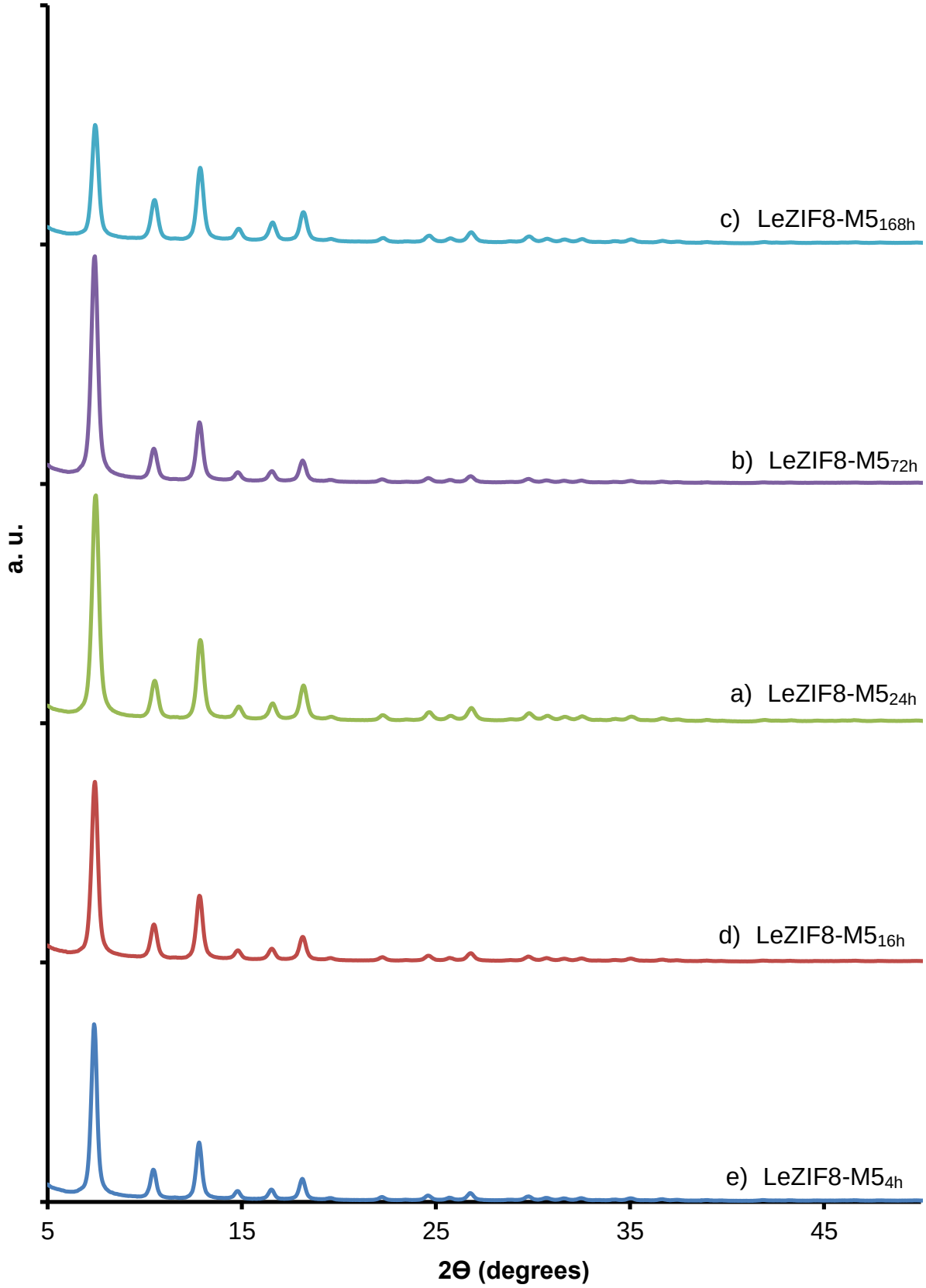

Figure D.4 PXRD pattern of LeZIF8-M5 between nZIF-8 and methyl benzimidazole-2-ylthio valerate in methanol at different synthesis times: a) 4h, b) 16h, c) 24h, d) 72h and e) 168h.

E. Thermogravimetric Analysis

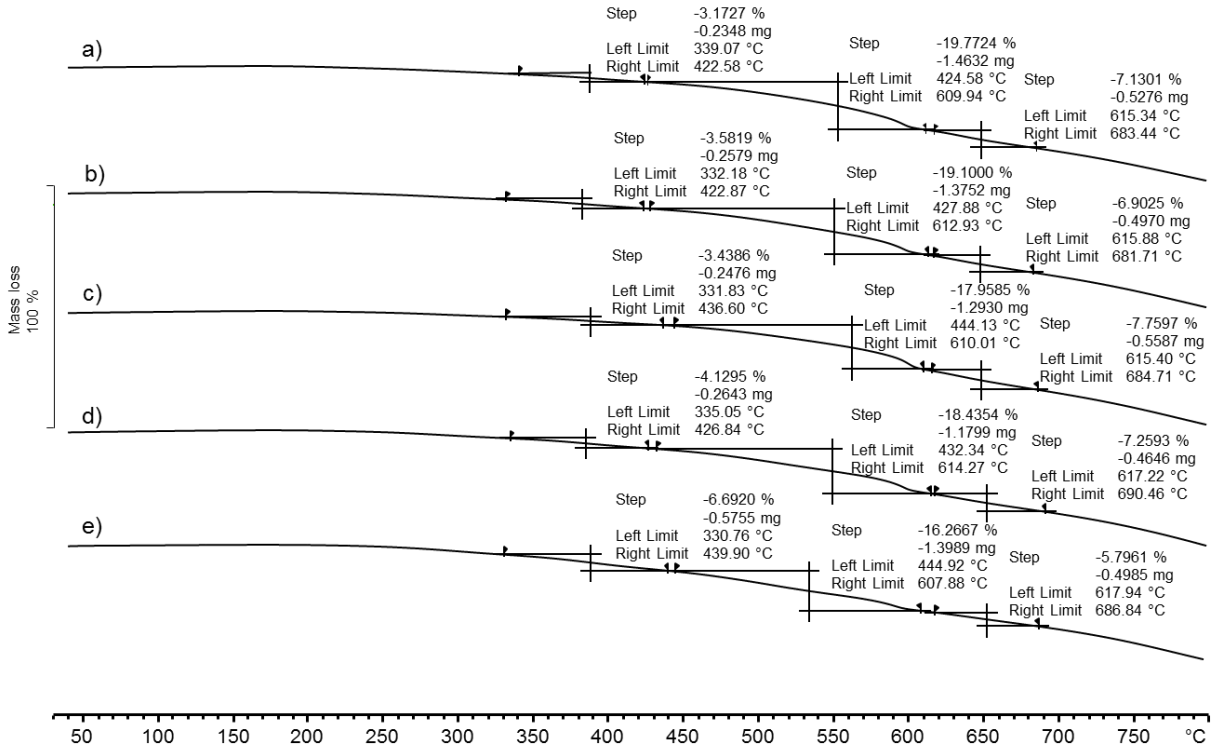

Figure E.1 TGA thermogram in N_2 of LeZIF8-M2 between nZIF-8 and methyl benzimidazole-2-ylthio acetate in methanol at different synthesis times: a) 4h, b) 16h, c) 24h, d) 72h and e) 168h.

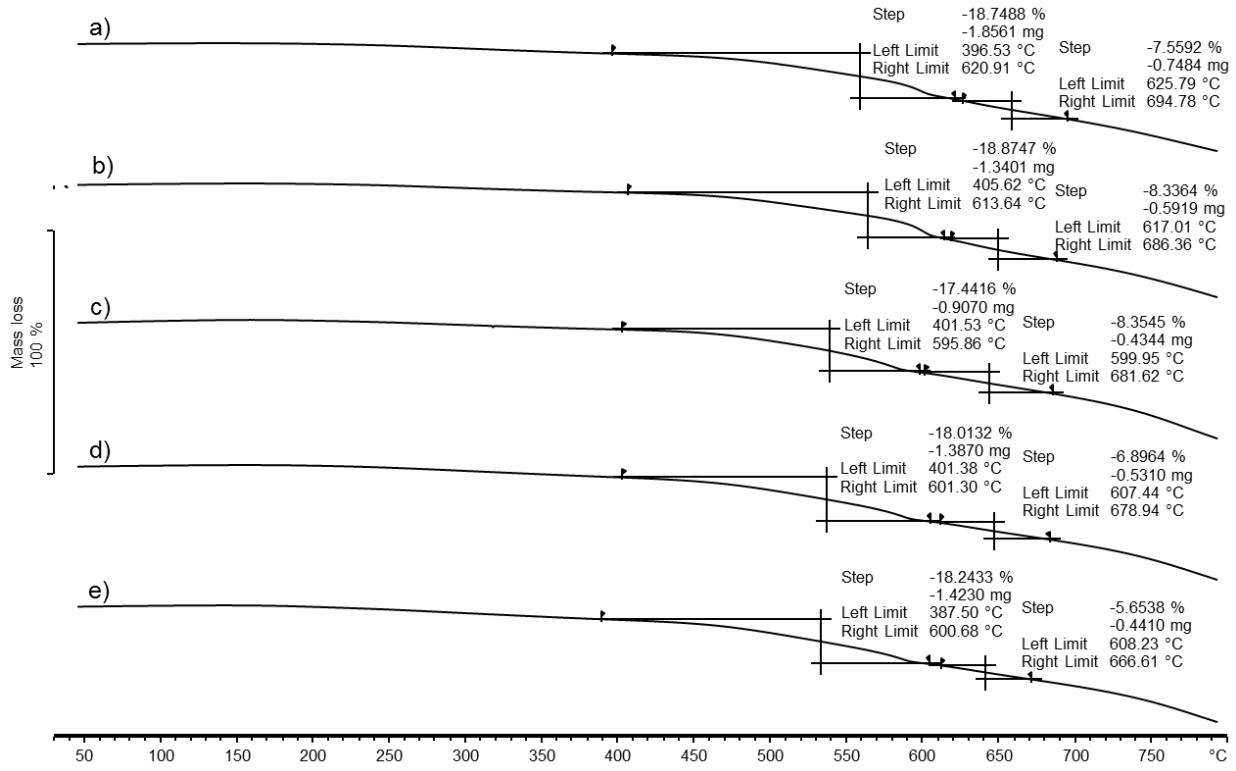

Figure E.2 TGA thermogram in N_2 of LeZIF8-E3 between nZIF-8 and ethyl benzimidazole-2-ylthio propionate in methanol at different synthesis times: a) 4h, b) 16h, c) 24h, d) 72h and e) 168h.

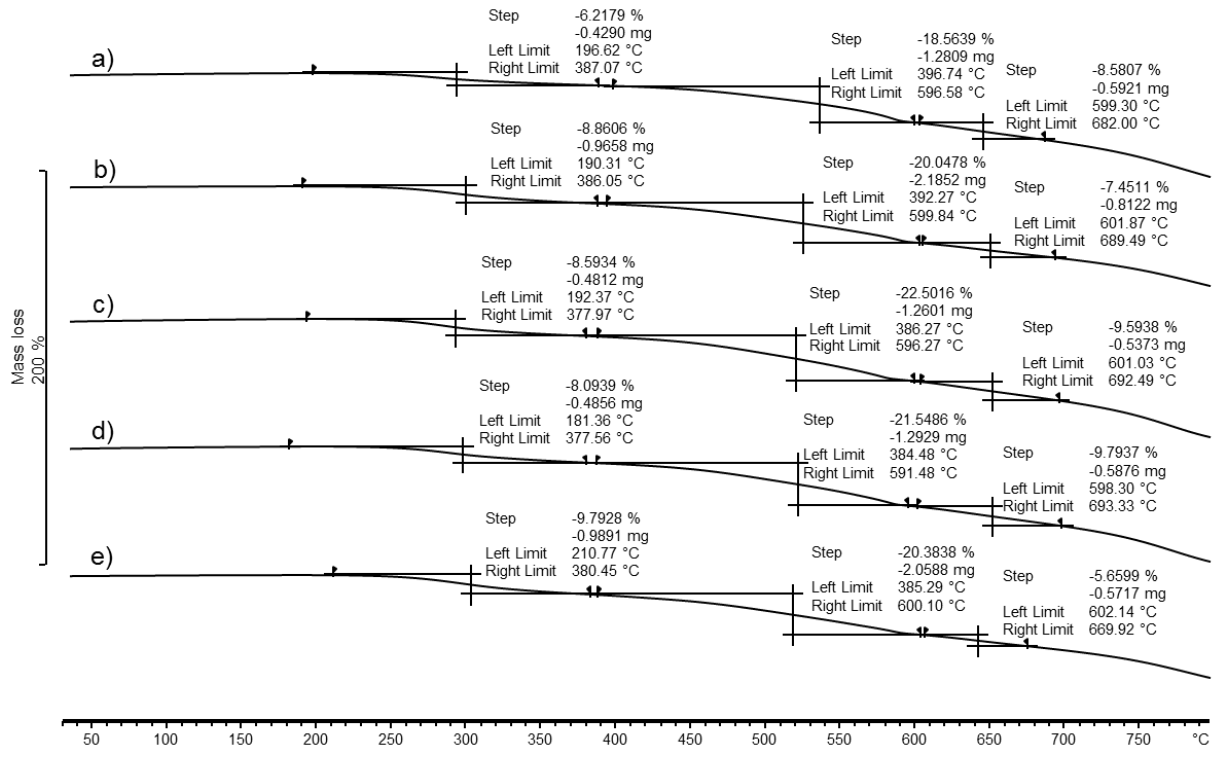

Figure E.3 TGA thermogram in N_2 of LeZIF8-E4 between nZIF-8 and ethyl benzimidazole-2-ylthio butyrate in methanol at different synthesis times: a) 4h, b) 16h, c) 24h, d) 72h and e) 168h.

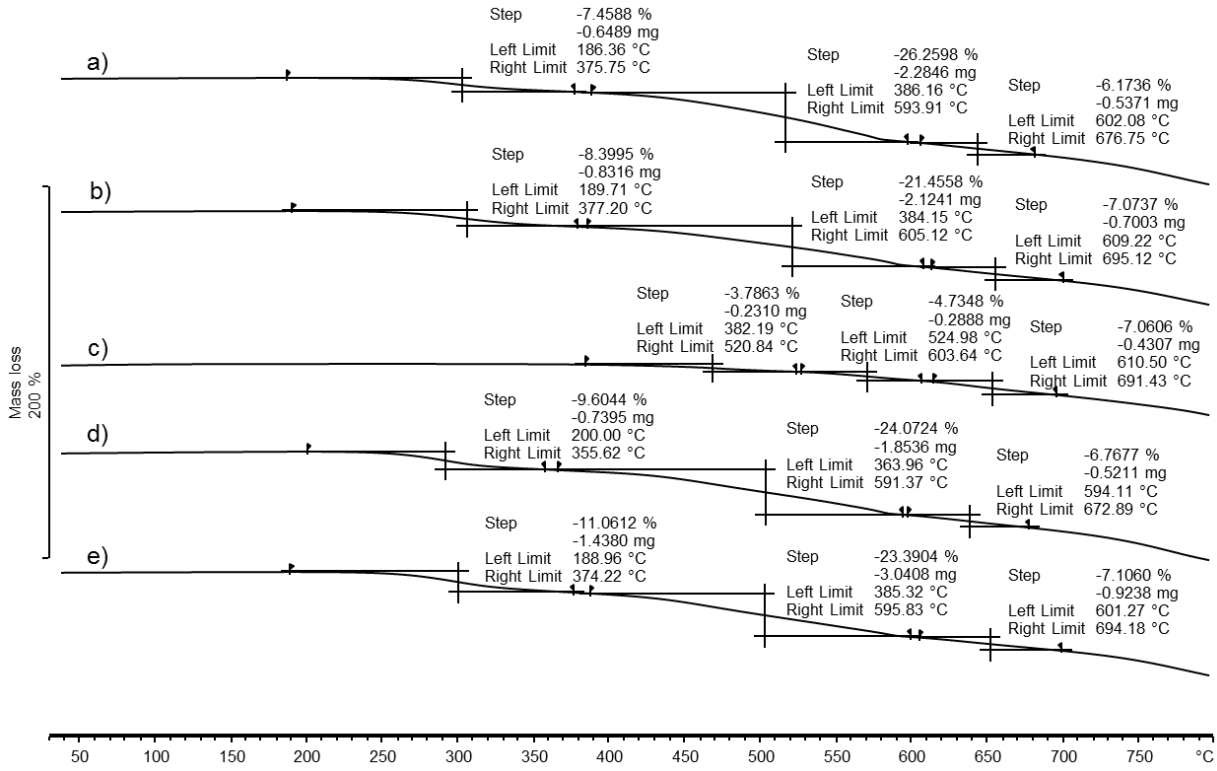

Figure E.4 TGA thermogram in N_2 of LeZIF8-M5 between nZIF-8 and methyl benzimidazole-2-ylthio valerate in methanol at different synthesis times: a) 4h, b) 16h, c) 24h, d) 72h and e) 168h.

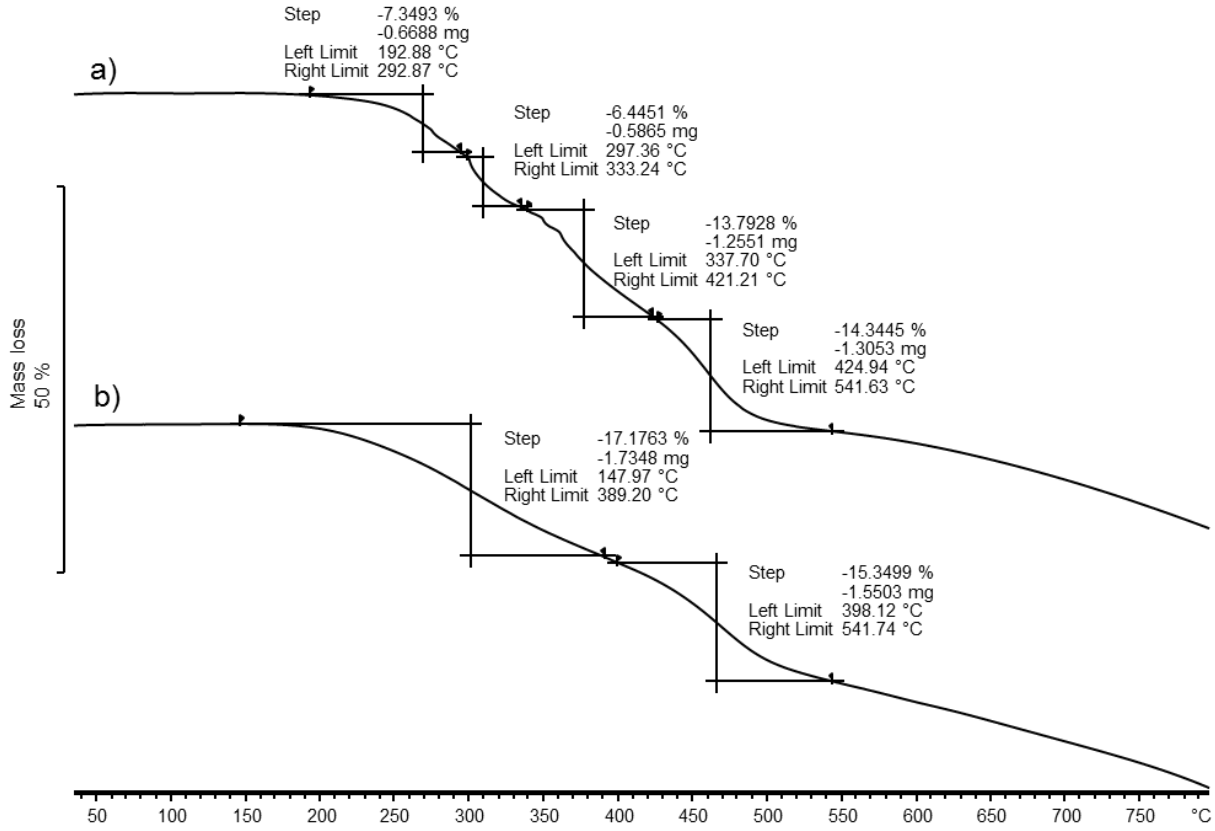

Figure E.5 TGA thermogram in N_2 of a) LeZIF8-NH_2BzIm(17h)-Seba(17h) and b) LeZIF8-NH_2BzIm(4h)-Seba(10min).

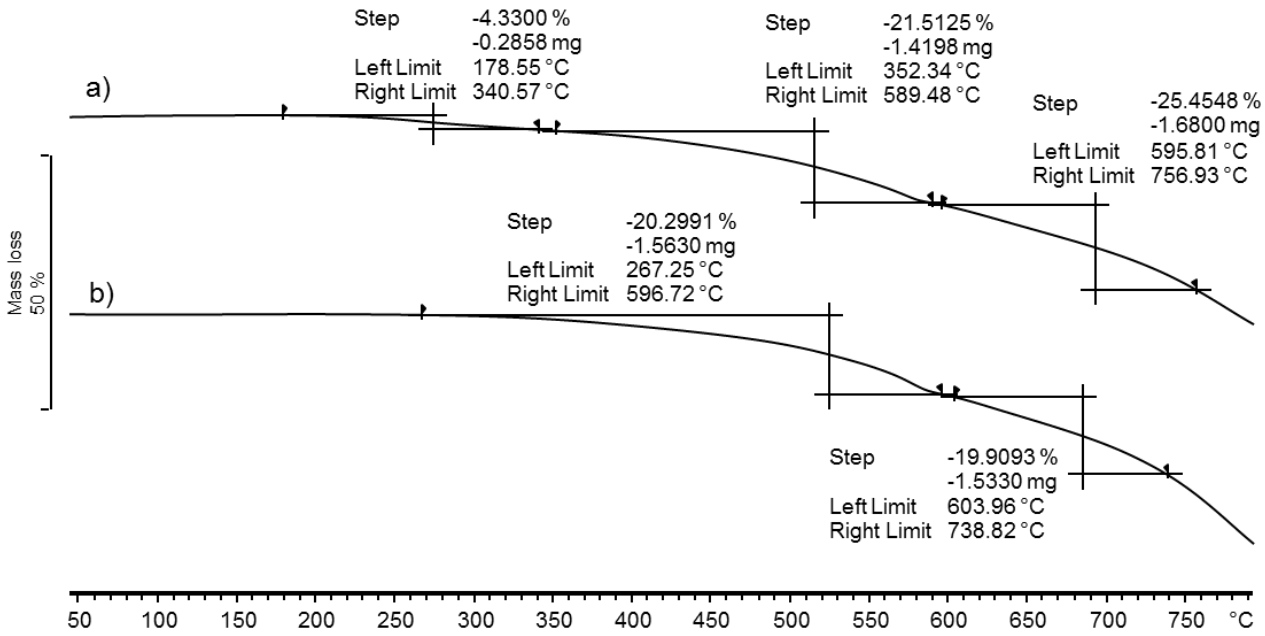

Figure E.6 TGA thermogram in N_2 of a) LeZIF8-E4$_{24h}$-Fc-diketone, b) LeZIF8-M2$_{24h}$-FcMNH.

F. Crystallographic Data

The ZIF-8 structure was solved to be in the cubic *I*-43m space group with Z = 4 using direct methods with the following crystal data with a unit cell dimension of 16.32 Å .

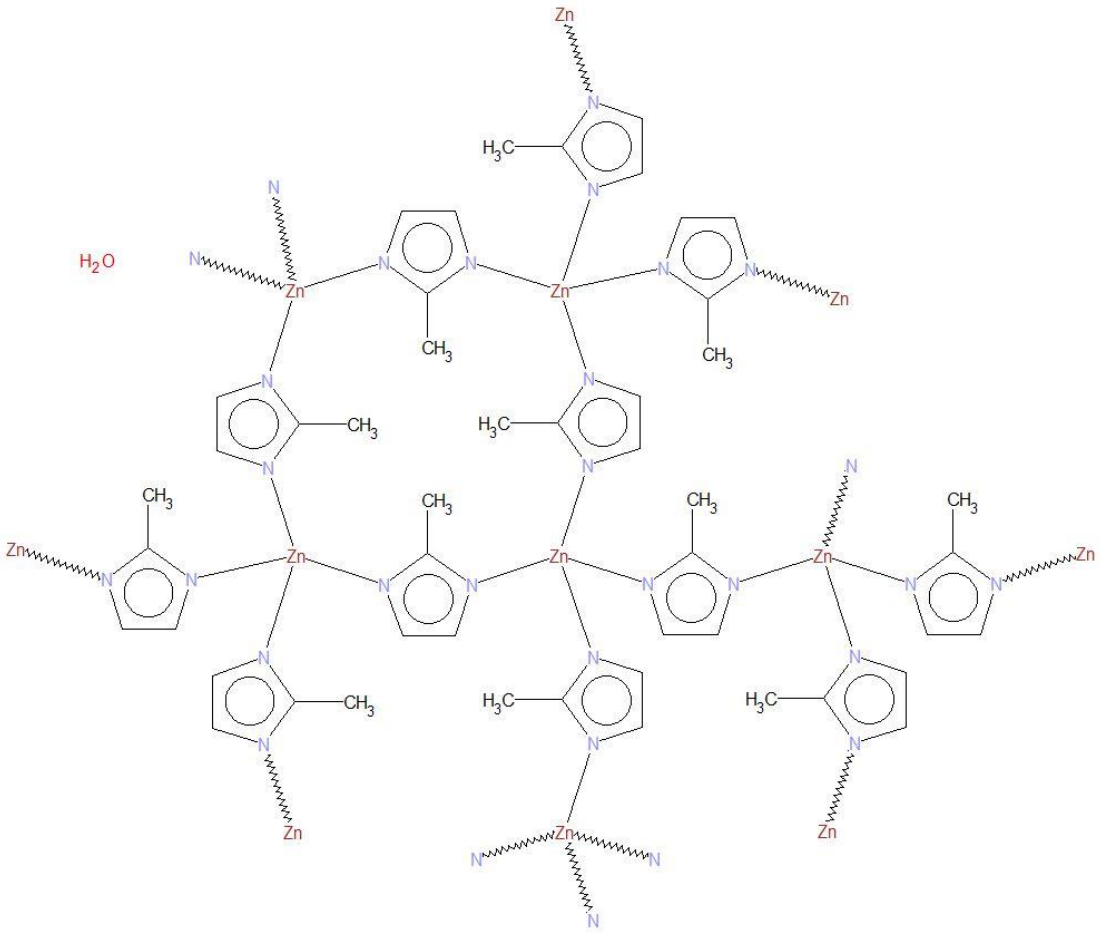

Figure F.1 Crystal structure of ZIF-8 (FAWCEN).

Table F.1 Crystal Data of ZIF-8.

Unit Cell dimension	a = 16.9910(12) Å	α= 90°.
	b = 16.9910(12) Å	β= 90°.
	c = 16.9910(12) Å	γ = 90°.
Volume	4905.2(6) Å	
Density (calculated)	1.141 mg m^{-3}	

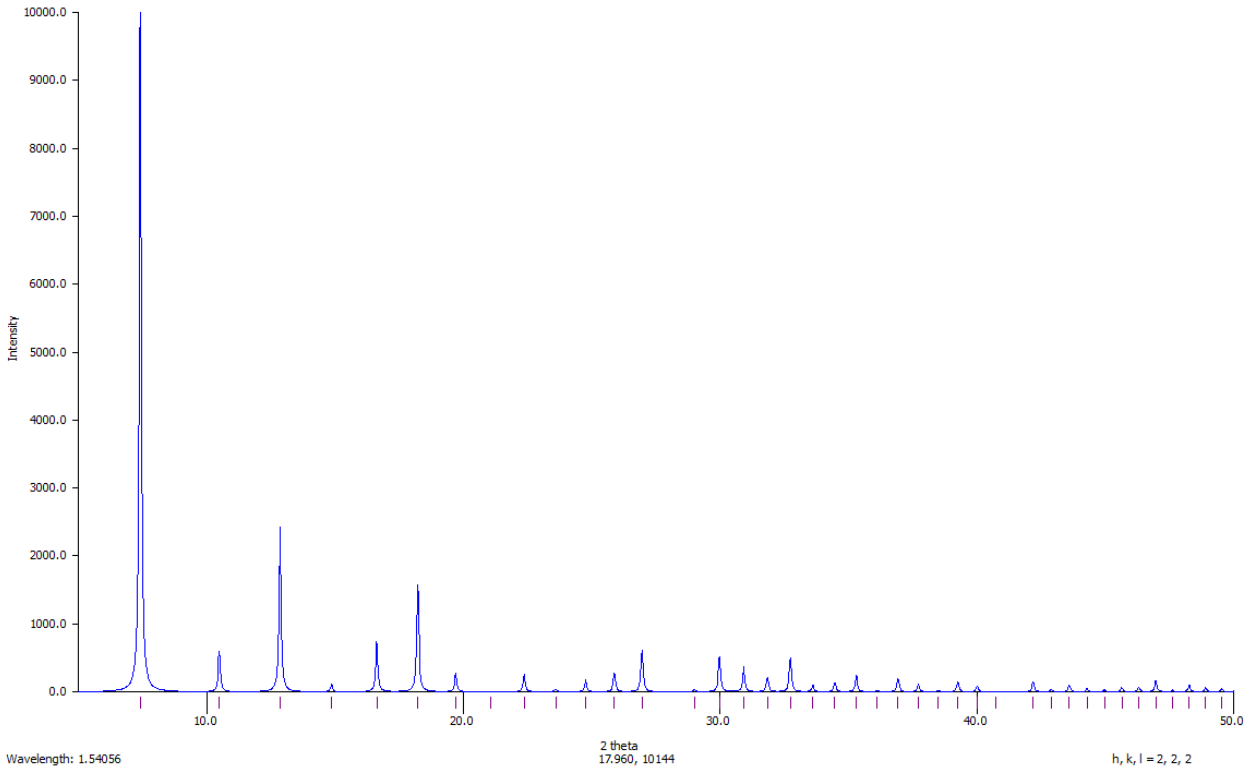

Figure F.2 Simulated PXRD pattern of ZIF-8 from single crystallography (FAWCEN).

Table F.2 Positions of as-synthesized PXRD and simulated PXRD of ZIF-8 with indices of diffraction.

As-synthesized PXRD		Simulated PXRD		Indices
2-Theta	d	2-Theta	d	hkl
7.31	12.085	7.35	12.015	011
10.24	8.629	10.40	8.496	002
12.65	6.994	12.75	6.937	112
14.67	6.035	14.73	6.007	022
16.03	5.433	16.48	5.373	013
17.84	4.905	18.07	4.905	222
22.02	4.033	22.18	4.005	114
24.38	3.648	24.55	3.623	233
26.64	3.343	26.73	3.332	134
29.72	3.004	29.72	3.004	044
30.44	2.934	30.65	2.914	334
31.69	2.821	31.57	2.832	244
32.41	2.760	32.46	2.756	235

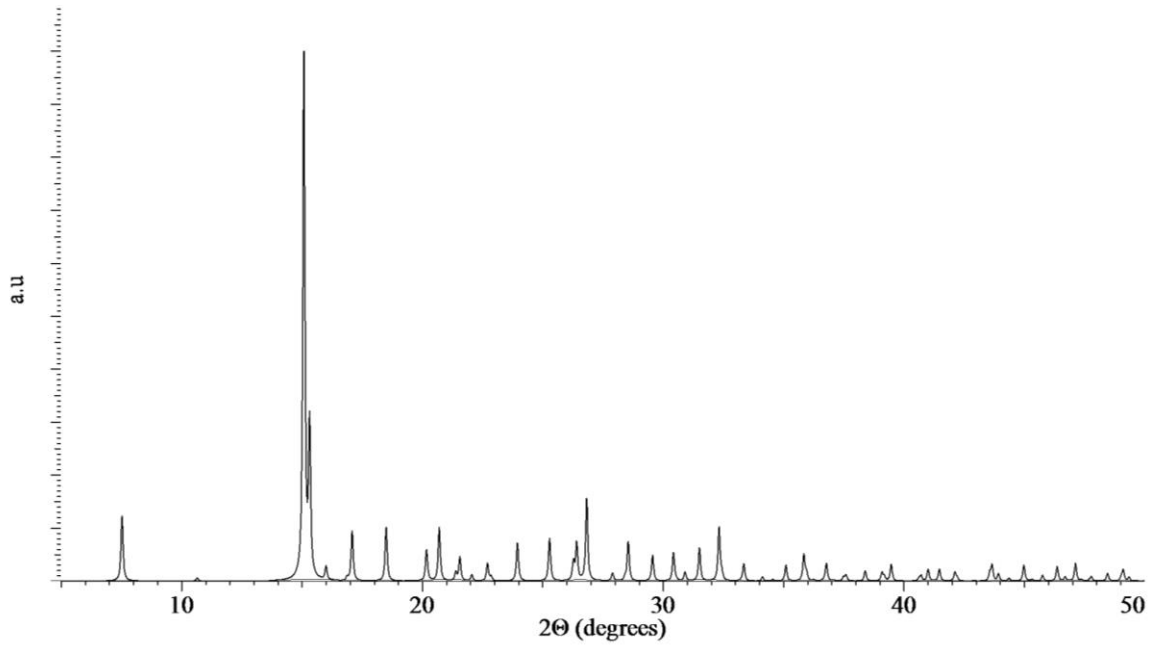

Figure F.3 Simulated PXRD pattern of $Zn(Im)_2$ from single crystallography (GITTAF).

G. Porosity Analysis

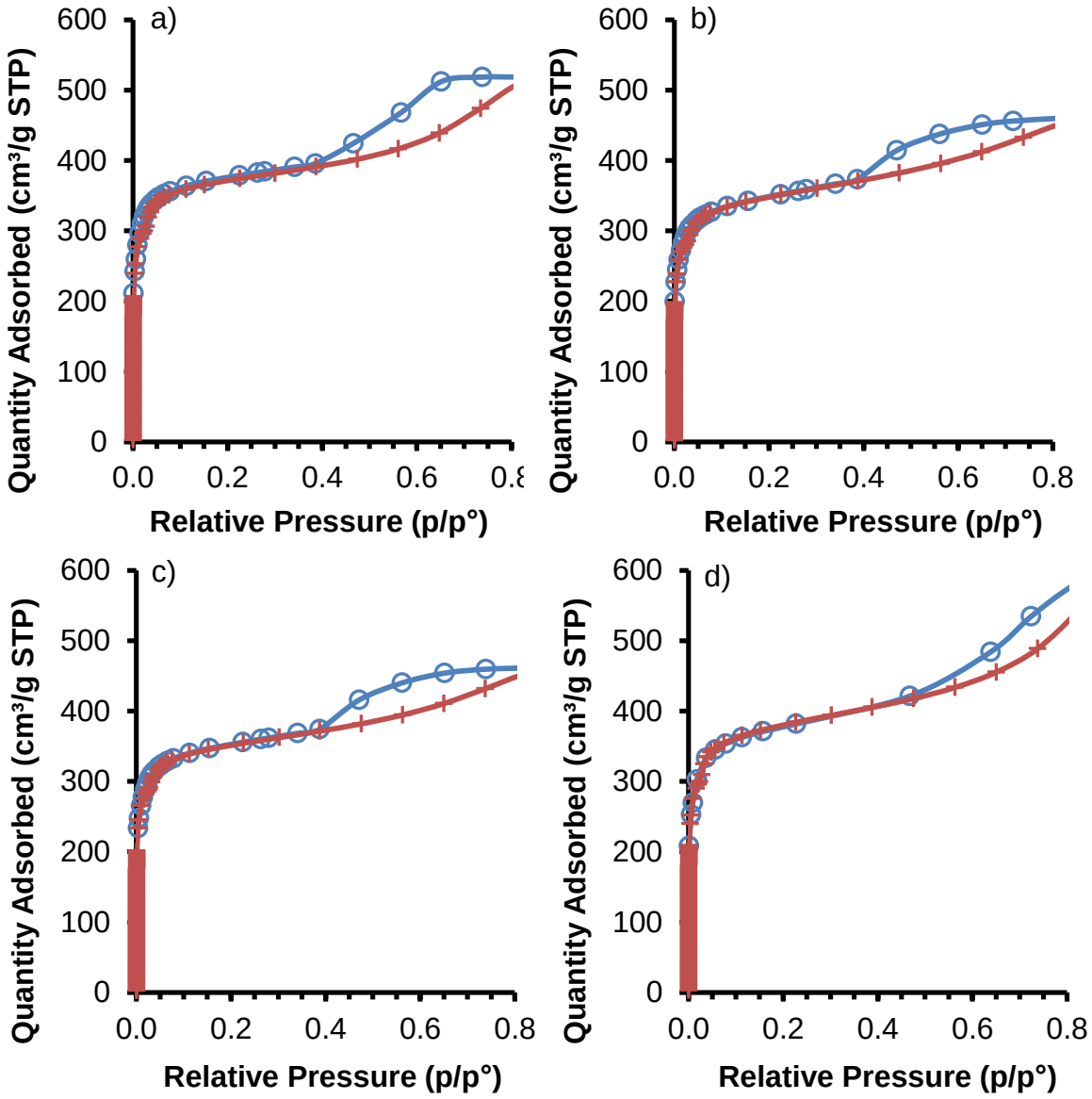

Figure G.1 N_2 isotherms at 77 K of nZIF-8 synthesised with TEA at different molar ratios: a) 2, b) 3, c) 4 and d) 8.

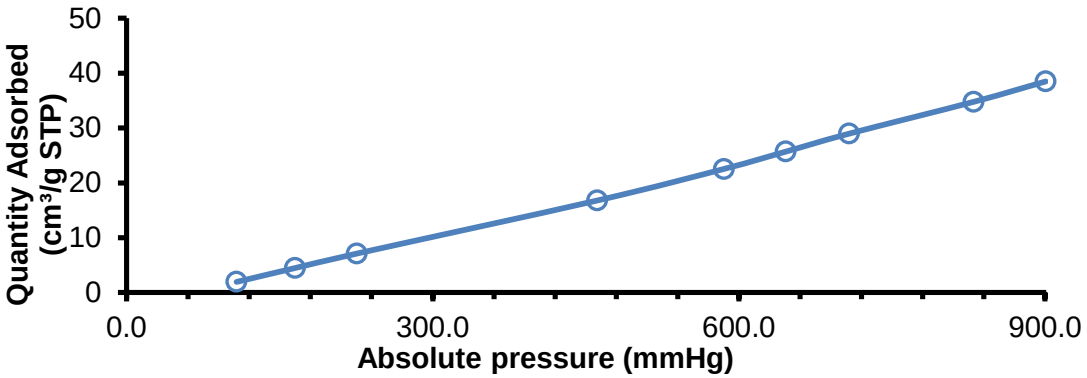

Figure G.2 CO_2 isotherms at 273 K absolute pressure of nZIF-8_{1500}.

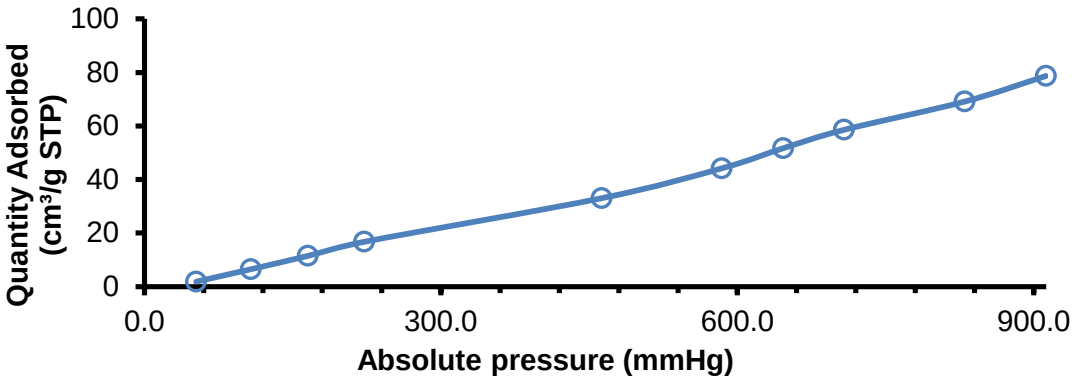

Figure G.3 CO_2 isotherms at 273 K absolute pressure of nZIF8-$SHBzIm_{72h}$.

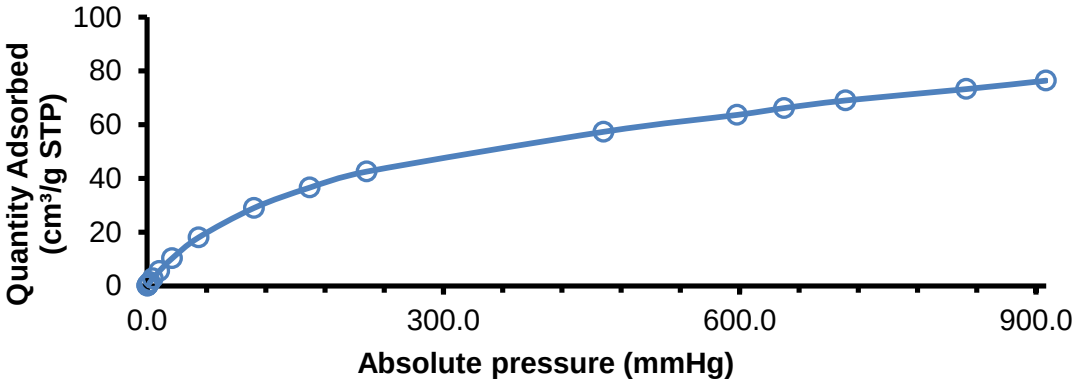

Figure G.4 CO_2 isotherms at 273 K absolute pressure of LeZIF8-NO_2Im_{168h}.

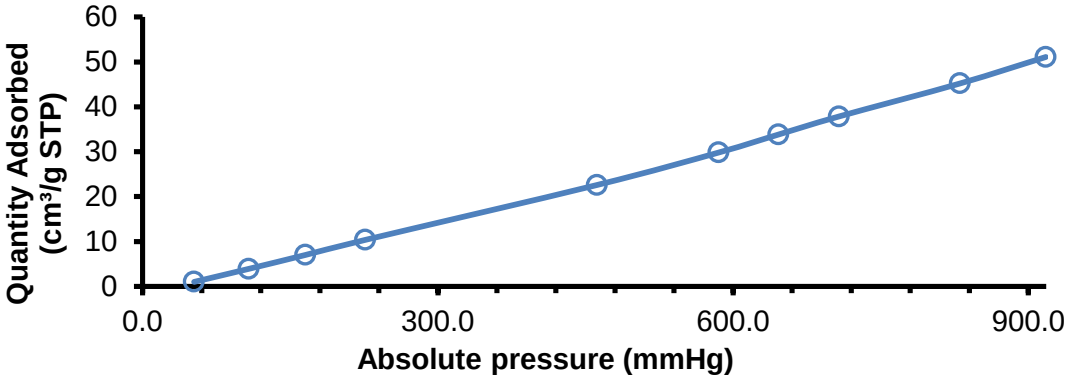

Figure G.5 CO_2 isotherms at 273 K absolute pressure of LeZIF8-$PhIm_{168h}$.

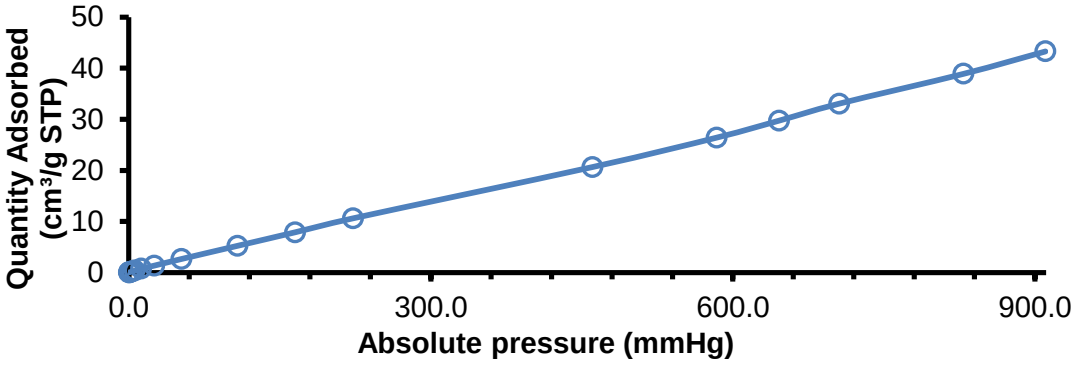

Figure G.6 CO_2 isotherms at 273 K absolute pressure of LeZIF8-NH_2BzIm$_{4h}$.

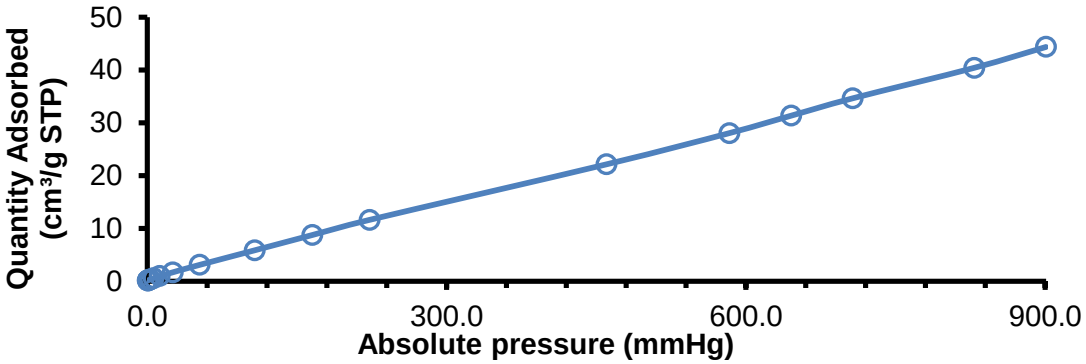

Figure G.7 CO_2 isotherms at 273 K absolute pressure of LeZIF8-NH_2BzIm$_{16h}$.

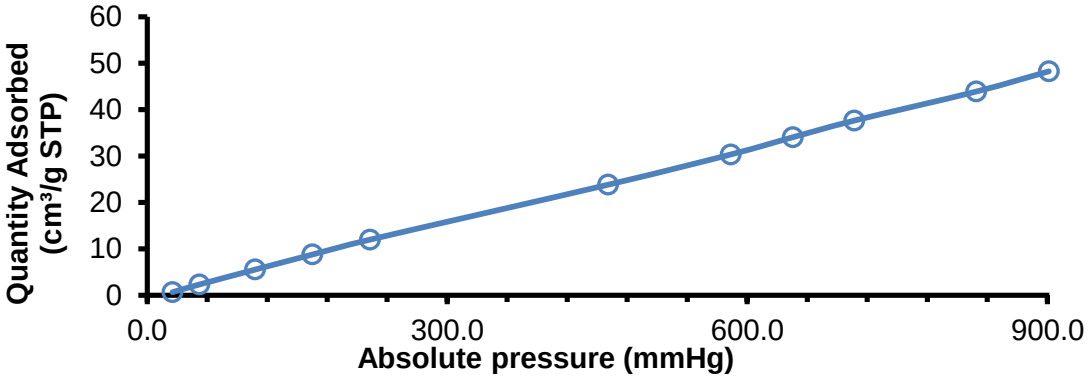

Figure G.8 CO_2 isotherms at 273 K absolute pressure of LeZIF8-NH_2BzIm$_{168h}$.

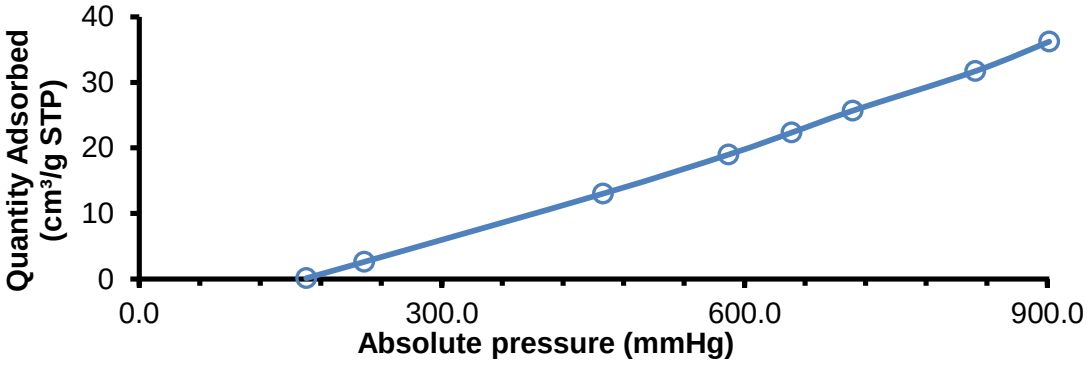

Figure G.9 CO_2 isotherms at 273 K absolute pressure of LeZIF8-M5$_{168h}$.

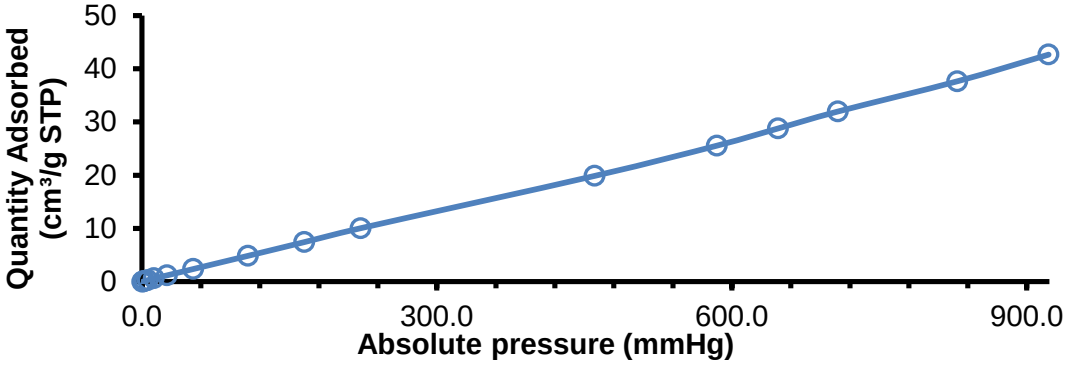

Figure G.10 CO_2 isotherms at 273 K absolute pressure of LeZIF8-E3$_{168h}$.

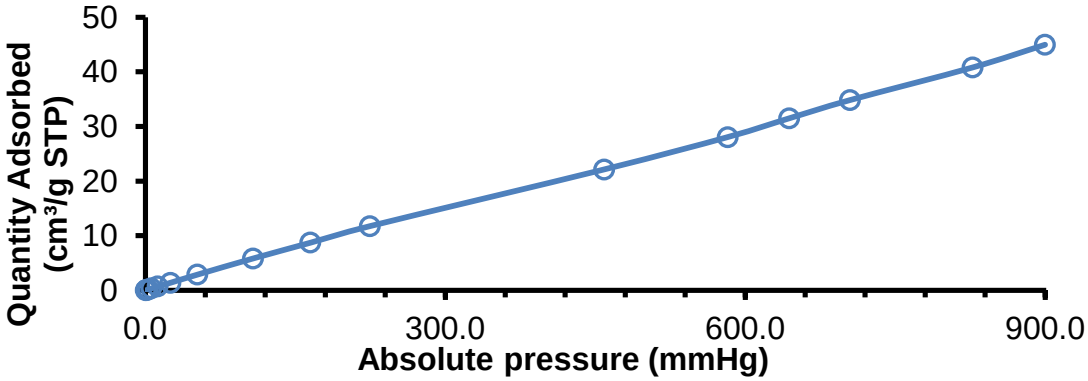

Figure G.11 CO_2 isotherms at 273 K absolute pressure of SALEM-2$_{16h}$.

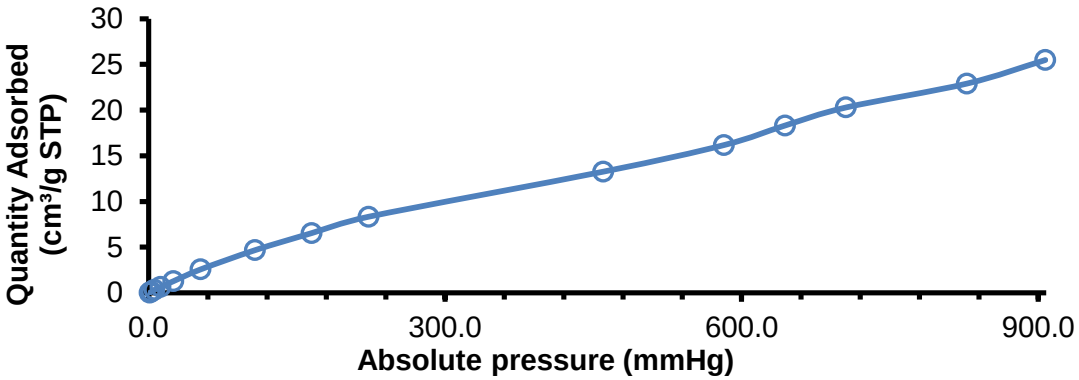

Figure G.12 CO_2 isotherms at 273 K absolute pressure of SALEM-2$_{168h}$.

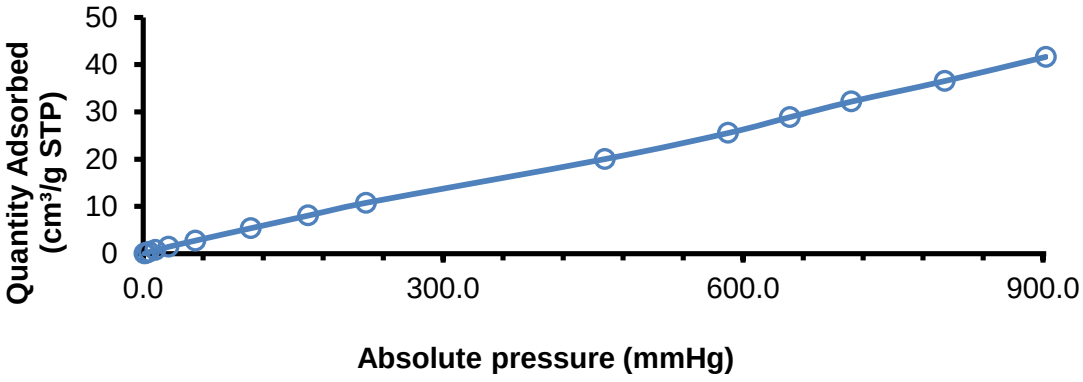

Figure G. 13 CO_2 isotherms at 273 K absolute pressure of LeZIF8-NH_2BzIm-PAA.

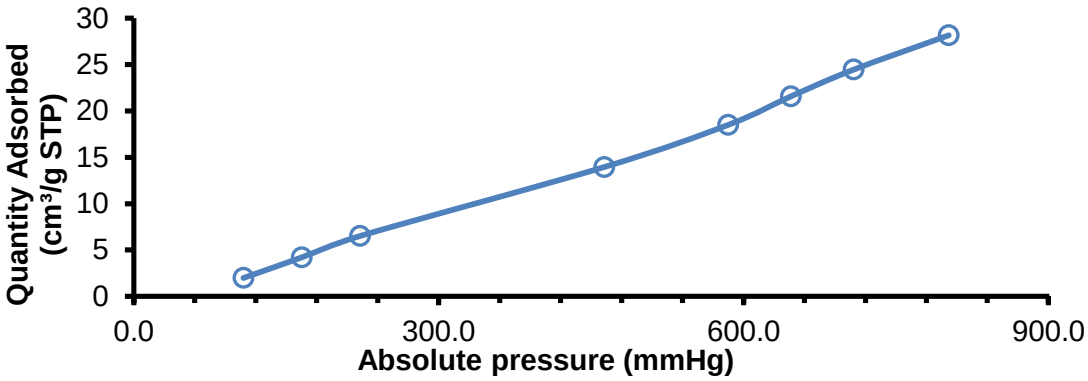

Figure G.14 CO_2 isotherms at 273 K absolute pressure of LeZIF8-NH_2BzIm(17h)-Seba(10min).

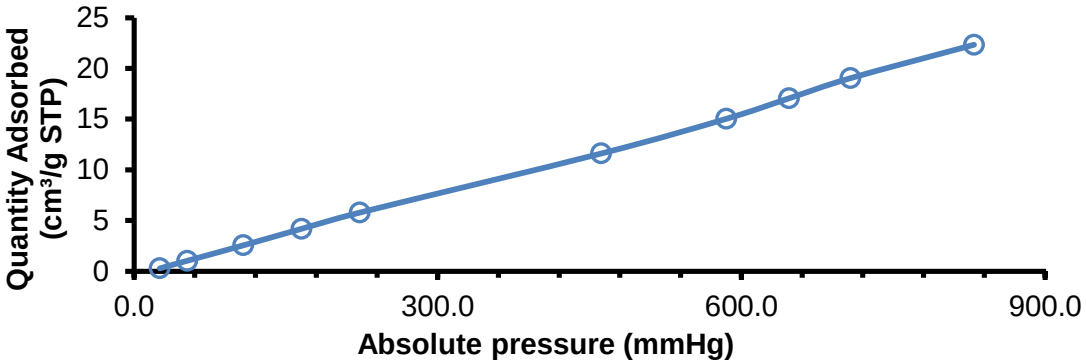

Figure G.15 CO_2 isotherms at 273 K absolute pressure of LeZIF8-NH_2BzIm-FcCO.

H. XPS Analysis

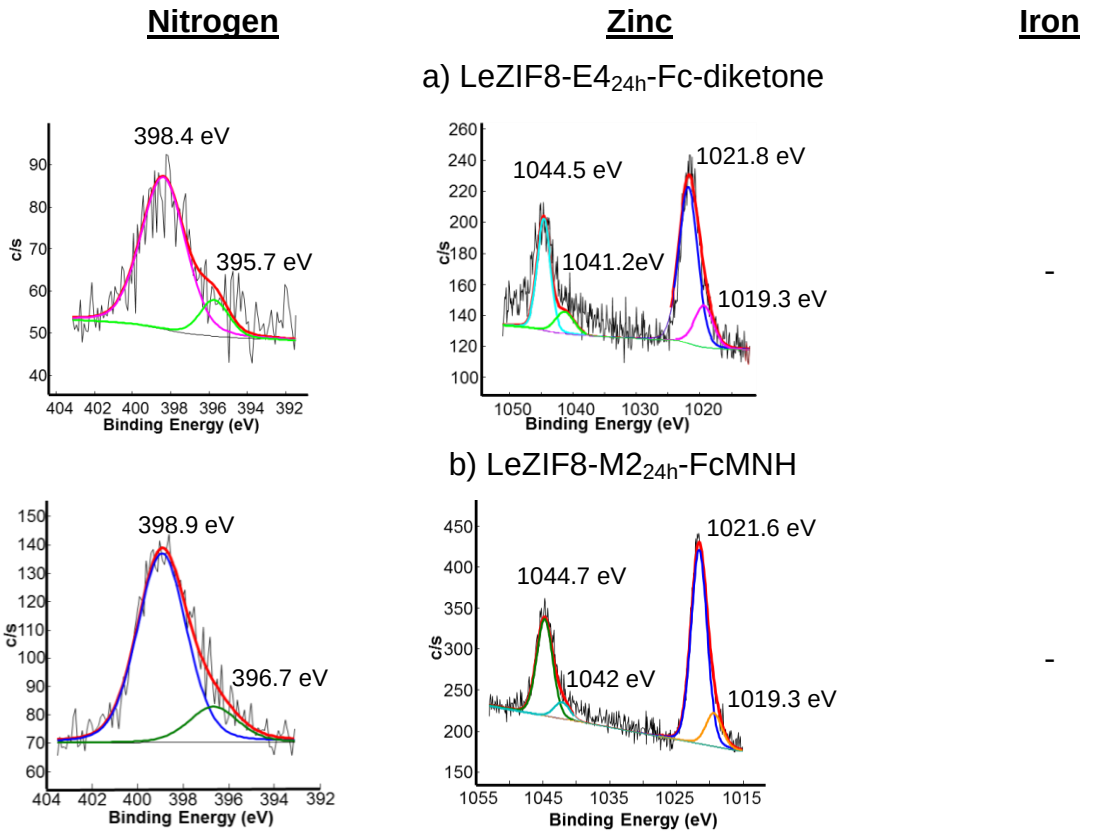

Figure H.1 XPS spectrum of N, Zn and Iron (where applicable) of a) LeZIF8-E4$_{24h}$-Fc-diketone and b) LeZIF8-M2$_{24h}$-FcMNH. Red line: theoretical fit. Other lines: Peaks introduced to replicate the experimental fit.

Appendix

Declaration

I, Chih-Wei Tsai, declare that the thesis hereby handed in for the qualification Philosophiae Doctor in Department of Chemistry at the University of the Free State is my own independent work and that I have not previously submitted the same work for a qualification at/in another university/faculty. I hereby declare that all royalties as regards intellectual property that was developed during the course of and/or in connection with the study at the University of the Free State, will accrue to the University. I furthermore cede copyright of the thesis in favour of the University of the Free State.

Signed 蔡志委

Date 4/4/2017